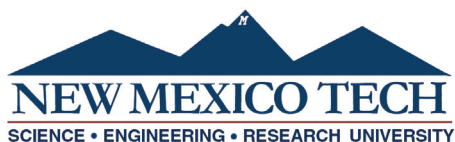


**NEW APPROACHES TO
GEOTHERMAL RESOURCE EXPLORATION
AND CHARACTERIZATION**

by

Jeffrey Donald Pepin

Submitted in Partial Fulfillment
of the Requirements for the Degree of
Doctor of Philosophy in Earth and Environmental Science
with Dissertation in Hydrology



New Mexico Institute of Mining and Technology
Socorro, New Mexico
February, 2019

ProQuest Number: 10978436

All rights reserved

INFORMATION TO ALL USERS

The quality of this reproduction is dependent upon the quality of the copy submitted.

In the unlikely event that the author did not send a complete manuscript and there are missing pages, these will be noted. Also, if material had to be removed, a note will indicate the deletion.



ProQuest 10978436

Published by ProQuest LLC (2018). Copyright of the Dissertation is held by the Author.

All rights reserved.

This work is protected against unauthorized copying under Title 17, United States Code
Microform Edition © ProQuest LLC.

ProQuest LLC.
789 East Eisenhower Parkway
P.O. Box 1346
Ann Arbor, MI 48106 – 1346

I dedicate this work to my family and friends. Thank you for all of the encouragement over the years, for being an inspiration, and for always being there for me.

Jeffrey Donald Pepin
New Mexico Institute of Mining and Technology
February, 2019

"Get busy living, or get busy dying."

Andy Dufresne

ABSTRACT

Advancement in the geothermal industry can be accelerated by the development of new and innovative tools to prospect, characterize, and evaluate geothermal resources. This work describes our efforts to develop two new approaches to studying geothermal systems. Additionally, electrical resistivity and hydrothermal modeling are used in conjunction to refine the conceptual model of crystalline-base ment hosted geothermal resources in tectonically-active rift environments. We begin by attempting to improve our ability to estimate subsurface hydraulic permeability patterns. Crustal permeability has profound implications on geothermal resource development potential and sustainability. We examine whether incorporating magnetotelluric (MT) geophysical observations into hydrothermal model calibration has potential to estimate permeability on a regional scale. This is done by modeling the electrical resistivity of a simplified regional groundwater flow system and then converting the results to MT data, which are directly sensitive to crustal fluids over a dynamic range of depths. All transport regimes and permeabilities considered yield distinctly different MT responses, which indicates that MT data is systematically affected by crustal permeability. By using a combination of hydrologic, forward MT, and inverse MT modeling, we conclude that electrical resistivity from MT data can likely estimate permeability by being integrated into hydrologic model calibration. Successful implementation of this approach hinges on having adequate control of subsurface porosity, mineralogy, and solute reaction rates.

The tectonically-active Rio Grande rift of New Mexico is believed to contain extensively-fractured and permeable crystalline basement rocks in select regions, which permit deep groundwater circulation. This deeply circulating groundwater ascends through gaps in overlying confining units and along faults to give rise to shallow geothermal resources. We combined forward hydrothermal modeling with MT and transient electromagnetic (TEM) geophysics to image a deep (6 to 10 km) crystalline basement-hosted groundwater flow system that is associated with the Truth or Consequences (T or C) geothermal resource along the central Rio Grande rift. Previously published hydrothermal models indicate that the effective hydraulic permeability of the crystalline basement in the T or C watershed must be unusually high (10^{-12} m^2) to explain measured hot-spring temperatures (41°C), geothermometer reservoir temperature estimates (170°C), vertical specific discharge rates (3 to 6 m/yr), and mean carbon-14 groundwater residence times (7,000 yr). We further evaluate this conceptual model using electrical resistivity and aquifer testing. Regional subsurface resistivity patterns imply the presence of a single-pass and deeply circulating regional groundwater flow system between the upland recharge area to the west and the T or C

hot-springs district near the Rio Grande to the southeast. The resistivity of the crystalline basement is observed to be between 100 and 200 ohm-m to depths of 10 km, which is typical of altered and saturated igneous and metamorphic rocks and is much more conductive than typical intact crystalline rocks. The homogeneity of basement resistivities indicates that fractures at depth are likely to be well-connected and prevalent throughout much of the watershed. Regional faults do not appear to compartmentalize the groundwater system but may serve as conduits for upwelling fluids. There is also a conductive (50 ohm-m) feature at 6 to 10 km depth below the T or C hot-springs district that may represent upwelling brackish geothermal fluids. This feature is reproduced well by hydrothermal models that we use to simulate electrical resistivity patterns. Aquifer testing carried out within the T or C hot-springs district estimate local crystalline basement permeability to be on the order of 4×10^{-10} m². Overall, these results indicate the likely presence of extremely permeable crystalline rocks on a regional scale that permit geothermal groundwater circulation to depths of up to 10 km within this watershed. This work provides evidence that seismically active rift settings with prolonged tectonic histories may contain extensive regions of highly-fractured crystalline rocks that facilitate groundwater circulation to great depth.

Lastly, we use principal component analysis (PCA) and k-means clustering to explore distinguishing characteristics between known-geothermal resources (KGRs) in southwest New Mexico. We then use those characteristics to outline a sub-region of higher geothermal potential and then prospect this sub-region by identifying non-KGR locations that are similar to its KGRs. Twenty geological, thermal, geochemical, and hydrologic datasets are incorporated into this analysis. Our approach indicates that geothermal resources in this area are distinguishable by their physiographic/tectonic province (e.g. Rio Grande rift, Basin and Range) and identifies two primary exploration areas that are related to classic forced-convection geothermal systems and secondary fracture permeability resources, respectively. The secondary permeability region is comprised primarily of low-temperature hot spring systems. The forced-convection region contains some of the hottest liquid-dominated resources in New Mexico. Further analysis of this hotter region indicates that the southeast portion of the study area is most likely to yield new economically-viable geothermal resources. Areas near Lordsburg, Las Cruces, Deming, and south of Socorro are believed to be particularly promising due to their strong relation to developed moderate (90 to 150°C) temperature geothermal resources within the study area. These target areas agree well with a recently published geothermal prospectivity map of the region. The PCA and clustering framework used in this study is most applicable to the preliminary and exploration phases of geothermal resource discovery, as it was able to classify KGRs on a regional scale, while also identifying regions of elevated geothermal potential.

Keywords: Geothermal Resource Characterization; Hydraulic Permeability; Hydrothermal Modeling; Magnetotellurics; Transient Electromagnetics; Principal Component Analysis

ACKNOWLEDGMENTS

Funding for this work was provided by National Science Foundation EP-SCoR Energize New Mexico grant IIA-1301346 and National Science Foundation grant EAR 1830172.

Many people have contributed to this work over the years in numerous ways; without them this would not have been possible. I'd like to thank my PhD committee, especially my advisor Mark Person, for their invaluable input, assistance, and mentorship; learning from and having them as examples has made me a much better scientist and researcher. Thanks to the several friends and colleagues that have pitched in to help out with field work; namely Reid Brown, John Ortiz, Kyle Stark, Luke Blom, Michelle Sherman, Adrianna Nieto, and Matthew Folsom. I'd like to thank Brad Sion for all of his help with this work, insightful conversations, and for being such a good friend to me throughout my time in graduate school. Thank you to Jim Witcher for believing in me and sharing his extensive knowledge of New Mexico and geothermal systems over the years. I've met a lot of friends for life during my time in Socorro and they have all helped me become a better person and ensured that I have kept (mostly kept) my sanity while in graduate school. I could not have done this without the unwavering support of my family and close friends. Thank you to Michael Hawkshaw for always being there and making sure my life did not become consumed by research. Special thanks to my brother, James Pepin, for being the best man that I know and for being the most incredible big brother anyone could ask for. Thank you to my parents, especially my mother, for being role models and always putting me in a position to fulfill my dreams and achieve my goals. Finally, I'd like to thank Carolyn Medin for her love, support, and partnership.

This dissertation was typeset with \LaTeX ¹ by the author.

¹The \LaTeX document preparation system was developed by Leslie Lamport as a special version of Donald Knuth's \TeX program for computer typesetting. \TeX is a trademark of the American Mathematical Society. The \LaTeX macro package for the New Mexico Institute of Mining and Technology dissertation format was written by John W. Shipman.

CONTENTS

	Page
LIST OF TABLES	vi
LIST OF FIGURES	vii
PREFACE	xi
INTRODUCTION	1
CHAPTER 1. CONSTRAINING HYDRAULIC PERMEABILITY AT GREAT DEPTH BY USING MAGNETOTELLURICS	2
1.1 Introduction	2
1.2 Methods	4
1.2.1 Flow & Transport Modeling	5
1.2.2 Magnetotelluric Modeling	8
1.3 Results & Discussion	8
1.4 Conclusions & Future Work	11
1.A Supporting Information	13
1.A.1 Introduction	13
1.A.2 Text S1.	13
1.A.3 Text S2.	15
1.A.4 Data Set S1.	17
1.A.5 Data Set S2.	17
1.A.6 Data Set S3.	17
1.A.7 Data Set S4.	18
CHAPTER 2. THE TRUTH OR CONSEQUENCES, NEW MEXICO GEOTHERMAL SYSTEM: INSIGHTS FROM ELECTRICAL RESISTIVITY AND AQUIFER TESTING	30
2.1 Introduction	31
2.2 Tectonic Setting & Conceptual Model	34

2.3	Methods	37
2.3.1	Aquifer Test	38
2.3.2	Transient Electromagnetic Survey	39
2.3.3	Magnetotelluric Survey	42
2.3.4	Hydrothermal Modeling	45
2.4	Results	47
2.4.1	Aquifer Test Results	47
2.4.2	Magnetotelluric Results	48
2.4.3	Transient Electromagnetic Results	49
2.4.4	Hydrothermal Modeling Results	52
2.5	Discussion	53
2.5.1	Interpretation	53
2.5.2	Synthesis	59
2.5.3	Additional Considerations & Limitations	60
2.6	Conclusions & Future Work	61
2.A	Aquifer Test Production Well Data	64
2.B	Electromagnetic Station Information	65
2.C	Magnetotelluric Sensitivity Analysis	67
2.D	Magnetotelluric Phase Tensors, Dimensionality Metrics, & Inverse Model Fits	69

CHAPTER 3. USING PRINCIPAL COMPONENT ANALYSIS & CLUSTERING FOR GEOTHERMAL RESOURCE EXPLORATION	100	
3.1	Introduction	101
3.2	Methods	102
3.2.1	Data Compilation and Preparation	105
3.2.2	Analysis of Known Geothermal Resources	106
3.2.3	Comprehensive Dataset Analysis	107
3.3	Results & Discussion	108
3.3.1	Known-Geothermal Resource Analysis Results	108
3.3.2	Comprehensive Dataset Analysis Results	112
3.3.3	Applicability & Limitations	119
3.4	Conclusions & Future Work	121
3.A	Dataset Preparation Processing Steps and Metadata	123
3.A.1	Extraction Grid	123
3.A.2	Spatial Density Layers	124

3.A.3	Contoured Layers	132
3.B	Compiled USGS Known-Geothermal Resource Layer	144
3.C	Correlation Heatmaps for Known Geothermal Resources	145
3.D	Additional Known Geothermal Resource Analysis Biplots	147
3.E	Winsorization Summary	150
3.F	KGR Scatter Plots and Correlations of Data Layers with Estimated Reservoir Temperature	151
CONCLUSION		155
REFERENCES		157

LIST OF TABLES

Table	Page
1.1 Damköhler numbers of all modeling scenarios explored	18
1.2 Parameters held constant in hydrothermal simulations.	19
1.3 Compariosn of Ucok et al. (1980) fluid resistivity model to the model derived in this study	19
2.1 Production well aquifer test data	64
2.2 TEM transect station location information	65
2.3 MT survey station location information	66
3.1 Datasets considered in the study. Eight spatial density layers and 12 contoured layers are included for a total of 20 datasets.	106
3.2 Summary of KGR cluster characteristics.	111
3.3 Compiled USGS known-geothermal resource layer	144
3.4 Summary of winsorized and identified outliers	150
3.5 KGR data layer correlations with reservoir temperature	153

LIST OF FIGURES

Figure	Page
Figure 1.1 Permeability depth-decay representations used in the hydrologic modeling effort. The high and low permeability curves correspond to the results presented in this paper. The Manning and Ingebritsen (M&I 1999) and Ingebritsen and Manning (I&M 2010) curves are commonly applied permeability relationships for regional models and are shown for reference.	6
Figure 1.2 Simulated temperatures (a,b), salinities (c,d) and effective electrical resistivities (e,f) from hydrologic modeling for the low permeability (a,c,e) and high permeability (b,d,f) simulations. Temperatures, salinity, and resistivity patterns are distinctly different for these two permeability scenarios.	9
Figure 1.3 Magnetotelluric invariant forward modeling results for two permeability scenarios (high and low) from the recharge (a; station 6, $x = 6$ km), middle (b; station 22, $x = 20$ km), and discharge (c; station 38; $x = 36$ km) areas of the model domain; see Figure 4a for station locations. The curves show a significant MT contrast across the entire domain for these permeabilities.	10
Figure 1.4 Forward model resistivity patterns compared with the recovered resistivity patterns after 2D inversion. The inversion results are unique for each scenario and compare well with the forward model resistivity patterns.	12
Figure 1.5 Thin-plate spline 10-fold cross-validation error verses model complexity (degrees of freedom) for 1,150 cross-validation realizations	20
Figure 1.6 Resistivity surface produced by the generalized cross-validated 76 degrees of freedom thin-plate spline model	21
Figure 1.7 Resistivity predicted by the thin-plate spline model as a function of salinity at various temperatures	22
Figure 1.8 Percent difference error of model predictions verses 243 previously-published resistivity measurements	23
Figure 1.9 Percent difference error of model predictions verses resistivity for 243 previously-published resistivity measurements	24

Figure 1.10 Percent difference error of model predictions verses concentration (i.e. salinity) for 243 previously-published resistivity measurements	25
Figure 1.11 Percent difference error of model predictions verses temperature for 243 previously-published resistivity measurements	26
Figure 1.12 Magnetotelluric (MT) WinGLink mesh used for inverse analysis	27
Figure 1.13 WinGLink settings used for all magnetotelluric inversions	28
Figure 1.14 Simulated resistivity from hydrothermal modeling effort for numerous permeability-decay schemes and solute source terms	29
 Figure 2.1 Electrical resistivity of common fluids and earth materials	33
Figure 2.2 Study area basemap	35
Figure 2.3 Conceptual model for the geothermal system	36
Figure 2.4 Aquifer test layout and stratigraphy	39
Figure 2.5 Depiction of the transient electromagnetic method.	40
Figure 2.6 Basemap showing TEM transect across the Cuchillo Negro fault zone near Alamosa Creek	41
Figure 2.7 Aquifer test drawdown and drawdown derivative plots	48
Figure 2.8 Depth slices of MT inversion resistivity results	50
Figure 2.9 Cross-sectional slices of MT inversion resistivity results	51
Figure 2.10 MT phase tensors and normalized skew angle overlaid on fault locations	51
Figure 2.11 TEM inversion resistivity results	52
Figure 2.12 Hydrothermal modeling temperature, salinity, and electrical resistivity results	54
Figure 2.13 Fault density, gravitational Bouger anomaly, and magnetic intensity maps of T or C watershed	56
Figure 2.14 MT resistivity compared to simulated resistivity	58
Figure 2.15 Sensitivity analysis results for two prominent features in the MT inversion results.	68
Figure 2.16 MT #3 phase tensors, dimensionality, and model fits	70
Figure 2.17 MT #4 phase tensors, dimensionality, and model fits	71
Figure 2.18 MT #5 phase tensors, dimensionality, and model fits	72
Figure 2.19 MT #6 phase tensors, dimensionality, and model fits	73
Figure 2.20 MT #7 phase tensors, dimensionality, and model fits	74
Figure 2.21 MT #8 phase tensors, dimensionality, and model fits	75

Figure 2.22 MT #9 phase tensors, dimensionality, and model fits	76
Figure 2.23 MT #10 phase tensors, dimensionality, and model fits	77
Figure 2.24 MT #11 phase tensors, dimensionality, and model fits	78
Figure 2.25 MT #12 phase tensors, dimensionality, and model fits	79
Figure 2.26 MT #13 phase tensors, dimensionality, and model fits	80
Figure 2.27 MT #14 phase tensors, dimensionality, and model fits	81
Figure 2.28 MT #15 phase tensors, dimensionality, and model fits	82
Figure 2.29 MT #16 phase tensors, dimensionality, and model fits	83
Figure 2.30 MT #17 phase tensors, dimensionality, and model fits	84
Figure 2.31 MT #18 phase tensors, dimensionality, and model fits	85
Figure 2.32 MT #19 phase tensors, dimensionality, and model fits	86
Figure 2.33 MT #20 phase tensors, dimensionality, and model fits	87
Figure 2.34 MT #21 phase tensors, dimensionality, and model fits	88
Figure 2.35 MT #22 phase tensors, dimensionality, and model fits	89
Figure 2.36 MT #23 phase tensors, dimensionality, and model fits	90
Figure 2.37 MT #24 phase tensors, dimensionality, and model fits	91
Figure 2.38 MT #25 phase tensors, dimensionality, and model fits	92
Figure 2.39 MT #26 phase tensors, dimensionality, and model fits	93
Figure 2.40 MT #27 phase tensors, dimensionality, and model fits	94
Figure 2.41 MT #28 phase tensors, dimensionality, and model fits	95
Figure 2.42 MT #29 phase tensors, dimensionality, and model fits	96
Figure 2.43 MT #30 phase tensors, dimensionality, and model fits	97
Figure 2.44 MT #31 phase tensors, dimensionality, and model fits	98
Figure 2.45 MT #32 phase tensors, dimensionality, and model fits	99
 Figure 3.1 Southwest New Mexico study area.	103
Figure 3.2 PCA scree plot (A), WSS cluster plot (B) and Euclidean-distance plot (C) that are used to determine the appropriate number of PCs and clusters to consider in the KGR analysis.	109
Figure 3.3 PC1 vs. PC2 biplot and spatial map summarizing KGR PCA results	110
Figure 3.4 Comprehensive dataset biplot cluster summary.	113
Figure 3.5 All comprehensive dataset clusters plotted spatially.	115
Figure 3.6 PCA results for the cluster one sub-dataset.	117
Figure 3.7 Geothermal potential results and prospectivity contours of Bielicki et al. (2015, 2016) for comparison.	118

Figure 3.8	Grid used to extract data values for all data layers.	123
Figure 3.9	Drainage density data layer.	124
Figure 3.10	Earthquake density data layer.	125
Figure 3.11	Quaternary fault density data layer.	126
Figure 3.12	Quaternary fault intersection data layer.	127
Figure 3.13	Spring density data layer.	128
Figure 3.14	State map fault density data layer.	129
Figure 3.15	Volcanic dike density data layer.	130
Figure 3.16	Volcanic vent density data layer.	131
Figure 3.17	Boron concentration data layer	132
Figure 3.18	Crustal thickness data layer.	133
Figure 3.19	Depth to basement data layer.	134
Figure 3.20	Depth to water data layer.	135
Figure 3.21	Elevation data layer.	136
Figure 3.22	Gravity anomaly data layer.	137
Figure 3.23	Heat flow data layer.	138
Figure 3.24	Hydraulic gradient data layer.	139
Figure 3.25	Lithium concentration data layer.	140
Figure 3.26	Magnetic intensity data layer.	141
Figure 3.27	Precipitation data layer.	142
Figure 3.28	Silica geothermometer temperature data layer.	143
Figure 3.29	Pre-wisnorization KGR Pearson correlation heatmap	145
Figure 3.30	Post-winsorization KGR Pearson correlation heatmap	146
Figure 3.31	PC1 vs. PC3 KGR biplot.	147
Figure 3.32	PC1 vs. PC4 KGR biplot.	148
Figure 3.33	PC2 vs. PC3 KGR biplot.	148
Figure 3.34	PC2 vs. PC4 KGR biplot.	149
Figure 3.35	PC3 vs. PC4 KGR biplot.	149
Figure 3.36	Scatter plots for select KGR variables vs. estimated reservoir temperature	154

This dissertation is accepted on behalf of the faculty of the Institute by the following committee:

Mark A. Person

Academic and Research Advisor

Fred M. Phillips

Shari Kelley

Jared R. Peacock

Jesus Gomez-Velez

I release this document to the New Mexico Institute of Mining and Technology.

Jeffrey Donald Pepin

December 5, 2018

PREFACE

This dissertation is written as three independent journal manuscripts; each chapter is a separate manuscript. The first chapter was submitted to *Geophysical Research Letters* at the time that this document was finalized. The second chapters are drafts of manuscripts that will be submitted after the acceptance of this dissertation. The anticipated author lists and their affiliations are provided below:

Chapter 1: ¹Pepin JD, ²Gomez-Velez JD, ¹Person MA, ³Kelley S, ⁴Peacock JR (*submitted*) Constraining hydraulic permeability at great depth by using magnetotellurics. *Geophysical Research Letters*.

Chapter 2: ¹Pepin JD, ⁴Peacock JR, ¹Person MA, ⁵Sion BS, ³Kelley S, ⁶Butler Jr. JJ (*in prep*) The Truth or Consequences, New Mexico geothermal system: Insights from electrical resistivity and aquifer testing.

Chapter 3: ¹Pepin JD, ²Gomez-Velez JD, ⁵Sion BS, ³Kelley S, ¹Person MA (*in prep*) Using principal component analysis and clustering for geothermal resource exploration.

¹Hydrology Program, Department of Earth and Environmental Science, New Mexico Institute of Mining and Technology, Socorro, New Mexico, USA

²Department of Civil & Environmental Engineering, Vanderbilt University, Nashville, Tennessee, USA

³New Mexico Bureau of Geology and Mineral Resources, New Mexico Institute of Mining and Technology, Socorro, New Mexico, USA

⁴U.S. Geological Survey, Menlo Park, California, USA

⁵Division of Earth and Ecosystem Sciences, Desert Research Institute, Reno, Nevada, USA

⁶Kansas Geological Survey, Lawrence, Kansas, USA

INTRODUCTION

Geothermal resources are found worldwide within continental crust that has adequate heat, water, and hydraulic permeability (Anderson et al. 2011). Temperatures of these systems vary and dictate the application(s) that a resource can be developed for. High temperature resources are most often developed for electricity generation. Low temperature systems are more commonly developed for direct-use applications. Examples of direct use applications include district heating, commercialized hot springs, greenhouse agriculture, snow melting, and aquaculture (Lund et al. 2011, Quick et al. 2013). Geothermal development is often burdened with high prospecting and exploration costs. Accelerated industry advancement may result from the development of new and innovative tools that reduce these expenses (Harvey & Beardmore 2014). This study explores two new approaches that aim to enhance our understanding of geothermal resources. The first includes using subsurface electrical resistivity from magnetotelluric geophysical data to estimate the hydraulic permeability patterns of continental crust on regional scales. The second approach combines principal component analysis with k-means clustering to determine distinguishing characteristics between known-geothermal resources. These characteristics are then used to identify promising exploration targets within the area of interest.

The cost of geothermal exploration can also be reduced by better understanding how geothermal resources form. Specifically, learning more about their associated regional groundwater flow patterns and controlling geologic features can likely greatly improve geothermal exploration success rates. The Rio Grande rift of New Mexico is thought to host geothermal systems that involve deep groundwater circulation within very permeable and highly fractured crystalline basement rocks. Previously published hydrothermal models indicate the permeability of the basement rocks in these systems is likely exceptionally high (10^{-14} to 10^{-12} m^2) with values that are more often typical of silty sand, karst limestone, and sandstone (Freeze & Cherry 1979, Mailloux et al. 1999, Person et al. 2013, Pepin et al. 2015). We further evaluate the conceptual model of these unique resources by imaging and modeling the subsurface electrical resistivity patterns of the Truth or Consequences basement-hosted geothermal system in the central Rio Grande rift. Aquifer testing is also undertaken within the geothermal upflow zone of this resource to provide a direct measurement of basement permeability.

It is our hope that this work will serve to provide new tools and insight to enable hydrologists, geophysicists, and researchers in the geothermal industry to less expensively and more effectively explore and characterize the Earth's crust on regional scales.

CHAPTER 1

CONSTRAINING HYDRAULIC PERMEABILITY AT GREAT DEPTH BY USING MAGNETOTELLURICS

This chapter is presented as first submitted to *Geophysical Research Letters*.

Pepin JD, Gomez-Velez JD, Person MA, Kelley S, Peacock JR (*submitted*) Constraining Hydraulic Permeability at Great Depth by Using Magnetotellurics. *Geophysical Research Letters*.

Abstract

Knowledge of crustal hydraulic permeability patterns is limited, but has profound implications for advancing fields including water sustainability, nuclear waste disposal, and enhanced geothermal system development. Novel approaches that can more affordably quantify crustal permeability, or at least reduce its uncertainty, are required. The purpose of this study is to determine if incorporating electrical resistivity observations into hydrologic model calibration can potentially estimate hydraulic permeability. Electrical resistivity of a simplified regional groundwater flow system is modeled and converted to magnetotelluric (MT) data, which is directly sensitive to crustal fluids over a dynamic range of depths (0.1–100 km). By using a combination of hydrologic, forward MT, and inverse MT modeling, we conclude that electrical resistivity derived from MT data can likely identify advection-dominated environments and estimate permeability through integration into hydrologic model calibration. Successful implementation of this approach hinges on having adequate control of subsurface porosity, mineralogy, and solute reaction rates.

1.1 Introduction

Constraining hydraulic permeability within the continental crust has been a topic of interest for over 35 years (Brace, 1980; Manning & Ingebritsen, 1999). And yet, knowledge of regional permeability, especially at depths below 3 km, remains limited (Gleeson & Ingebritsen, 2017). Researchers have invested substantial effort in compiling global crustal permeability information to define a

typical relationship between permeability and depth (Ingebritsen & Manning, 2010; Manning & Ingebritsen, 1999; Stober & Bucher, 2007 2015a). However, some studies indicate that crustal permeability may be too complex to be represented by a general relationship and that there is little permeability depth-dependence in the upper 2.5 km of the crust, where the majority of permeability data are available (Ranjram et al., 2015; Rojstaczer et al., 2008). Deep (> 3 km) permeability knowledge is primarily based on data collected in a handful of exceptionally deep wells, along with inferences from geothermal observations and numerical models (Ingebritsen & Manning, 2010; Juhlin & Sandstedt, 1989; Manning & Ingebritsen, 1999; Stober & Bucher, 2015a). Despite a large effort, crustal permeability remains an ongoing topic of debate.

Permeability is often a major source of uncertainty in regional hydrologic models (Franssen et al., 2009; Refsgaard et al. 2012). In some instances, assumptions about permeability can have important implications. For example, in the search for suitable disposal sites for nuclear waste, Sandia National Laboratories investigated the feasibility of disposing high-level radioactive waste in 3 to 5 km-deep boreholes (Brady et al., 2009). Their computational simulations represent the crust as having marginal permeability (10^{-19} m^2) at these depths. The authors conclude that radionuclides are expected to remain sequestered until radioactivity is negligible due to the lack of advection and permeability in the crust at the disposal depth. Quantitative reconstructions of induced seismicity (Zhang et al., 2016) and analysis of temperature disturbances from deep boreholes (Townend & Zoback, 2000) suggest that mid-continent crustal permeability at depths below 4 km may actually be much higher than that assumed by Brady et al. (2009). The nuclear waste disposal researchers reasonably make the assumption of minimal permeability in the deep crust but have to rely on an extremely limited dataset to do so (Juhlin & Sandstedt, 1989). The high stakes associated with their study and importance of permeability in their conclusions emphasizes the need to improve our ability to estimate deep crustal permeability.

Regional permeability knowledge also has immediate implications for groundwater sustainability and geothermal applications. Enhanced geothermal systems (EGS) involve using hydraulic fracturing to increase the permeability of the crust in areas that have elevated heat flow but little permeability. Once permeability is adequately enhanced, water can be circulated through the subsurface to mine heat for electricity generation (Jeanloz & Stone 2013). Total United States energy consumption in 2005 amounts to an estimated 0.0007% of the geothermal energy underlying the country at depths between 3 and 10 km (Polsky et al., 2008). Current EGS success rates are low, primarily due to the inability to increase permeabilities to production levels (Stober & Bucher, 2015b). Philipp et al. (2007) stress the need to focus EGS efforts in regions where the structural and tectonic settings promote successful permeability enhancement. Hydrologic modeling results of Mailloux et al. (1999) and Pepin et al. (2015) indicate that tectonically active rift environments have extensive regions of naturally-elevated permeability at great depth (4 to 10 km), which would require less dramatic permeability enhancement. However, these models are subject

to large permeability uncertainties that would benefit greatly from additional constraints.

The primary challenge with estimating deep permeability is a lack of wells that permit deep aquifer testing, as drilling is often prohibitively expensive (Gleeson & Ingebritsen, 2017). Novel approaches that can more affordably quantify crustal permeability, or at least reduce its uncertainty, are required. A potential solution is to incorporate magnetotelluric (MT) data into hydrologic model calibration to inversely determine permeability. MT is an electromagnetic geophysical method that has the ability to estimate subsurface electrical resistivity ($1/\text{conductivity}$) to depths from 0.01 to over 100 km (Chave & Jones 2012). The resistivity of deep groundwater is often much less than its surroundings due to elevated fluid salinity and temperature. This resistivity contrast tends to be greater when the fluid is well-connected via fractures (i.e. higher permeability). It is becoming increasingly more common for geophysicists and hydrogeologists to use MT to infer groundwater flow and fracture patterns (Jiang et al. 2014, Jiracek et al., 1996; Munoz 2014, Peacock et al., 2013, 2015; Pellerin et al., 1996; Wannamaker et al., 1983, 2004, 2010, 2013). However, little work has been done to directly link magnetotellurics and hydrologic models. Pritchett (2004) and Garg et al. (2007) perhaps make the most prominent contributions, by using hydrologic models, along with geophysical post-processors, to investigate the effectiveness of multiple geophysical methods for imaging geothermal reservoirs. These authors conclude that self-potential, direct-current resistivity, and magnetotellurics all show promise for imaging geothermal systems. The purpose of this study is to explore the sensitivity of MT to hydraulic permeability by estimating the MT response to several modeled permeability scenarios for a generalized regional groundwater flow system. We demonstrate that each transport regime results in an exclusive MT inversion result, thereby implying MT can be a valuable tool for hydrologic model calibration and reduction of permeability uncertainty.

1.2 Methods

Our approach begins by simulating groundwater, heat, and solute transport using a hydrologic model of an idealized regional flow system with a given permeability. We use the resulting salinities and temperatures to calculate the theoretical electrical resistivity of the flow system. These resistivity patterns are input to a forward MT modeling program to estimate theoretical MT field data as if measured at stations along the surface of the flow system. Finally, noise is added to the synthetic MT data and it is inversely modeled as if it is real data. This process is repeated for different permeabilities. Recovery of unique inversion results for different scenarios would indicate MT is likely a useful model calibration tool for estimating permeability. Each of these steps are detailed in the following sections and Supporting Information.

1.2.1 Flow & Transport Modeling

The hydrologic modeling approach employs COMSOL Multiphysics to solve fully-coupled single-phase, transient groundwater flow and solute and heat transport equations in two dimensions (see Supplemental Information Text S1, Table 1.1, and Table 1.2). The model domain is constructed to mimic that of Smith and Chapman (1983) to represent a generalized topography-driven groundwater flow system that is 6 km in depth and 40 km in length. The elevation of the land surface decreases from 1 km in the recharge area to 0 km in the discharge area. Mesh-independent solutions are obtained for a finite element grid composed of 65,000 triangular elements. Each triangular element has a maximum dimension of 100 m, with refinement close to the domain boundaries. Groundwater flow boundary conditions include a specified head along the top boundary, assuming the water table is a subdued replica of topography, and no-flux along the sides and bottom boundaries. Similarly, a prescribed concentration of 10^{-3} kg-solute per kg-fluid is imposed along the top boundary and no-flux along the bottom and side boundaries. For heat-transport, we assume that temperature varies linearly with elevation $T_{surface} = T_{valley} - \gamma(z - z_{valley})$, where T_{valley} is the temperature at the lowest surface elevation in the model, z_{valley} , and γ is a lapse-rate assumed to be around $6.5^{\circ}\text{C}/\text{km}$ (Lundquist & Cayan, 2007; Martinec & Rango, 1986; Wallace & Hobbs, 2006). Finally, a prescribed heat flux of 60 mW/m^2 is assigned to the bottom boundary and no-flux is imposed along the side boundaries. Hydraulic permeability is varied and decays as a power law with depth in a fashion similar to the expressions proposed by Manning & Ingebritsen (1999) and Ingebritsen & Manning (2010), except in the first kilometer of the subsurface where we use an exponential decay (Figure 1.1). All simulations are run for one million years to reach steady-state conditions.

Groundwater salinity in regional flow systems can be controlled by many processes such as: mineral dissolution and alteration, fluid-inclusion leaching, sorption, mixing with seawater or magmatic fluids, and evaporite dissolution (Langmuir, 1997; Frape et al., 2003). Similar to Lemieux et al. (2008a) and Provost et al. (1998), we use a first-order, temperature-dependent source term in the solute transport equation to mimic the buildup of salinity due to fluid-rock interactions. The source term is expressed as $R = k_{mt}(C_{max} - c)$, where C_{max} is the maximum allowable fluid concentration, c is concentration, and k_{mt} is a mass transfer reaction rate. Like Provost et al. (1998), we assign C_{max} as 0.3 kg-solute per kg-fluid, which corresponds approximately to a fully-saturated sodium-chloride fluid. The mass transfer rate is a function of temperature through the Arrhenius expression (Langmuir 1997; see Supporting Information Text S1). This representation is not appropriate for all environments, but permits consideration of realistic and applicable salinity scenarios.

Conversion of hydrologic model results to electrical resistivity is done by using a modified version of Archie's law (Glover et al., 2000). Archie's law estimates effective resistivity as a function of porosity and fluid resistivity, while the Glover et al. (2000) modification adds a term that takes into account rock matrix

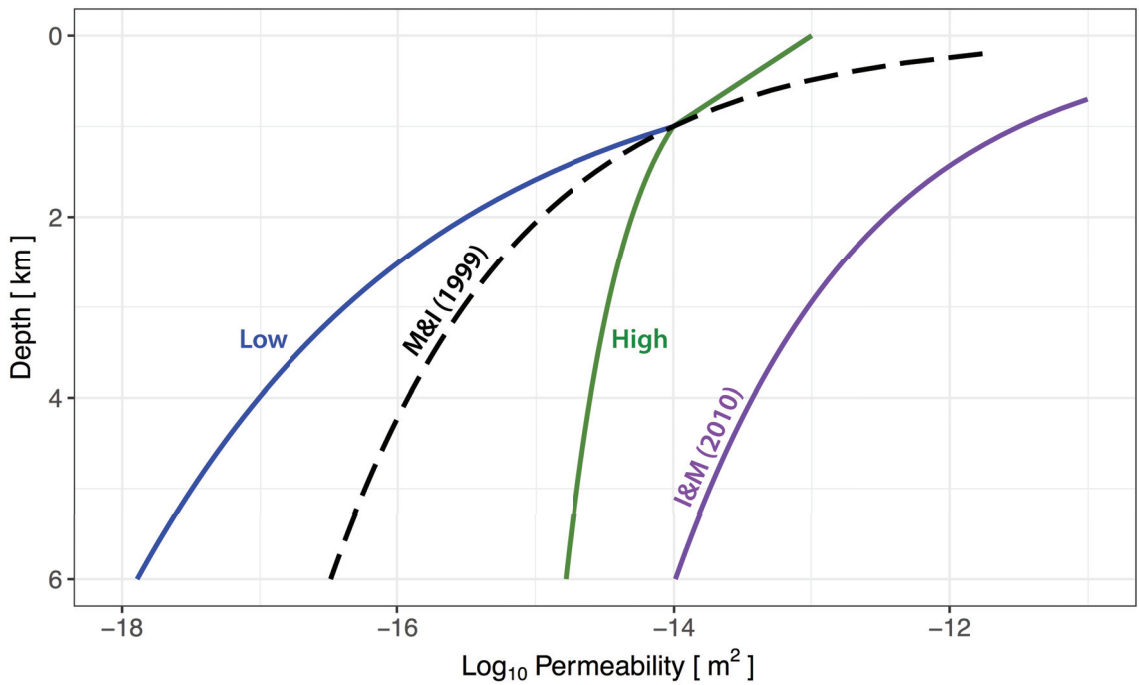


Figure 1.1: Permeability depth-decay representations used in the hydrologic modeling effort. The high and low permeability curves correspond to the results presented in this paper. The Manning and Ingebritsen (M&I 1999) and Ingebritsen and Manning (I&M 2010) curves are commonly applied permeability relationships for regional models and are shown for reference.

resistivity (Archie, 1942). Both equations also include an empirical exponent (m) that typically ranges from 1.3 to 2.5 (Telford et al., 1990). Rock resistivity is set to 10,000 ohm-m, porosity to 0.05, and m to 2 in order to represent typical continental crust (Fetter, 2001; Telford et al., 1990). In favor of simplicity, porosity decay functions are not considered in this study but should be explored in future work. Fluid resistivity is assumed to be a function of salinity and temperature, which is appropriate for the temperature range considered (Nesbitt, 1993; Quist & Marshall, 1968; Ucok et al., 1980). Deep flow systems commonly yield sodium-chloride waters (Frape et al., 2003). Therefore, fluid resistivity is estimated using our newly-derived thin-plate spline model (Hastie et al., 2009) that is fit to 243 previously-published sodium-chloride fluid resistivity lab measurements (see Supporting Information Data Set S1). Spline model selection is determined by using cross-validation techniques, which identify appropriate model smoothness by fitting splines of various complexity with a subset of calibration data and then predicting the leftover calibration data; model complexities that yield less prediction error are preferred (Hastie et al., 2009). Training of a new fluid resistivity spline model is undertaken to improve upon the frequently-utilized Ucok et al. (1980) sodium-chloride fluid resistivity model, which is applicable to a narrower salinity range than what is considered in this study. The new model is calibrated to data ranging from 0 to 309°C and concentrations of 6 to 321,420 ppm; which covers the salinity and temperatures widely observed in regional flow systems (Arehart et al., 2003; Park et al., 2009). Due to its non-parametric nature and complexity, it is not practical to provide the utilized spline model's mathematical form; an R-script is instead contributed for future users (see Supporting Information Text S2, Data Set S2, Table 1.3, and Figures 1.5-1.11). This spline model is an improved and versatile tool for estimating the resistivity of sodium-chloride waters.

In our flow and transport model, permeability and the solute source term strongly affect the pressure, salinity, and temperature patterns, and therefore the spatial variability of resistivity. The results section focuses on representative solutions derived from a modeling effort that included adjusting the solute reaction rate and permeability (see Supporting Information for all scenarios considered). Two of the solutions result from varying permeability between a high and low permeability decay model (Figure 1.1). The third presented solution uses the low permeability decay model but increases the solute reaction rate by two orders of magnitude. It is instructive to consider these solutions in terms of the Damköhler (Da) number, which is the ratio of the mass transport and solute reaction time scales (Ingebritsen et al. 1998, Supporting Information Text S1). This ratio depicts the interplay between solute advection and accumulation, which are primarily controlled by permeability and the solute source term. Advection dominates when the Da number is less than one, while reaction rates dominate for Da numbers greater than one. The three simulations presented herein correspond to Da numbers of 0.2 (high permeability), 1 (low permeability), and 99 (low permeability with increased reaction rate). These Da numbers are selected to depict various transport regimes that may be interpreted in terms of transport environments rather than the magnitude of the source term and permeability. In our

study, the $\text{Da} = 0.2$ scenario represents a high-permeability advection-dominated end member in which salinity is flushed from the system, while the $\text{Da} = 99.0$ corresponds to a low-permeability diffusion-dominated end member where solutes accumulate; the $\text{Da} = 1.0$ scenario also represents a low permeability environment but is an intermediate case in which reaction and transport processes are of similar importance.

1.2.2 Magnetotelluric Modeling

The simulated electrical resistivity fields from the flow and transport modeling effort are used to generate the magnetotelluric response at synthetic stations placed along the top of the domain using the 3D forward-modeling package of WinGLink (Version 2.20.02). The two-dimensional resistivity fields are input into the software and then duplicated throughout the rest of the 3D domain. MT responses are modeled for periods ranging from 0.001 to 10,000 seconds using 10 periods per decade. Minimum error for model convergence is 10^{-8} , as recommended by Geosystem SRL (1998). Station spacing is 1 km, except near the domain edges where 500 m spacing is used. Mesh discretization and geometry is nearly identical to our inversion mesh (Figure 1.12) with the same geometry as the flow and transport model. The EDI files for the forward modeling are included in Data Set S3.

The synthetic MT response curves are inverted using the two-dimensional inversion WinGLink software package (Version 2.20.02). Prior to inversion, Gaussian-distributed noise (mean of 0%, standard deviation of 2%) is added to the MT curves to emulate measured data; the 2% noise criteria adequately represents the variation in 30 MT stations collected by New Mexico Tech near Truth or Consequences, New Mexico. The inversion domain is similar to the hydrologic and forward modeling meshes (Figure 1.12). The noisy synthetic MT stations are spaced at 2 km intervals along the surface of the domain. Inversion settings are held constant for all inversions, with the exception of the smoothing parameter (Tau), and are shown in Figure 1.13. The smoothing parameter is varied from 0.1 to 300 for all simulations to facilitate the selection of appropriate model smoothness by using the L-curve optimization method (Chave & Jones, 2012).

1.3 Results & Discussion

Herein, we compare two high and low permeability scenarios in which both simulations use the same temperature-dependent solute dissolution rate. A third scenario is included in the last section of the results that represents an extremely saline, low-permeability end member by increasing the solute dissolution rate by two orders of magnitude. Distinct differences in the results would

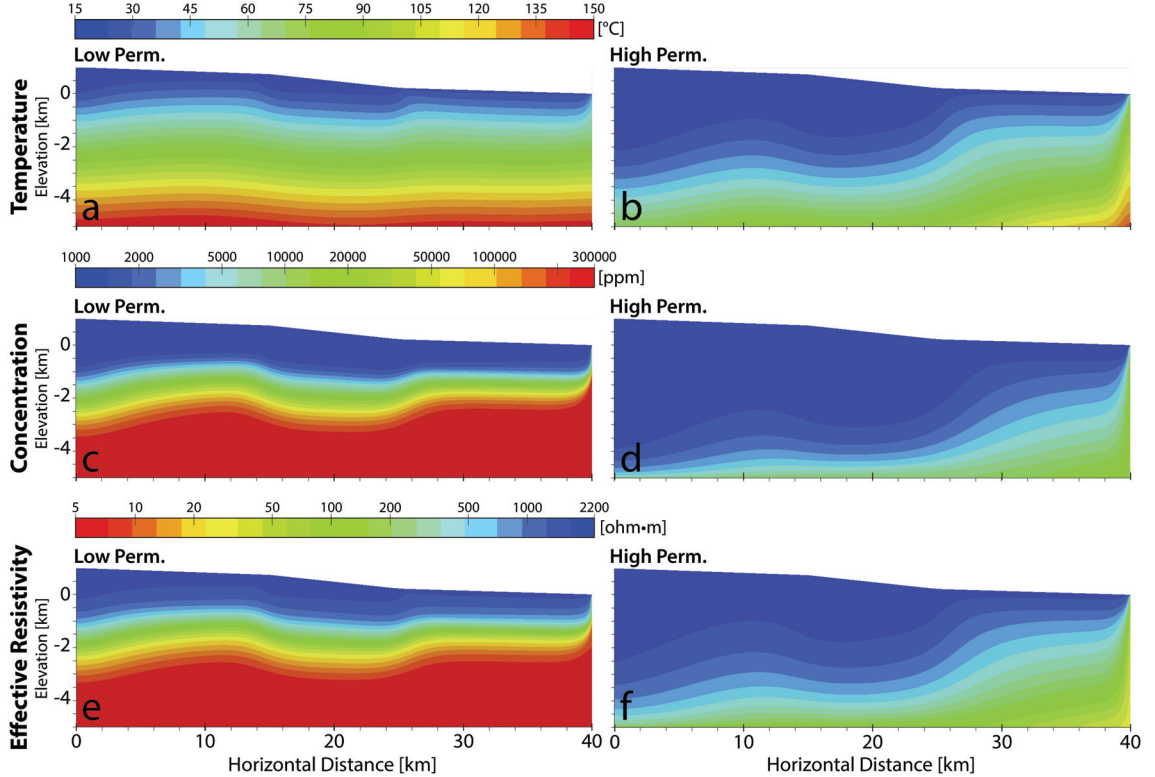


Figure 1.2: Simulated temperatures (a,b), salinities (c,d) and effective electrical resistivities (e,f) from hydrologic modeling for the low permeability (a,c,e) and high permeability (b,d,f) simulations. Temperatures, salinity, and resistivity patterns are distinctly different for these two permeability scenarios.

indicate that MT is systematically sensitive to permeability and can likely help constrain permeability when integrated into hydrothermal models.

Computed temperatures, concentrations (i.e. salinity), and effective electrical resistivities for both a high- and low-permeability hydrothermal modeling scenario are shown in Figure 1.2. The only modeling parameter that differs between these two scenarios is permeability magnitude (see Figure 1.1). This adjustment results in sharp contrasts between temperature, concentration, and resistivity. The temperature and concentration patterns in the high-permeability scenario have pronounced curvature due to the dominance of advection over solute accumulation ($Da = 0.2$; Figures 1.2b, 1.2d). Advection is balanced by solute accumulation in the low-permeability scenario ($Da = 1$), which leads to less prevalent curvature in temperature and concentration patterns (Figures 1.2a, 1.2c). The high-permeability scenario has depressed temperatures and concentrations, as elevated permeabilities permit the flushing of solutes and heat out of the system. Since electrical resistivity is a function of salinity and temperature, this contrast leads to very different resistivity patterns and magnitudes for the permeability scenarios (Figures 1.2e, 1.2f).

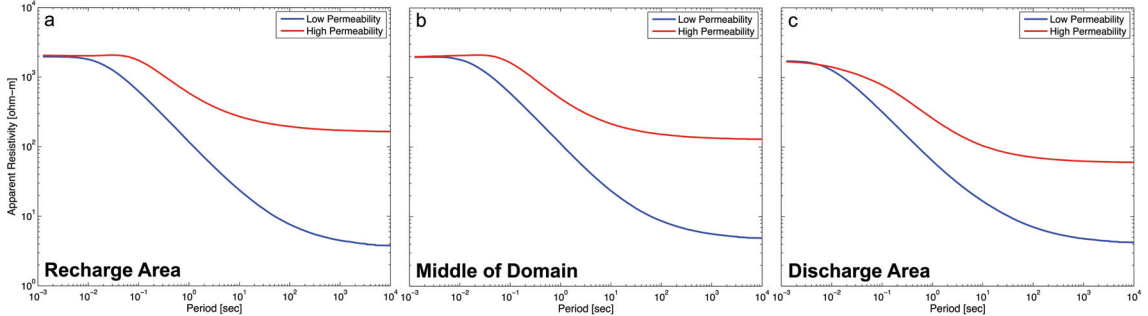


Figure 1.3: Magnetotelluric invariant forward modeling results for two permeability scenarios (high and low) from the recharge (a; station 6, $x = 6$ km), middle (b; station 22, $x = 20$ km), and discharge (c; station 38; $x = 36$ km) areas of the model domain; see Figure 4a for station locations. The curves show a significant MT contrast across the entire domain for these permeabilities.

Simulated resistivity patterns are analyzed in MT forward modeling software to estimate what MT instrumentation would theoretically record for the two permeability scenarios. Figure 1.3 shows the MT response for the recharge (a), middle (b), and discharge (c) areas of the model domain. These plots display apparent resistivity as a function of period. The apparent resistivity is the resistivity as if the earth is a homogeneous half-space, while period is related to depth; shorter periods provide shallow information and longer periods give deeper information. The apparent resistivity of the low- and high-permeability curves differ by at least one order of magnitude throughout most of the domain, which is a very considerable contrast relative to the typical error floors that are assumed in MT data analysis (5 to 20%; Chave & Jones, 2012). Looking at each simulation independently shows a lesser degree of variation between the recharge, middle, and discharge areas of the domain, although the recharge area is consistently more resistive than the discharge area.

Noise is added to the forward modeling results and the consequent MT curves are inverted as if they are field-measured data. Adequate recovery of the original noise-free forward model resistivity patterns would indicate that MT is systematically sensitive to regional permeability. Forward model resistivity patterns are compared to those of the inverse analysis in Figure 1.4. The high- and low-permeability resistivities are well-recovered and have distinctly different inversion results from one another (Figure 1.4b and 1.4d). The stark contrast consequent from variation of permeability is clearly evident in the simulated resistivity images, MT response curves, and MT inversion results. This is strong evidence that MT is systematically sensitive to permeability and can likely estimate regional permeability fields by being integrated into hydrologic model calibration. However, these results are influenced by the relative magnitudes of solute reaction rates and permeability, in addition to flow system geometry (e.g. regional hydrologic gradient). For these reasons, we offer interpretation in terms of the Damköhler (Da) number in a transport environment context and present a third simulation with an increased solute reaction rate (Figure 1.4e and 1.4f). The Da numbers for all simulations presented are 0.2 (high-permeability scenario),

1 (low-permeability scenario), and 99 (low-permeability scenario with an elevated dissolution rate). The $\text{Da} = 0.2$ scenario represents a highly-permeable, advection-dominated end member, whereas the $\text{Da} = 99$ scenario is analogous to a low-permeability, diffusion- and conduction-dominated end member; the $\text{Da} = 1$ scenario is an intermediary where solute accumulation is balanced by advection. Forward modeled resistivities and inversion results for all three of these transport regimes are distinguishable from each other in Figure 1.4. The fact that very different inversion images are recovered from all of these transport environments is evidence that MT can be a helpful calibration tool for systems of geometry different than the one considered in this study. Furthermore, it implies that MT can distinguish conduction- and diffusion-dominated transport environments from advection-dominated flow systems. However, the result that the $\text{Da} = 1.0$ and $\text{Da} = 99$ simulations have identical permeability fields, but yield different resistivity results emphasizes the importance of solute reaction rates. As a result, successful application of this methodology to constrain permeability in a real-world setting will be highly-dependent on possessing adequate geological understanding of the study area so that reaction rates can be appropriately represented in the hydrologic simulation. In absence of being able to well-represent solute reaction rates, this approach cannot uniquely estimate permeability fields (Beven & Freer 2001, Beven 2006). Geological understanding will also need to include estimates of porosity and the consideration of conductive mineralogy (e.g. sulphides, clays). Spatial scale needs to be taken into account as well, since our results suggest large-scale flow patterns should be evident but small features may not be as distinguishable. Overall, the amount of ancillary data that is needed to yield well-constrained permeability estimates when taking this approach, suggests it may be best suited for relatively simple, tectonically stable geologic settings that can be more readily characterized. A suggested implementation workflow for such environments is as follows: (1) acquire geological control; (2) develop hydrologic model without MT by using multiple calibration parameters such as temperature, pressure, groundwater residence time, and flow rates; (3) use model to inform optimal MT data collection sites; (4) collect MT data; (5) refine model permeability by comparing simulated resistivity with the acquired MT results. Despite the associated challenges, our results indicate that MT can likely be a powerful model calibration tool and reduce permeability uncertainty when adequate geological information is known.

1.4 Conclusions & Future Work

By using hydrologic, forward magnetotelluric (MT), and inverse MT modeling, we determine that MT can likely estimate permeability by being integrated into hydrologic model calibration. Distinct simulated electrical resistivities, MT response curves, and MT inversion results are obtained from all permeability schemes considered in this study. Interpretation of results in terms of the Damköhler (Da) number implies that MT can distinguish conduction- and diffusion-dominated transport environments from advection-dominated flow

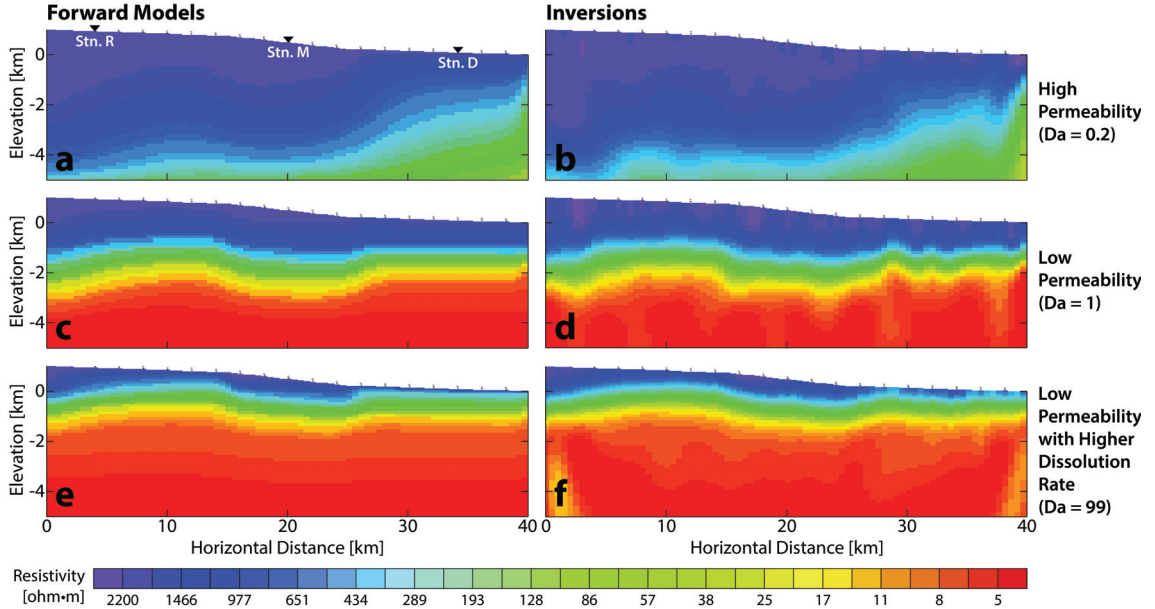


Figure 1.4: Forward model resistivity patterns compared with the recovered resistivity patterns after 2D inversion. The inversion results are unique for each scenario and compare well with the forward model resistivity patterns.

systems. Successful implementation of this approach hinges on having adequate control of subsurface porosity, mineralogy, and the ability to well-represent solute reactions at depth. For this reason, this technique is likely most suitable for relatively simplistic geologic environments that are most easily characterized. Future work should focus on evaluating specifically which geological settings, spatial scales, and other resistivity geophysical methods this approach is most applicable to, in addition to reducing uncertainty associated with solute reaction rates at depth. Furthermore, this methodology should be validated at several regional flow systems in which permeability and solute reaction rates are well understood. In general, the incorporation of electrical resistivity into hydrologic models has the potential to significantly advance our knowledge of regional permeability.

Acknowledgments

Funding was provided by the National Science Foundation under awards EPSCoR Energize New Mexico (IIA-1301346) and EAR 1830172.

1.A Supporting Information

1.A.1 Introduction

This supporting information section includes additional text, figures, and tables regarding the hydrothermal model used in this study, the conversion of simulated fluid salinity and temperature to electrical resistivity, and the magnetotelluric (MT) inversion setup. It also includes additional simulated electrical resistivity results that are not explicitly presented in the main text; the three simulations featured in the main text were selected to represent this larger set of simulations.

Four supporting data files are also described in this document. The first is a compilation of previously published laboratory-measured electrical resistivity data taken at various temperatures and salinities for sodium-chloride fluids. While all of this data is considered reliable, the measurement accuracy is likely variable, since the data was compiled from work that was published over a time period ranging from 1907 to 2009. These data were used to derive a thin-plate spline model that permits accurate estimation of sodium-chloride fluid resistivity over an extensive range of salinities (10 to 320,000 ppm) and temperatures (0 to 309°C). The supporting information also includes a zip folder containing an R script and the necessary input files to use this spline model independently. Lastly, the magnetotelluric forward responses and calculated inversion fits to those responses are enclosed. The forward responses include both noise-free magnetotelluric curves and those with 2% Gaussian noise added; the noisy curves were used exclusively for the inverse analysis.

1.A.2 Text S1.

Our flow and transport model incorporates fully-coupled, single-phase, groundwater flow and heat and solute transport (Bear, 1972; Furbish, 1997; and Ingebritsen et al., 1998):

$$\frac{\partial(\phi\rho)}{\partial t} + \nabla \cdot (\rho\vec{q}) = 0 \quad (1.1)$$

$$\frac{\partial [\phi\rho c_f T + (1 - \phi)\rho_s c_s T]}{\partial t} - \nabla \cdot (\bar{\kappa}_T \nabla T) + \nabla \cdot (\rho c_f \vec{q} T) = 0 \quad (1.2)$$

$$\frac{\partial(\phi\rho C)}{\partial t} - \nabla \cdot (\phi\rho \bar{D} \nabla C) + \nabla \cdot (\rho \vec{q} C) = R \quad (1.3)$$

where $\vec{q} = -(\bar{\kappa}\rho g / \mu) \nabla(p/(\rho g) + z)$ is the specific discharge vector; t is time; $\rho = \rho(p, T, C)$ and $\mu = \mu(p, T, C)$ are the fluid density and dynamic viscosity, respectively, at pressure p , temperature T , and salinity (volumetric concentration)

C from the equation of state proposed by Adams & Bachu (2002)); ϕ is porosity; $\bar{\kappa}$ is the intrinsic permeability tensor; g is gravitational acceleration; z is elevation above the datum; c_f is fluid heat capacity; ρ_s is solid density; c_s is solid heat capacity; $\bar{\kappa}_T$ is the thermal conductivity tensor; \bar{D} is the diffusive-dispersive tensor; and R is a solute mass rate of dissolution or precipitation (solute source term). Similar to Lemieux et al. (2008a) and Provost et al. (1998), we used a first-order reaction rate for the source term to mimic the buildup of salinity due to fluid-rock interactions:

$$R = k_{mt}(C_{max} - C) \quad (1.4)$$

where C_{max} is the maximum allowable fluid concentration and k_{mt} is a mass transfer reaction rate. Like Provost et al. (1998) we assigned C_{max} as 0.3 kg-solute per kg-fluid, which corresponds approximately to a fully-saturated sodium-chloride fluid. Fluid-rock interactions are influenced temperature; therefore, we represented the mass transfer reaction rate as a function of temperature through the Arrhenius expression (Langmuir 1997):

$$k_{mt} = A_0 e^{-E_0/R_0 T} \quad (1.5)$$

where A_0 is a temperature-independent coefficient, E_0 is activation energy, and R_0 is the ideal gas constant. We assumed $E_0 = 10$ kcal/mol for the activation energy, which typically ranges from 8 to 36 kcal/mol for mineral dissolution or precipitation (Langmuir 1997). Reasonable values were explored for A_0 by replacing k_{mt} with a range of values used by Provost et al. (1998) and Lemieux et al. (2008a) and then solving for A_0 at their approximate mean simulated temperature of 100°C. In the main text of this paper, we present results using values of 10^{-16} and 10^{-14} s⁻¹ for k_{mt} , which are similar to those suggested by Provost et al. (1998) and Lemieux et al. (2008a), although k_{mt} values from 10^{-16} to 10^{-12} s⁻¹ were considered and are presented in this supporting information.

Hydraulic permeability varies with depth as (Ingebritsen & Manning, 2010; Lemieux et al., 2008a; Manning & Ingebritsen, 1999):

$$\kappa(d) = \begin{cases} \log_{10}(\kappa) = B_{ks} d - A_{ks} & \text{if } d < 1 \text{ km} \\ \log_{10}(\kappa) = B_{kd} \log_{10}(d) - A_{kd} & \text{if } d \geq 1 \text{ km} \end{cases}$$

where κ is hydraulic permeability in m², d is depth in km, and all remaining terms are empirical coefficients. For all simulations, A_{ks} , B_{ks} , and A_{kd} were constant while B_{kd} was varied from -1 (high permeability scenario) to -5 (low-permeability scenarios); this range brackets the -3.2 value empirically estimated by Manning & Ingebritsen (1999) for continental crust.

To characterize the relative importance of mass transport verses solute reaction rates in the model, we estimate a bulk Damköhler number based on the

time scales for each of these processes. The transport and reaction time scales are defined as follows:

$$t_{transport} = \frac{L(B - z_{ref})}{\int_{-B}^{-z_{ref}} \left[\frac{\rho g}{\mu} (10^{A_{kd}} z^{-B_{kd}}) \frac{\Delta h}{L} \right] dz} \quad (1.6)$$

$$t_{reaction} = \frac{B - z_{ref}}{\int_{-B}^{-z_{ref}} \left[A_0 e^{(-E_0 / R_0 T_{profile})} \right] dz} \quad (1.7)$$

where L is the horizontal length of the model domain, B is the maximum depth of the model domain, z_{ref} is the depth where the power-law behavior of hydraulic permeability begins, Δh is the topographic relief of the model domain, and $T_{profile}$ is an approximation of a subsurface temperature profile defined as:

$$T_{profile} = T_{valley} + z(q_{Hb}/\kappa_T) \quad (1.8)$$

where T_{valley} is temperature at the lowest surface elevation in the model and q_{Hb} is the heat flux imposed along the bottom boundary of the model. Then, the bulk Damköhler (Da) number can be defined as:

$$Da = \frac{t_{reaction}}{t_{transport}} \quad (1.9)$$

In this case, $Da \gg 1$ represents systems where solutes accumulate rapidly and stay within the system. On the other hand, $Da \ll 1$ corresponds to a flow regime in which solutes are flushed out of the system.

Table 1.1 displays all scenarios explored during this modeling effort along with their Da numbers, while Table 1.2 is a list constant modeling parameters.

1.A.3 Text S2.

The methodology used to convert simulated fluid temperature and salinity to electrical resistivity is detailed in this section. Archie's law (Archie, 1942) is an empirically derived relationship that is commonly used to estimate the electrical resistivity of the subsurface (i.e. effective resistivity); it is expressed as follows for fully saturated conditions:

$$\sigma_{eff} = \sigma_{fluid} \phi^m \quad (1.10)$$

$$\rho_{eff} = \frac{1}{\sigma_{eff}} \quad (1.11)$$

where ρ_{eff} is the effective resistivity, σ_{eff} is the effective conductivity, σ_{fluid} is the conductivity of the saturating fluid, ϕ is porosity, and m is a cementation factor that describes the connectivity of the fluid (typically around 2). Archie's law assumes that the conductivity of the rocks themselves is negligible. This assumption is typically valid but can break down when the rocks are good conductors relative to the saturating fluid (e.g. clays, graphite, sulfides, or very dilute saturating fluid). In these instances, it is more appropriate to use a modification to Archie's law published by Glover et al. (2000), which can account for conductive rocks and minerals:

$$\sigma_{eff} = \sigma_{fluid}\phi^m + \sigma_{rock}(1 - \phi)^p \quad (1.12)$$

$$p = [\log(1 - \phi^m)] [\log(1 - \phi)]^{-1} \quad (1.13)$$

where σ_{rock} is the conductivity of the rock and p is a cementation factor that describes the connectivity of the rock.

To simulate resistivity using a hydrothermal model, porosity and rock resistivity need to be constrained from geologic records or estimated using typical values; we used 0.05 and 10,000 ohm-m for these values, respectively, to represent a simplified continental crust. Fluid resistivity varies with pressure, temperature, and salinity. Therefore, a relationship relating these three factors to fluid resistivity is also required. Deeply circulating groundwater often has a Na^+/Cl^- chemical signature (Frape et al., 2003). Quist and Marshall (1968) and Nesbitt (1993) show that pressure has a negligible impact on Na^+/Cl^- fluid resistivity at temperatures less than 375°C. Maximum temperatures in our simulations do not exceed 200°C, therefore, we assume that the influence of pressure on fluid resistivity is negligible in our study. Ucok et al. (1980) developed a model that describes Na^+/Cl^- fluid resistivity as a function of temperature and salinity (herein referred to as the Ucok model). Their model is calibrated to salinities of about 30,000 to 260,000 ppm and temperatures from 22 to 375°C. While this model's temperature range is readily applicable to many regional flow systems, the calibrated concentrations are too saline to be suitable for some areas. Therefore, we derived a more versatile model by fitting a cross-validated thin-plate spline (Wahba, 1990; Hastie et al., 2009) to 243 previously published Na^+/Cl^- fluid resistivity lab measurements (Ho et al., 2000; Lide & Haynes, 2009; National Research Council, 1930; Noyes, 1907; Quist & Marshall, 1968; Ucok et al., 1980; Zimmerman et al., 1995). The thin-plate spline model was fit using the Tps function from the fields package in the open-source R programming language (R version 3.4.1, R Core Team, 2013); data used in the fit and a R script are included with this supporting information (Data Set S1 and Data Set S2). Generalized (GCV), 5-fold, and 10-fold cross validation were all employed to determine the appropriate level of smoothness for the spline. Cross-validation techniques assist in determining model smoothness by fitting models of various complexity with a subset of calibration data and then predicting the leftover calibration data (Hastie et al., 2009). Model complexities that yield less prediction error are preferred. Ultimately, the

76 degrees of freedom smoothness level indicated by the cross-validation methods is utilized for the final spline fit (Hastie et al., 2009, Figure 1.5). The resistivity predictions of the spline model and fits to calibration data are shown in Figures 1.6 and 1.7. A percent-error summary comparing the fit of this new model and the Ucok et al. (1980) to the published resistivity measurements is shown in Table 1.3 while plots comparing the models are shown in Figures 1.8 through 1.11. Overall, our spline model well-approximates the resistivity of sodium-chloride waters for temperatures ranging from 0 to 309°C over salinities of 10 to 320,000 ppm with a mean error of less than one percent and is a notable improvement upon the Ucok et al. (1980) model (Table 1.3, Figures 1.7 through 1.11). By using simulated temperatures and concentrations from our two-dimensional hydrothermal model, simulated fluid resistivity can be estimated using this spline model in conjunction with the aforementioned modified Archie's law (Glover et al., 2000). These resistivity cross-sections can then be input into magnetotelluric (MT) forward modeling software to predict the corresponding MT response curves.

1.A.4 Data Set S1.

Compilation of published sodium-chloride resistivity data measured at numerous temperatures (0 to 309°C) and concentrations (6 to 321,420 ppm). These data were used for the fitting of the spline fluid resistivity surface derived in this study. Measurements reported at non-unique temperature and salinity are averaged; these data are flagged in the "notes" column of the data set. Literature sources for the data include Noyes 1907, National Research Council 1930, Quist & Marshall 1968, Ucok et al. 1980, Zimmerman et al. 1995, Ho et al. 2000, and Lide & Haynes 2009.

1.A.5 Data Set S2.

R script and associated data files required to estimate resistivity as a function of temperature and concentration using the thin-plate spline model derived in this study. This model was developed using R version 3.4.1. (2017-06-30) and RStudio version 1.0.153. Reference the "READ_ME.txt" file that is included in the zip folder for instructions on running the script.

1.A.6 Data Set S3.

Magnetotelluric forward model response at synthetic stations for the three simulations that are featured in the main text. These files are in the industry-standard EDI file format and were generated by WinGLink. EDI files for noise-free forward modeled response is included in addition to that with two-percent

Gaussian noise added. Gaussian noise was not added to the tipper data, as the tipper was not utilized in the inversions in order to be more conservative. These files are organized by the Damköhler number associated with each simulation (see Figure 1.4 and Table 1.1). Horizontal distance (X) and elevation (Z) of the stations are indicated in the "Synthetic_Station_Locations.csv" file.

1.A.7 Data Set S4.

Two-percent Gaussian noise forward modeled magnetotelluric response with inversion fit for each synthetic station. Inversion root-mean-squared error is shown for each station. The three simulations featured in the main text (Damköhler number = 0.2, 1, and 99) are all represented.

Table 1.1: Damköhler numbers of all modeling scenarios explored. Simulations featured in the main text are in bold. Higher b_{kd} values represent higher permeabilities while lower k_{mt} values correspond to lower solute reaction rates. Explanation: * = featured high-permeability simulation; ** = featured low-permeability simulation; *** = featured low-permeability simulation with elevated reaction rate.

	b_{kd}		
k_{mt}	-5	-3	-1
-16	1.0**	0.5	0.2*
-14	99***	51	15
-12	9889	5132	1528

Table 1.2: Parameters held constant in hydrothermal simulations.

Symbol	Variable Name	Value
α_l	Longitudinal Dispersivity	100 m
α_t	Transverse Dispersivity	10 m
A_{kd}	Permeability Coefficient	-14
A_{ks}	Permeability Coefficient	-13
c_f	Fluid Heat Capacity	4,184 J/(kg °C)
C_{max}	Maximum Salinity	0.3 kg-solute per kg-fluid
c_s	Solid Heat Capacity	836.8 J/(kg °C)
E_0	Activation Energy	10 kcal/mol
g	Gravitational Acceleration	9.81 m/s ²
$\bar{\kappa}_{Tf}$	Fluid Thermal Conductivity	0.58 W/(m °C)
$\bar{\kappa}_{Tr}$	Rock Thermal Conductivity	2.5 W/(m °C)
m	Cementation Exponent	2
ρ_{rock}	Rock Resistivity	10,000 ohm-m
ρ_s	Solid Density	2,600 kg/m ³
q_{Hb}	Basal Heat Flux	60 mW/m ²
R_0	Ideal Gas Constant	1.9872 × 10 ⁻³ kcal/(mol L)
T_{valley}	Minimum Surface Temperature	20°C
γ	Thermal Lapse Rate	6.5°C/km
ϕ	Porosity	0.05

Table 1.3: Comparison of Ucok et al. (1980) fluid resistivity model to the thin-plate spline model derived as part of this study in terms of percent error of 243 previously-published resistivity measurements. The spline model errors are significantly lower.

	Ucok Model [%]	Spline Model [%]
Mean	-1.94	0.04
Median	-2.13	-0.01
Min	-23.77	-11.24
Max	29.36	11.26

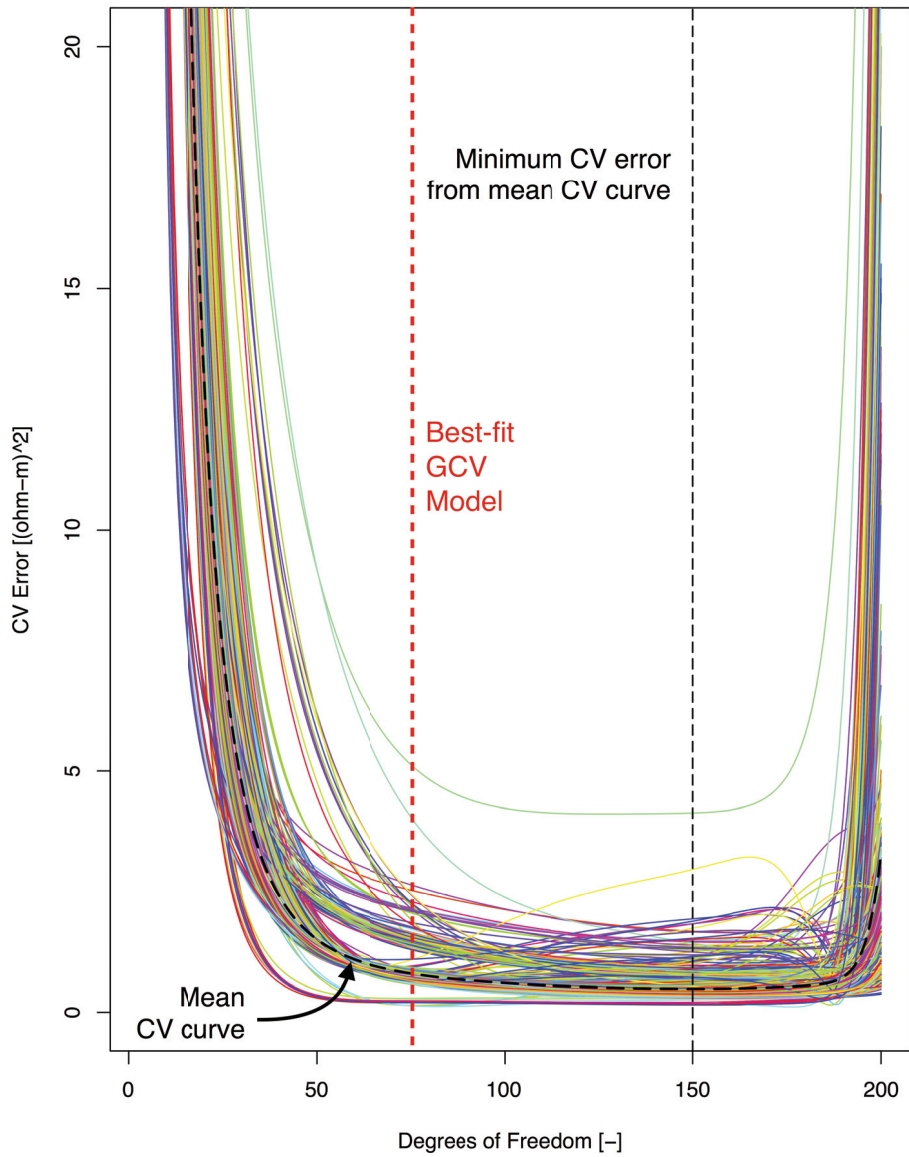


Figure 1.5: Thin-plate spline 10-fold cross-validation error versus model complexity (degrees of freedom) for 1,150 cross-validation realizations. The CV errors more or less plateau around the best-fit generalized cross-validation (GCV) model of 76 degrees of freedom; the GCV model was selected for the final spline fit.

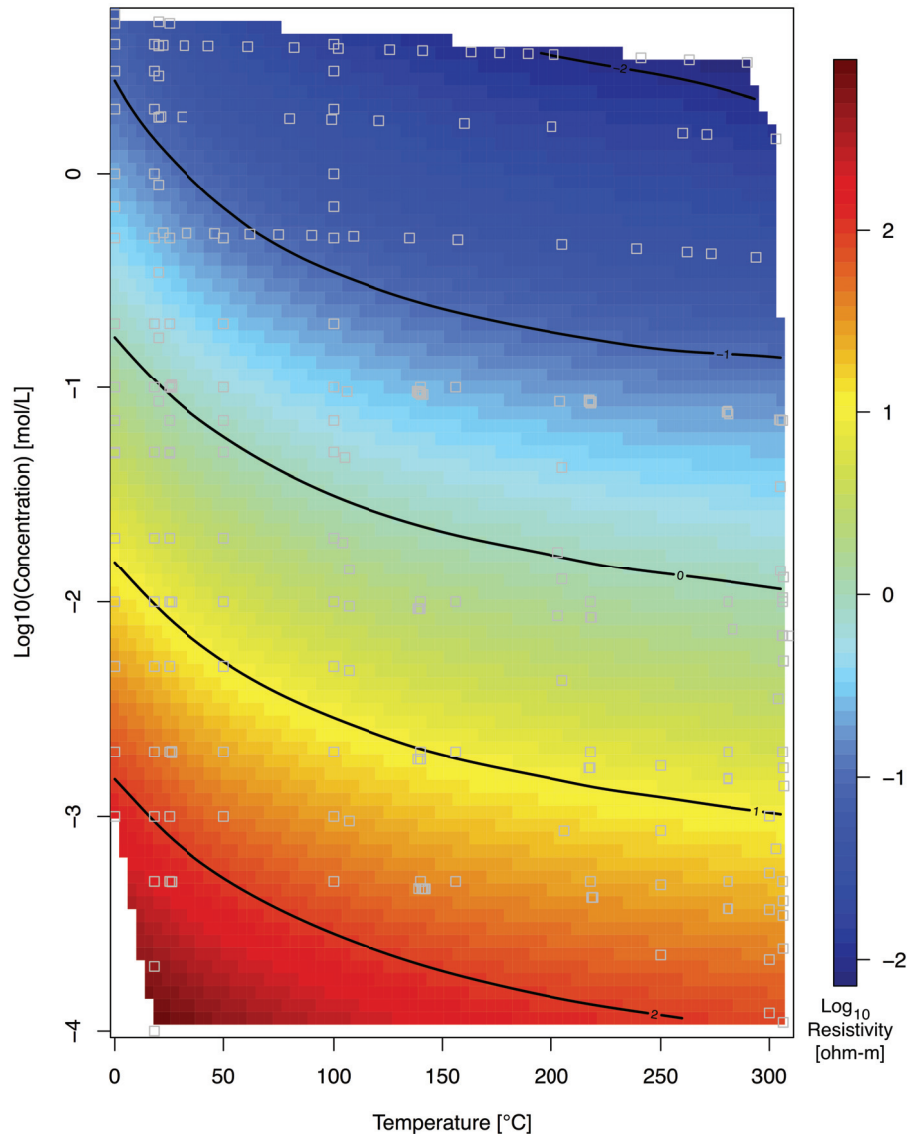


Figure 1.6: Resistivity surface produced by the generalized cross-validated 76 degrees of freedom thin-plate spline model. Resistivity is a non-linear function of temperature and concentration (i.e. salinity). Gray squares are the 243 previously-published resistivity lab measurements that are used to fit the spline model.

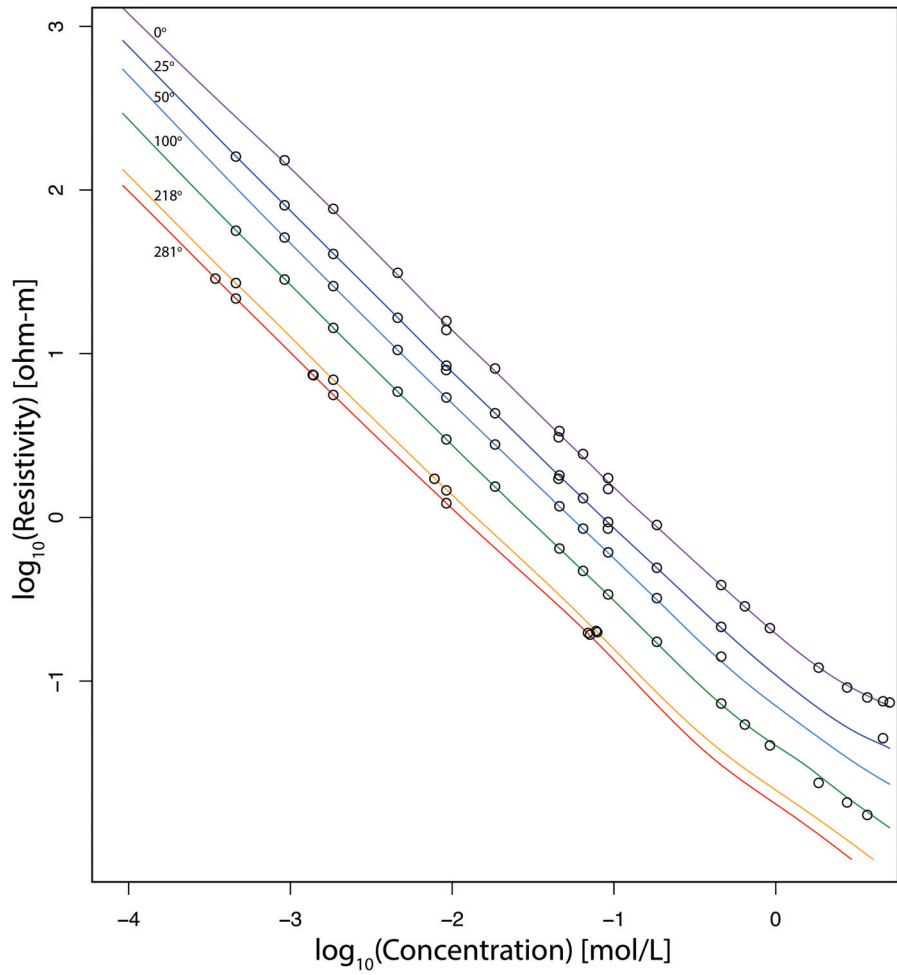


Figure 1.7: Resistivity predicted by the thin-plate spline model as a function of salinity at various temperatures. Black circles are calibration data that was used to fit the spline model at the underlying temperature value. Temperatures are in $^{\circ}\text{C}$.

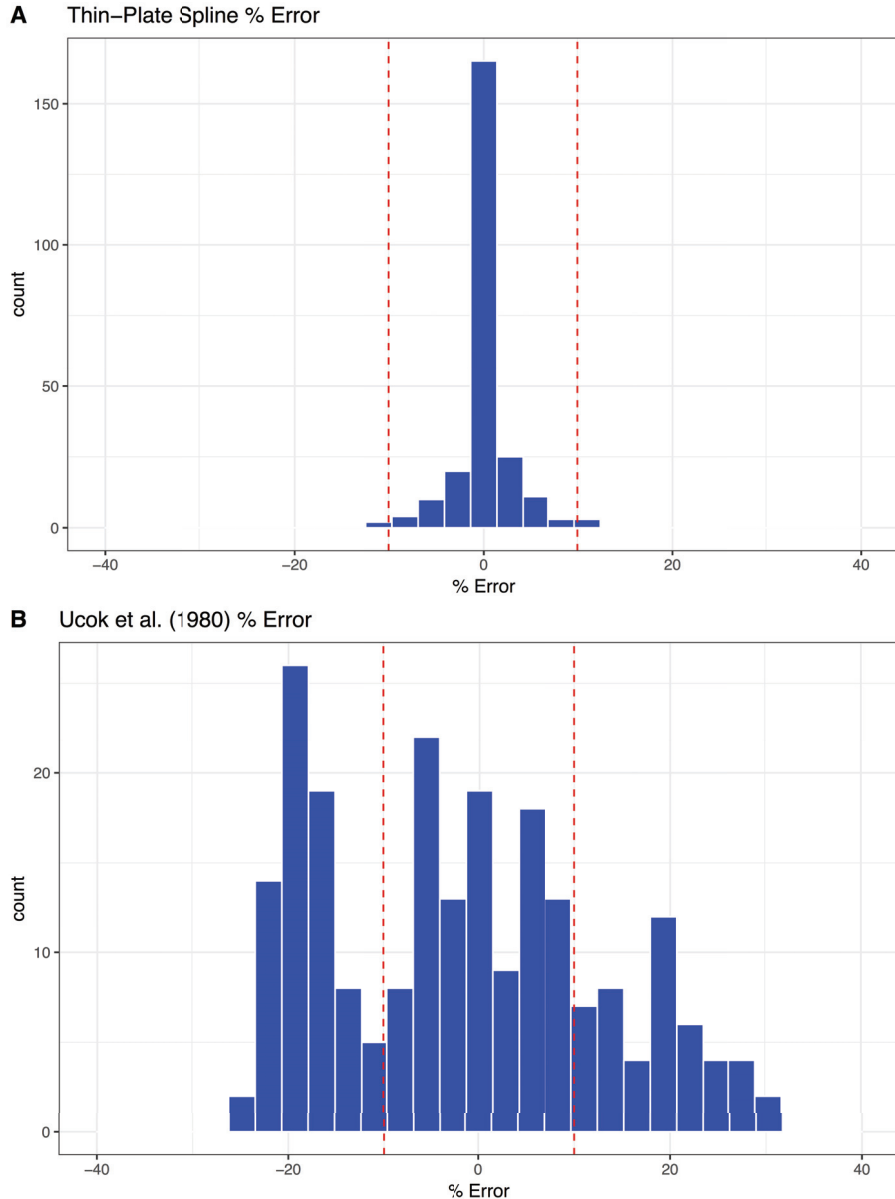


Figure 1.8: Percent difference error of model predictions versus 243 previously-published resistivity measurements. Errors from the spline model [A] derived as part of this study are much lower than the Ucok et al. (1980) model [B] and are normally distributed with a mean of 0.04%. Dashed red lines correspond to $\pm 10\%$ error.

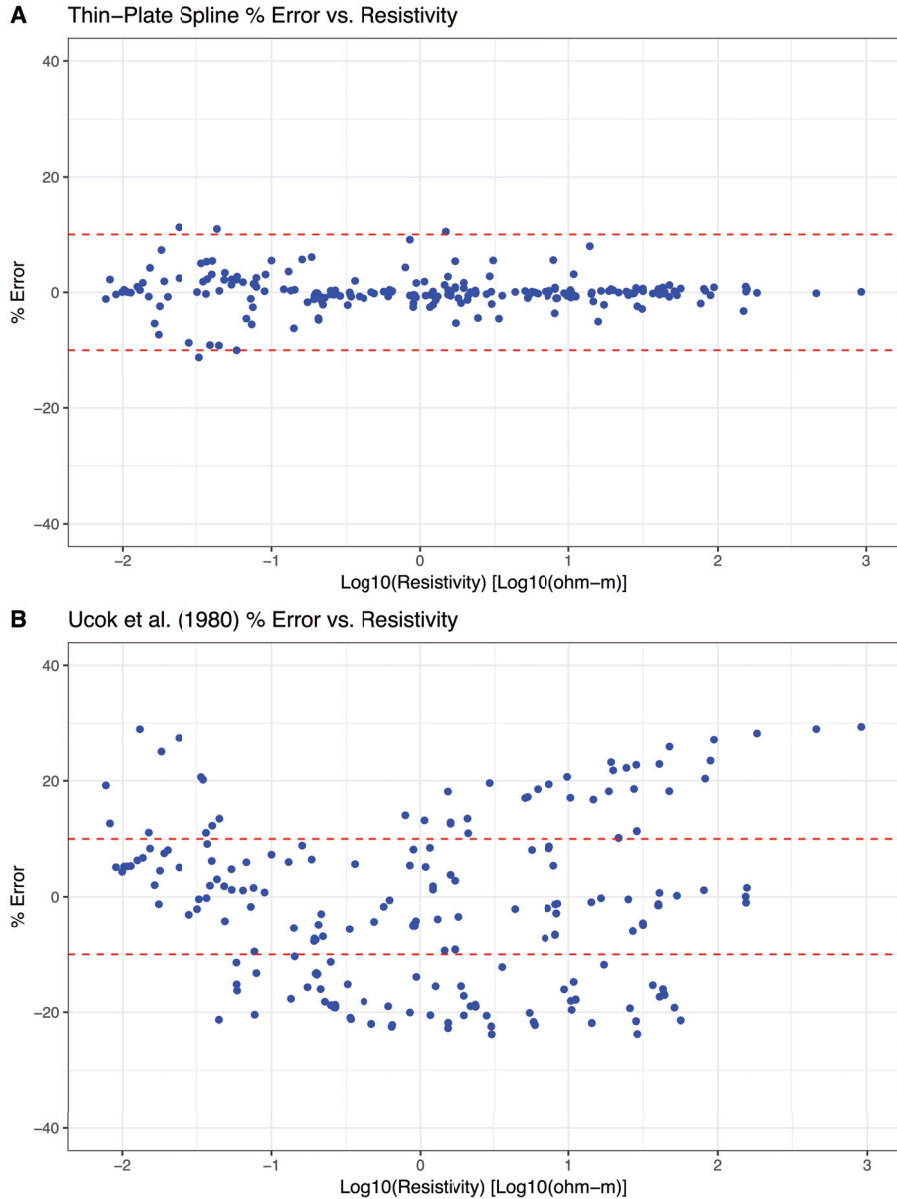


Figure 1.9: Percent difference error of model predictions versus resistivity for 243 previously published resistivity measurements. Errors from the spline model [A] derived as part of this study are much lower than the Ucok et al. (1980) model [B] and show no functional relationship to resistivity. Dashed red lines correspond to $\pm 10\%$ error.

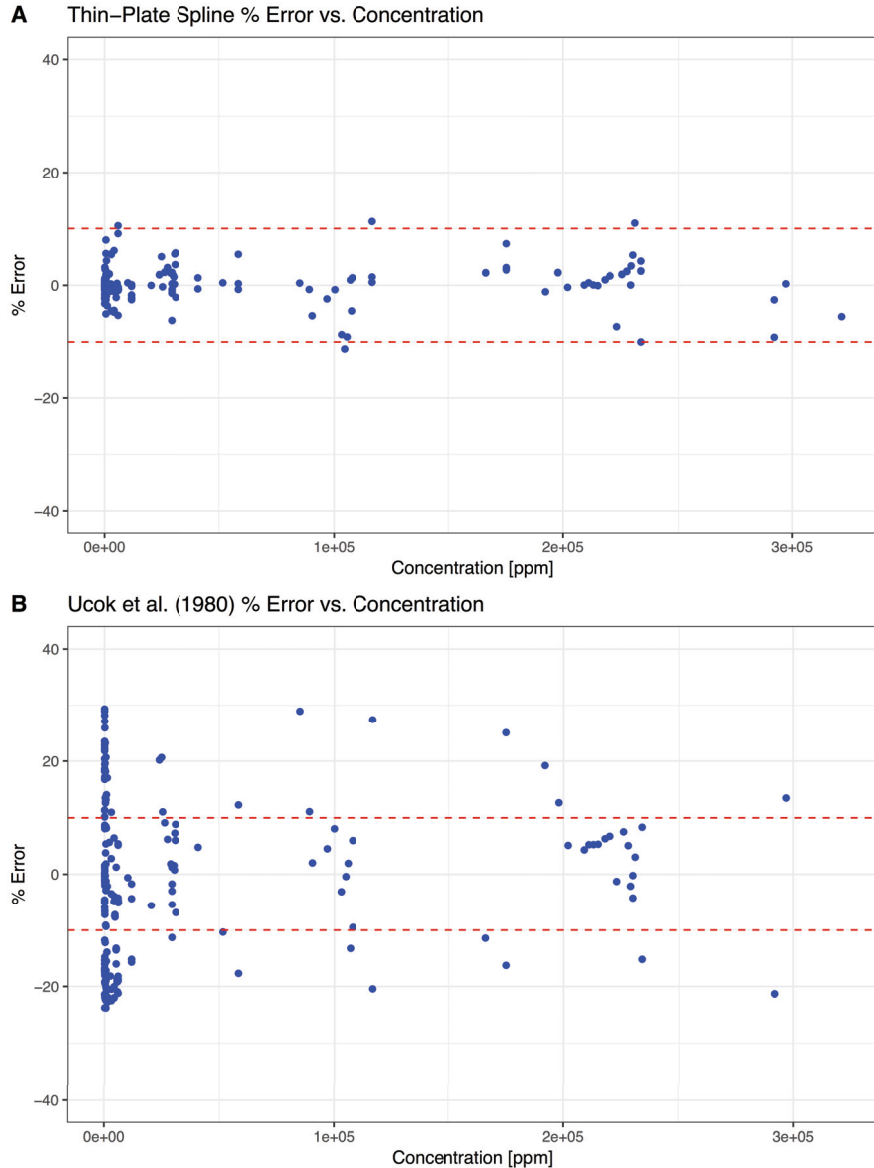


Figure 1.10: Percent difference error of model predictions versus concentration (i.e. salinity) for 243 previously-published resistivity measurements. Errors from the spline model [A] derived as part of this study are much lower than the Ucok et al. (1980) model [B] and show no functional relationship to salinity. Dashed red lines correspond to $\pm 10\%$ error.

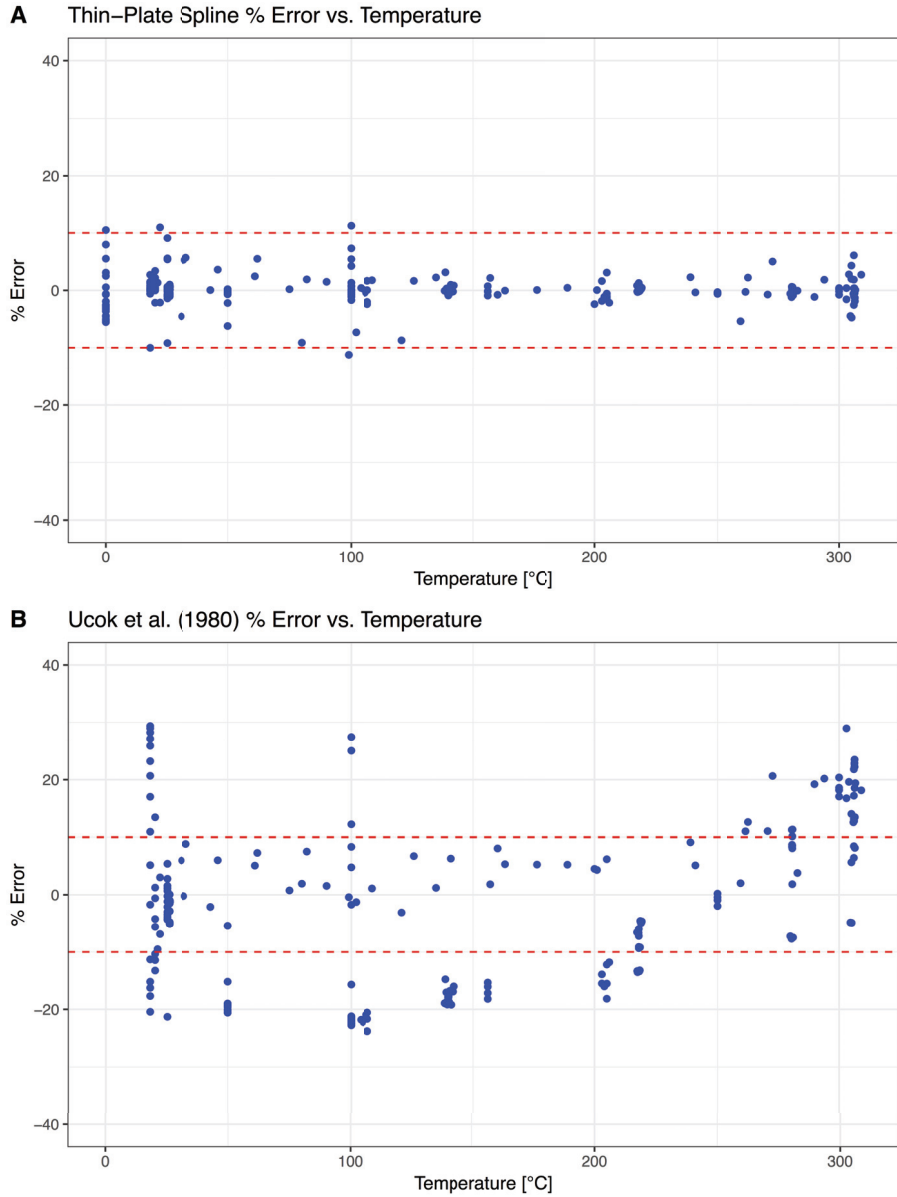


Figure 1.11: Percent difference error of model predictions versus temperature for 243 previously-published resistivity measurements. Errors from the spline model [A] derived as part of this study are much lower than the Ucok et al. (1980) model [B] and show no functional relationship to temperature. Dashed red lines correspond to $\pm 10\%$ error.

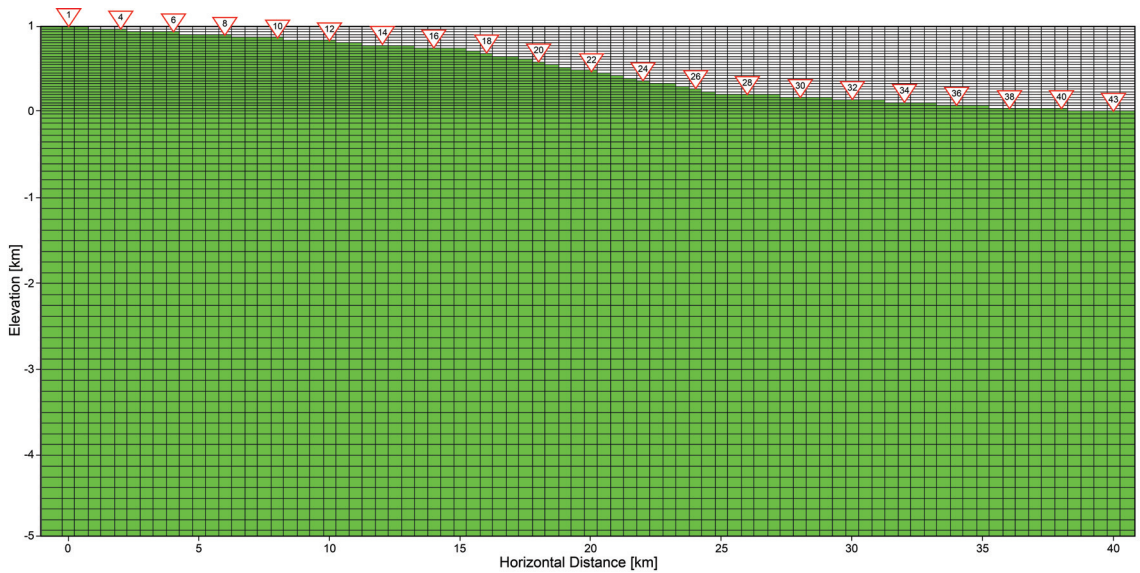


Figure 1.12: Magnetotelluric (MT) WinGLLink mesh used for inverse analysis. Synthetic MT stations are shown as triangles at 2 km spacing. Green cells depict the initial condition of 100 ohm-m resistivity while air cells are white. Mesh discretization and geometry is consistent with the magnetotelluric forward modeling mesh.

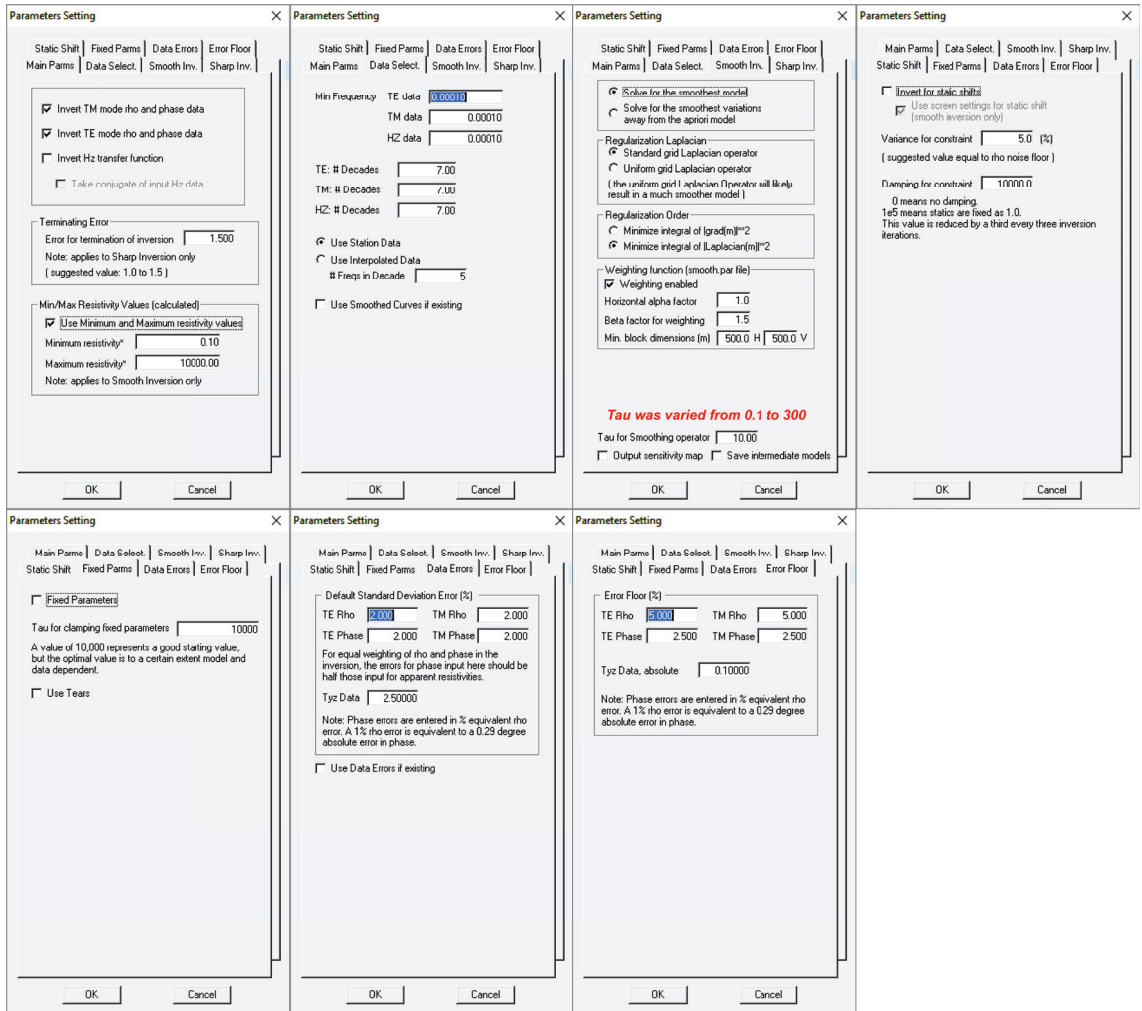


Figure 1.13: WinGLink settings used for all magnetotelluric inversions. These selections are in line with the recommendations from the WinGLink user manual (Geosystem SRL, 1998). Note that the smoothing parameter (Tau) was varied from 0.1 to 300 for all modeled scenarios. Even though only 2% noise was added to the synthetic data prior to inversion, an error floor of 5% was used in the inverse analysis to be conservative.

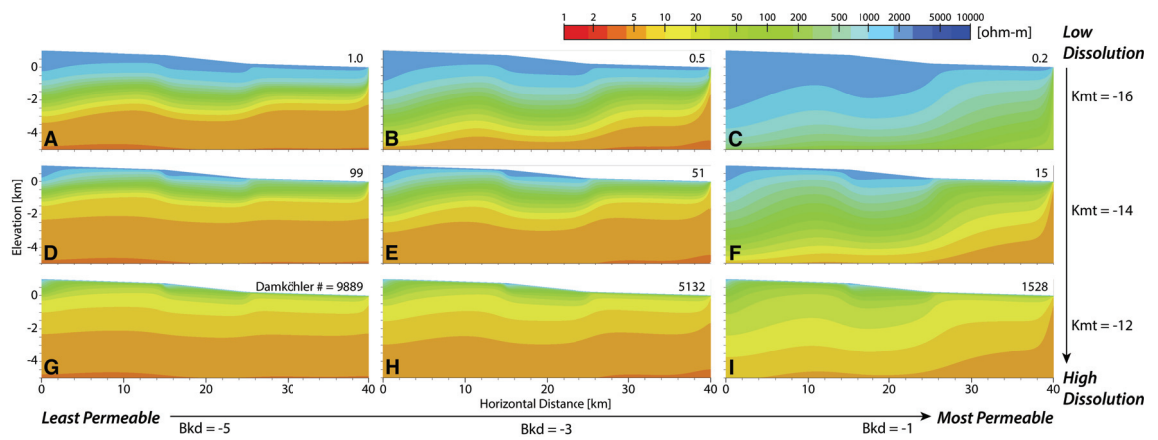


Figure 1.14: Simulated resistivity from hydrothermal modeling effort for numerous permeability-decay schemes and solute source terms. Simulations featured in the main text are shown in a, c and d and were chosen to portray representative results of this larger analysis. $B_{kd} = -5$ corresponds to the low permeability decay model and B_{kd} is the high permeability decay model shown in Figure 1.1. These results and previously-published work suggest the $k_{mt} = -12$ source term is an unrealistically high rate of dissolution and was therefore not featured in the main text.

CHAPTER 2

THE TRUTH OR CONSEQUENCES, NEW MEXICO GEOTHERMAL SYSTEM: INSIGHTS FROM ELECTRICAL RESISTIVITY AND AQUIFER TESTING

This chapter is written as a manuscript in preparation.

Abstract

We combined forward hydrothermal modeling with magnetotelluric (MT) and transient electromagnetic (TEM) geophysics to image a deep (4 to 10 km) crystalline basement-hosted groundwater flow system that is associated with the Truth or Consequences (T or C) geothermal resource along the central Rio Grande rift of New Mexico, USA. Previously published hydrothermal models indicate that the effective hydraulic permeability of the crystalline basement in the T or C watershed must be unusually high (10^{-12} m^2) to explain measured hot-spring temperatures (41°C), geothermometer reservoir temperature estimates (170°C), vertical specific discharge rates (3 to 6 m/yr), and mean carbon-14 groundwater residence times (7,000 yr). We further evaluate this conceptual model using electrical resistivity and aquifer testing. Regional subsurface resistivity patterns imply the presence of a single-pass and deeply circulating regional groundwater flow system between the upland recharge area to the west and the T or C hot-springs district near the Rio Grande to the southeast. The resistivity of the crystalline basement is observed to be between 100 and 200 ohm-m to depths of 10 km, which is typical of altered, fractured and saturated igneous and metamorphic rocks and is much more conductive than typical intact crystalline rocks. The homogeneity of basement resistivities indicates that fractures at depth are likely to be well-connected and prevalent throughout much of the watershed. Regional faults do not appear to compartmentalize the groundwater system but may serve as conduits for upwelling fluids. There is also a conductive (50 ohm-m) feature at 6 to 10 km depth below the T or C hot-springs district that may represent upwelling brackish geothermal fluids. This feature is reproduced well by hydrothermal models that we use to infer electrical resistivity patterns. Aquifer testing carried out within the T or C hot-springs district estimate local crystalline basement permeability to be on the order of $4 \times 10^{-10} \text{ m}^2$. Overall, these results indicate the likely presence of extremely permeable crystalline rocks on a

regional scale that permit geothermal groundwater circulation to depths of up to 10 km within this geothermal system. This work provides evidence that seismically active rift settings with prolonged tectonic histories may contain extensive regions of highly-fractured crystalline rocks that facilitate groundwater circulation to great depth.

2.1 Introduction

Groundwater flow patterns associated with the Truth or Consequences (T or C), New Mexico geothermal system within the Rio Grande rift are thought to be representative of a high permeability end-member for continental rift systems (Morgan & Witcher 2011). Many geothermal systems in the western United States involve meteoric fluids being heated by the elevated heat flow of their geologic province or by magmatic intrusions (Smith & Chapman 1983, Witcher 1988, Moeck 2014). These systems are commonly linked with relatively deep groundwater circulation within basin sediments followed by the ascent of geothermal fluids via faults or gaps in overlying confining units (Barroll & Reiter 1990, McKenna & Blackwell 2004, Howald et al. 2015). The discharge areas of these systems are attractive geothermal exploration targets, as financially viable resources can commonly be accessed at depths of less than 500 m. The conceptual model for the T or C geothermal system is similar, except it involves deep (6 to 10 km) circulation within highly-fractured and exceptionally permeable crystalline basement rocks, rather than permeable sediments (Person et al. 2013, Pepin et al. 2015).

Hydrothermal modeling of the T or C system by Pepin et al. (2015) required an effective crystalline basement hydraulic permeability of 10^{-12} m^2 in order to replicate the hot spring temperatures, groundwater upflow velocities, groundwater carbon-14 ages, and geothermometer reservoir temperature estimates of the resource. This permeability value is ultrahigh for crystalline basement, and while not unreasonable for fractured crystalline rocks (10^{-15} to 10^{-11} m^2), it is still considered uncommon on a regional scale for basement rocks and is more typical of silty sand aquifers (Freeze and Cherry 1979, Ingebritsen & Manning 2010). The elevated permeability is thought to be a result of secondary fracture permeability associated with the multiple tectonic events that have affected central New Mexico.

The T or C system shares many common features with the Socorro geothermal system, which is located in the Rio Grande rift about 115 km north of T or C, including similar discharge temperatures, salinities, and groundwater residence times. Shallow temperature gradient data and hydrothermal models by Barroll and Reiter (1990) and Mailloux et al. (1999) indicate that the Socorro geothermal system also involves deep (4 to 6 km) circulation within fractured crystalline basement rocks. The estimated effective regional basement permeability of the Socorro system is also quite high and is on the order of 10^{-14} m^2 . Both the Socorro and T or C regions are associated with high fault density. The Socorro area

is also linked with elevated seismic activity due to the underlying Socorro magma body. While this 100-m thick sill is responsible for the increased seismicity under Socorro, it is likely too deep (19 km) to appreciably affect near-surface ground-water temperatures and both the T or C and Socorro geothermal resources are considered amagmatic (Rinehart & Sanford 1981, Balch et al. 1997, Barroll & Reiter 1990, Mailloux et al. 1999, Person et al. 2013, Pepin et al. 2015). Both of the aforementioned geothermal resources have yet to be thoroughly drilled to permit comprehensive crystalline basement characterization; questions still remain regarding the actual depth of groundwater circulation and permeability structure.

Understanding crystalline basement groundwater flow patterns has important implications for refining geothermal exploration techniques and nuclear waste isolation (Brady et al. 2009). In the absence of drilling, geophysical methods provide a potential avenue to advance our understanding of these hydrothermal flow systems. Specifically, geophysical methods that estimate electrical resistivity (1/conductivity) structure can be effective at imaging hydrothermal flow systems and distinguishing their subsurface geologic materials (Pellerin et al. 1996, Ussher et al. 2000). Subsurface electrical resistivity is strongly impacted by geologic material, porosity and its connectivity, and groundwater salinity (Figure 2.1; Olhoeft 1985, Telford et al. 1990). Crystalline basement porosity is typically low (<10%; Fetter 2001) and is usually in the form of fractures (i.e. secondary porosity; Mazurek 2000). These fractures may be well-connected at depth, which would decrease saturated resistivity, or may be isolated and have limited effect on resistivity. Dry crystalline rocks are often electrically resistive but can have appreciable conductivity when altered to conductive minerals (Palacky 1988, Telford et al. 1990). Plagioclase grains in crystalline rocks can be strongly affected by hydrothermal fluids and may alter to electrically conductive clays such as kaolinite, smectite, and illite (Mazurek 2000, Lagat 2009). High-permeability conditions tend to lead to more pronounced basement alteration than low-permeability regimes (Mazurek 2000). The salinity of the saturating geothermal fluids also plays a prominent role in controlling basement resistivity (Ucok et al. 1980, Palacky 1988). Salinity of groundwater that primarily circulates within crystalline rocks can be influenced by mineral dissolution, fluid-inclusion leaching, and mixing with magmatic fluids (Frape et al. 2003). The common sodium-chloride signature of basement groundwater is thought to mainly be the result of dissolution of biotite that releases sodium-chloride lattice fluids (up to 7 eq.wt%) and sodium-chloride fluid-inclusion leaching (0 to 70 eq.wt%; Nordstrom et al. 1989, Frape et al. 2003). Nordstrom et al. (1989) performed lab experiments and detailed analyses of Swedish Stripa granite and found that fluid inclusions accounted for 1 to 2% of granitic porosity and had sodium-chloride salinities ranging from 0 to 25 eq.wt%. Mass balance calculations by these researchers indicates that these fluid inclusions can easily account for observed saturating groundwater salinities and may be released into groundwater by tectonic activity, thermally-induced microcracking, and mineral dissolution. Both the Socorro and T or C geothermal systems have brackish (less than 3,000 mg/L TDS) sodium-chloride groundwater signatures that are likely

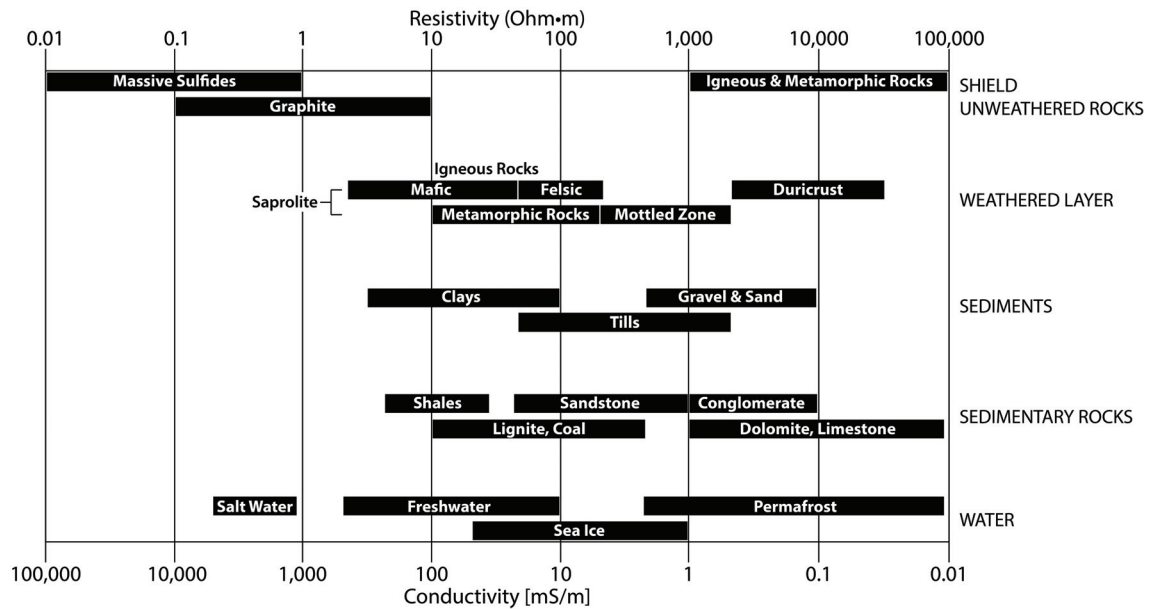


Figure 2.1: Electrical resistivity of common fluids and earth materials (after Palacky 1988).

influenced by fluid-inclusion leaching.

Magnetotellurics (MT) and transient electromagnetics (TEM) are two prominent electrical resistivity geophysical techniques that have a history of imaging groundwater and geothermal systems (Pellerin et al. 1996, Ussher et al. 2000, Spichak & Manzella 2009, Munoz 2014). Newman et al. (2008) and Lindsey et al. (2017) imaged the fault networks and fluid compartmentalization of the Coso geothermal resource in California using MT. Peacock et al. (2015) were able to improve the conceptual model of the Mono Basin geothermal region in California by imaging fluid-filled fracture networks, partial melt zones, cold plutons, and regional faults. Mikucki et al. (2015) used airborne TEM to image brines within permafrost in Antarctica. Aizawa et al. (2014) imaged the deep groundwater flow patterns associated with the Kirishima volcanic geothermal system in Japan. Wannamaker et al. (2006) were able to image magmatic fluid mixing with meteoric groundwater in the subsurface underlying the Dixie Valley geothermal system in Nevada. These studies illustrate the ability of electromagnetic geophysics (e.g. MT, TEM) to image groundwater flow patterns and improve the conceptual models of geothermal systems.

Land access restrictions impede a comprehensive electromagnetic investigation of the Socorro geothermal system. However, a localized high-frequency MT survey that was conducted immediately down-hydrologic gradient of the geothermal upflow zone identified a preferred future development drill site (Baars et al. 2006). These authors found that the crystalline basement near the upflow zone had electrical resistivities ranging between 20 to 200 ohm·m, which is typical of altered crystalline rocks (Figure 2.1). The T or C geothermal flow system has yet to be imaged with MT/TEM and is not burdened with widespread

land access restrictions. We therefore focus our efforts on this resource, in hopes of better understanding these basement flow systems. Specifically, we want to know if the basement rocks are essentially fractured uniformly with depth, if the flow system is compartmentalized, or if groundwater flow is channeled through discrete connected fracture networks. Furthermore, the current conceptual model for this system involves groundwater circulation to depths of up to 10 km; but is the crust actually fractured extensively to these depths?

This study attempts to address these questions by using MT, TEM, aquifer testing, and hydrothermal modeling. MT and TEM both have the ability to image the electrical resistivity of the crust, but do so at different depths and resolutions. TEM is commonly used for high-resolution investigations to depths of less than 0.5 km, while MT can provide resistivity structure to depths of over 500 km, but at lower resolution (Nabighian & Macnae 1991, Simpson & Bahr 2005, Christiansen et al. 2009, Hersir & Flovenz 2013). We collect MT data to create a 3D electrical resistivity image of the regional T or C geothermal flow system to a depth of 10 km. The main goal of this MT survey is to assess the resistivity of the crystalline basement to depths of 10 km. The resistivity of saturated intact crystalline rocks is typically upwards of 1,000 ohm-m, while fractured and altered crystalline rocks tend to be closer to 100 ohm-m (Figure 2.1; Palacky 1988, Jones 1992). This contrast should allow our MT survey to provide insight into the general geometry and prevalence of fracturing within the crystalline basement along the presumed T or C geothermal groundwater flow path; thereby allowing refinement of the geothermal conceptual model. We also collect a transect of TEM data that crosses a regional fault zone within the T or C watershed that is associated with the up-welling of warm (about 30°C) groundwater. The aim of this transect is to better characterize the role that faults play in controlling groundwater flow patterns within the basin. The temperatures and salinities from the best-fit hydrothermal model of Pepin et al. (2105) are then used to produce a simulated regional electrical resistivity image for comparison to the TEM and MT resistivity results. Lastly, an aquifer test is performed in the one well that produces hydrothermal fluids from the crystalline basement rocks of the T or C hot-springs district. The aquifer test seeks a direct measurement of permeability of the crystalline basement within the geothermal upflow zone. All results are synthesized to evaluate the present conceptual model of the T or C geothermal system and advance the understanding of geothermal resources in tectonically active environments.

2.2 Tectonic Setting & Conceptual Model

The Rio Grande rift is an active extensional tectonic province that ranges from 100 to 300 km in width as it bisects New Mexico (Seager & Morgan 1979, Morgan et al. 1986, Baldridge et al. 1995). This extensional regime has thinned continental crust, which results in naturally elevated conductive background heat flow (77-95 mW/m²; Reiter et al. 1986). The T or C geothermal system is located in the town of Truth or Consequences, formerly known as Hot Springs, along

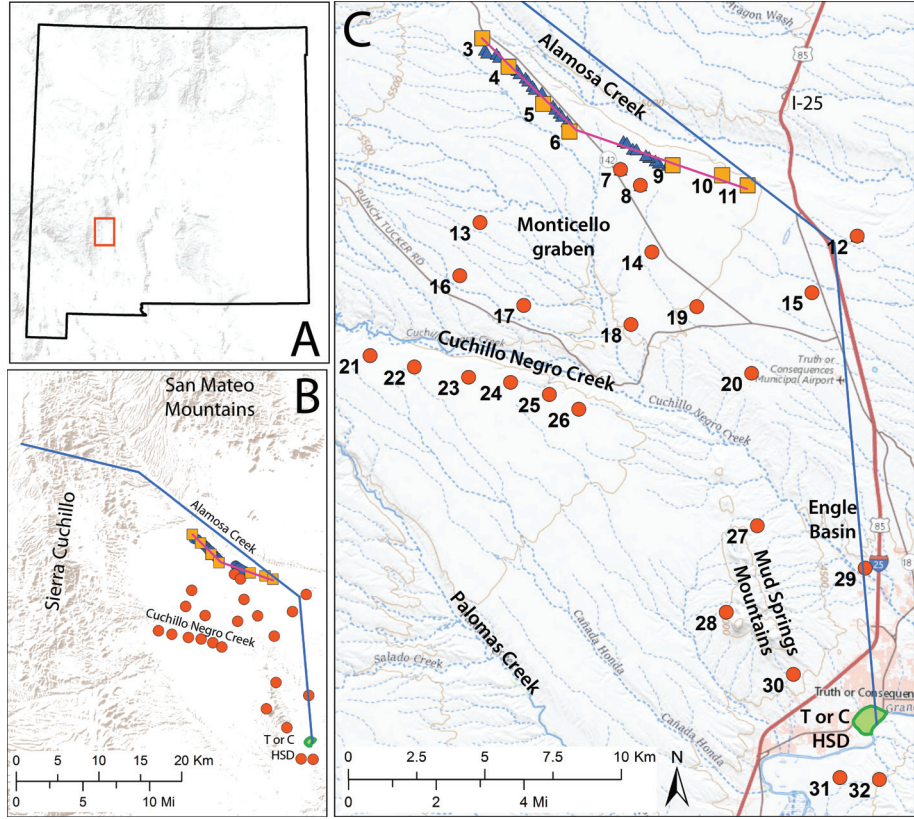


Figure 2.2: Study area basemap. Inset (A) Location of the study area within New Mexico. Map (B) identifies the mountain ranges that are the presumed recharge area for the geothermal fluids. Basemap (C) shows additional key geologic features and is a more localized view of the study area. Explanation: Blue transect = hydrothermal model and cross section profile of Pepin et al. (2015) and of Figure 2.3; pink transect = TEM profile across the Cuchillo Negro fault zone; green polygon = hot-springs district (HSD); red circle = MT station; orange square = co-located MT and TEM data used in TEM transect; blue triangle = TEM station for TEM transect. Note: TEM data was collected at the majority of MT stations to allow for assessment of static shift.

the western bank of the Rio Grande in south-central New Mexico just south of Elephant Butte Reservoir (Figure 2.2). More than ten commercial spa resorts and numerous domestic wells utilize the hot (41°C on average) groundwater supplies residing less than 5 meters below the town's historic hot-springs district (HSD; Person et al. 2013).

The position of the hot-springs district is thought to be largely controlled by high crystalline basement permeability and the absence of regional confining units, which have been displaced or eroded away. The region's tectonic history is extensive and complex. The most immediately relevant events are likely (1) the Laramide orogeny, (2) volcanism in the Mogollon-Datil volcanic field, and (3) Rio Grande rift extension (Pepin et al. 2015). The Laramide orogeny began at approximately 75 million years ago (Ma) and concluded at around 45 Ma (Kelley & Silver 1952, Seager & Mack 2003, Harrison & Cather 2004). This time period of uplift

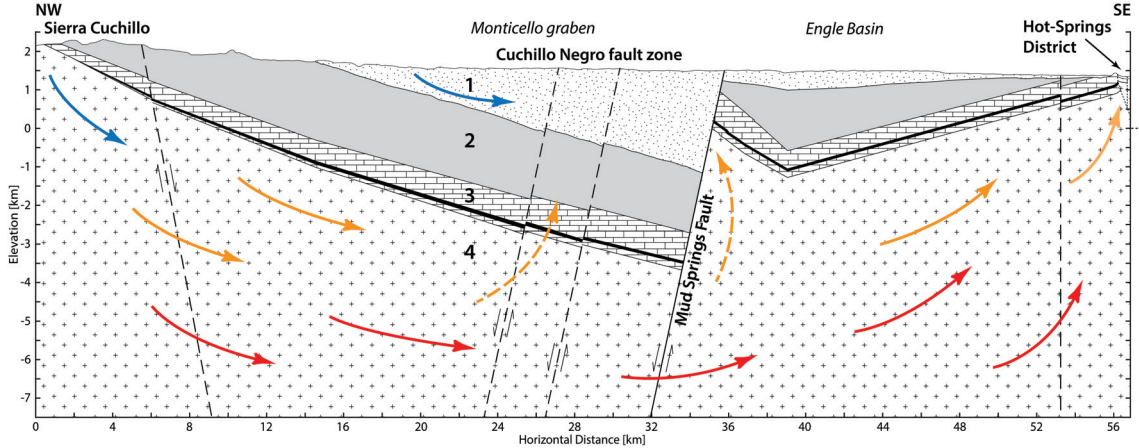


Figure 2.3: Conceptual model and stratigraphy for the geothermal system. Cool colors represent low temperature fluids, while warmer colors indicate hotter fluids. Groundwater circulates deeply within fractured crystalline basement rocks before ascending through gaps in overlying confining units and possibly along the Cuchillo Negro fault zone. The location of this cross section is shown on Figure 3.2. The lithologic units can be described as follows: [1] Palomas formation alluvial fill; [2] Tertiary volcanics, Cretaceous sediments, Cretaceous Mancos Shale and Dakota Sandstone, Permian San Andres Formation, Yeso Formation, and Abo Formation; [3] Pennsylvanian Magdalena Group, Percha Shale (thick black line), Lake Valley Formation, Kelley Limestone, and additional Paleozoics; [4] Precambrian granitic and metamorphic basement (after Pepin et al. 2015).

was a result of the North American Plate colliding with the Farallon Plate and its ensuing subduction. Northeast-east crustal shortening was prevalent, leading to the formation of the Rocky Mountains, abundant folds, NW-striking reverse faults, and N-S striking strike-slip faults throughout the T or C area. The hot-springs district is bound by one of these folds and a low angle fault to the north. These features are believed to be critical in allowing the T or C geothermal fluids to ascend towards the surface under the hot-springs district (Pepin et al. 2015). The increasing subduction angle of the Farallon Plate resulted in eventual intense volcanism, yielding the Mogollon-Datil volcanic field starting about 37 Ma (Harrison et al. 1993). Volcanic units from eruptions preserved in the San Mateo Mountains northwest of T or C cover the Sierra Cuchillo west of town and are buried within the Engle basin (Figure 2.2; Pepin et al. 2015). Beginning about 36 Ma, northeast-southwest crustal extension began to form the modern-day Rio Grande rift. Sedimentary basins began taking shape around 26 ma (Cather et al. 2005). Rifting peaked between 16 to 5 Ma but still continues today (Kelley & Chapin 1997, Seager & Mack 2003). Extension caused the uplift of the Caballo Mountains southeast of the HSD, San Mateo Mountains, and Sierra Cuchillo that form the T or C watershed. The Mud Springs Mountains also formed as a result of this extension and split the watershed into the Monticello graben and Engle basin (Figure 2.2C, Figure 2.3). The Monticello graben contains about a 5 km thick sedimentary sequence before reaching crystalline basement, while the Engle basin is shallower at an approximate 3 km sedimentary thickness (Figure 2.3).

The T or C hot-springs district is located at the terminus of the Engle basin, where an estimated $0.1 \text{ m}^3/\text{s}$ or 2.26 million gallons per day of thermal water upwells and then seeps into the Rio Grande (Theis et al. 1941). Previous studies hypothesized a shallow groundwater flow path for the geothermal waters within carbonate rocks that are buried in the Engle basin, in addition to a magmatic heat source (Powell 1929, Theis et al. 1941, Wells & Granzow 1981). However, magma heat flow models, the lack of seismicity, groundwater chemistry, and hydrothermal modeling results indicate the system is amagmatic and likely involves deep (6 to 10 km) groundwater circulation within highly-fractured crystalline basement rocks (see Figure 2.3; Person et al. 2013, Pepin et al. 2015). It is believed that the integrated effects of the aforementioned tectonic events led to elevated rock fracturing at depth. In this conceptual model, the fluids are presumed to be recharged in the San Mateo Mountains northwest of T or C and in the Sierra Cuchillo to the west. This groundwater then infiltrates into the fractured crystalline basement where it is heated by the naturally-elevated heat flow of the Rio Grande rift. The waters are sequestered in the basement below the sedimentary stack, except where there are gaps in overlying confining units. One of these gaps is along the Mud Springs fault, where previous hydrothermal modeling results predict the presence of a geothermal upflow zone (Figure 2.3; Person et al. 2013, Pepin et al. 2015). Warm groundwater temperatures (about 30°C) have been encountered along Alamosa Creek that suggest the presence of another groundwater upflow zone near the Cuchillo Negro fault zone (Figure 2.3). Lastly, faults and folds and the associated removal of regional confining units in the vicinity of the terminus of the Engle basin create a pathway (i.e. hydrologic window; Morgan & Witcher 2011) for geothermal waters to ascend and form the T or C hot-springs district (41°C). The fluids ascend through the Pennsylvanian Magdalena Group and the Precambrian crystalline basement rocks that underlie the HSD. Theis et al. (1941) performed aquifer tests that were most recently re-evaluated by Person et al. (2013) to estimate permeability of the HSD carbonate Magdalena Group aquifer. These tests yield permeability estimates that range from 10^{-11} to 10^{-10} m^2 , which is very high and is characteristic of karst limestone and clean sand aquifers (Freeze & Cherry 1979). Hydrothermal modeling results of Pepin et al. (2015) indicate the permeability of the crystalline basement underlying the HSD is also likely to be exceptionally high; we further evaluate this with an aquifer test in the crystalline basement rocks. It is this deep circulation, high basement permeability conceptual framework that we have adopted and aim to further evaluate and refine in our study.

2.3 Methods

Our approach includes conducting an aquifer test in a well within the hot-springs district to estimate the permeability of the crystalline basement. Additionally, we use TEM and MT to interrogate the electrical resistivity structure of the T or C watershed. Lastly, we use the best-fit hydrothermal model of Pepin et

al. (2015) to create a simulated resistivity image of the geothermal flow system. This section describes the details associated with each of these steps.

2.3.1 Aquifer Test

On June 12, 2015, we conducted a 96.8-minute-duration aquifer test on a 73-m deep geothermal exploratory well residing within the southeastern portion of the hot-springs district. This test marked the first aquifer test within the HSD of a geothermal well that is completed in the crystalline basement rocks. The well is located approximately 35-m northwest of the Rio Grande and is about 0.5 km southeast of limestone outcrops that mark a NW-striking reverse fault. Two shallower geothermal observation wells are adjacent to the exploratory well (Figure 2.4A). Observation well #1 is 29.5 m away from the production well, while observation well #2 is slightly closer at a distance of 25.8 m. The monitoring wells are completed in the fine-grained sediments overlying the crystalline basement rocks (Figure 2.4B). This fine layer serves as a leaky confining unit throughout the HSD. Drawdown was measured in all three wells during the aquifer test using In-Situ Level TROLL 700 data loggers, which can take up to four water level readings per second at an accuracy of $\pm 0.05\%$. The production well was pumped at a constant rate of 287 gpm, which was monitored using an orifice plate and manometer. Flow was channeled through a PVC pipe that discharged directly to the Rio Grande. Pumping was continued until water levels in all three wells appeared to stabilize.

Drawdown data for the production well is presented in Table 2.1 of Appendix 2.A. No drawdown was observed in either of the observation wells, so their data are not further analyzed. Analysis of production well drawdown data is done using Aqtesolv and the Cooper-Jacob model for confined aquifers (Cooper & Jacob 1946). This approach allows the estimation of transmissivity. Permeability can also be calculated by assuming a thickness for the aquifer. In this case, aquifer thickness is uncertain, so the thickness of the screened interval (24.4 m) of the well is used in its place. Use of the Cooper-Jacob model is appropriate when the following assumptions are adequately met: (1) the pumping well fully penetrates the aquifer, is pumped at a constant discharge rate, has a negligible diameter relative to the horizontal extent of the aquifer, and has marginal well-bore storage and (2) the aquifer is confined, homogeneous, isotropic, and infinite in extent (Schwartz & Zhang 2003). For this study, the two most questionable assumptions are that the aquifer is confined and that the well is fully penetrating. We know that the clays overlying the basement rocks are discontinuous in portions of the hot-springs district, which implies they form a leaky confining unit (Theis et al. 1941, Person et al. 2013). However, the lack of drawdown in the shallow observation wells during the duration of the aquifer test suggests leakage across the confining unit in this portion of the hot-springs district is minimal; thereby indicating the basement can locally be considered a confined aquifer for the analysis. The assumption that the well

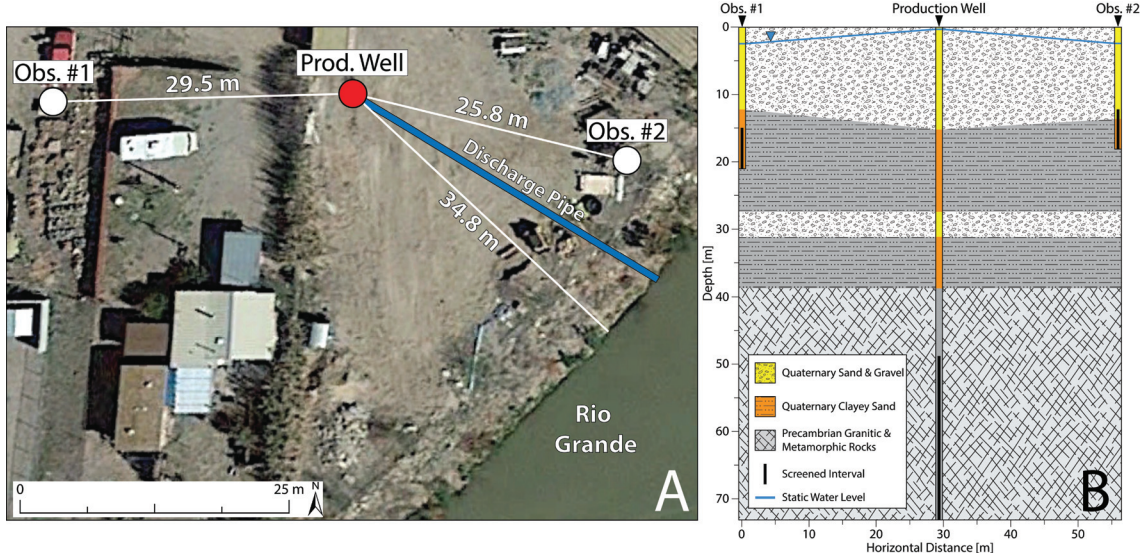


Figure 2.4: Aquifer test layout (A) and stratigraphy (B). This aquifer test was conducted in a exploratory well located in the southeast part of the hot-springs district along the west bank of the Rio Grande. Drawdown data from the test is used to estimate crystalline basement permeability and storativity.

is fully penetrating is a less comfortable assumption to make. Unfortunately, no nearby wells are completed in the crystalline basement to provide further insight into the depth of the bedrock aquifer. Analysis methods that can account for a partially penetrating well require the specification of aquifer depth, which cannot be known without deeper well information (Schwartz & Zhang 2003). Therefore, we are compelled to make the simplifying assumption that the screened thickness of the well is analogous to the aquifer thickness and that the well is thereby a fully-penetrating well. This simplification likely introduces errors into our results due to vertical flow effects near the well bore that we do not account for. Therefore, this increased uncertainty should be kept in mind and our permeability estimate is considered an order-of-magnitude approximation.

2.3.2 Transient Electromagnetic Survey

The transient electromagnetic (TEM) geophysical method, also referred to as time-domain electromagnetics (TDEM), is an induction approach that estimates subsurface electrical resistivity structure at high resolution to depths of several hundred meters (Nabighian & Macnae 1991, Christiansen et al. 2009). TEM theory starts with Maxwell's equations and is based on the fact that a time-varying magnetic field will induce a proportionate electrical current in nearby conductive materials. The induced current produces a secondary magnetic field, which dissipates over time as a function of material resistivity.

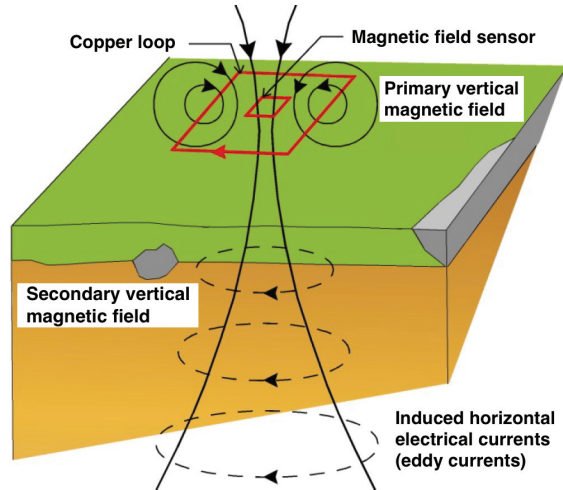


Figure 2.5: Depiction of the transient electromagnetic method (after Hersir & Flovenz 2013).

TEM data collection begins by laying a loop of copper wire on the surface of the Earth (Figure 2.5). A vertically leveled magnetic induction coil or receiver loop is placed near the center of the copper loop; this instrument measures vertical magnetic fields. An electrical current is then transmitted through the copper loop. This current is then rapidly shutoff, which creates a decaying magnetic field. The decaying magnetic field is a time-varying magnetic field, since it decays over time, and is called the primary magnetic field. The primary field induces horizontal electrical currents, called eddy currents, that diffuse into the Earth's subsurface. The eddy currents create a secondary vertical magnetic field that is measured at the surface using the magnetic field sensor placed in the center of the copper loop. The rate in which this secondary magnetic field dissipates is related to the resistivity of the subsurface. Since the eddy currents diffuse downward into the subsurface over time, measuring the secondary field at the surface allows the estimation of subsurface resistivity as a function of depth. Unlike many other electromagnetic methods, the dissipating secondary magnetic field is analyzed in the time-domain, thereby giving rise to the method's name. Early time data provides shallow resistivity information, while late time data gives insight into deeper resistivity structure. The secondary magnetic field is dissipated more rapidly by resistive layers and is sustained for longer time periods by conductors. Therefore, slope changes in plots of the secondary magnetic field strength as a function of time indicate layering in the resistivity of the earth. The transmission and elimination of the current through the copper loop is cycled and the responses from the earth are stacked many times to provide a large number of samples at a given station location.

In our study, we use a 100 m x 100 m diamond-shaped loop at each station. A 10.5 amp current is pulsed through this loop using a Zonge ZT-30 geophysical transmitter and two 24-volt batteries. Vertical magnetic fields are measured near the center of the loop using a Zonge TEM/3 induction coil. Data is recorded and viewed in the field using a Zonge GDP3224 24-bit multi-channel receiver. All

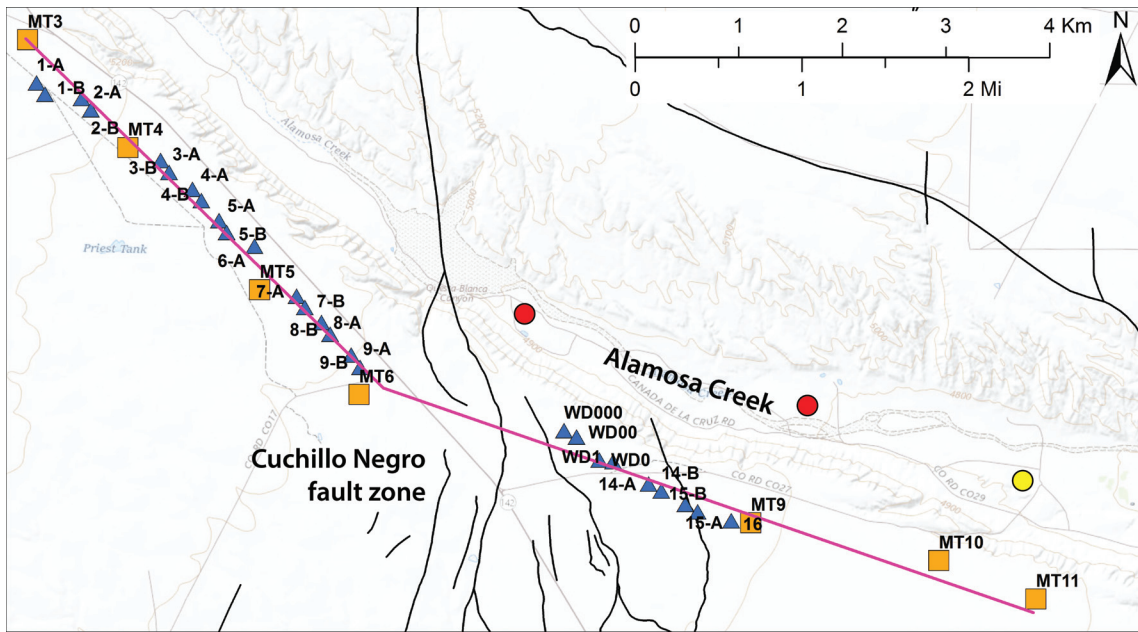


Figure 2.6: Basemap showing TEM transect across the Cuchillo Negro fault zone near Alamosa Creek. Explanation: black line = Quaternary fault; pink transect = TEM profile along the Cuchillo Negro fault zone; orange square = co-located MT and TEM data used in TEM transect; blue triangle = TEM station, red circle = discharge well temperature $>30^{\circ}\text{C}$, yellow circle = discharge well temperature between 20 and 30°C .

data collection is done using a 2-16 Hz pulse frequency, 128-1024 pulse cycles (depending on the frequency used), and 6-10 data stacks. We collect 54 TEM stations within the T or C watershed using this approach. Twenty-eight of these sites are co-located with MT station locations, primarily to enable corrections to the MT data (see MT methods section for details). A total of 26 independently-located TEM sites are collected along an east-west transect that crosses the Cuchillo Negro fault zone near Alamosa Creek (Figure 2.6). Seven of the MT sites also fall along this transect, so their TEM data is included in the transect as well. Warm (about 30°C) groundwater has been encountered along Alamosa Creek near the Cuchillo Negro fault zone. Therefore, this localized TEM transect is collected to advance the understanding of the role that faults play in controlling geothermal groundwater flow throughout the basin.

The TEM data is processed and reviewed using the Zonge TEMAVGW software package (MacInnes 2010a). The data is then modeled to estimate resistivity as a function of depth using the Zonge STEMINV smooth-model inversion package (MacInnes & Raymond 2009). The layer thicknesses in this inverse modeling algorithm are fixed during the inversion by calculating the source-field penetration depths for time windows within the dataset. Layer resistivities are then iteratively adjusted until the inverse model well-represents the data. Convergence is determined by minimization of an objective function that includes terms representing the difference between observed and calculated data, the de-

viation from the initial resistivity model, and inversion model roughness. The relative importance of these factors is primarily controlled by a smoothing weight that is input by the user. Optimal solutions are acquired when using smoothing weights ranging from 1 to 5 and 32 for a maximum number of allowable iterations; most models converged in less than ten iterations. This inversion method is a one-dimensional approach, which is required for TEM applications. MT dimensionality in the shallow subsurface along the transect was confirmed to be one-dimensional (see dimensionality metrics in Appendix 2.B for MT stations in Figure 2.5), thereby indicating the 1D assumption implicit in using TEM is applicable to this portion of the study area. The 1D inversion results for stations along the Cuchillo Negro fault zone transect are contoured in Tecplot to create a 2D cross section of the subsurface. Elevations used for each station in the contouring are extracted from a 30-meter digital elevation model of the region.

2.3.3 Magnetotelluric Survey

Magnetotelluric (MT) theory is similar to TEM in that it is based on Maxwell's equations of electromagnetism (Simpson & Bahr 2005, Chave & Jones 2012, Hersir & Flovenz 2013). However, unlike TEM, MT is a passive method, meaning it does not require an artificial signal transmitter. Instead, the method measures subsurface electrical responses to natural variations in the Earth's magnetic field, which are caused by global-scale phenomena such as solar wind variations and atmospheric lightning. These natural magnetic field variations induce eddy currents in the Earth's crust that can be measured at the surface to better understand subsurface electrical resistivity. Low frequency (long period) signals penetrate deeper than high frequency (short period) waves. Therefore, measuring signals over a large frequency range provides resistivity information to depths from a few meters to hundreds of kilometers. The penetration depth (z in meters) is related to the period (T in seconds) of the inducing magnetic field and can be estimated using the skin depth equation:

$$z(T) \approx 500\sqrt{T\rho_a} \quad (2.1)$$

where ρ_a is the apparent resistivity in ohm-m, or the Earth's mean resistivity as if it were a homogeneous half space. An MT field setup involves using magnetic induction coils to measure the Earth's magnetic field as a function of time, and an array of electrodes to capture subsurface electrical responses to magnetic field variations. These data are measured in the time domain but later converted to the frequency domain using Fourier transform methods, making MT a frequency-domain approach. The ratio of the electric and magnetic fields can be used to calculate the impedance tensor (\mathbf{Z}) for the frequency range of interest:

$$\begin{pmatrix} E_x \\ E_y \end{pmatrix} = \begin{pmatrix} Z_{xx} & Z_{yx} \\ Z_{xy} & Z_{yy} \end{pmatrix} \begin{pmatrix} H_x \\ H_y \end{pmatrix} \quad (2.2)$$

where E is the electric field and H is the magnetic field as measured at the surface. The impedance tensor is related to the apparent resistivity of the earth through angular frequency (ω) and the magnetic susceptibility of free space (μ_0) as follows:

$$\rho_a^{ij}(\omega, t) = \frac{1}{\mu_0 \omega} |Z_{ij}(\omega, t)|^2 \quad (2.3)$$

where i and j are components of the measured horizontal magnetic and electric fields, respectively, and $|Z_{ij}(\omega, t)|$ is the determinant of the impedance tensor. Note that this equation indicates apparent resistivity is a function of time. In practice, we assume no time dependence of this relationship over the span of the MT survey, which is appropriate for most geologic settings except in very rare cases involving rapidly changing environments. Apparent resistivity can be plotted as a function of frequency and inverse modeled to estimate true subsurface resistivity structure. The impedance tensor can also be used to evaluate the electrical dimensionality of the subsurface. In a one-dimensional (1D) "layer cake" earth, the diagonal components of Z are zero and the off-diagonal components are of equal magnitude but have opposite signs. A two-dimensional (2D) earth is similar, except the off-diagonal values of Z are no longer of equal magnitude. A three-dimensional (3D) earth will have all non-zero impedance tensor components. Plots of phase tensors, ellipticity, and normalized skew angle are commonly used to evaluate and visualize this dimensionality (Caldwell et al. 2004, Bibby et al. 2005, Booker 2014). In addition to providing insight into the complexity of the subsurface, dimensionality constraints inform the choice of the employed inverse modeling scheme.

In our study, we collect 30 MT stations in the T or C watershed using Zonge 32-bit ZEN data loggers (Figure 2.2). Zonge ANT-4 induction coils with a frequency range of 10^{-4} to 10^3 Hz are used to measure vertical and horizontal magnetic fields; two stations had no vertical measurement due to difficulty digging the holes for the vertical coil. The vertical magnetic field can be used to estimate induction vectors, which aid in identifying the lateral boundaries of conductors in the subsurface (Parkinson 1983). Electric fields are measured using a L-shaped electrode array with 100 m dipoles and three STELTH 3 silver-silver chloride SRE-011-SPB electrodes. The electrical array and induction coils are oriented using magnetic north. Data is collected using a variable sample rate time schedule that repeats for 36 hours as follows: 4096 Hz for 5 minutes, 1024 Hz for 15 minutes, and 256 Hz for 8 hours and 40 minutes. This schedule allows for sampling of the MT response across the frequency range of interest during different times of the day to promote high data quality.

The MT impedance tensor is calculated as a function of frequency using the Zonge International processing software suite (MacInness 2010b, 2014a, 2014b). All stations, except for station #25, are remote referenced using other MT stations that collected data on the same time schedule to reduce incoherent noise effects (Gamble et al. 1979). Distortion arising from near-surface heterogeneities

can sometimes affect the electrodes and result in a static shift of the apparent resistivity curves (Pellerin & Hohmann 1990, Chave and Jones 2012). TEM can be used to interrogate static shift, since it does not rely on electrodes to estimate resistivity structure (Pellerin & Hohmann 1990). Static shift effects are evaluated using TEM soundings at all but two of the MT stations and are found to be minimal (less than 5%), and therefore do not require correction. MTpy (Krieger & Peacock 2014) is used to calculate phase tensors (Caldwell et al. 2004), ellipticity (Bibby et al. 2005), and normalized skew angle (Booker 2014) to allow dimensionality assessment of the resistivity structure. The subsurface of the study area is complex and yields highly 3D data in many cases, thereby requiring a 3D inversion algorithm for comprehensive resistivity modeling.

The 3D inverse modeling scheme of Egbert & Kelbert (2012) [ModEM] is chosen to invert for subsurface resistivity in our study. Horizontal model cell dimensions are 250 m x 250 m inside the station coverage with a vertical refinement that starts at 10 m depth near the surface and increases exponentially with depth. Topography is not included in the model, since topographic relief is minimal across the surveyed area (about 350 m) and negligible relative to the skin depth of our longest-period MT data. Total model size is 201 km north-south x 196 km east-west x 193 km deep and is comprised of 98 x 85 x 49 cells. All components of \mathbf{Z} and induction vectors are modeled using 23 periods ranging from 10^{-3} to 10^3 seconds. Inverse modeling is completed in three steps. First, we model \mathbf{Z} using a 100 ohm-m half space as an initial condition, a 7% error floor, and a covariance value of 0.4. The covariance is used to adjust the smoothness of the ModEM model. This setup provides a simple smooth model that brings out general features that are evident in the data. We then use this converged model as an initial condition and invert the induction vectors using an error floor of 0.04 and a covariance value of 0.3. This refines the horizontal contacts that the induction vectors are typically sensitive to. Lastly, we use this converged model as an initial condition to model \mathbf{Z} using an error floor of 3%, induction vectors with an error floor of 0.02, and a covariance value of 0.2 that is applied twice. The more strict error floor and reduced smoothing covariance is used to bring out additional structure in the data.

Inversion results are inherently non-unique due to the large number of possible solutions that will fit the data. Uncertainty of these results is typically interrogated through testing the robustness of key inversion resistivity features (Winther 2009). Ideally, this involves numerous inversion runs in which sensitivity to initial conditions and inversion settings are systematically evaluated. However, three-dimensional inversions are computationally expensive, which often makes this approach cumbersome and impractical. Instead, the robustness of key features is tested by removing the features one at a time (i.e. blending their resistivities into the background resistivity) and assessing the effect this change has on the fit of the inverse model to observed data in terms of root-mean-squared error (RMS; Winther 2009). If removing the feature of interest appreciably alters station RMS, then the anomaly is found to be robust and well-constrained by station data. In this case, we are primarily interested in the large scale resistivity structure of the crystalline basement, but perform sensitivity analysis on two of

the more localized but prominent features evident in the inversion results (see Appendix 2.C for details). Removal of both features greatly impacts RMS and leads us to believe they are robust. Overall, the general patterns in the resistivity model are considered well-constrained and interpretable, although prudence is advised when interpreting the smallest-scale resistivity anomalies, as sensitivity analysis has not been performed on these more minor features. The final resistivity model is plotted in ArcGIS and in Paraview to facilitate interpretation.

2.3.4 Hydrothermal Modeling

The final best-fit model of Pepin et al. (2015) is used to estimate a simulated electrical resistivity image of the subsurface. This model solves numerical approximations of transient heat, groundwater, and solute transport equations using the finite element method of characteristics (FEMOC) hydrothermal modeling package (Person et al. 2008, Pepin et al. 2015). Density and viscosity are calculated as functions of temperature, pressure, and salinity using the expressions of Battelle & Wang (1992), which are valid for temperatures between 10 and 350°C. The finite element mesh consists of 14 hydrostratigraphic units using 3,904 nodes and 7,493 triangular elements and is of similar geometry to Figure 2.3. This model is a two-dimensional representation of the flow system that was constructed perpendicular to regional groundwater contours along the transect shown in Figure 2.2B and was run for 300,000 years to reach steady-state conditions. Pepin et al. (2015) used typical permeability values for most hydrostratigraphic units but focused on calibrating the permeability of the crystalline basement to reproduce carbon-14 groundwater ages, vertical geothermal specific discharge rates, geothermometry temperature estimates, and groundwater temperatures measured within the hot-springs district. Their calibration approach yielded a best-fit crystalline basement effective permeability of 10^{-12} m^2 . Reduction of permeability with depth using the Ingebritsen & Manning (1999) relationship did not improve the fit. Readers are referred to Pepin et al. (2015) for additional details of the model and its calibration.

Their study did not include calibration to total dissolved solids (TDS, salinity) concentrations (about 2,500 mg/L; Pepin et al. 2015) measured in the hot-springs district. Since electrical resistivity is strongly affected by salinity, we added a temperature-dependent solute reaction rate source term to the FEMOC solute transport equation and calibrated its magnitude to match measured concentrations in the hot-springs district. No other parameters of the model were altered during this calibration process. Transport of chemically conservative solutes through porous media is controlled by advection, Fickian diffusion, and hydrodynamic dispersion (Freeze and Cherry 1979, Furbish 1997). For relatively low flow velocities, solute transport is dominated by diffusion. Dispersive transport and advective transport are more important when fluid velocities are greater. Nonconservative solutes may also have geochemical sources or sinks in

the porous medium. FEMOC solves a Lagrangian form of the following equation to represent solute transport:

$$\nabla \cdot (\phi \bar{D} \nabla C) - \nabla \cdot (\vec{q}C) + R = \phi \frac{\partial C}{\partial t} \quad (2.4)$$

where ∇ is the gradient operator, \vec{q} is the specific discharge vector, t is time, ρ is fluid density, C is species concentration (TDS concentration is in units of solute mass fraction denoting kilograms of solute per kilogram of solution), ϕ is porosity, \bar{D} is the diffusive-dispersive tensor, and R is a solute rate of dissolution or precipitation (solute source term). We used a first-order reaction rate for the source term to mimic the buildup of salinity due to fluid-rock interactions, as shown below (Lemieux et al. 2008a, Provost et al. 1998):

$$R = k_{mt}(C_{max} - C) \quad (2.5)$$

where C_{max} is the maximum allowable fluid concentration and k_{mt} is a mass transfer reaction rate. We assigned C_{max} as 0.3 kg-solute per kg-fluid (Provost et al. 1998), which corresponds approximately to a fully-saturated sodium-chloride fluid. We represented the mass transfer reaction rate as a function of temperature through the Arrhenius expression as follows (Langmuir 1997):

$$k_{mt} = A_0 e^{-E_0 / R_0 T} \quad (2.6)$$

where A_0 is a temperature-independent empirical constant, E_0 is activation energy, R_0 is the ideal gas constant, and T is temperature. We use a mean value of 22 kcal/mol for the activation energy, since this value typically ranges from 8 to 36 kcal/mol for mineral dissolution or precipitation (Langmuir 1997). An A_0 value of 1.76×10^6 was determined by calibrating to measured TDS concentrations in the T or C hot-springs district; this yields an average mass transfer reaction rate that is similar to that used in the Provost et al. (1998) and Lemieux et al. (2008a) regional modeling studies. The resulting simulated salinities and temperatures can be used to produce a simulated electrical resistivity image of the subsurface. Archie's law (Archie 1942) is the most commonly used empirical equation to estimate subsurface electrical resistivity and is expressed as follows for fully-saturated conditions:

$$\rho_{eff} = \rho_{fluid} \phi^{-m} \quad (2.7)$$

where ρ_{eff} is the effective resistivity, ρ_{fluid} is the conductivity of the saturating fluid, ϕ is porosity, and m is a cementation factor that describes the connectivity of the fluid (typically around 2; Hyndman & Shearer 1989, Ussher et al. 2000). The T or C geothermal waters have a Na^+/Cl^- chemical signature, which is common for deeply circulating groundwater, with TDS concentrations that range from 556 to 3720 mg/L (Theis et al. 1941, Frapé et al. 2003, Person et al. 2013, Pepin et al. 2015). Temperatures in the hydrothermal model range from 14 to 272°C, while

TDS concentrations are as high as 19,646 mg/L. For these ranges, fluid resistivity is mainly a function of salinity and temperature (Quist and Marshall 1968, Nesbitt 1993). We derived a thin-plate spline Na^+/Cl^- fluid resistivity model for temperatures ranging from 0 to 309°C over salinities of 10 to 320,000 mg/L in Chapter 1 of this text. We use this fluid resistivity model in conjunction with Archie's law to estimate the simulated electrical resistivity of the subsurface for the T or C region. The resulting resistivity patterns are contoured in Paraview to enable comparison to the MT and TEM results produced in this study.

2.4 Results

2.4.1 Aquifer Test Results

Aquifer test drawdown curves for the production well are presented in Figure 2.7 and have several noteworthy features. The pump test yielded inertia-induced oscillations near the onset of pumping, which is characteristic of extremely permeable aquifers (Butler & Zhan 2004; Figure 2.7A). These oscillations quickly diminish and can be ignored for the quantitative analysis, consistent with the solution of Butler and Zhan (2004). Well losses dominate the drawdown throughout the pumping period. These losses are most likely caused by non-Darcian flow as a result of groundwater flow velocities exceeding the upper limit for laminar flow due to ultrahigh permeability conditions. However, as shown by Butler (1988), the well losses will not affect changes in drawdown after a short period of pumping as long as the pumping rate is held essentially constant. Small, relatively high-frequency fluctuations in drawdown occur throughout the pump test. These fluctuations are likely caused by small variations in flow rate and are magnified by the well losses. This pump noise is a minor feature of the data and does not prevent the estimation of changes in drawdown. The drawdown derivative plot (Figure 2.7B) indicates an increase in drawdown at late time that could be caused by one or more lateral flow boundaries.

We estimate aquifer transmissivity using the 1.9 to 39.8 minute time interval (Figure 2.7). This interval is chosen to get beyond the early time inertia-induced oscillations and to not be affected by the possible late-time boundary effects. The drawdown curve within this time interval yields a very high transmissivity estimate of $0.13 \text{ m}^2/\text{sec}$. Assuming a 24.4 m aquifer thickness of the well-screen interval indicates a hydraulic conductivity of $5.3 \times 10^{-3} \text{ m/s}$ and corresponds to an intrinsic permeability of $3.6 \times 10^{-10} \text{ m}^2$.

The drawdown plot in Figure 2.7B can be used to evaluate the appropriateness of applying the Cooper-Jacob method to estimate transmissivity. The derivative of the drawdown data should have a mean of approximately zero throughout the interval used to estimate transmissivity for the method to yield a reliable transmissivity estimate. The derivative data are very noisy as a result of

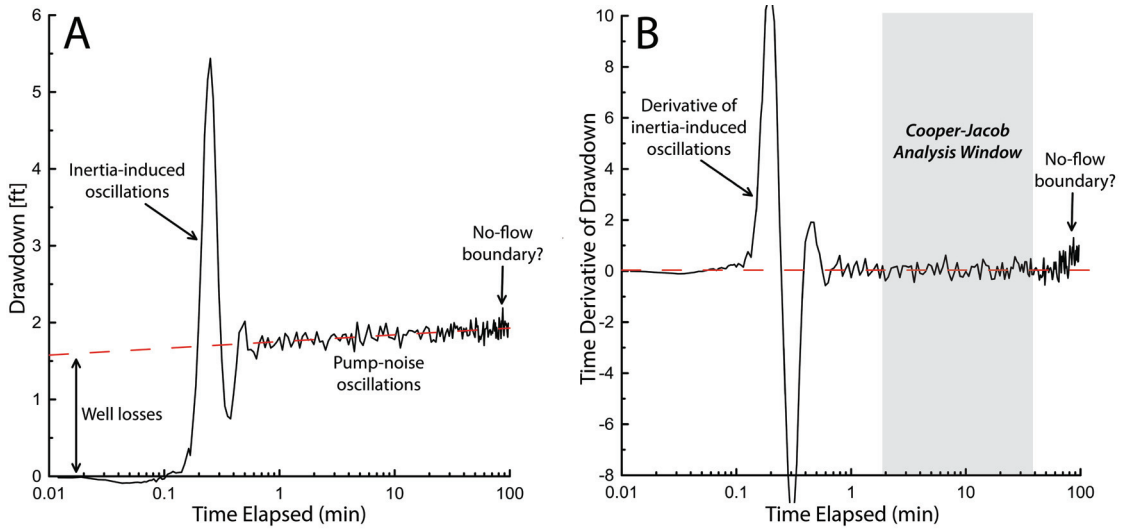


Figure 2.7: Aquifer test drawdown (A) and drawdown derivative (B) plots. Red dashed line in (A) is the Cooper-Jacob trend line for the analysis window shown in (B).

pump noise and the inertia-induced oscillations. However, the Bourdet derivative method has been successfully used by hydrologists and petroleum engineers for many years to clean up noisy derivative data and provides a reasonably well-behaved derivative in this case (Bourdet et al 1983, Bourdet et al. 1989, Spane and Wurstner 1993). The derivative data fluctuate about zero throughout the time interval used for the Cooper-Jacob analysis, which supports the use of this method to estimate transmissivity and suggests the value is trustworthy.

Overall, while the data is fairly noisy and have been significantly affected by well losses, this test suggests that the crystalline basement directly underlying the hot-springs district is extremely permeable. The no-flow boundary that is indicated in the late time of the drawdown data requires a longer-duration aquifer test to permit reliable analysis.

2.4.2 Magnetotelluric Results

Final MT inversion fits for all components of the impedance tensor are presented in Appendix 2.D. The model represents the data well throughout the survey area and has a total normalized root-mean squared error (nRMS) of 1.6. Depth slices ranging from 254 to 6,776 m are shown in Figure 2.8. The shallow subsurface in the northern half of the survey area is conductive ($< 50 \text{ ohm-m}$) to depths of around 1.5 km. The area becomes more resistive with depth after that, but is still typically around 200 ohm-m or less, even at depths of nearly 7 km. The shallow subsurface in the southeast portion of the study area is more resistive, with values that are commonly greater than 100 ohm-m and upwards of 600 ohm-m in some zones. This section of the model also gets more resistive with

depth but only until about 2.5 km. Below 2.5 km, the subsurface in the south-east region gets more conductive with depth and commonly contains values that are less than 100 ohm-m. There is a persistently conductive zone in the southwest corner of the survey, however, this area has limited station coverage and thereby this feature is considered to be very poorly constrained and should not be interpreted. MT cross sections are shown along Alamosa Creek and Cuchillo Negro Creek that terminate in the vicinity of the hot-springs district in Figure 2.9. Both the Cuchillo Negro Creek and Alamosa Creek sections show similar patterns, with a conductor (1 to 50 ohm-m) in the shallowest few kilometers of the subsurface that is underlain by more resistive material (100 to 200 ohm-m). The subsurface under the hot-springs district has a similar pattern, albeit with a thinner shallow conductor, but is underlain by a broad conductor (50 ohm-m) that begins at approximately 6 km depth and continues to beyond 10 km depth.

Figure 2.10 includes phase tensors (Caldwell et al. 2004) that are shaded by normalized skew angle (Booker 2014) at three different skin depths (equation 2.1 using $\rho_a = 50$ ohm-m) for all MT stations. The degree of phase tensor ellipticity is related to the dimensionality of the subsurface. Circular phase tensors indicate one-dimensional environments, whereas elliptical phase tensors imply two- or three-dimensional resistivity structure (Heise et al. 2006). The long axis of the phase tensor is parallel to geo-electric strike and thereby aligns with the preferred direction of electrical current flow, which is often observed to be in the direction of fractures (Peacock et al. 2013). Normalized skew magnitudes that are greater than 6 typically indicate complex three-dimensional structure (Booker 2014), while sign changes in skew are evidence of a pronounced geologic boundary (Chave & Jones 2012, Peacock et al. 2013). Shallow (about 1 km; Figure 2.10A) phase tensor and skew patterns for the T or C region are one-dimensional to the west of the Mud Springs fault, but become at least two-dimensional eastward of the fault. Dimensionality of the resistivity structure increases as a function of depth, with stations that are east of the Mud Springs fault being consistently more complex (Figure 2.10B and 2.10C). The Cuchillo Negro fault zone serves as a distinct boundary, as described by phase tensor orientation and skew magnitude at longer periods. This is most evident in Figure 2.10C, where the Cuchillo Negro fault zone separates NW-SE orientated phase tensors from those with a NE-SW strike. Tensor orientation along Alamosa Creek is similar to that of Cuchillo Negro Creek, although skew angle magnitudes are higher near Cuchillo Negro Creek, suggesting higher fracture density. Skew angles and phase tensors near the hot-springs district are consistently some of the more complex for each depth slice and imply complex structure.

2.4.3 Transient Electromagnetic Results

The contoured TEM resistivity results are presented in Figure 2.11; these 1D inversion results have been combined to make a 2D image of the subsurface. Penetration depth of the TEM soundings averaged about 300 m at each site. The

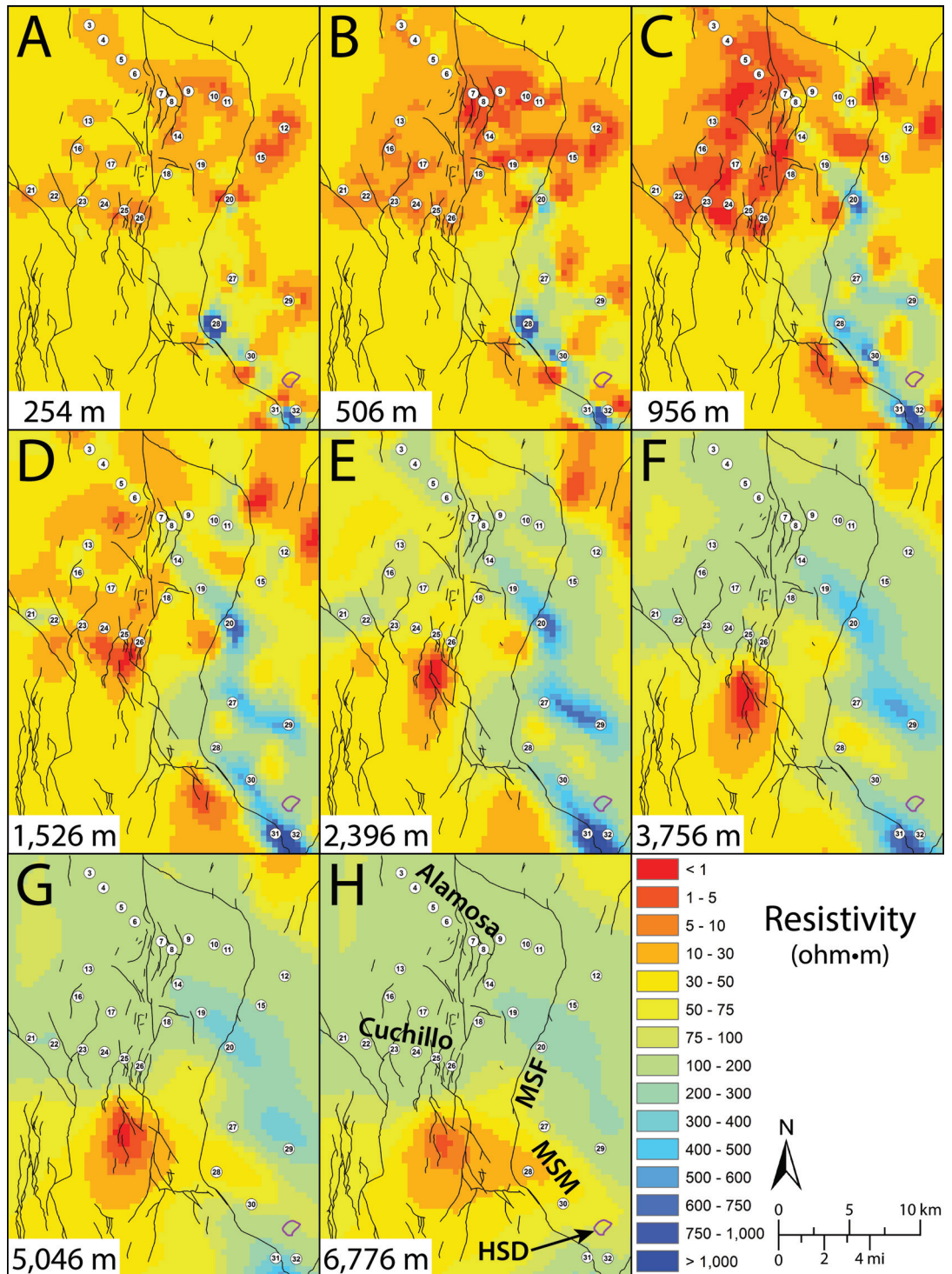


Figure 2.8: Depth slices of MT inversion resistivity results. Depth of the slice is noted in the bottom left corner of each image. Key features of the area are labeled in (H). Explanation: Alamosa = Alamosa Creek, Cuchillo = Cuchillo Negro Creek, MSF = Mud Springs fault, MSM = Mud Springs Mountains, HSD = Hot-springs district.

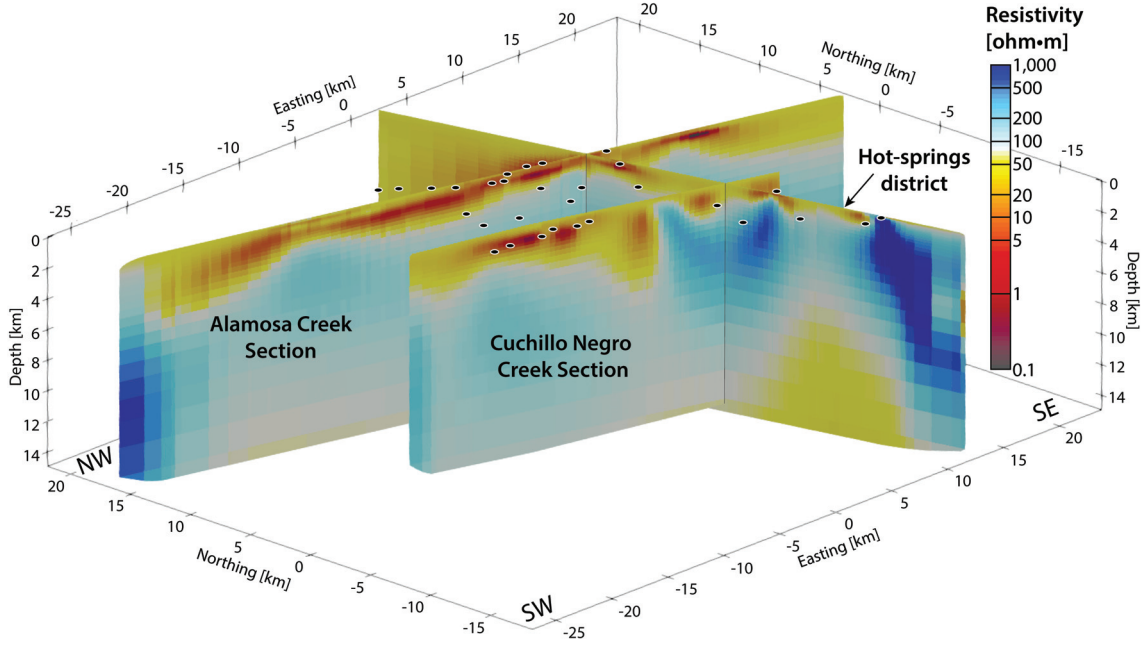


Figure 2.9: Cross sectional slices of MT inversion resistivity results. Transects along Alamosa Creek and Cuchillo Negro Creek are both indicated. Station locations are shown with black circles. The location of the hot-springs district is indicated in the right side of this figure. Easting and northing along the axes are relative to the center of the inversion model.

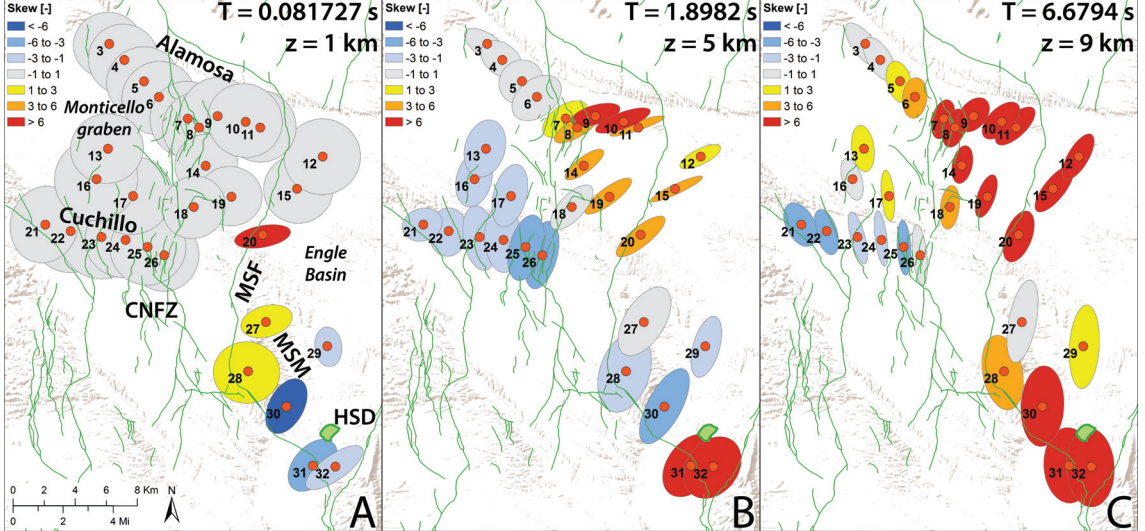


Figure 2.10: MT phase tensors (ellipses; Caldwell et al. 2004) and normalized skew angle (ellipse color shading; Booker 2014) overlaid on fault locations (green lines). Three periods (T) are included, which correspond to skins depths (z) of 1 (A), 5 (B), and 9 (C) km when using an apparent resistivity of 50 ohm·m in equation 2.1. Greater magnitude of phase tensor ellipticity and skew angle are indicative of complex structure at depth. Explanation: CNFZ = Cuchillo Negro fault zone, MSF = Mud Spring fault, MSM = Mud Springs Mountains, HSD = Hot-springs district, Alamosa = Alamosa Creek, Cuchillo = Cuchillo Negro Creek.

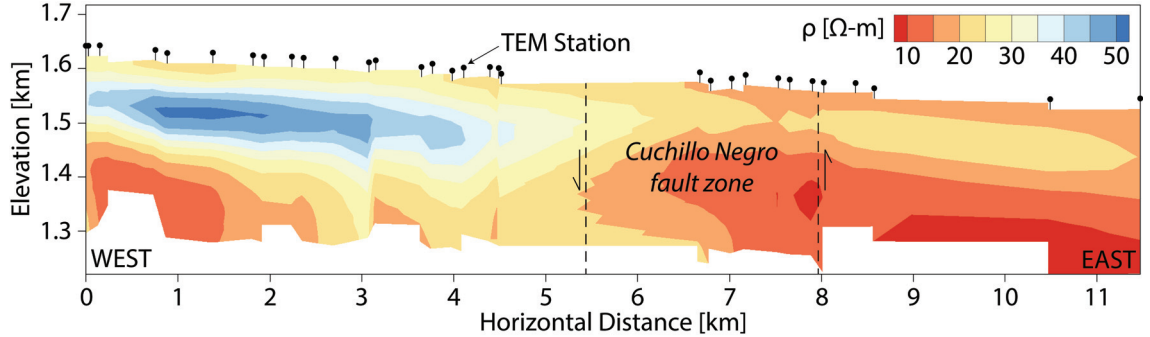


Figure 2.11: TEM inversion resistivity results. The east-west path of this transect is indicated in Figures 2.2 and 2.6. TEM station locations are indicated along the surface of the model. Surface elevations are derived from a 30-m digital elevation model.

resistivities along the transect range from approximately 5 ohm-m to a little over 50 ohm-m. The western portion of the transect is more resistive (> 25 ohm-m) than the eastern section of the transect (predominantly 20 ohm-m or less). This transition in resistivity is coincident with the location of the Cuchillo Negro fault zone. Resistivities within the western portion of this fault zone are considered to be poorly constrained, due to a lack of station coverage resulting from land access restrictions.

2.4.4 Hydrothermal Modeling Results

The hydrothermal modeling results are presented in Figure 2.12. The general structure of model hydrostratigraphy is depicted in Figure 2.3. Salinities and temperature patterns in the model are strongly affected by advection, which results in higher values being preferentially skewed towards the discharge area. Concentrations are highest in the sedimentary stack overlying the crystalline basement and in the bottom-right corner of the model domain below the regional discharge area that is near the hot-springs district (Figure 2.12A). Much of the basement and recharge area have salinities of less than 100 mg/L. The highest temperatures are in the bottom-right corner of the domain and directly underlie the hot-springs district at about 9 km depth (Figure 2.12B). The temperature contours are perturbed near the Mud Springs fault (MSF), with higher temperatures being deflected to shallower depths, due to the upwelling of groundwater. No deflection in temperatures is evident near the Cuchillo Negro fault zone (CNFZ), since this fault zone is not represented in the hydrostratigraphic framework of the model. Temperatures are lowest within the recharge area of the model domain due to the reduced temperatures of infiltrating recharge.

Simulated temperatures and salinities are used to compute an electrical resistivity estimate of the subsurface (Figure 2.12C). The sediments are consistently 50 ohm-m or less. The underlying crystalline basement is very resistive to the west of the Mud Springs fault, with resistivities that are well above 10,000

ohm-m. These high resistivities continue up into the recharge area. The basement becomes more conductive to the east of the Mud Springs fault, with values that range from about 1,000 ohm-m directly beneath the sediment stack that grade down to approximately 50 ohm-m in the bottom-right corner of the model domain.

2.5 Discussion

2.5.1 Interpretation

Each of the results provide valuable insight into the controls of ground-water flow in the basin. The aquifer test estimates that crystalline basement permeability underlying the hot-springs district is on the order of 10^{-10} m², which is commonly representative of gravel, clean sand, and karst limestone (Freeze & Cherry 1979). This permeability is incredibly high for crystalline rocks, as it is an order of magnitude greater than the typical upper bound for fractured crystalline rocks and is seven orders of magnitude higher than that of unfractured crystalline rocks (Freeze & Cherry 1979). The basement below the hot-springs district has clearly been significantly affected by intense faulting, as evidenced by this permeability estimate and the overturned syncline that bounds the hot-springs district less than 0.5 km northwest of the aquifer test site.

The MT resistivity patterns also indicate the presence of highly-fractured crystalline basement rocks throughout much of the watershed. The observed shallow conductors (< 50 ohm-m) correspond well with the position and resistivities of fine sediments, clays, and possibly saline fluids in the sedimentary stack that overlies the crystalline basement (Figures 2.1, 2.3, 2.8, & 2.9). The underlying crystalline basement is more resistive (100 to 200 ohm-m), but is still well below the lower bound of intact crystalline rocks (1,000 ohm-m; Figure 2.1). The resistivity of the basement agrees well with the typical resistivities of altered igneous and metamorphic rocks (Figure 2.1). The conductive (50 ohm-m) feature underlying the hot-springs district in the crystalline basement corresponds well with brackish geothermal fluids circulating within fractured crystalline rocks (Figure 2.1). This resistivity value is also in the appropriate range for clays, although high clay concentration at this depth would likely be a product of geothermal alteration, which would also suggest extensive faulting and deep groundwater circulation. There are smaller scale features of interest in the resistivity patterns as well, such as the resistive feature south of the hot-springs district that underlies stations 31 and 32 (Figure 2.8). The high resistivity (>1,000 ohm-m) of this feature suggests it is competent bedrock (Figure 2.1). Surface geology mapping by Jochems & Koning (2014) shows that Precambrian granitic basement outcrops 1-2 km to the north of these stations. This area also has much lower fault density relative to the study area to the west of the Mud Springs fault (Figure 2.8A), which may be indicative of low secondary permeability. Therefore, this resistor is hypothesized to be intact crystalline basement and likely serves as a barrier to groundwater

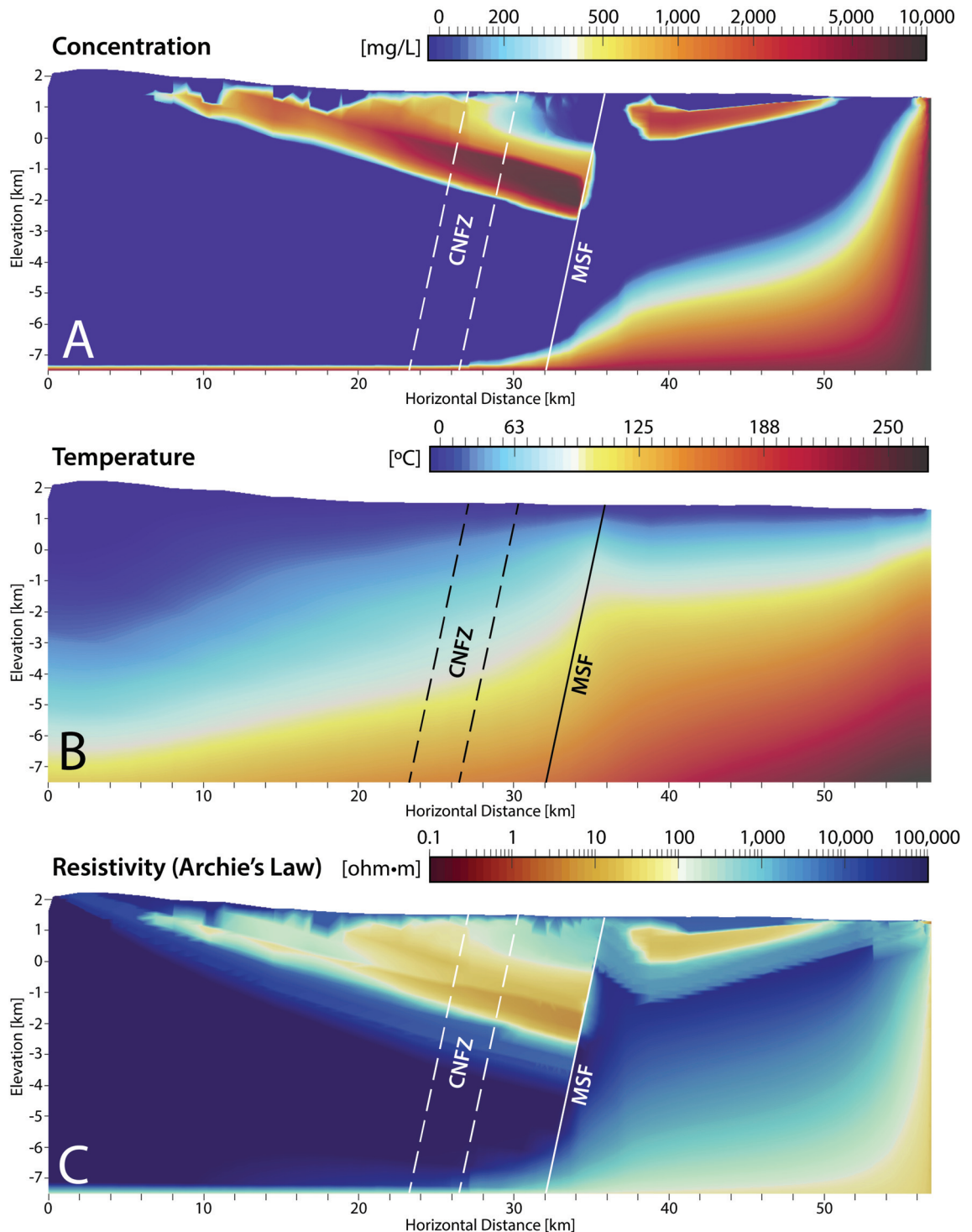


Figure 2.12: Hydrothermal modeling temperature, salinity, and electrical resistivity results. The simulated salinities and temperatures are combined to estimate electrical resistivity using Archie's law. Explanation: MSF = Mud Springs fault, CNFZ = Cuchillo Negro fault zone.

flow, which may be a key factor controlling the location of the hot-springs district. Collection of additional MT and aquifer test data to the south of the HSD would permit evaluation of this hypothesis in the future. A second smaller scale feature of interest in the resistivity results is the conductive feature (<10 ohm-m) located to the south of Cuchillo Negro Creek near stations 24, 25, and 26 (Figure 2.8D-H). This conductor is prevalent from 1.5 km depth to over 7 km and is much more conductive than its surroundings in the deeper portions of the model. Even though overlying station coverage is minimal, sensitivity analysis of this feature (see Appendix 2.C) indicates that it is well-constrained by neighboring MT stations. The anomalously high conductivity at depths greater than 3 km and the lack of an associated magnetic (Figure 2.13B) or gravitational (Figure 2.14B) signature implies that this may represent significant clay alteration. It is possible that this feature is the remnants of a past hydrothermal upflow zone, in which groundwater flow was focused through basement faults; this idea agrees well with the appreciable fault density in the vicinity of this anomaly (Figure 2.13A). Koning et al. (2018) note that the western part of the Mud Springs fault in this localized area was a main conduit for past hydrothermal alteration and silver-base metal mineralization. Figure 2.8H shows the conductive feature extending towards the Mud Springs mountains in the deeper portions of the subsurface, thereby suggesting that these hypothesized conduits could be linked at depth. Additional MT stations west of the Mud Springs mountains that could better delineate the size of the anomaly and possibly groundwater age dating to search for any sign of old upwelling groundwater may better constrain the plausibility of this feature being a former hydrothermal conduit.

The MT & TEM resistivity results provide insights into the role that faults play in controlling groundwater flow in the watershed. The prevalence and homogeneity of the reduced basement resistivity suggests fractures in the basement are well-connected and indicate the region could support deep circulation of groundwater on a regional scale. This is corroborated by the complex nature of the MT phase tensors at depth and their indication that faults, particularly those of the Cuchillo Negro fault zone, extend deep into the basement rocks with variable orientations. There is limited evidence for compartmentalization of the flow system in the MT results, which implies that regional faults are likely not substantial barriers to groundwater flow, although they may still act as conduits for fluids. The TEM results are most conductive down-hydrologic gradient from and within the Cuchillo Negro fault zone (Figure 2.11). There are several plausible scenarios that might account for this reduction in resistivity. One possibility is that faulting has created a higher clay content in and near the fault zone, thereby reducing sediment resistivity within and to the east of the fault zone. Another possible explanation is that the fault zone acts as a conduit for saline fluids to upwell from depth and increase the salinity of the shallow aquifer system. The resulting salinity contrast would reduce resistivity within the fault zone as well as down-hydrologic gradient, but not up-gradient of the fault zone. Brackish warm ($\gtrsim 30^{\circ}\text{C}$) waters have been encountered along Alamosa Creek within the Cuchillo Negro fault zone (Figure 2.6). Discharge temperatures of these fluids cool with increasing distance from the faults, thereby implying the fault zone acts as geother-

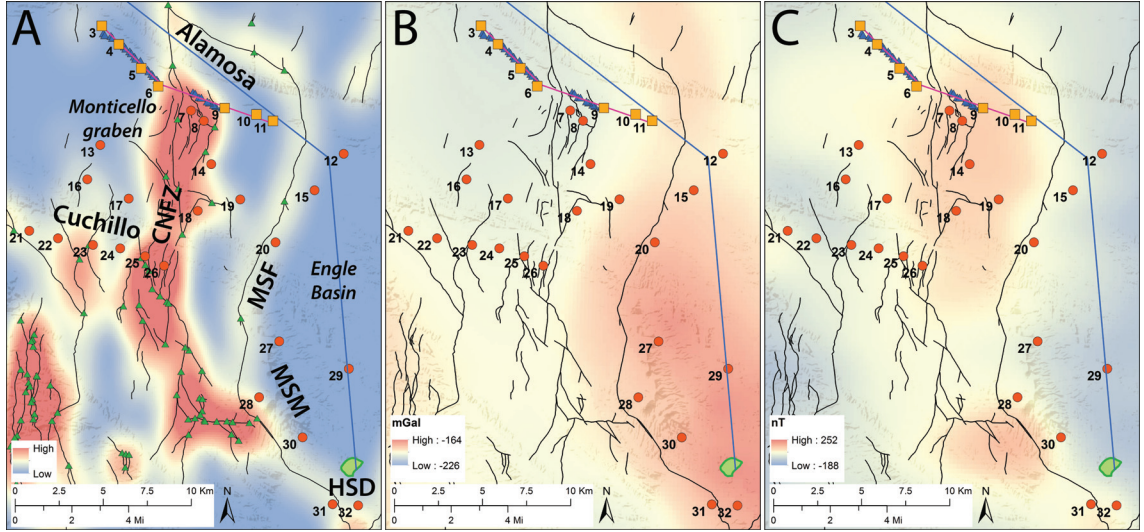


Figure 2.13: Quaternary Fault density with fault intersections (A), gravitational Bouger anomaly (B), and magnetic intensity (C) maps of T or C watershed (after Bielicki et al. 2015). Explanation: Black line = Quaternary faults, Blue transect = hydrothermal model and cross section profile of Pepin et al. (2015) and of Figure 2.3; pink transect = TEM profile across the Cuchillo Negro fault zone; green polygon = hot-springs district (HSD); red circle = MT station; orange square = co-located MT and TEM data used in TEM transect; blue triangle = TEM station for TEM transect; green triangle = Quaternary fault intersection.

mal conduit. Increased vegetation coverage is observed in the field within the Cuchillo Negro fault zone near fault scarps. This vegetation change supports both the idea of increased clay content, possibly leading to higher water table elevations, as well as the possibility of the faults serving as fluid conduits. Alternatively, the fault scarps could be focusing shallow soil moisture and creating a 'green strip'. Overall, the resistivity results suggest that faults are not regional barriers to groundwater flow, extend deep into the basement in some cases, and may serve as conduits that facilitate upwelling of geothermal and saline groundwater from depth.

Electromagnetic resistivity results are inherently non-unique due to the inversion process, so it is always good practice to compare results with independent geophysical measurements and geology. Fault density, gravitational Bouger anomaly, and magnetic intensity maps created using the datasets of Bielicki et al. (2015) are presented in Figure 2.13. The Cuchillo Negro fault zone (CNFZ) is a dominant influence on all three variables. This is true of the MT resistivity patterns as well down to depths of about 2.5 km (Figure 2.8). Beyond this depth, the regional resistivity patterns become more homogeneous, which agrees with well-connected regional fracture networks being present in the basement rocks. The agreement of MT with gravity, magnetism, and fault density is encouraging in terms of the MT inversion results capturing the large-scale resistivity patterns of the watershed.

The patterns in the simulated resistivity image from our hydrothermal

modeling effort also agree well with the MT resistivities. The model and MT results are compared in Figure 2.14 along the portion of the hydrothermal model transect (Figure 2.2B) that has adequate MT station coverage. All plots in this image are shaded using an identical contouring interval to facilitate direct comparison. The simulated resistivity results using the typical Archie exponent of two (m in Equation 2.7) is presented in Figure 2.14B, which is the same resistivity image shown in Figure 2.12C, except Figure 2.14B uses the MT contour color scheme. The simulation provides a sedimentary sequence that is a little less conductive than the MT inversion results, but that well-approximates the size and resistivity of the conductive feature below the hot-springs district. This agreement further supports the idea that this conductive feature below T or C may represent up-welling deeply-circulating saline groundwater. Much of the modeled crystalline basement is a lot more resistive than the MT image. The over-estimated resistivity in both the modeled sediments and throughout much of the basement may result from using an Archie exponent that is too high. In practice, a value of two is most often used for this exponent, however, previous researchers note that it can sometimes range from 1.3 to 2.5 (Telford et al. 1990). Therefore, we present a more conductive modeling result in Figure 2.14C that arises from using an Archie exponent of 1.3. This value yields better agreement between simulated and observed sediment resistivities but extends the conductive feature below T or C too far and makes it too conductive. Furthermore, much of the basement is still far too resistive. This discrepancy suggests that factors other than the Archie exponent are contributing to basement resistivity.

The most likely explanations for the over-estimated simulated resistivities include: (1) the solute reaction rate used the in solute transport equation is too low, leading to groundwater that is too dilute and too resistive in the basement (see Equations 2.4 & 2.5). However, increasing the solute source term would also yield a worse match to salinities in the hot-springs district, which suggests some other factor is likely contributing to basement resistivity. (2) The porosity is underestimated in the basement rocks. Increasing the porosity would increase the influence of fluid resistivity on effective resistivity (see Equation 2.7) and make the basement uniformly more conductive, therefore bringing the results more in line with observed resistivities. However, increasing porosity would also require re-calibration of the hydrothermal model to all other calibration constraints, which may dampen the influence of this porosity adjustment on simulated resistivity patterns. (3) The assumption of negligible rock resistivity in Archie's law (Equation 2.7) may inadequately represent the system. Particularly, clays or other alteration and weathering products may provide electrically conductive pathways in the basement, which seems plausible given the MT resistivity patterns indicate the basement is likely to be highly altered. Glover et al. (2000) derived and validated a modification to Archie's law that includes a term that takes rock resistivity into account. This term becomes influential when the rock has non-negligible conductivity relative to the fluid phase. This may happen in the case of fresh water causing fluid resistivities to exceed those of the rock. Figure 2.14D depicts simulated resistivity results that are calculated by using the Glover et al. (2000) equation for the same modeling scenario and a rock resistivity of 150 ohm-

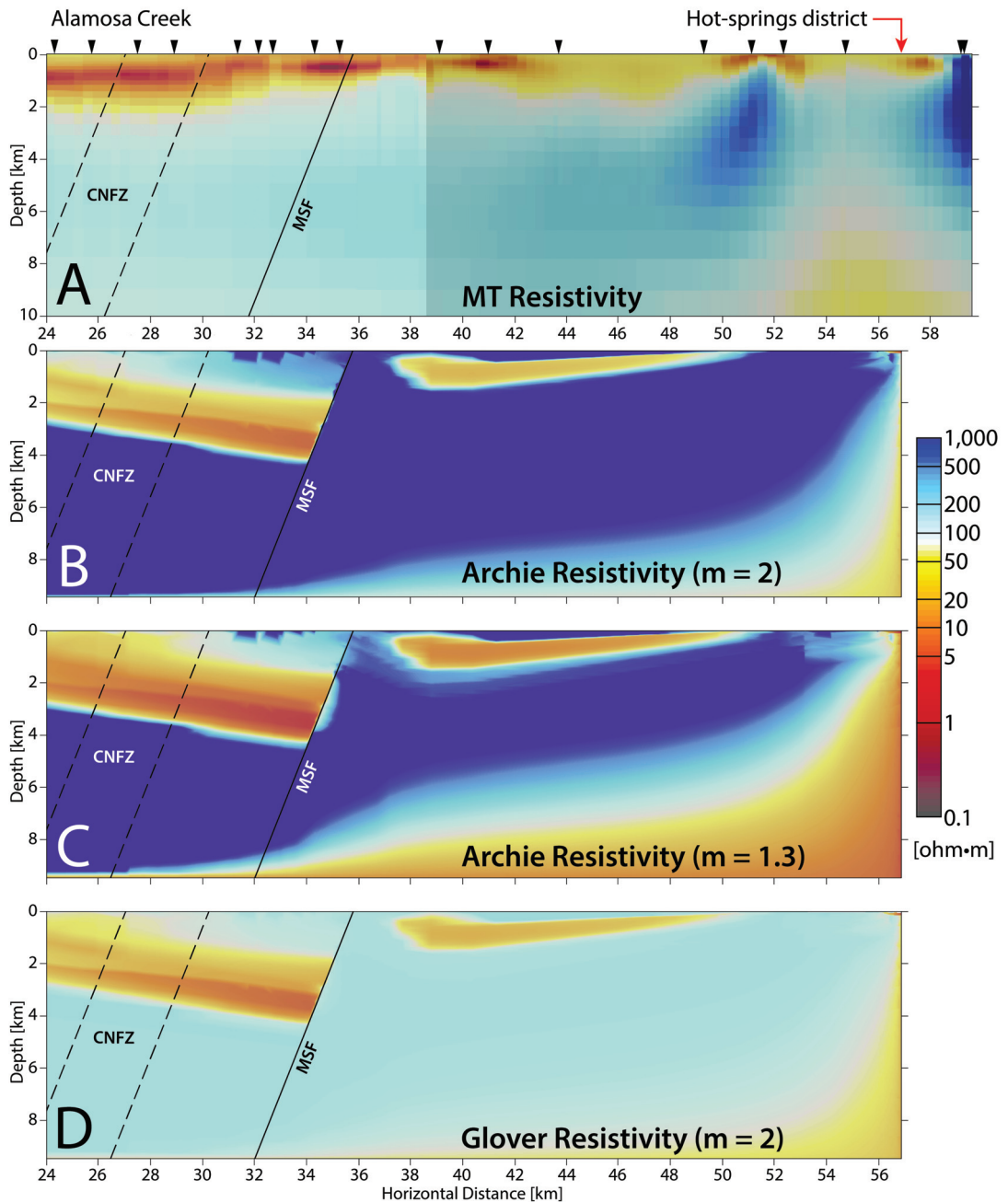


Figure 2.14: MT resistivity [A] compared to simulated resistivity. All images are on the same contouring color scheme to facilitate comparison and are along the segment of the blue transect in Figure 2.2 that has nearby MT station coverage. Simplified stratigraphy is shown in Figure 2.3. Simulated resistivity is calculated using Archie's law in [B] and [C] but with different Archie exponent magnitudes (m in Equation 2.7). In [D], resistivity is calculated using a modified form of Archie's law derived and validated by Glover et al. (2000). Unlike Archie's law, this modified version accounts for rock resistivity, which has been assigned as 150 ohm·m in [D]. Explanation: black triangle = MT station; CNFZ = Cuchillo Negro fault zone; MSF = Mud Springs fault.

m; this rock resistivity is suggested by the MT results and could represent an altered basement (Figure 2.1). The general simulated resistivity patterns agree very well with the MT resistivities and suggest that clays and/or other alteration and weathering products in the basement may be a key factor in controlling observed basement resistivities.

Overall, discrepancies between simulated and observed resistivity patterns may be accounted for through increases in solute reaction rates, porosity, and rock resistivity and a decrease in the Archie exponent. All of these adjustments would be justified for altered basement rocks with enhanced secondary fracture porosity and rock/water interaction surface area. Therefore, the discrepancies between the simulated and observed resistivity patterns further support the conceptual model that this flow system involves deep groundwater circulation within highly-fractured and well-connected crystalline basement rocks.

2.5.2 Synthesis

Our findings have immediate implications for the conceptualization of the T or C geothermal groundwater flow system. All of our results argue that very high basement permeability, in the form of well-connected fracture networks, is largely controlling groundwater circulation patterns on a regional scale. This basement evidently has permeabilities that are as high as 10^{-10} m² in some areas and has low electrical resistivities that are representative of saturated and altered crystalline rocks to depths greater than 10 km. These low resistivities prevail laterally throughout much of the watershed and are not strongly disturbed by regional faults, although phase tensor analysis suggests some of these faults extend deep into the basement. TEM resistivity patterns and upwelling brackish geothermal waters along the Cuchillo Negro fault zone indicate that faults act as conduits for upwelling geothermal fluids, while MT results indicate that they do not compartmentalize the system or serve as barriers to regional groundwater flow. The similarity between the Alamosa Creek and Cuchillo Negro Creek resistivity sections (Figure 2.9) suggests that both regions likely contribute geothermal groundwater to the hot-springs district, rather than just the Alamosa Creek section that was modeled by Pepin et al. (2015). This implies that the flow system is highly three-dimensional, which is also suggested by the persistent three-dimensionality of the MT data obtained in this study (see Appendix 2.D); this finding indicates that 3D hydrothermal modeling methods will likely yield the most accurate representations of this flow system and should be implemented in any future modeling studies. The resistive feature due south of the HSD may be competent crystalline basement rocks that serve as a barrier to groundwater flow and encourage upwelling in the HSD. The low resistivity feature just south of Cuchillo Negro Creek may represent hydrothermal clay alteration from a past fault-controlled geothermal discharge zone. This hypothesized discharge zone may be connected with the Mud Springs fault at depth. Generally, the findings of this study support the overall conceptual model put forth by Person et al. (2013)

and Pepin et al. (2015) and suggest this geothermal system is a basement-hosted resource that contains very permeable crystalline rocks to depths of up to 10 km.

2.5.3 Additional Considerations & Limitations

The main source of uncertainty of the aquifer test permeability estimate is the aquifer thickness used to convert transmissivity to permeability. However, even if the 10-km depth of the modeled flow system is used to calculate permeability, the aquifer test yields an extremely high basement permeability estimate of $8.8 \times 10^{-13} \text{ m}^2$ (Freeze & Cherry 1979). This is strong evidence that the crystalline basement permeability directly underlying the hot-springs district is very high. Additional uncertainty is introduced by our assumption that the well fully penetrates the aquifer, which is implicitly made when using the Cooper-Jacob analysis method (Schwartz & Zhang). Unfortunately, no local deep-well data exists to allow evaluation of aquifer thickness and analysis methods that can account for a partially-penetrating well still require knowledge of aquifer depth, which is unknown in this case. We therefore assume the screened interval of the borehole well-approximates aquifer thickness, but advise that the permeability estimate from the aquifer test be considered an order-of-magnitude approximation. The agreement of our permeability estimate (10^{-10} m^2) with that of the hot-springs district limestone aquifer (10^{-10} to 10^{-11} m^2) from Person et al. (2013) further encourages the notion that our value is representative of local subsurface conditions. However, ideally an additional basement well will be drilled in the future that is sufficiently deep and far away from the current well to allow drawdown analysis that is independent of this uncertainty.

The MT and TEM resistivity results are also subject to uncertainty and limitations. Namely, we lack localized hydrogeologic control throughout the upper 500 m along the TEM transect. Acquiring detailed stratigraphic records and groundwater chemistry along this transect would permit the differentiation between groundwater salinity and lithologic controls on the observed resistivity patterns; we currently cannot make this distinction with available data. The MT results suffer from relatively coarse station spacing as a consequence of the large study area considered, land access restrictions, and the necessity to avoid cultural noise (e.g. generators, operating automobiles, plumbing systems, electrical lines, etc.). Cultural noise is a particularly limiting factor near T or C, where the geothermal waters upwell. While the resistivity inversion results would certainly be better constrained with additional MT stations, the general large-scale features are thought to be adequately captured with the current station configuration.

The hydrothermal modeling effort could likely be a more accurate representation of the region by better capturing its 3D hydrogeologic geometry. The model currently ignores any groundwater inputs from the Cuchillo Negro Creek area as well as the Mud Springs Mountains, which could impact the model-derived basement permeability estimate of Pepin et al. (2015). The

three-dimensionality of the system is implied by our highly-3D MT data and the inverted resistivity patterns as discussed in Section 2.5.2. Acquiring measurements of rock resistivity for the lithologic units in the study area, specifically the crystalline basement, would allow for a more constrained use of the Glover et al. (2000) modified Archie equation to better interrogate the physical reasoning behind the observed basement and sedimentary resistivity magnitudes. Better constraints on porosity from borehole geophysical logs and laboratory measurements would also greatly improve the resistivity modeling effort. Lastly, the no-flow boundary condition along the southeast portion of the hydrothermal model is in very close proximity to the hot-springs district and has a non-negligible influence on simulation results. This no-flow boundary is physically justified, as it represents the Rio Grande, which is the regional topographic low and groundwater on the other side of the Rio Grande is cold relative to the hot-springs district waters. However, future models would ideally capture the asymmetry of the watershed and eliminate any influences of this boundary condition assignment by bounding the models using regional watershed divides at topographic highs rather than at the Rio Grande.

2.6 Conclusions & Future Work

This study aims to improve the conceptual model of crystalline-basement hosted geothermal systems in rift environments by focusing on the Truth or Consequences (T or C) hot-spring geothermal system in the Rio Grande rift of New Mexico. Previous hydrothermal modeling studies identify this system as likely involving deep (6 to 10 km) groundwater circulation within extremely permeable (10^{-12} m^2) crystalline basement rocks (Person et al. 2013, Pepin et al. 2015). We further evaluate this conceptual model by using electromagnetic geophysics (MT & TEM), aquifer testing, and hydrothermal modeling. This work particularly focuses on better constraining the role that faults play in controlling regional groundwater flow, the degree of compartmentalization along the geothermal flow path, and the plausibility that the basement rocks could be permeable to depths of 10 km.

All of our results support the deep-circulation, basement-hosted conceptual model for this geothermal system. Our aquifer test in the hot-springs district of T or C provides the first direct measurement of the crystalline basement permeability within the geothermal upflow zone. The permeability is incredibly high and is estimated to be on the order of $4 \times 10^{-10} \text{ m}^2$, which is typical of gravel, clean sand, and karst limestone aquifers (Freeze & Cherry 1979). The MT results depict a crystalline basement that is rather homogeneously conductive for crystalline rocks (100 to 200 ohm-m), with conductivities in line with altered and saturated igneous and metamorphic rocks (Figure 2.1); the basement resistivities are well below those of intact crystalline rocks. There is also a conductive (50 ohm-m) feature at 6 to 10 km depth directly below the hot-springs district that is well-reproduced by our hydrothermal model and may represent

upwelling geothermal groundwater. The TEM and MT results show minimal evidence for regional compartmentalization of the groundwater flow system and indicate faults serve as conduits for brackish upwelling groundwater within the Cuchillo Negro fault zone, but do not act as regional flow barriers. The homogeneity of the basement resistivity structure suggests that fractures are extensive and well-connected at depth, thereby facilitating large-scale groundwater circulation to great depth. Phase tensor analysis corroborates this notion by indicating some regional faults extend deep into the basement. Hydrothermal model results imply these fracture networks have increased the clay content, secondary porosity, fluid connectivity, and rock/water reaction surface area within the basement.

Overall, the crystalline basement within the T or C geothermal watershed appears to be some of the most permeable basement rocks at depth discovered to date; although comprehensive drilling and deep aquifer testing is required to undoubtedly confirm this notion. This work indicates that active rift settings with extensive tectonic histories may contain large regions of naturally-elevated secondary fracture permeability to depths of up to 10 km. Extending these findings to the crystalline-basement hosted Socorro geothermal system located 115 km north of T or C in the Rio Grande rift suggests that elevated fault density plays a prominent role in controlling the location of these flow systems. Confirming the presence of these permeable conditions at depth would have immediate implications for determining enhanced-geothermal system (EGS) site locations and likely improve their success rates if similar locations were sought out; since current EGS technology is challenged to achieve adequate and maintained permeability enhancement. Generally, geothermal exploration and development efforts undertaken in rift settings should strongly consider the possibility of highly-fractured crystalline rocks hosting deep groundwater circulation and governing regional geothermal groundwater flow patterns. Hydrogeologists typically view the crystalline basement as being nearly impermeable at depth. The deep groundwater flow patterns and associated high permeability conditions implied by this study suggest that the crystalline basement is not always impermeable and that it may greatly influence regional flow patterns. This finding is further support that nuclear waste isolation projects should avoid tectonically active environments and that groundwater flow within the basement should be considered for regional studies. Lastly, this work provides further evidence that electromagnetic geophysical methods (e.g. MT and TEM) when used in conjunction with hydrothermal models can aid in regional permeability quantification and conceptual model refinement.

Future refinements to the T or C conceptual model could likely be made by better interrogating some of the smaller scale features in the MT results. Particularly, there is a resistive ($>1,000$ ohm-m) feature 1-2 km south of the hot-springs district that we hypothesize is a barrier to groundwater flow and thereby encourages groundwater upwelling in the HSD. This concept could be tested with aquifer testing in this localized zone along with additional MT station converge to better constrain the lateral extent of the feature. Furthermore, there is a conductive (<10 ohm-m) anomaly to the south of Cuchillo Negro Creek that may be the remnants of a former fault-controlled hydrothermal upflow zone. Station

coverage is limited near this feature, although MT sensitivity analysis indicates that it is well-constrained by our data. This feature could be further investigated with groundwater age dating in search of deep (i.e. old) upwelling fluids, in addition to improving overlying MT station coverage to better constrain its extent and connection to the Mud Springs fault at depth. MT resistivity results and phase tensor analysis indicate this flow system is highly three-dimensional and would best be represented using 3D modeling techniques in the future that could interrogate the importance of groundwater contributions from the Cuchillo Negro Creek area and Caballo Mountains.

Acknowledgments

We thank the residents of Truth or Consequences, especially Lee Foerstner, for their invaluable aid in making this study possible. This work could not have been completed without the field support of Jim Witcher, Reid Brown, John Ortiz, Michelle Sherman, Adrianna Nieto, Matthew Folsom, and Kyle Stark. Funding was provided by National Science Foundation grant EAR 1830172 and EPSCoR Energize New Mexico grant IIA-1301346. Electromagnetic geophysical datasets and the hydrothermal model used in this study are maintained by Mark Person of the Earth & Environmental Science Department at New Mexico Tech.

2.A Aquifer Test Production Well Data

Table 2.1: Production well aquifer test data. Time (t) is the time elapsed since pumping began and drawdown (s) is the drawdown measured in the production well. The field configuration of this aquifer test is shown in Figure 2.4.

t [sec]	s [ft]								
0	-0.002	14.28	5.142	134.4	1.729	1248	1.728	3588	1.684
0.24	-0.019	15.06	5.418	142.2	1.741	1308	1.757	3648	1.895
0.72	-0.036	15.96	4.888	150.6	1.624	1368	1.728	3708	1.901
0.96	-0.037	16.92	3.672	159.6	1.743	1428	1.931	3768	1.908
1.14	-0.03	17.88	2.382	169.2	1.807	1488	1.802	3828	1.996
1.62	-0.063	18.96	1.477	178.8	1.831	1548	1.907	3888	1.794
1.86	-0.066	20.1	0.896	189.6	1.78	1608	1.736	3948	1.845
2.1	-0.083	21.3	0.762	201	1.744	1668	1.844	4008	1.886
2.58	-0.108	22.56	0.73	213	1.822	1728	1.897	4068	1.885
2.82	-0.105	23.88	1.032	225.6	1.83	1788	1.805	4128	1.821
3	-0.106	25.32	1.404	238.8	1.694	1848	1.959	4188	1.863
3.36	-0.098	26.82	1.852	253.2	1.835	1908	1.779	4248	1.844
3.54	-0.097	28.38	1.92	268.2	1.605	1968	1.979	4308	1.936
3.78	-0.102	30.06	1.998	283.8	1.984	2028	1.907	4368	2.013
4.02	-0.089	31.86	1.626	300.6	1.741	2088	1.935	4428	1.873
4.2	-0.092	33.9	1.63	318.6	1.685	2148	1.872	4488	1.977
4.44	-0.072	35.76	1.599	337.2	1.813	2208	1.914	4548	1.781
4.68	-0.07	37.86	1.51	357.6	1.952	2268	1.922	4608	1.919
4.86	-0.054	40.08	1.716	378.6	1.787	2328	1.771	4668	1.846
5.1	-0.09	42.48	1.807	400.8	1.767	2388	1.905	4728	1.767
5.34	-0.049	45	1.658	424.8	1.744	2448	1.862	4788	1.764
5.58	-0.035	47.64	1.782	450	1.931	2508	1.91	4848	2.043
5.76	-0.057	50.46	1.651	476.4	1.825	2568	1.811	4908	1.977
6	-0.05	53.46	1.68	504.6	1.971	2628	1.812	4968	1.941
6.24	-0.014	56.64	1.725	534.6	1.79	2688	1.824	5028	1.776
6.42	0.008	60	1.788	566.4	1.781	2748	2.013	5088	2.003
6.9	0.029	63.6	1.625	600	1.761	2808	1.904	5148	1.964
7.14	0.044	67.2	1.839	636	1.917	2868	1.87	5208	2.17
7.56	0.025	71.4	1.79	672	1.652	2928	1.828	5268	1.926
8.04	0.031	75.6	1.666	714	1.825	2988	1.79	5328	1.813
8.46	0.033	79.8	1.733	756	1.817	3048	2.038	5388	1.942
9	0.14	84.6	1.855	798	1.878	3108	1.925	5448	1.999
9.78	0.343	90	1.651	846	1.875	3168	1.937	5508	1.95
10.08	0.254	94.8	1.799	900	1.853	3228	1.729	5568	1.971
10.8	0.802	100.8	1.849	948	1.884	3288	1.802	5628	1.953
11.28	1.163	106.8	1.753	1008	1.767	3348	1.762	5688	1.858
11.94	1.995	112.8	1.763	1068	1.864	3408	1.809	5748	1.792
12.84	3.346	119.4	1.697	1128	1.929	3468	1.845	5808	1.972
13.44	4.43	126.6	1.86	1188	1.903	3528	1.981		

2.B Electromagnetic Station Information

Table 2.2: Transient electromagnetic (TEM) Cuchillo Negro fault zone transect station location information. Easting (X) and northing (Y) are derived from a handheld GPS and are in WGS84 UTM Zone 13 coordinates. Elevation is extracted at the coordinate locations from a 30-meter digital elevation model.

Station ID	X	Y	Elev. [m]	Collection Date
MT3	275360	3692556	1623	6/20/2016
MT4	276327	3691514	1610	6/9/2016
MT5	277599	3690141	1597	6/13/2016
MT6	278558	3689130	1581	6/16/2016
MT9	282339	3687893	1557	6/16/2016
MT10	284153	3687528	1537	6/20/2016
MT11	285090	3687157	1525	6/23/2016
WD000	280536	3688781	1576	7/20/2016
WD00	280657	3688719	1571	7/20/2016
WD0	280876	3688498	1563	7/20/2016
WD1	281010	3688481	1570	7/20/2016
16	282149	3687911	1556	7/21/2016
15-B	281825	3687997	1556	7/21/2016
15-A	281706	3688068	1559	7/21/2016
14-B	281475	3688197	1561	7/21/2016
14-A	281353	3688265	1565	7/21/2016
1-A	275446	3692137	1623	8/8/2016
1-B	275528	3692028	1624	8/8/2016
2-A	275880	3691987	1616	8/8/2016
2-B	275971	3691878	1610	8/15/2016
3-A	276643	3691389	1606	8/15/2016
3-B	276724	3691273	1604	8/15/2016
4-A	276950	3691109	1603	8/15/2016
4-B	277037	3691000	1601	8/16/2016
5-A	277206	3690808	1596	8/16/2016
5-B	277281	3690693	1600	8/16/2016
6-A	277549	3690562	1594	8/16/2016
7-A	277954	3690079	1597	8/17/2016
7-B	278035	3689969	1590	8/17/2016
8-A	278195	3689823	1590	8/17/2016
8-B	278279	3689711	1583	8/17/2016
9-A	278482	3689510	1586	8/17/2016
9-B	278568	3689392	1584	8/17/2016

Table 2.3: Magnetotelluric (MT) survey station location information. Easting (X) and northing (Y) are derived from a handheld GPS and are in WGS84 UTM Zone 13 coordinates. Elevation is extracted at the coordinate locations from a 30-meter digital elevation model. The Hz column denotes if vertical magnetic field data was collected at the station. MT and TEM dates are the data collection date of each method at the station location. The TEM data are used to evaluate static shift at the MT sites. In some instances, TEM was not collected or was too resistive to be used for accurate static shift correction. These stations are noted in the TEM date column or indicated with ** (TEM too resistive). Stations flagged with a * denote stations that were not remote referenced due to lack of successfully co-collected data.

Station ID	X	Y	Elev. [m]	Hz	MT Date	TEM Date
3	275360	3692555	1623	Yes	6/20/16	6/20/16
4	276327	3691514	1610	Yes	6/9/16	6/9/16
5	277599	3690141	1597	Yes	6/13/16	6/13/16
6	278558	3689130	1581	Yes	6/16/16	6/16/16
7	280428	3687736	1570	Yes	6/9/16	6/9/16
8	281158	3687160	1556	Yes	6/13/16	6/13/16
9	282339	3687893	1557	Yes	6/16/16	6/16/16
10	284153	3687528	1537	Yes	6/20/16	6/20/16
11	285090	3687157	1525	Yes	6/23/16	6/23/16
12	289107	3685295	1482	Yes	6/9/16	6/13/16
13	275276	3685794	1601	Yes	8/1/17	5/5/17
14	281578	3684707	1542	Yes	7/30/17	4/24/17
15	287452	3683223	1485	Yes	7/14/17	4/24/17
16	274541	3683844	1599	Yes	7/26/17	5/6/17
17	276889	3682752	1557	Yes	7/30/17	5/6/17
18	280814	3682050	1540	Yes	7/24/17	5/6/17
19	283232	3682705	1522	Yes	7/12/17	4/17/17
20	285240	3680262	1499	Yes	7/26/17	5/6/17
21	271246	3680912	1615	Yes	7/14/17	4/16/17
22	272872	3680494	1594	Yes	7/17/17	4/17/17
23	274863	3680114	1562	Yes	7/21/17	4/17/17
24	276407	3679923	1562	Yes	7/12/17	4/17/17
25*	277822	3679479	1546	Yes	7/10/17	4/17/17
26	278902	3678941	1543	Yes	4/10/17	4/15/17
27	285449	3674662	1440	No	7/12/17	Not Collected
28**	284305	3671491	1511	No	7/17/17	4/24/17
29	289402	3673107	1338	Yes	4/10/17	4/15/17
30	286771	3669215	1397	Yes	7/24/17	Not Collected
31	288477	3665419	1320	Yes	7/28/17	4/24/17
32**	289925	3665352	1375	Yes	7/28/17	4/23/17

2.C Magnetotelluric Sensitivity Analysis

A sensitivity analysis is performed on two key features that are evident in the inversion resistivity results to interrogate their robustness. The first feature is the approximately 50-ohm conductor that is below the hot-springs district, which is best illustrated in Figures 2.9 and 2.14A. The second feature focused on is the large conductor (less than 30 ohm-m) that is south of Cuchillo Negro Creek and west of the Mud Springs Mountains; this feature is most evident in Figures 2.8E-H. We evaluate the robustness of these conductive anomalies by removing them (i.e. replacing their resistivities with adjacent values) from the inversion results one at a time and assessing the effect this change has on station root-mean-squared error (RMS). If removing the feature of interest appreciably worsens station RMS (high Δ RMS), then the feature is considered to be robust and well-constrained by data.

Removal of the Cuchillo Negro Creek feature mainly affects stations 28, 30, 31, and 32, which are in closest proximity to the anomaly (Figure 2.15A and 2.15B). The RMS actually improves for some stations in the 10^{-1} to 10^1 sec period range upon removal of the feature, however, this improvement is at the expense of a much worse fit at longer periods for all stations. This feature is thereby not thought to be an inversion artifact but is instead considered well-constrained by surrounding station data. Removing the conductive feature south of Cuchillo Negro Creek has an even more dramatic impact on nearby station RMS, which primarily affects stations 17, 19, 23, 24, 25, and 26 (Figure 2.15C and 2.15D). This more pronounced impact is likely due to the larger areal extent and greater conductivity contrast of the anomaly with its surroundings. RMS is immensely worsened for all nearby stations and this degradation is generally exacerbated as period length increases. The evident robustness of this conductive feature is somewhat surprising, considering the limited station coverage above the anomaly. However, this analysis clearly demonstrates that nearby station data well-constrains this feature. Overall, RMS is negatively impacted for nearby MT stations in a significant manner when either feature is removed and both anomalies are therefore thought to be robust.

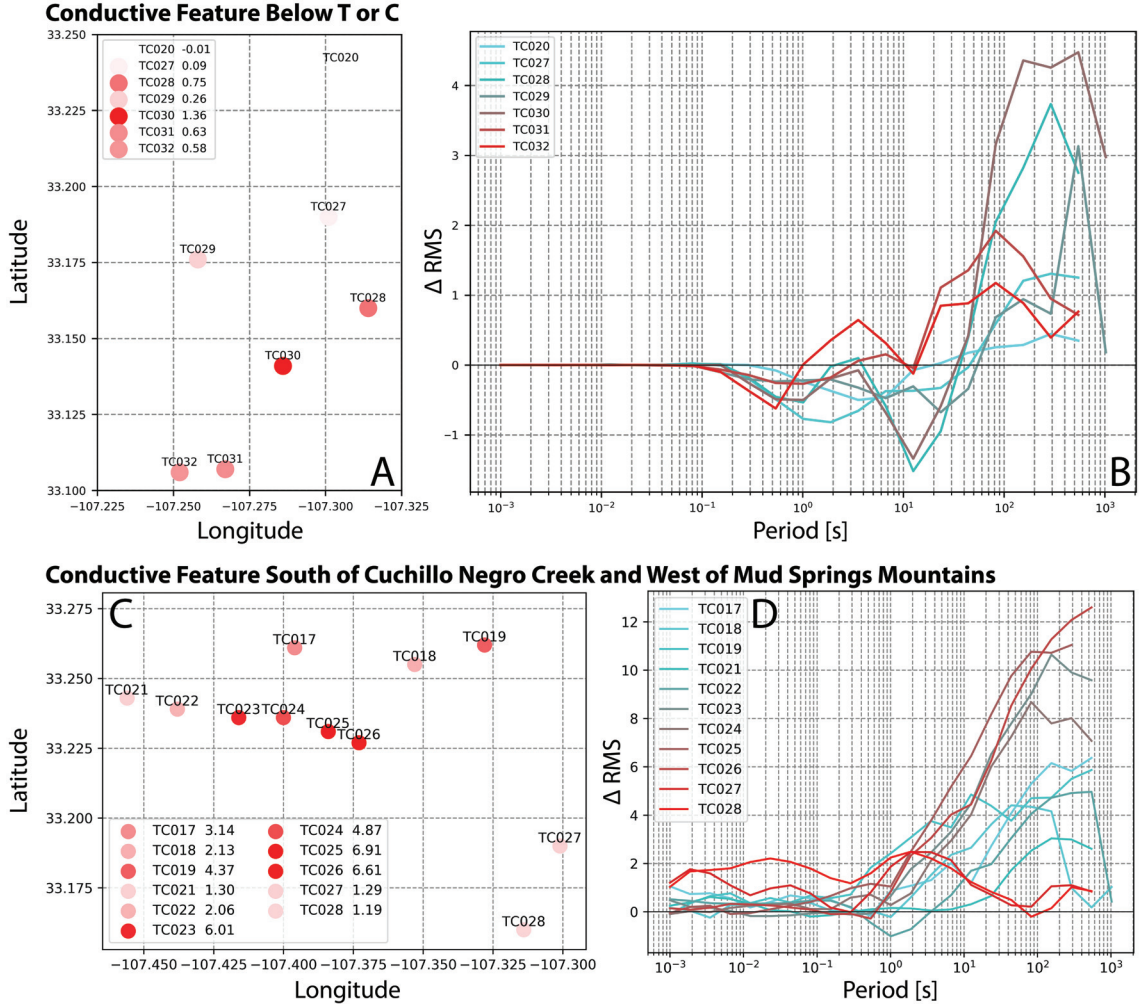
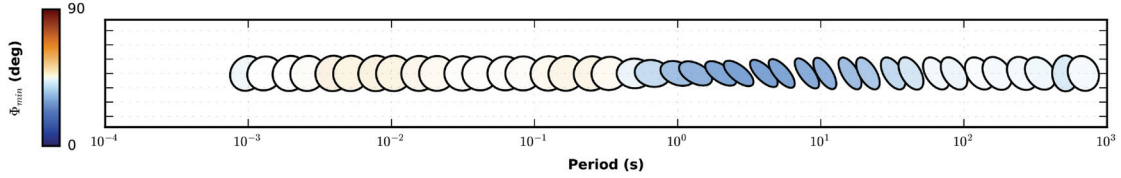


Figure 2.15: Sensitivity analysis results for two prominent features in the MT inversion results. The first feature tested (A,B) is the approximately 50-ohm conductor that is below the hot-springs district, which is best illustrated in Figures 2.9 and 2.14A. The second feature focused on (C,D) is the large conductor (less than 30 ohm-m) that is south of Cuchillo Negro Creek and west of the Mud Springs Mountains; this feature is most evident in Figures 2.8E-H. Inversion root-mean-squared error (RMS) of nearby stations is greatly impacted in an adverse way (high values for ΔRMS) when either of these features are removed from the inversion results. This is strong evidence that these anomalies are well-constrained by surrounding data.

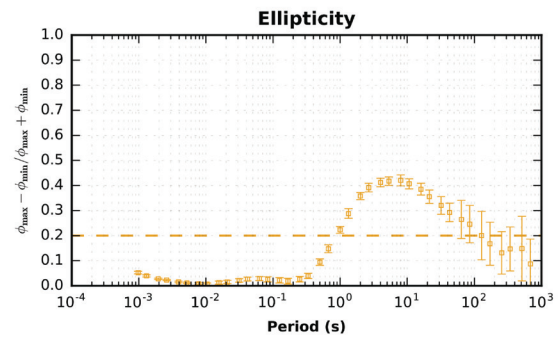
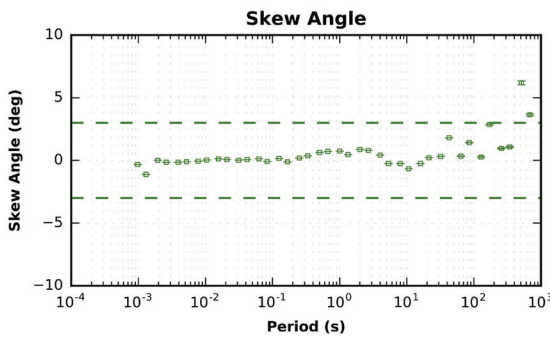
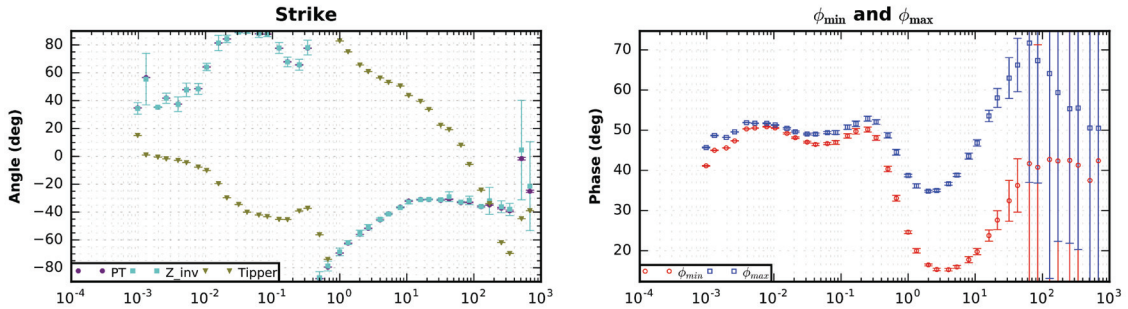
2.D Magnetotelluric Phase Tensors, Dimensionality Metrics, & Inverse Model Fits

Phase tensors (Caldwell et al. 2004), ellipticity (Bibby et al. 2005), normalized skew angle (Booker 2014), and multiple estimates of geo-electric strike have been calculated for each magnetotelluric station using MTpy (Krieger & Peacock 2014) and are presented in this appendix. Phase tensor ellipticity and normalized skew angle are both related to the dimensionality of the subsurface. Circular phase tensors with skews near zero indicate one-dimensional environments, whereas elliptical phase tensors with high skew magnitudes imply two- or three-dimensional resistivity structure. The long axis of the phase tensor is perpendicular to geo-electric strike and thereby aligns with the preferred direction of electrical current flow, which is often observed to be in the direction of fractures (Peacock et al. 2013). Skew magnitudes that are greater than three typically indicate complex three-dimensional structure, while sign changes in skew are evidence of a pronounced geologic boundary (Chave & Jones 2012, Peacock et al. 2013). Phase tensors also have the advantage of being free from galvanic distortion (i.e. static shift; Chave & Jones 2012). A station-by-station presentation of these metrics is provided in this appendix for reference. Map view visualization is often more conducive to spatial evaluation of parameter patterns; Figure 2.10 in the results section of this document includes three map-view images along with discussion of these dimensionality metrics. Geologic interpretation is also included in the discussion section of the paper. Final 3D ModEM inverse model fits for all components of the impedance tensor are also shown in this appendix for each station.

Phase Tensors



Dimensionality Metrics



Inverse Model Fits

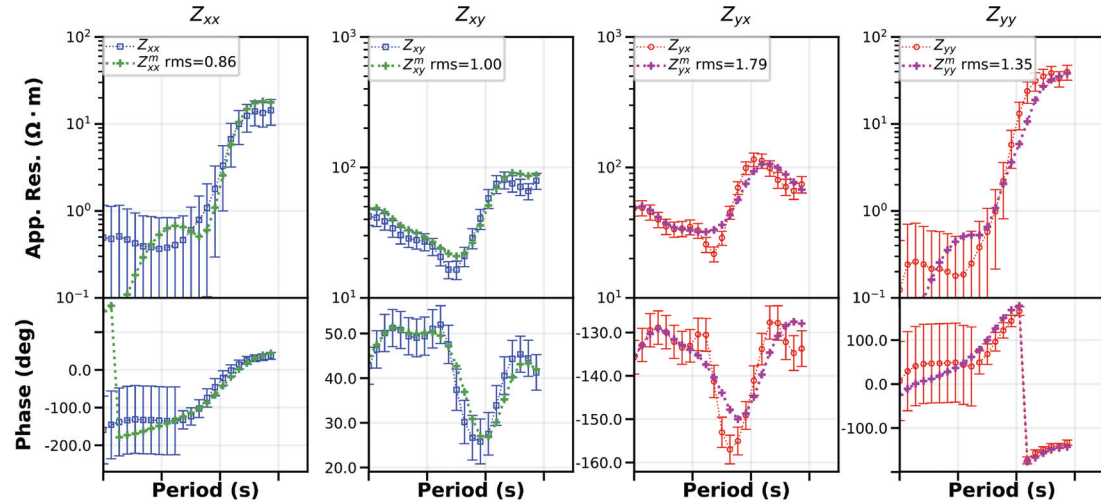
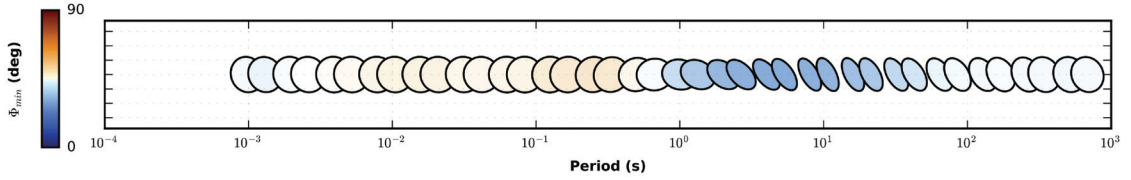
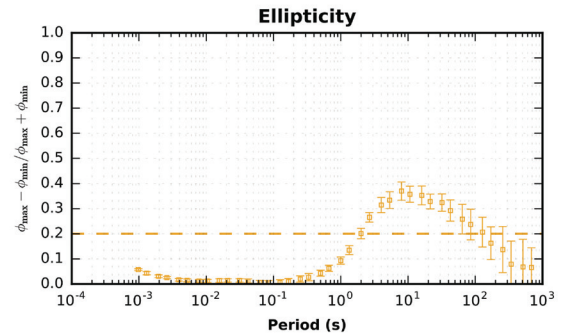
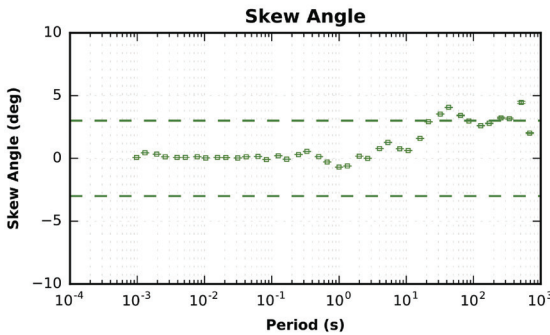
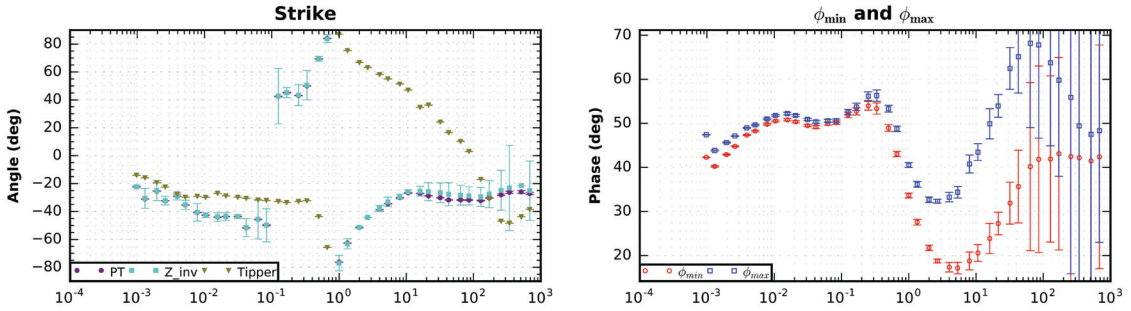


Figure 2.16: MT station #3 phase tensors, dimensionality metrics, and inverse model fits

Phase Tensors



Dimensionality Metrics



Inverse Model Fits

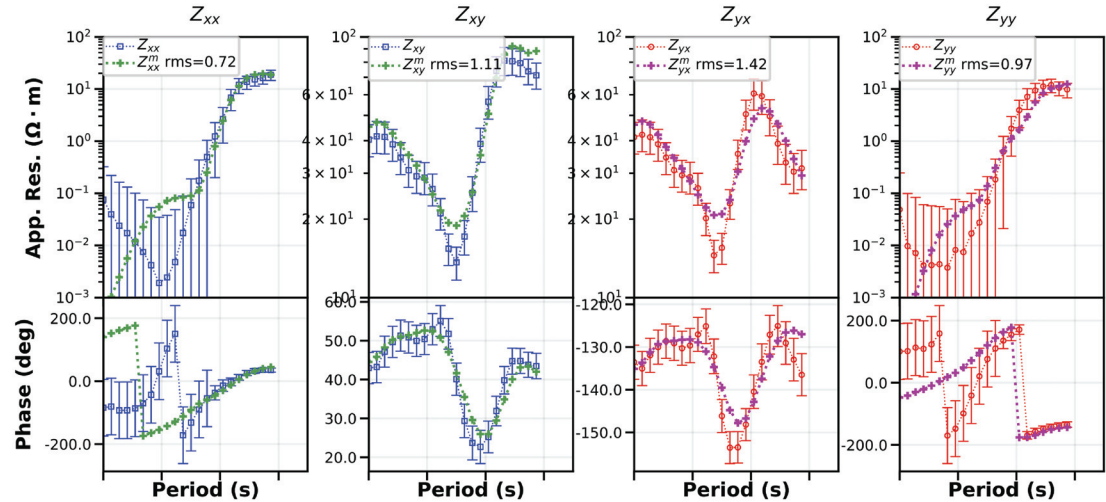
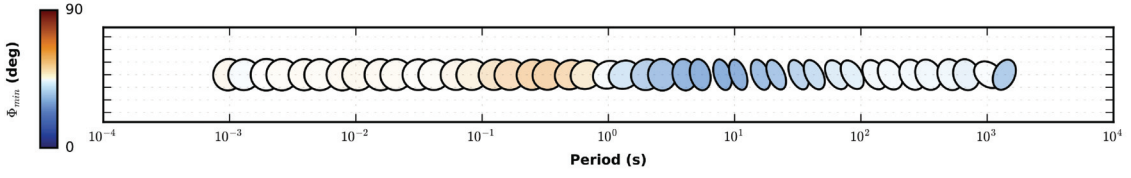
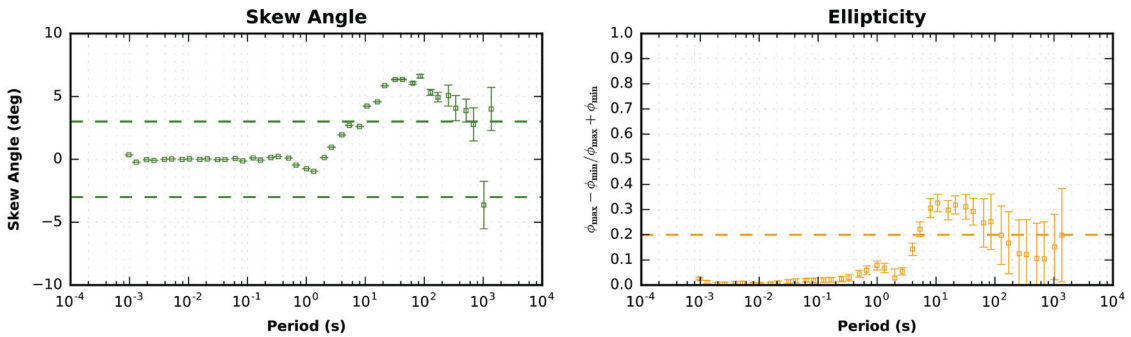
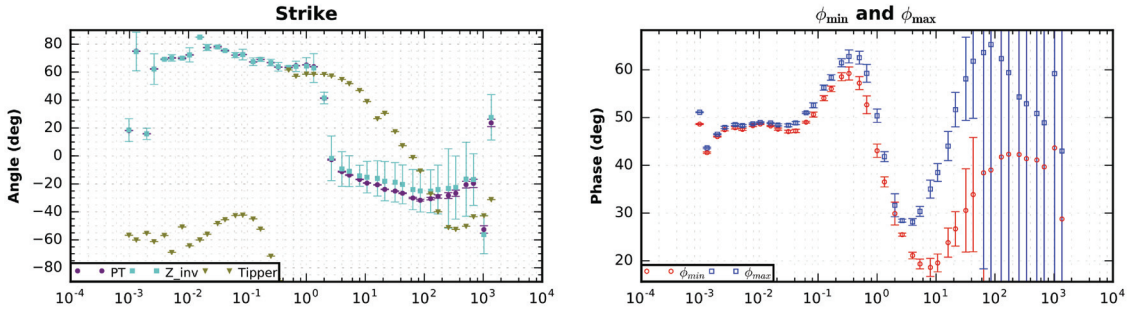


Figure 2.17: MT station #4 phase tensors, dimensionality metrics, and inverse model fits

Phase Tensors



Dimensionality Metrics



Inverse Model Fits

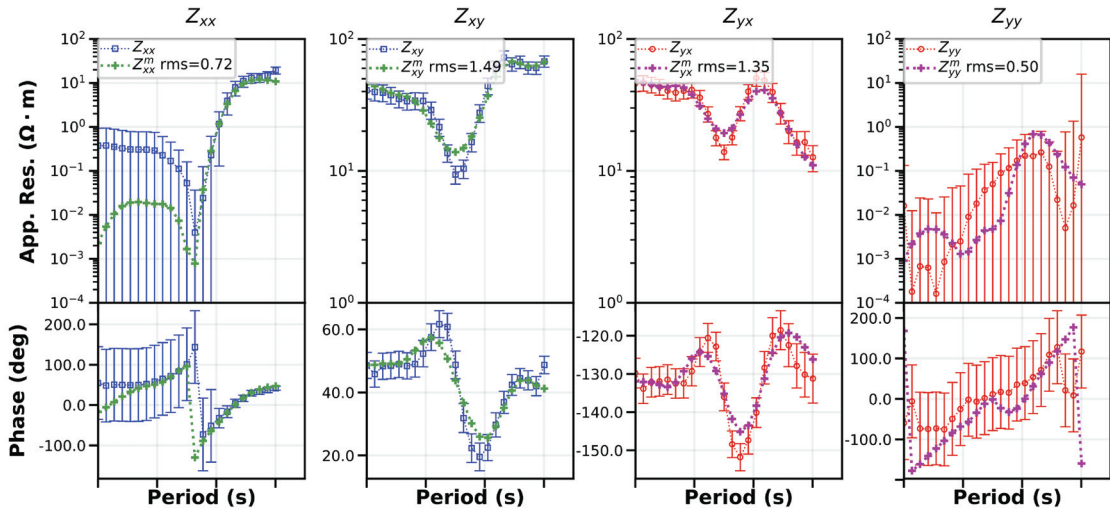
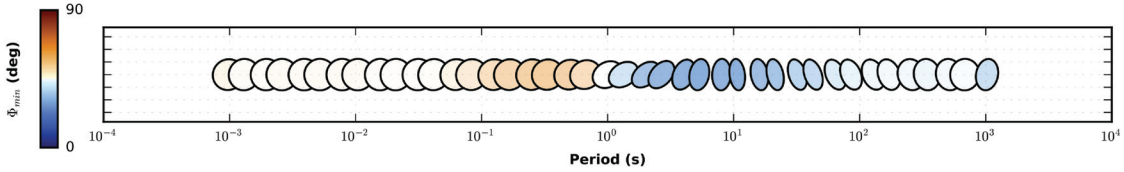
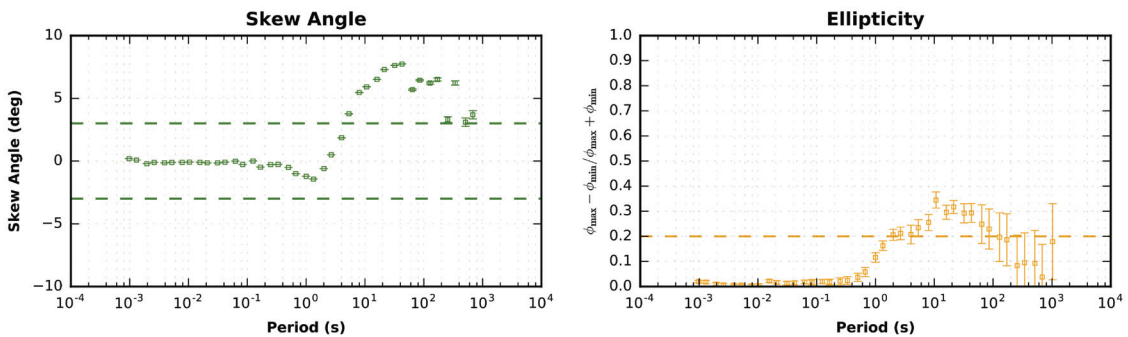
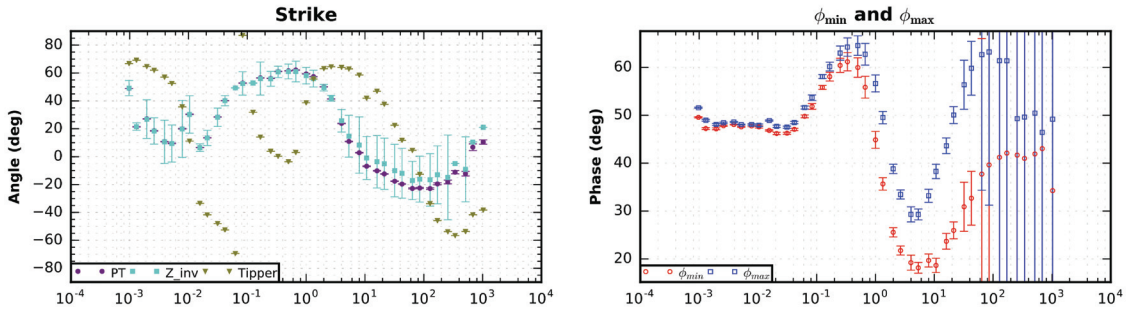


Figure 2.18: MT station #5 phase tensors, dimensionality metrics, and inverse model fits

Phase Tensors



Dimensionality Metrics



Inverse Model Fits

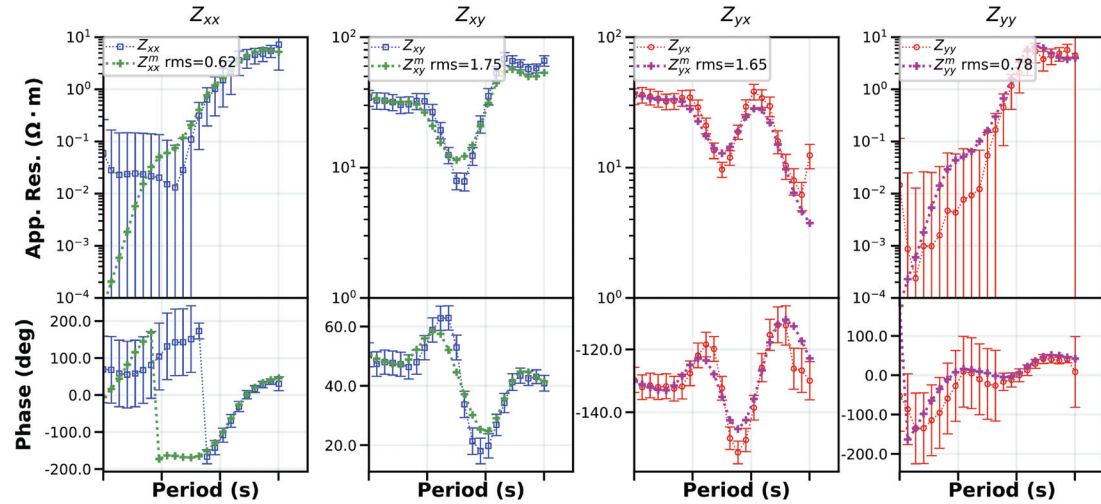
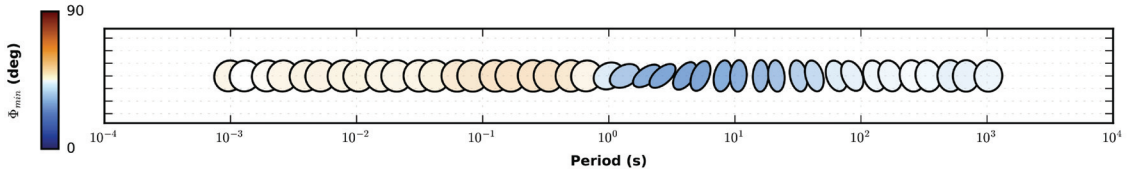
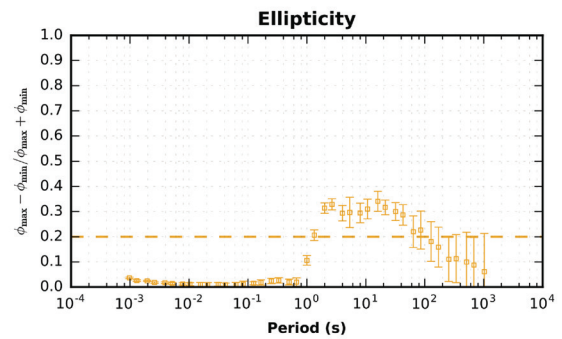
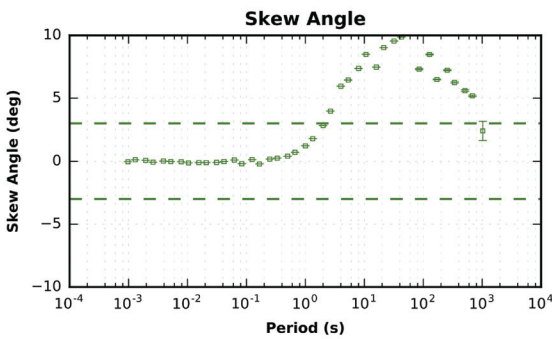
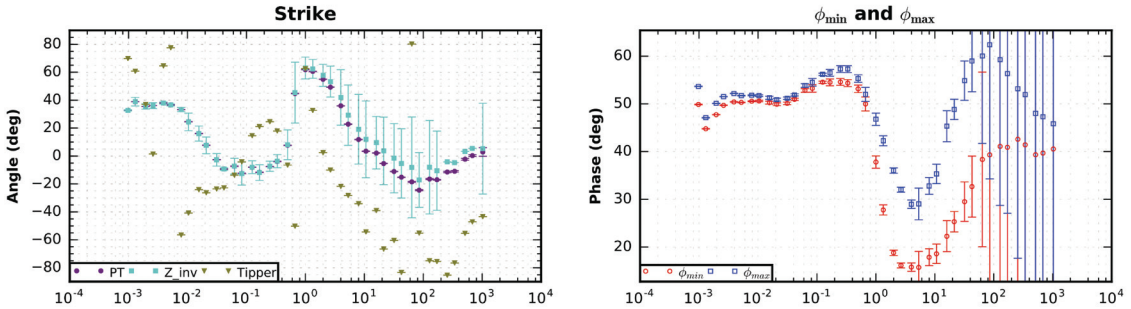


Figure 2.19: MT station #6 phase tensors, dimensionality metrics, and inverse model fits

Phase Tensors



Dimensionality Metrics



Inverse Model Fits

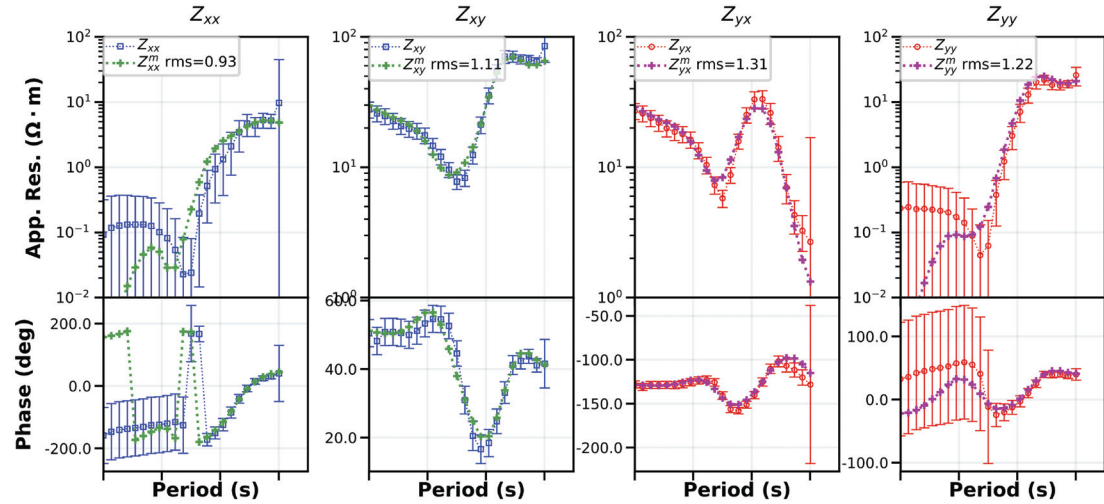
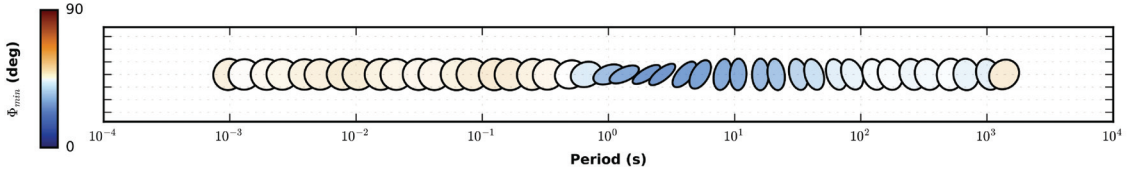
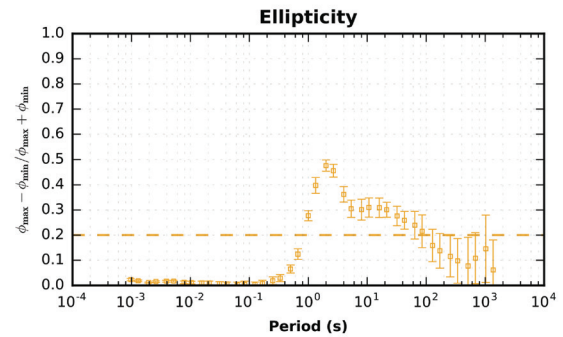
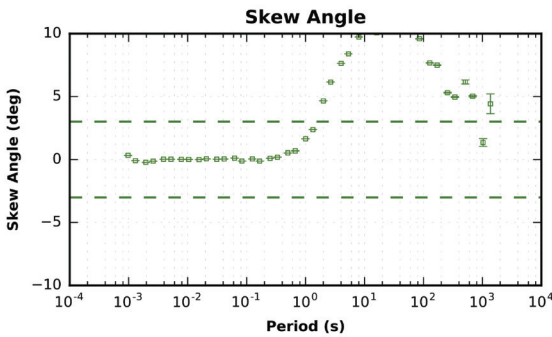
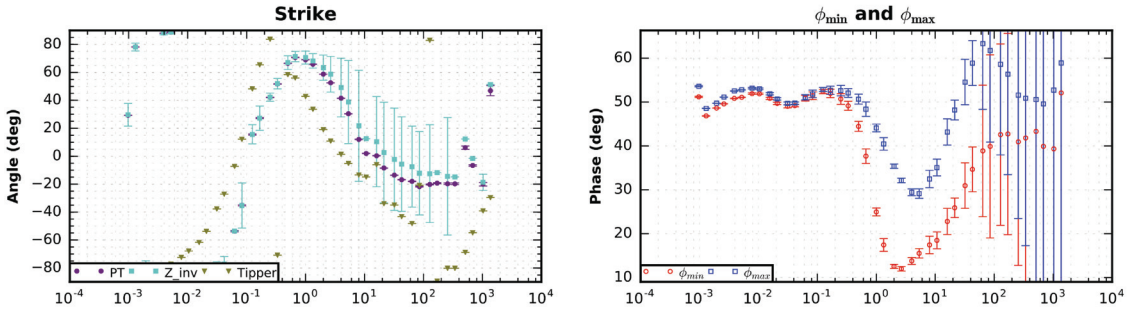


Figure 2.20: MT station #7 phase tensors, dimensionality metrics, and inverse model fits

Phase Tensors



Dimensionality Metrics



Inverse Model Fits

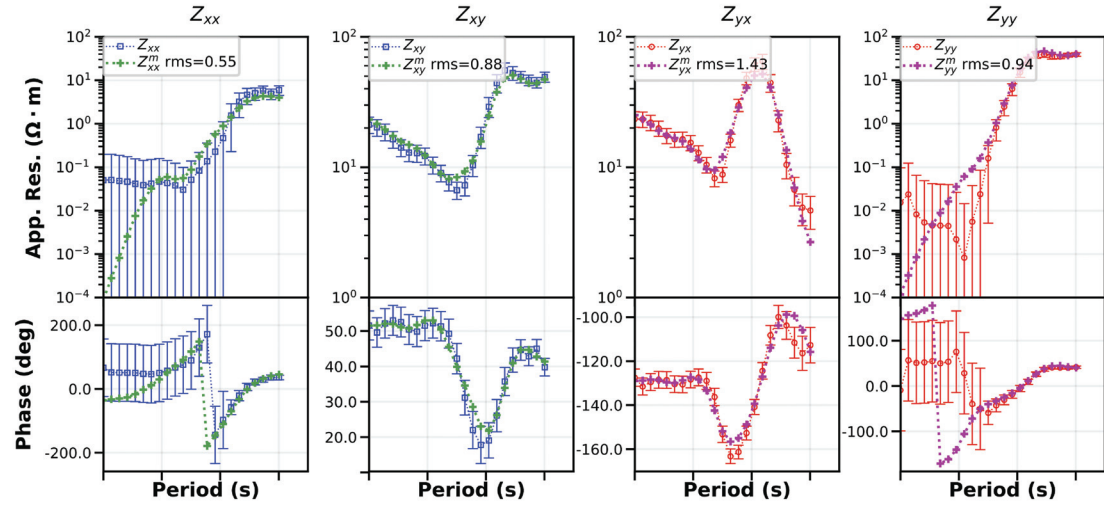
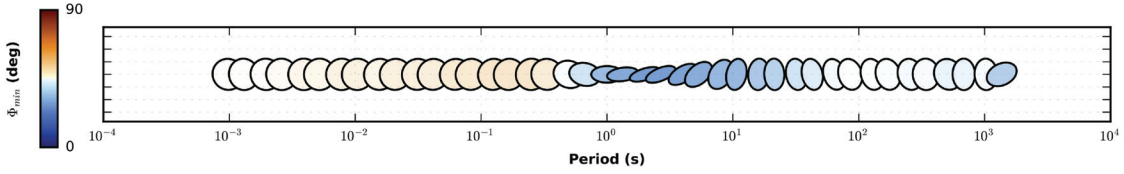
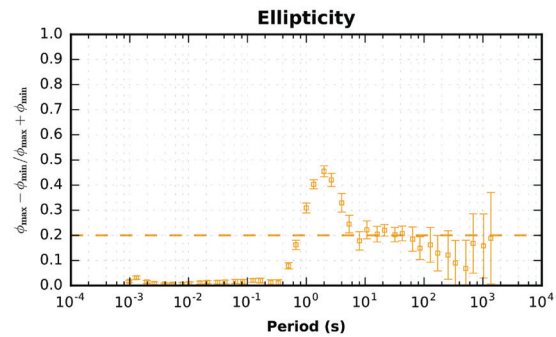
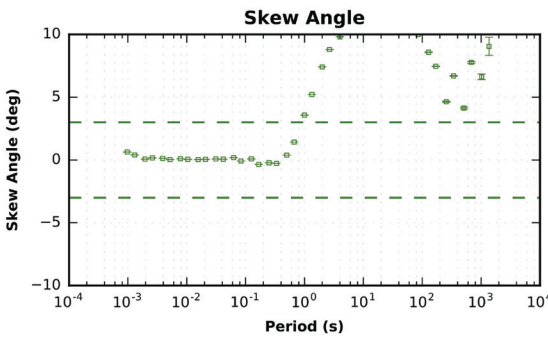
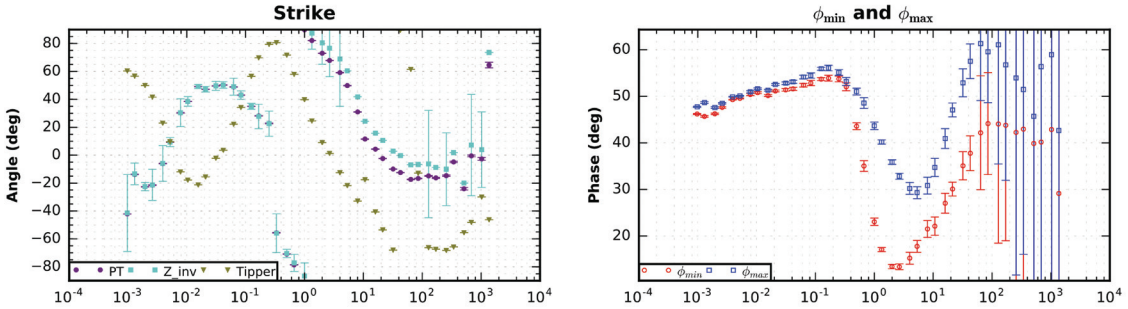


Figure 2.21: MT station #8 phase tensors, dimensionality metrics, and inverse model fits

Phase Tensors



Dimensionality Metrics



Inverse Model Fits

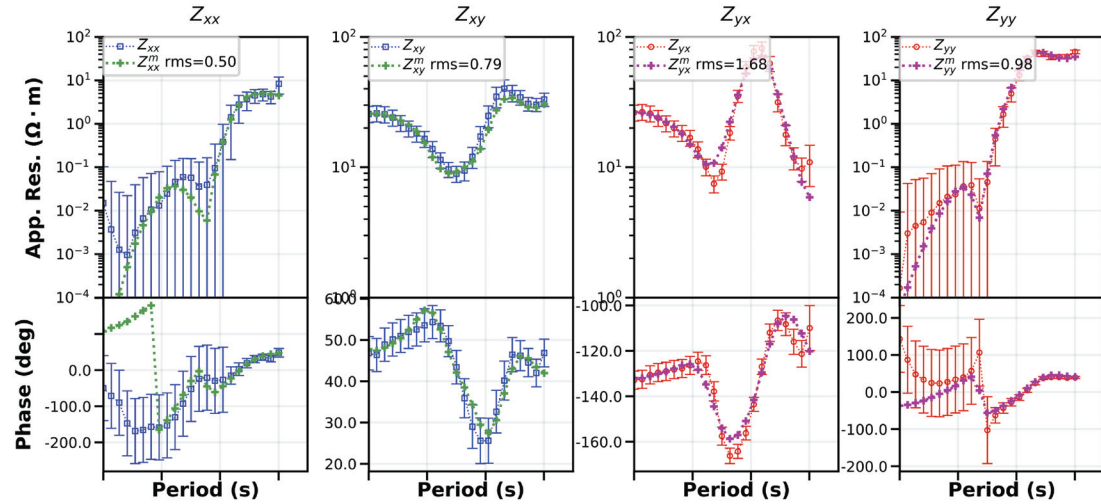
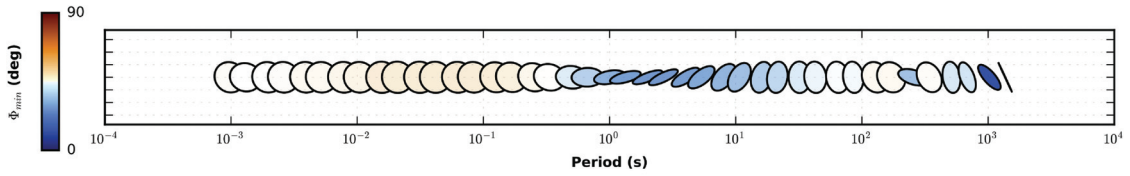
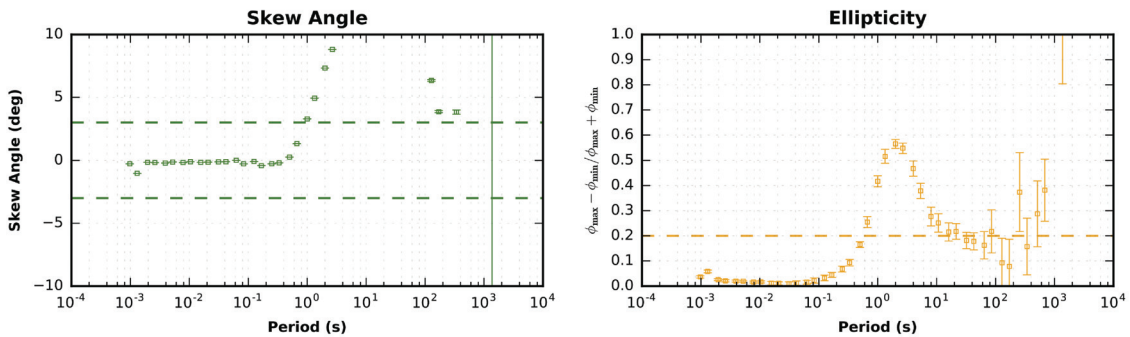
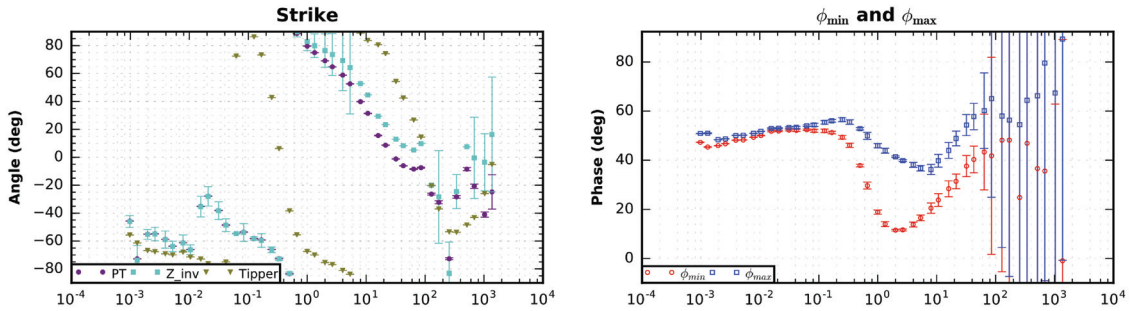


Figure 2.22: MT station #9 phase tensors, dimensionality metrics, and inverse model fits

Phase Tensors



Dimensionality Metrics



Inverse Model Fits

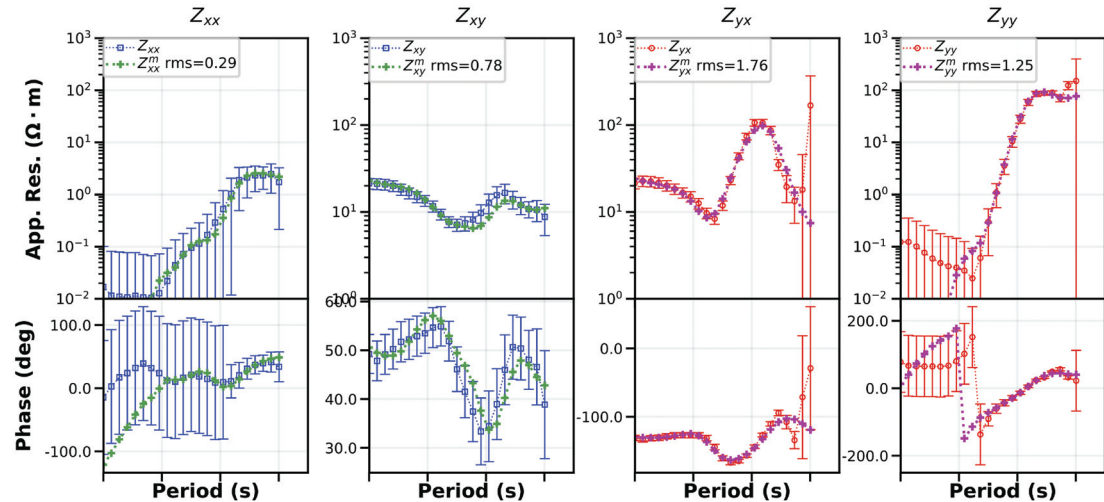
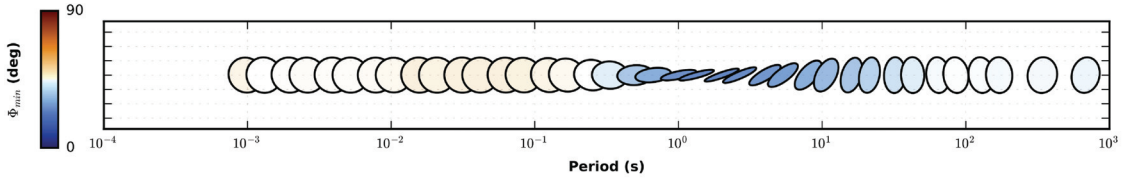
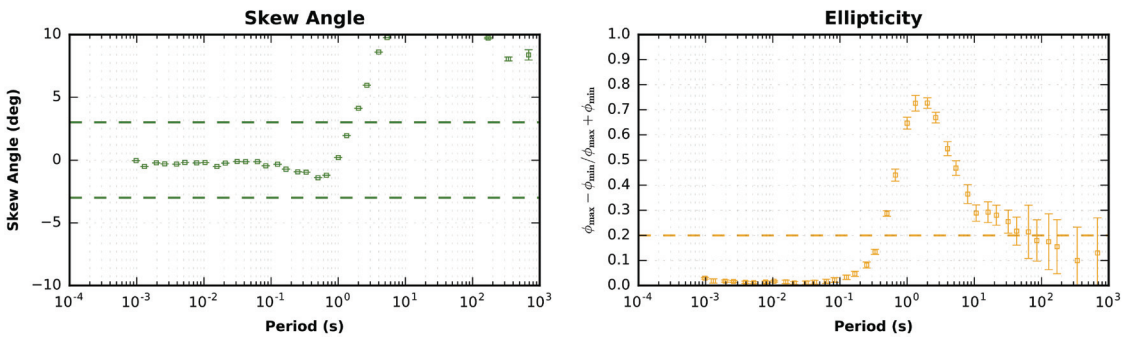
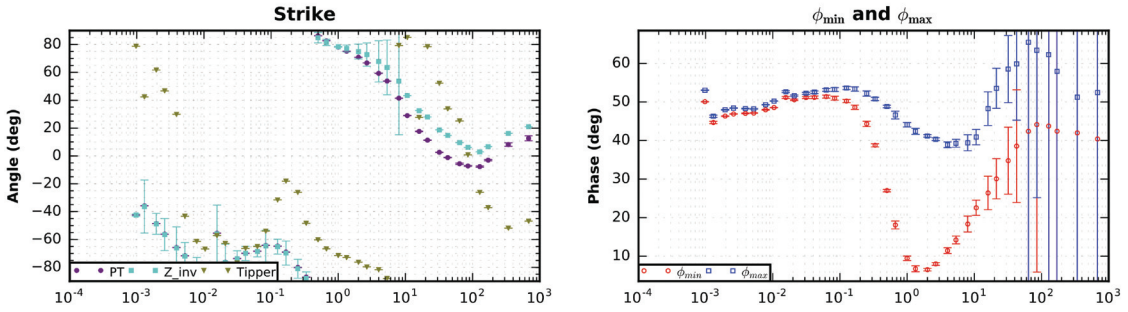


Figure 2.23: MT station #10 phase tensors, dimensionality metrics, and inverse model fits

Phase Tensors



Dimensionality Metrics



Inverse Model Fits

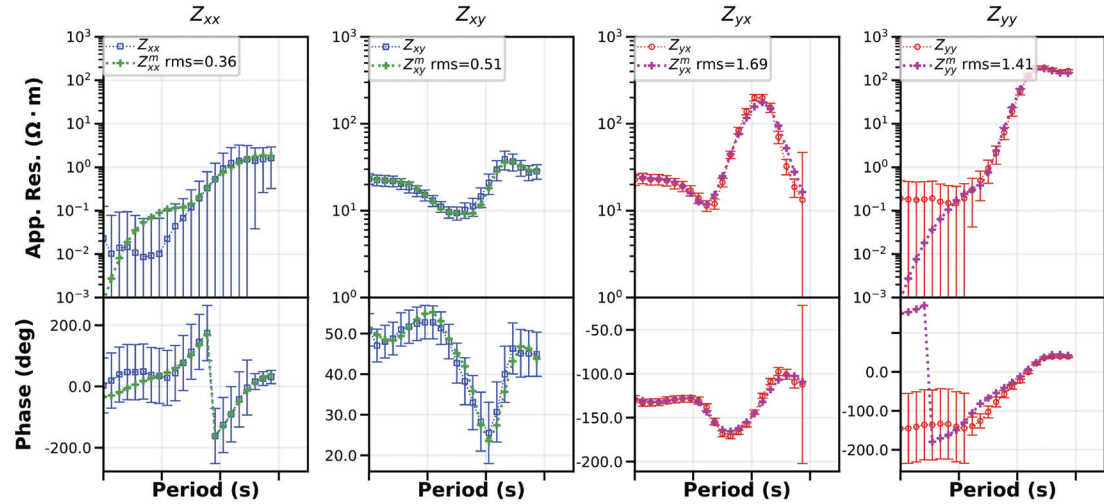
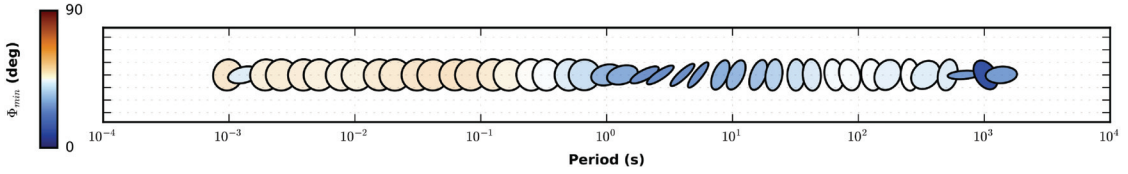
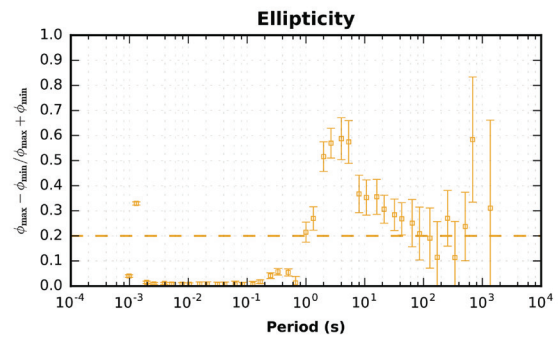
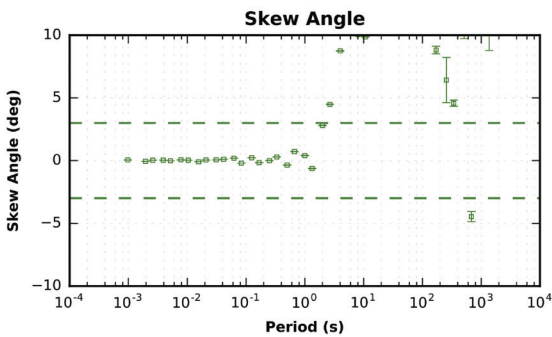
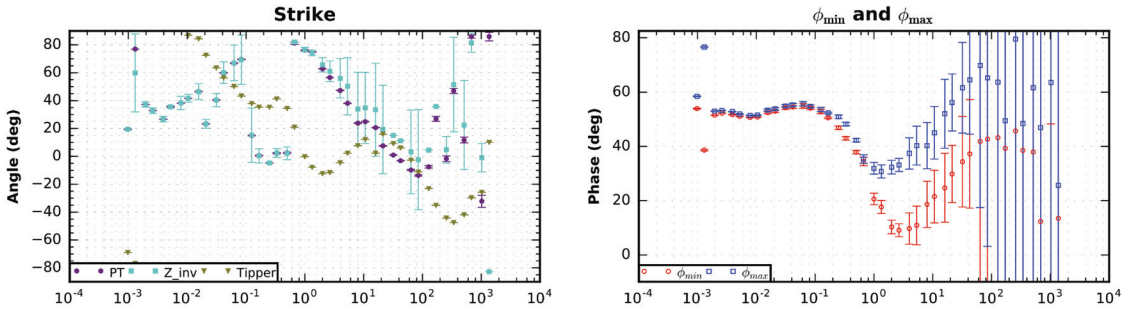


Figure 2.24: MT station #11 phase tensors, dimensionality metrics, and inverse model fits

Phase Tensors



Dimensionality Metrics



Inverse Model Fits

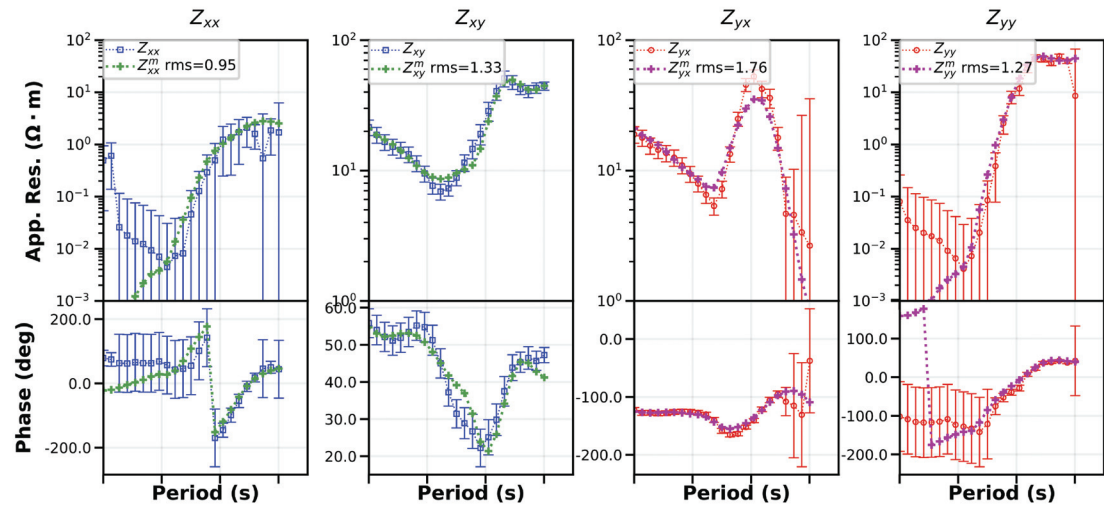
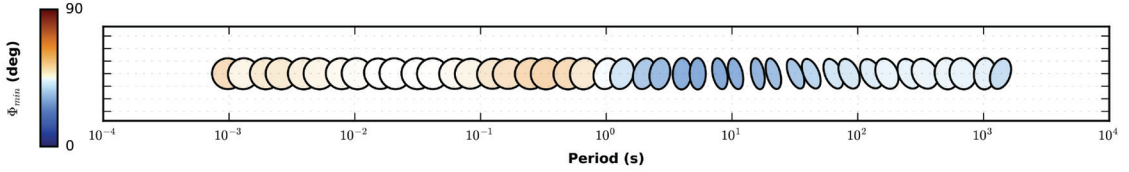
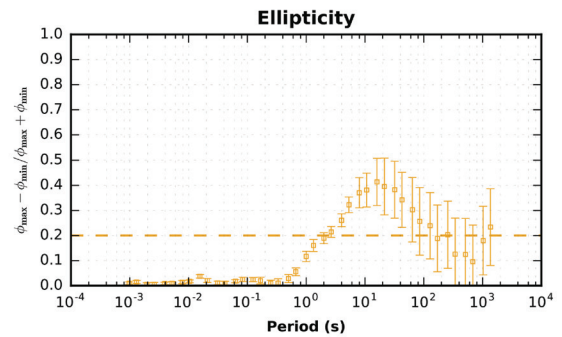
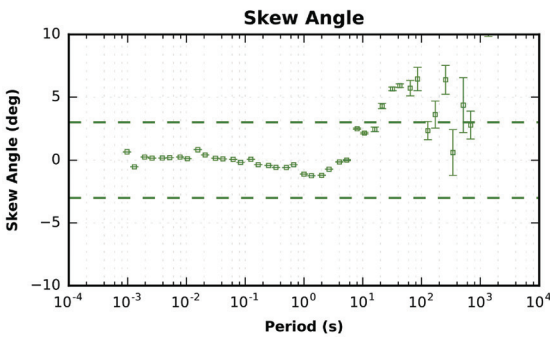
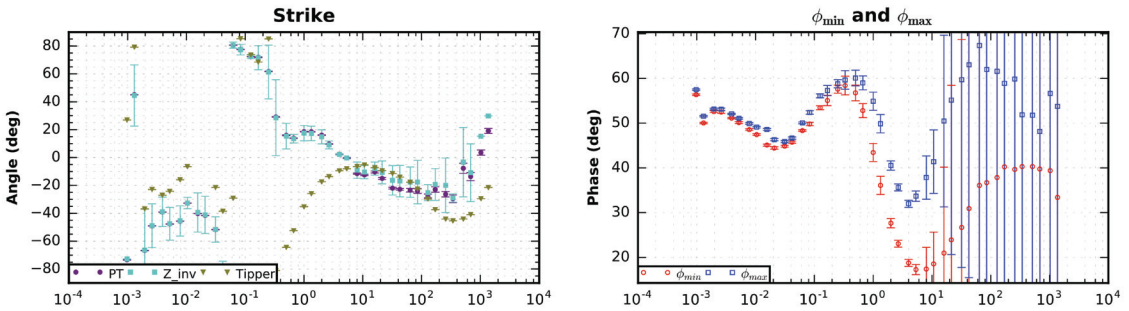


Figure 2.25: MT station #12 phase tensors, dimensionality metrics, and inverse model fits

Phase Tensors



Dimensionality Metrics



Inverse Model Fits

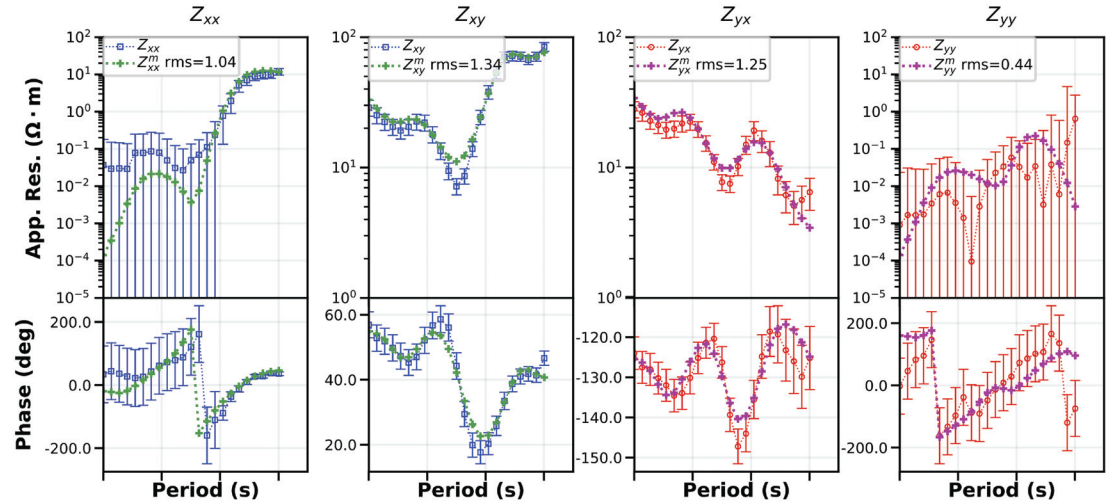
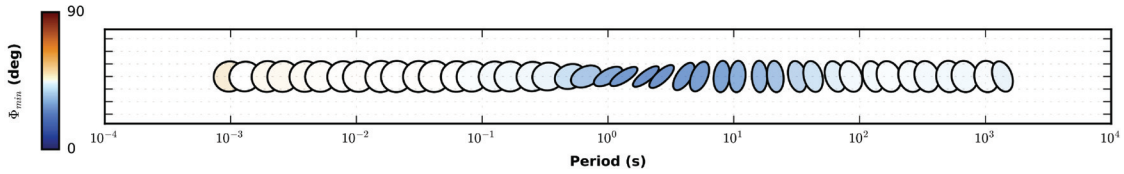
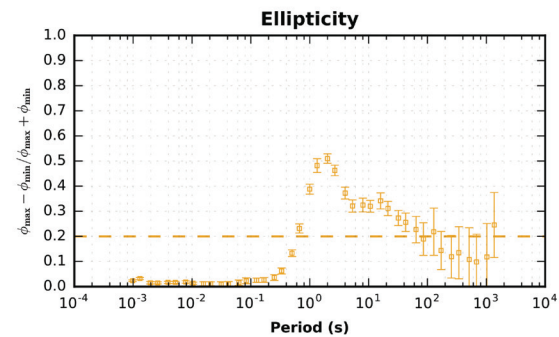
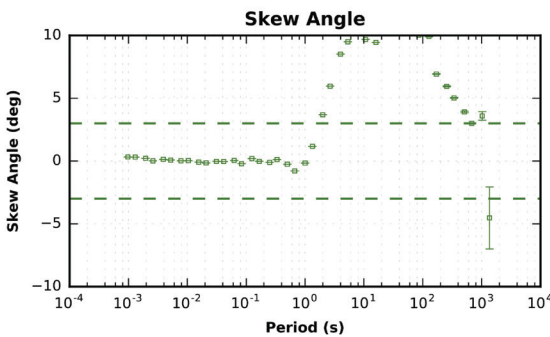
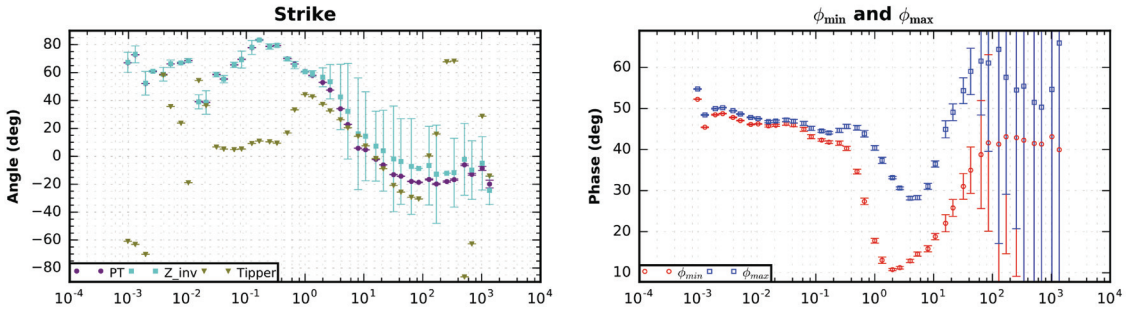


Figure 2.26: MT station #13 phase tensors, dimensionality metrics, and inverse model fits

Phase Tensors



Dimensionality Metrics



Inverse Model Fits

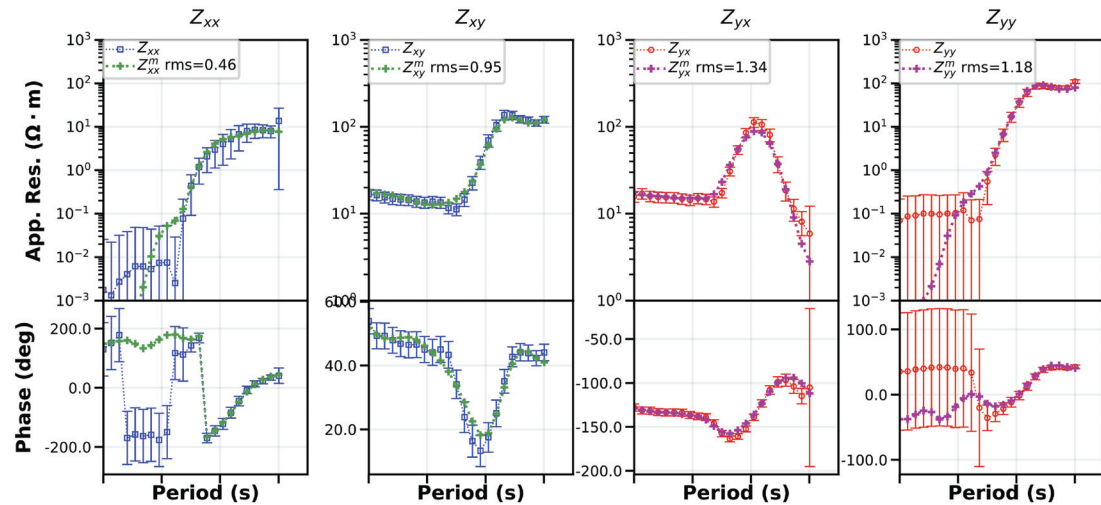
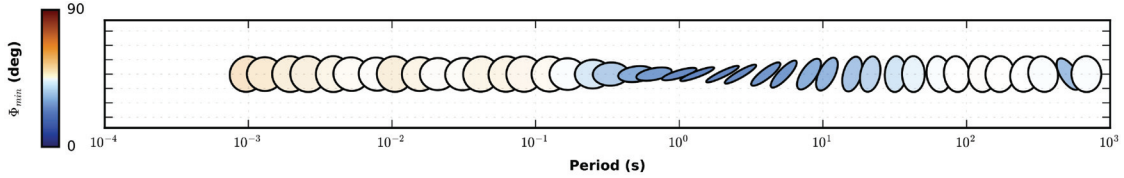
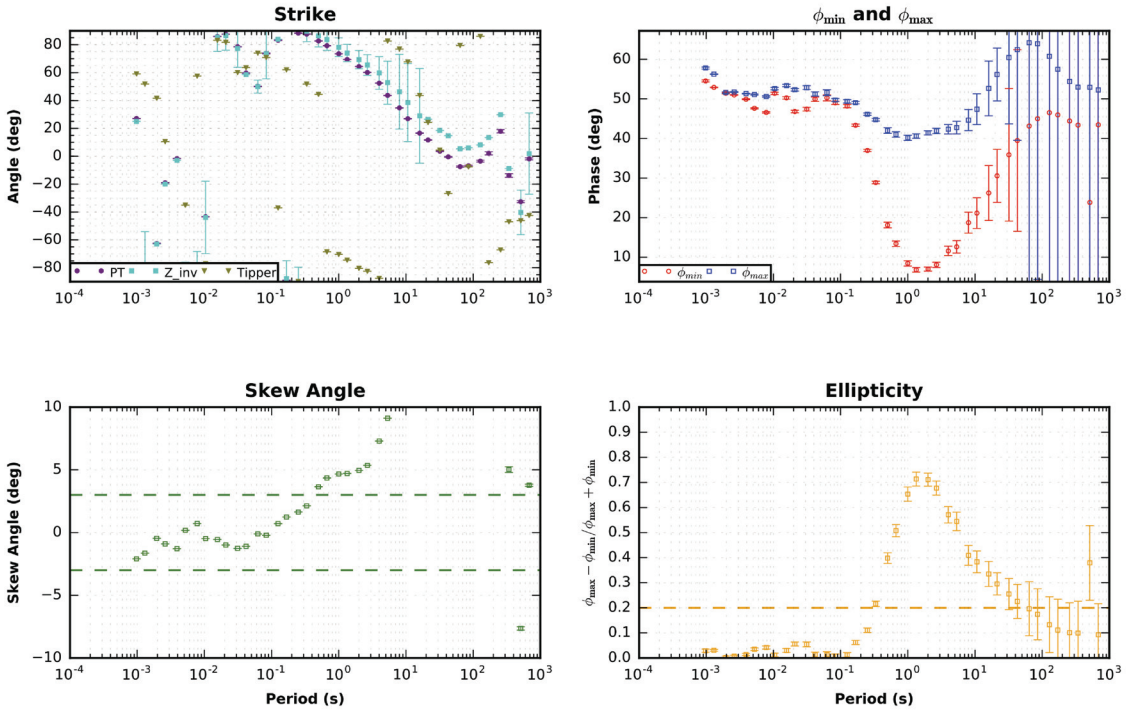


Figure 2.27: MT station #14 phase tensors, dimensionality metrics, and inverse model fits

Phase Tensors



Dimensionality Metrics



Inverse Model Fits

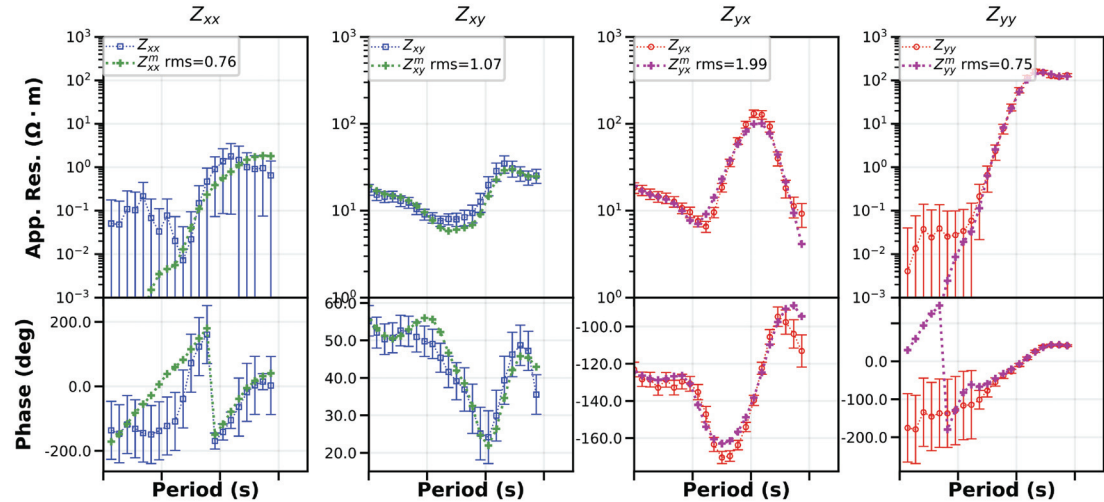
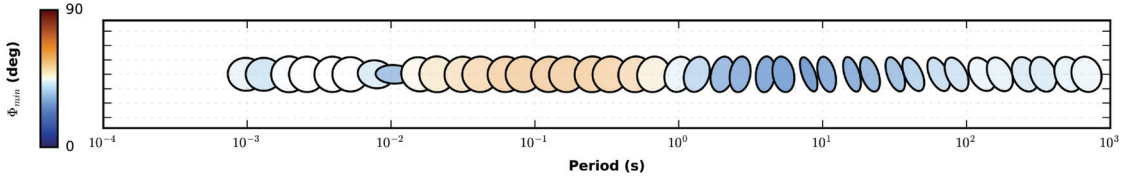
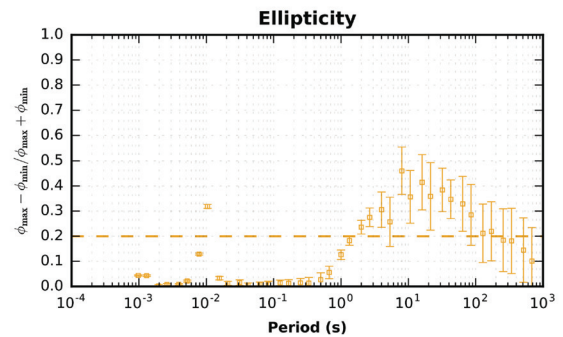
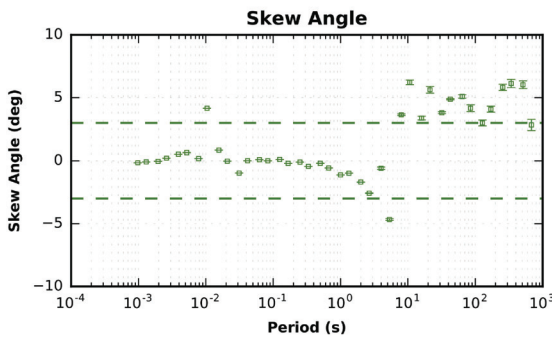
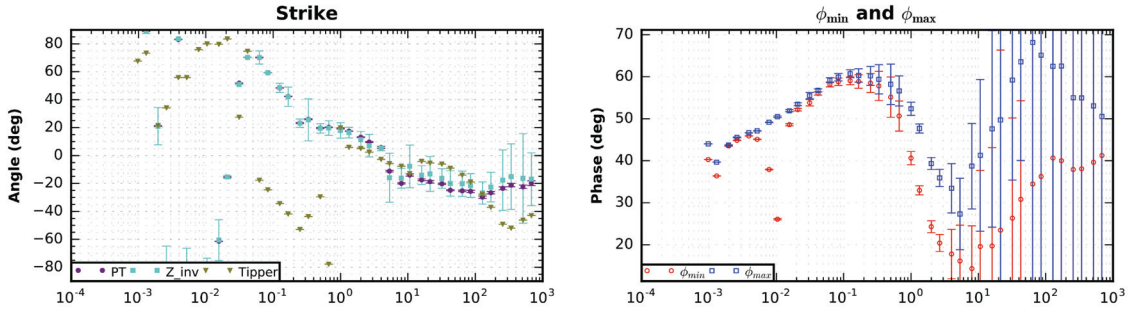


Figure 2.28: MT station #15 phase tensors, dimensionality metrics, and inverse model fits

Phase Tensors



Dimensionality Metrics



Inverse Model Fits

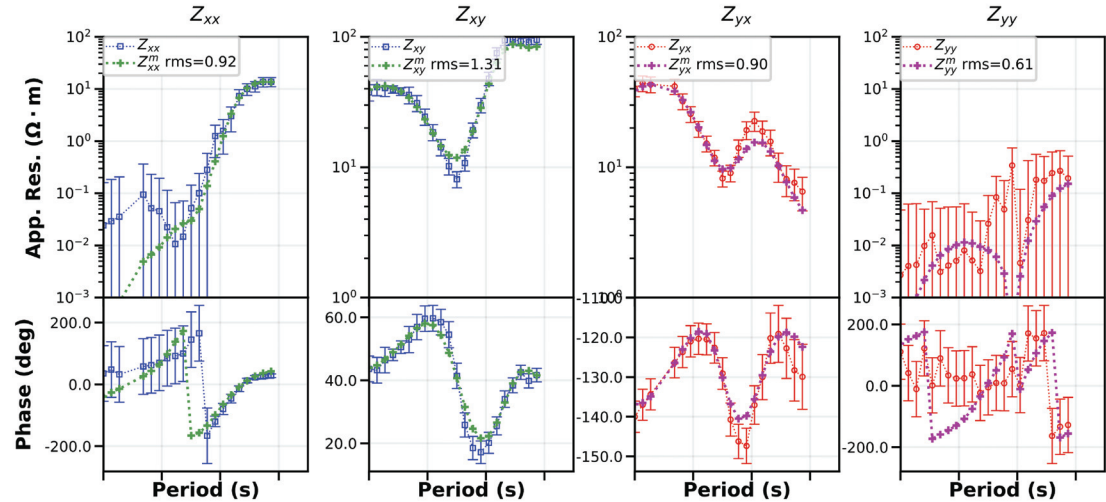
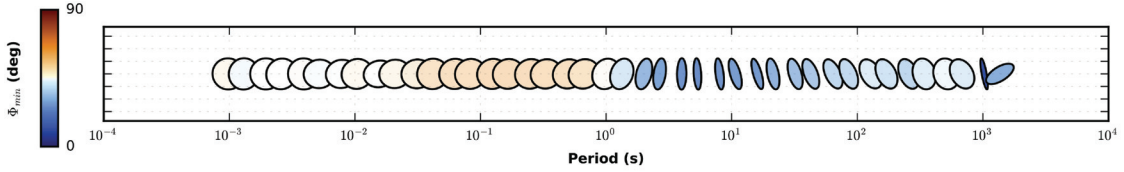
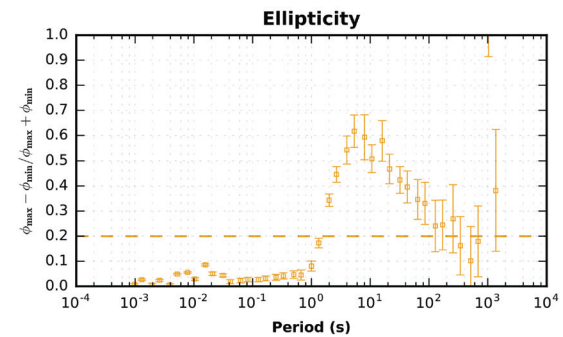
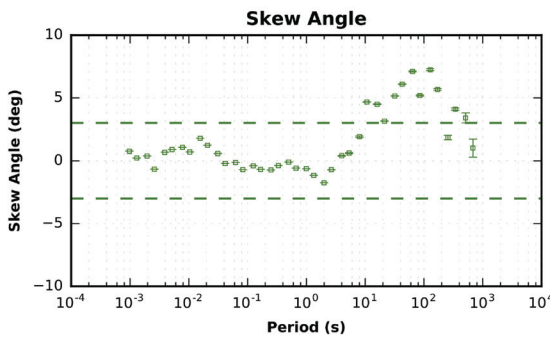
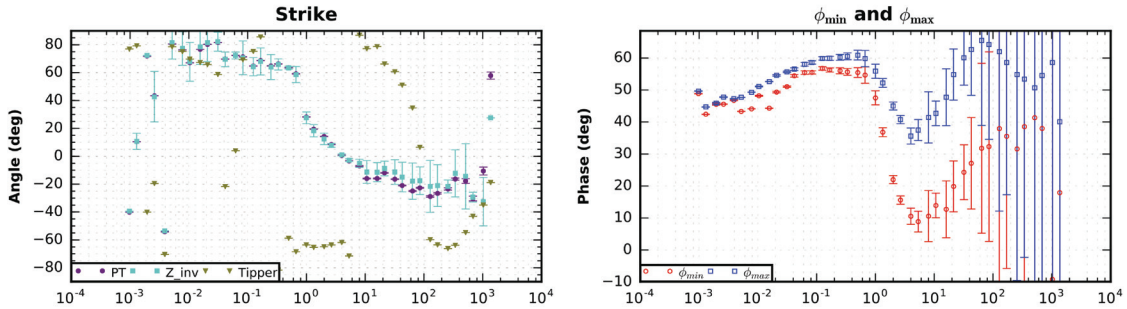


Figure 2.29: MT station #16 phase tensors, dimensionality metrics, and inverse model fits

Phase Tensors



Dimensionality Metrics



Inverse Model Fits

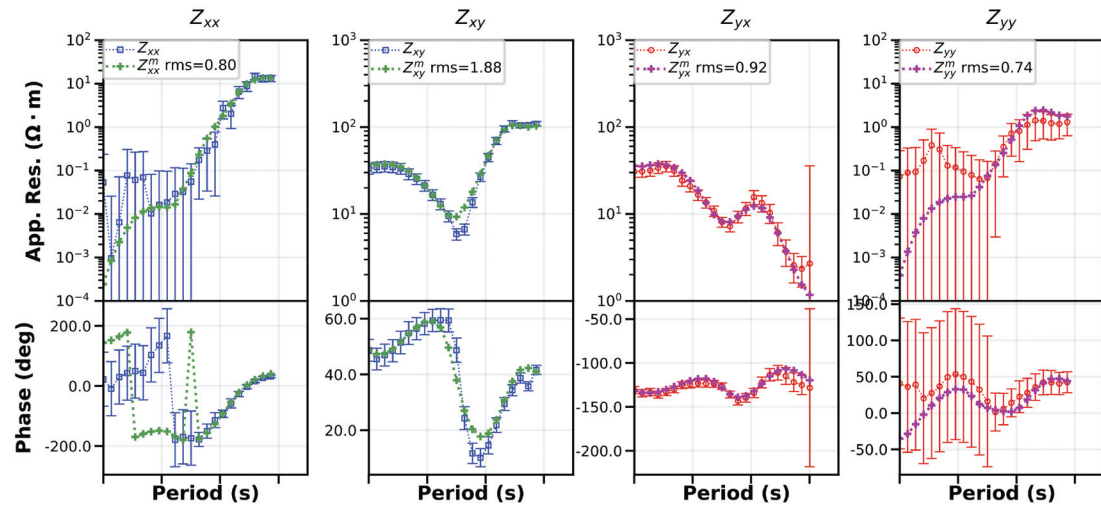
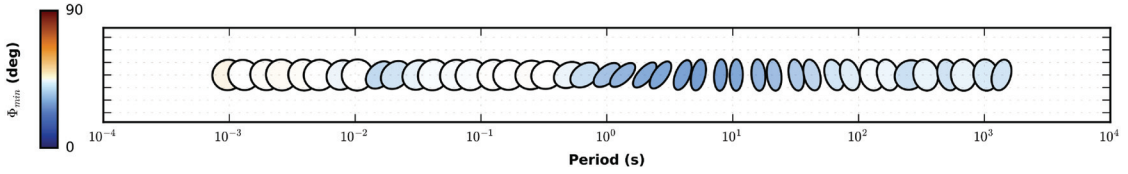
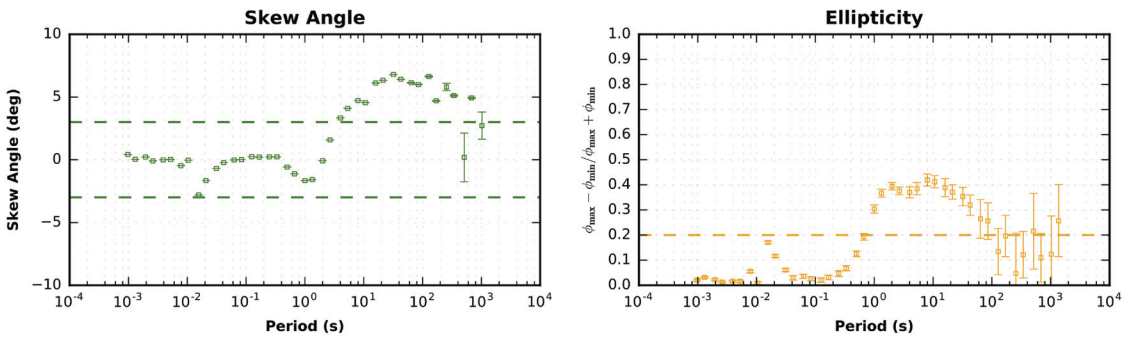
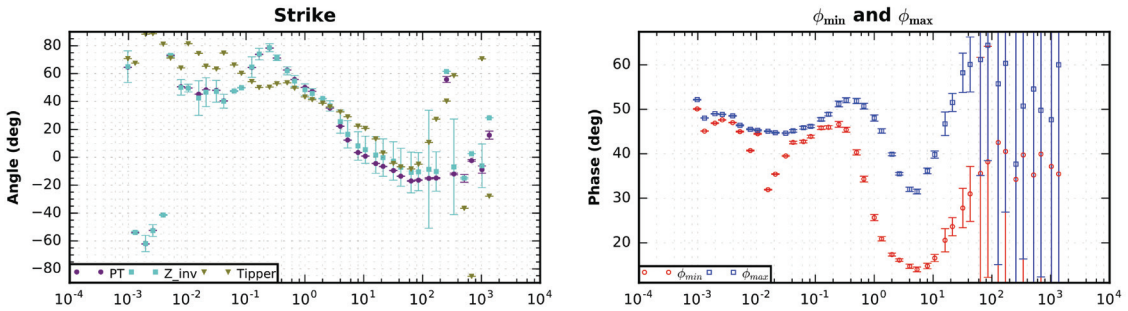


Figure 2.30: MT station #17 phase tensors, dimensionality metrics, and inverse model fits

Phase Tensors



Dimensionality Metrics



Inverse Model Fits

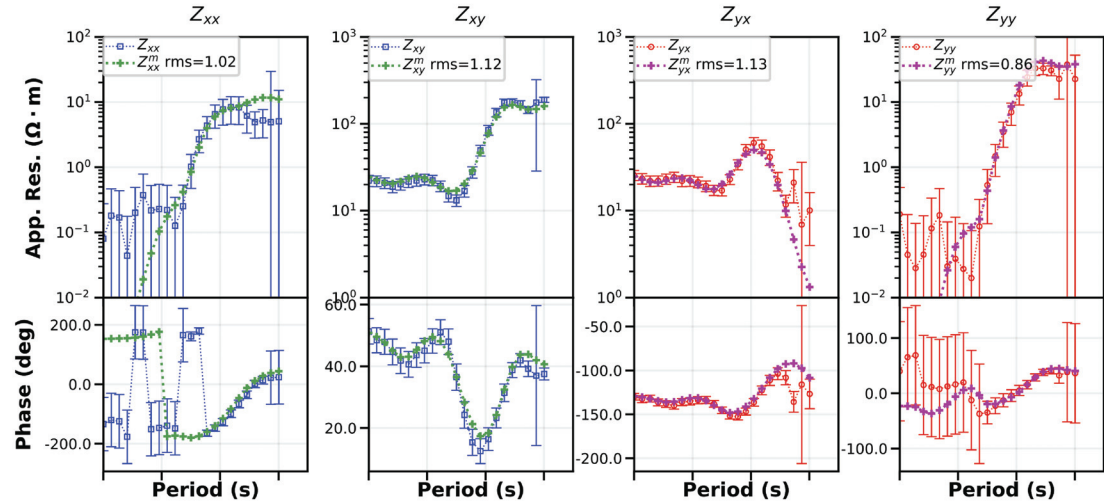
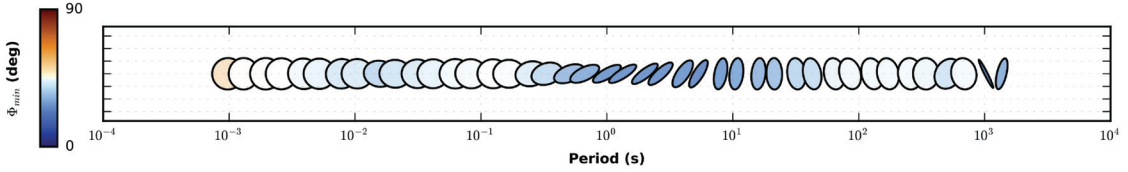
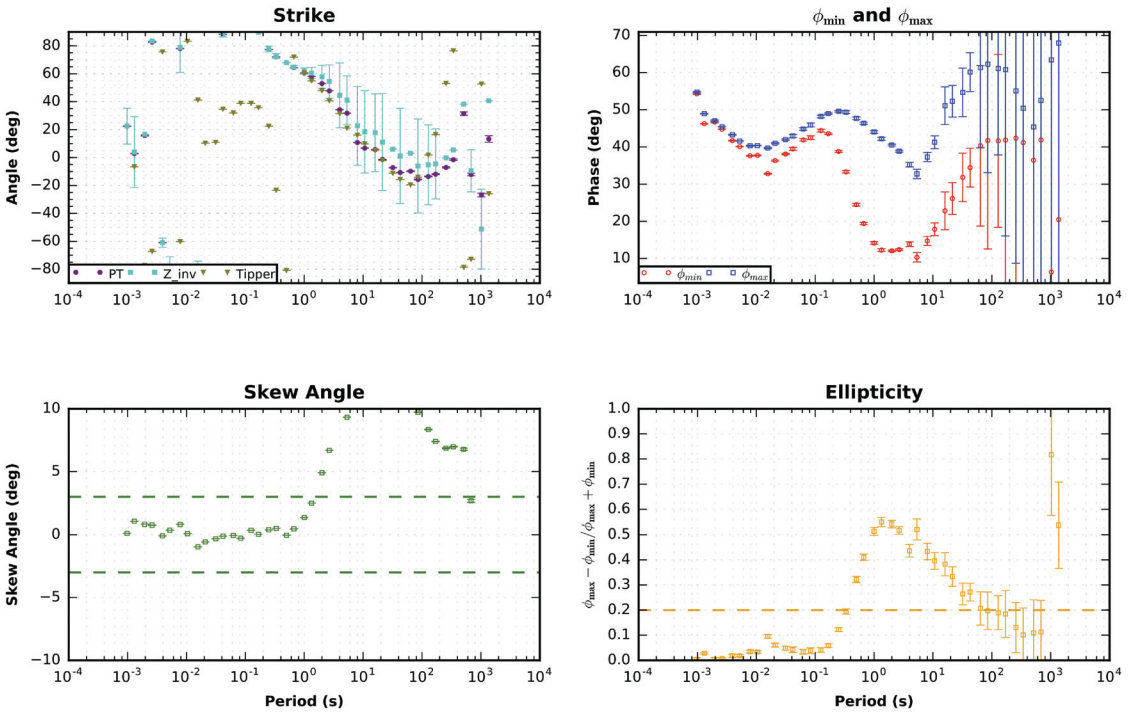


Figure 2.31: MT station #18 phase tensors, dimensionality metrics, and inverse model fits

Phase Tensors



Dimensionality Metrics



Inverse Model Fits

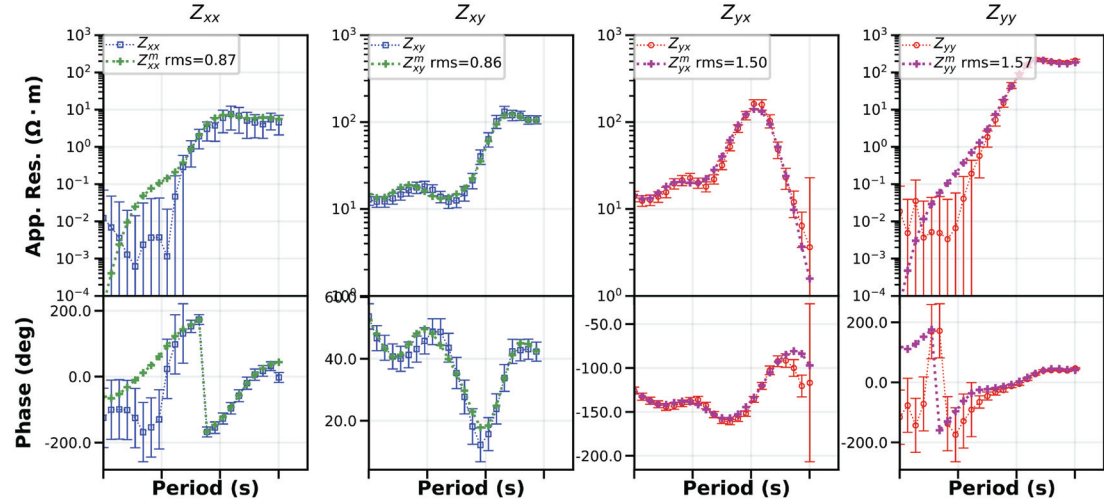
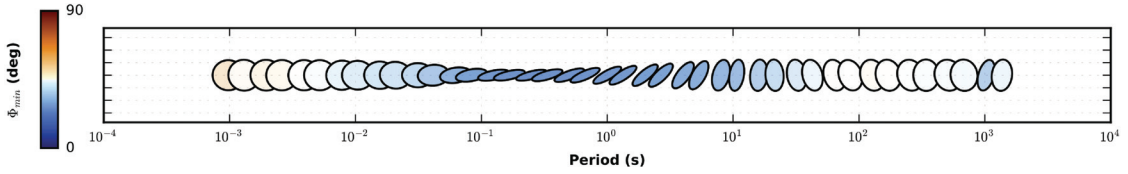
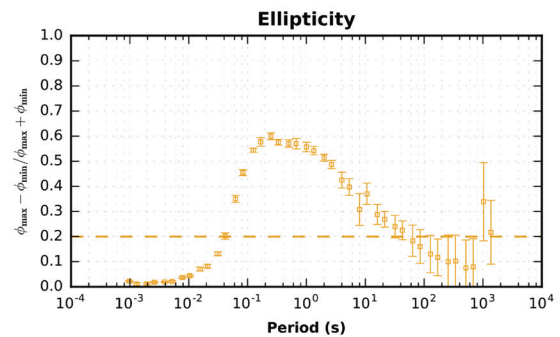
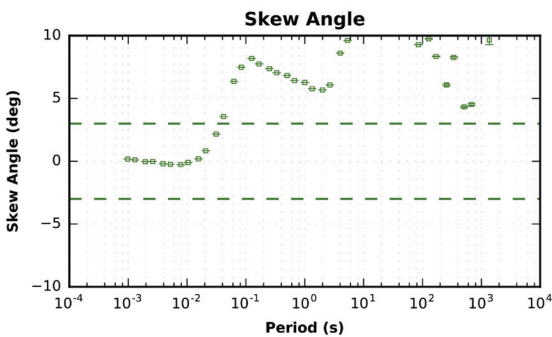
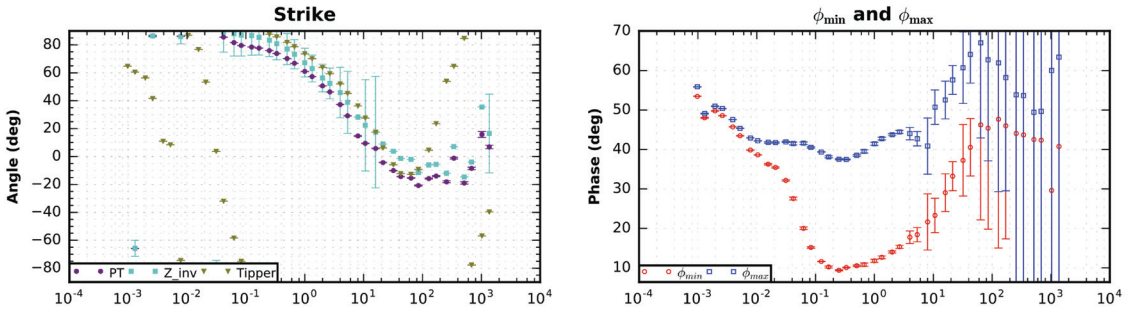


Figure 2.32: MT station #19 phase tensors, dimensionality metrics, and inverse model fits

Phase Tensors



Dimensionality Metrics



Inverse Model Fits

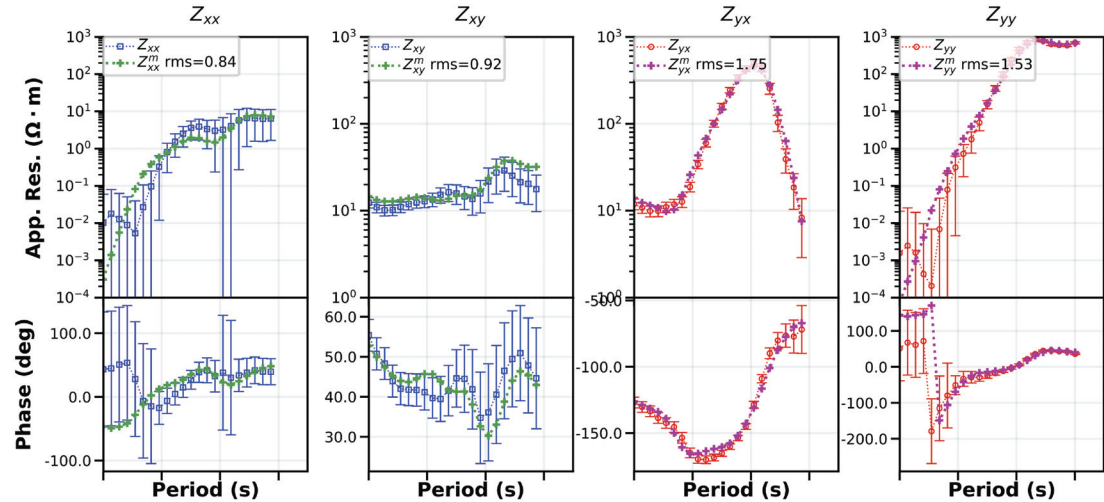
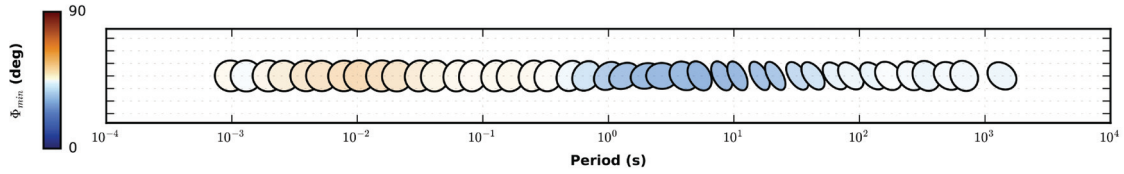
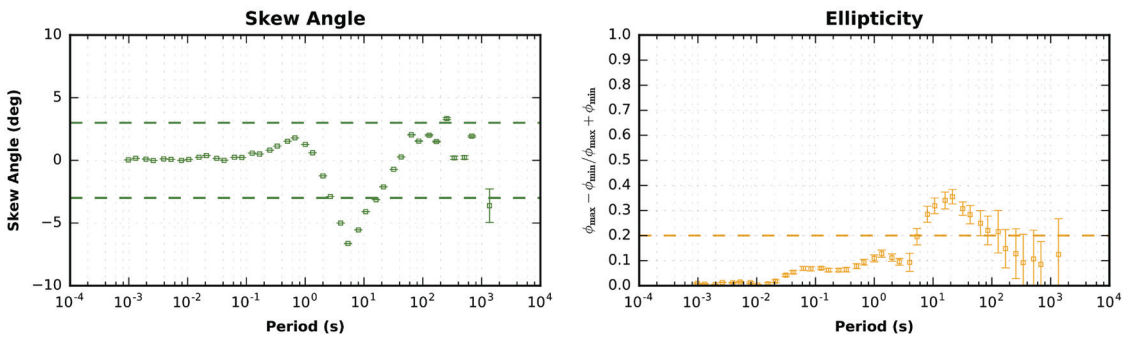
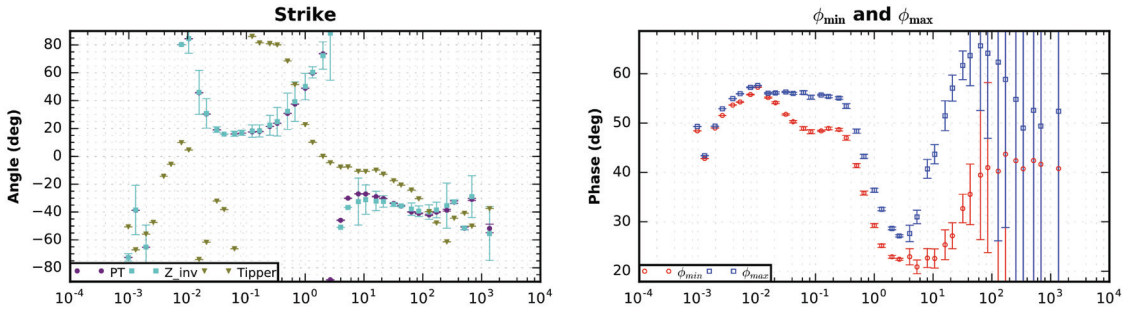


Figure 2.33: MT station #20 phase tensors, dimensionality metrics, and inverse model fits

Phase Tensors



Dimensionality Metrics



Inverse Model Fits

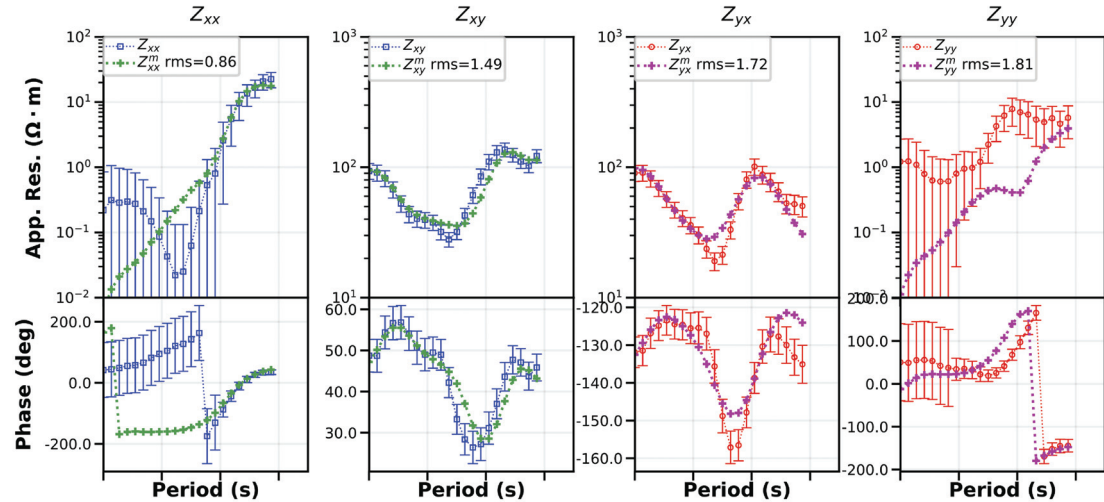
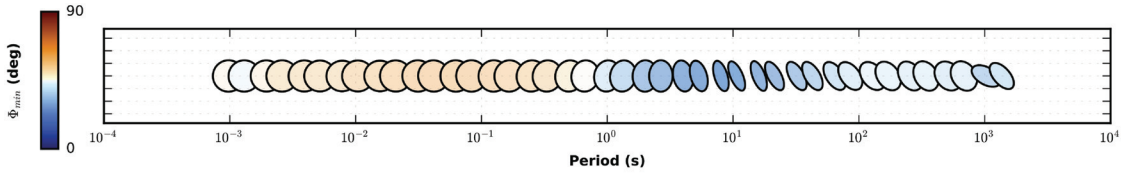
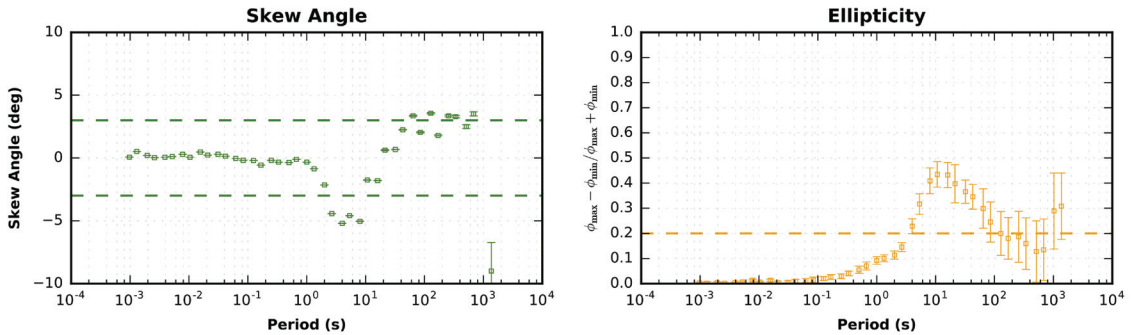
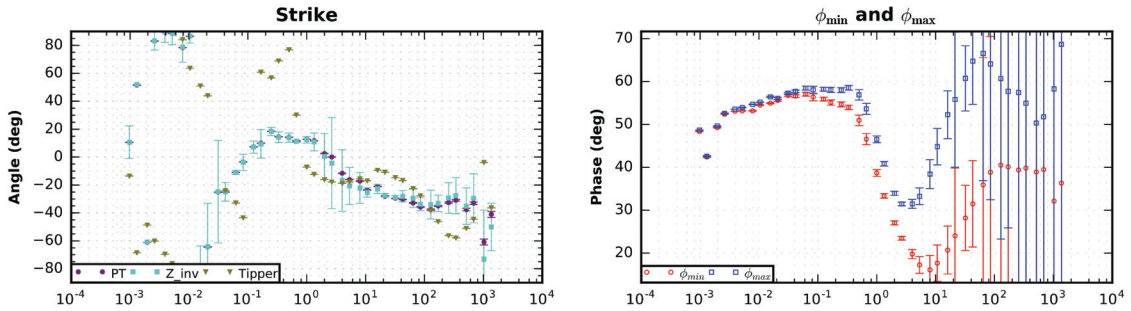


Figure 2.34: MT station #21 phase tensors, dimensionality metrics, and inverse model fits

Phase Tensors



Dimensionality Metrics



Inverse Model Fits

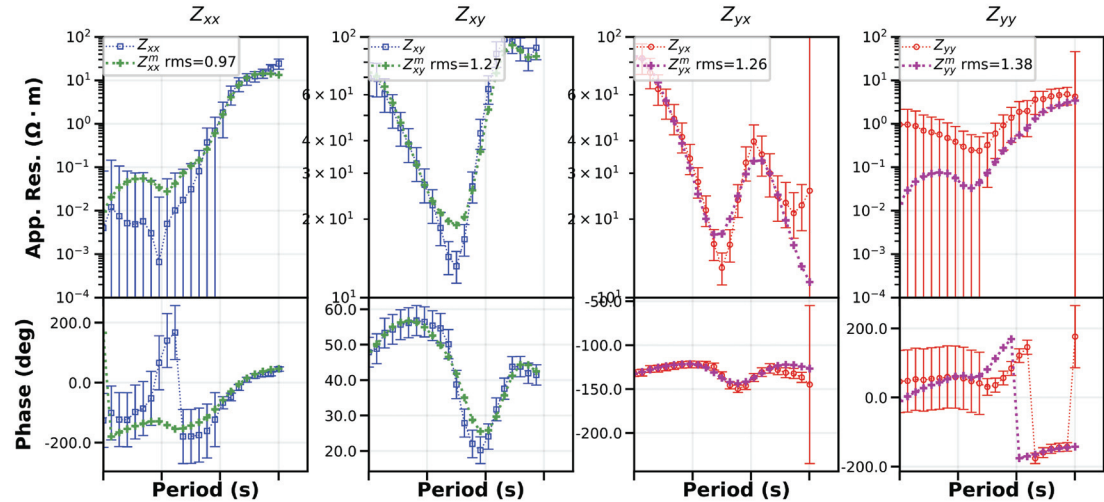
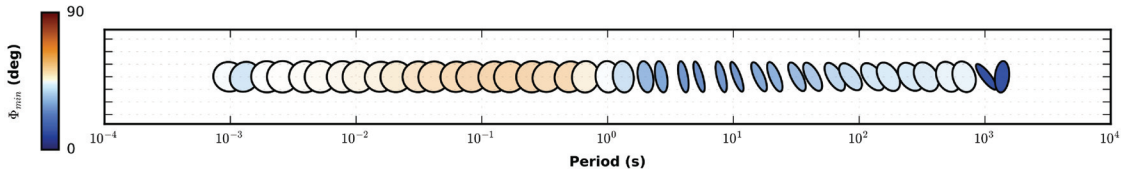
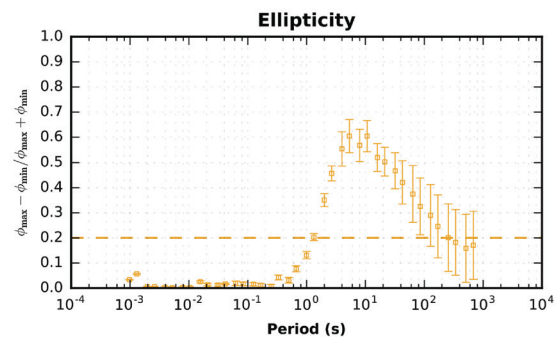
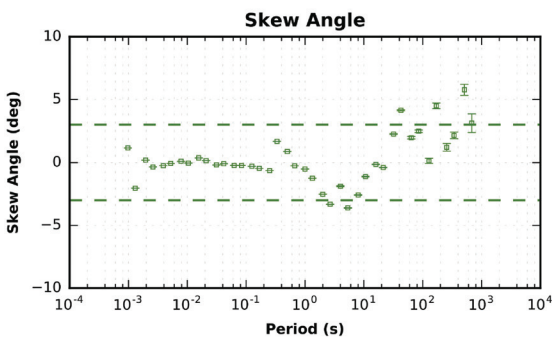
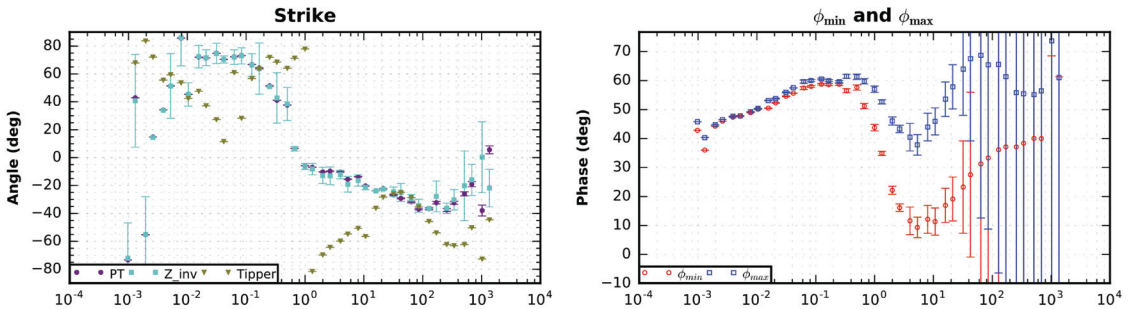


Figure 2.35: MT station #22 phase tensors, dimensionality metrics, and inverse model fits

Phase Tensors



Dimensionality Metrics



Inverse Model Fits

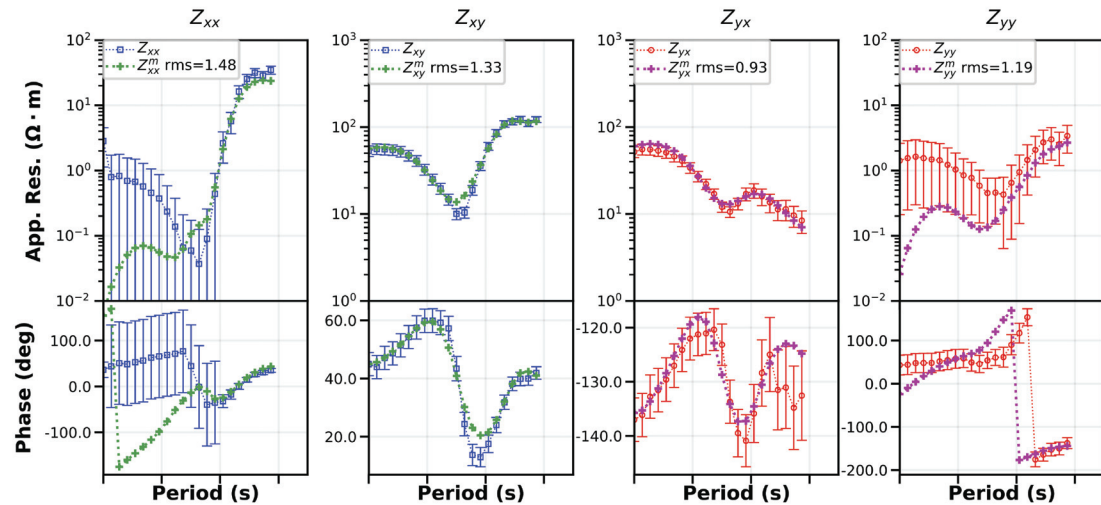
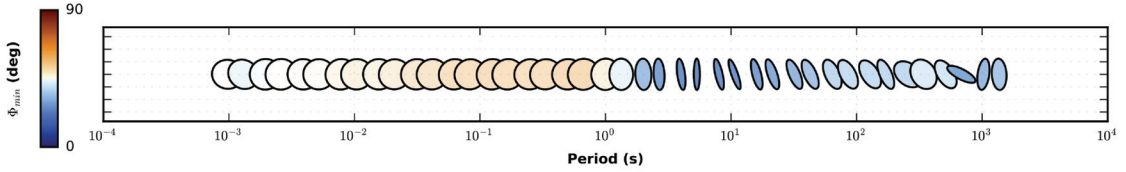
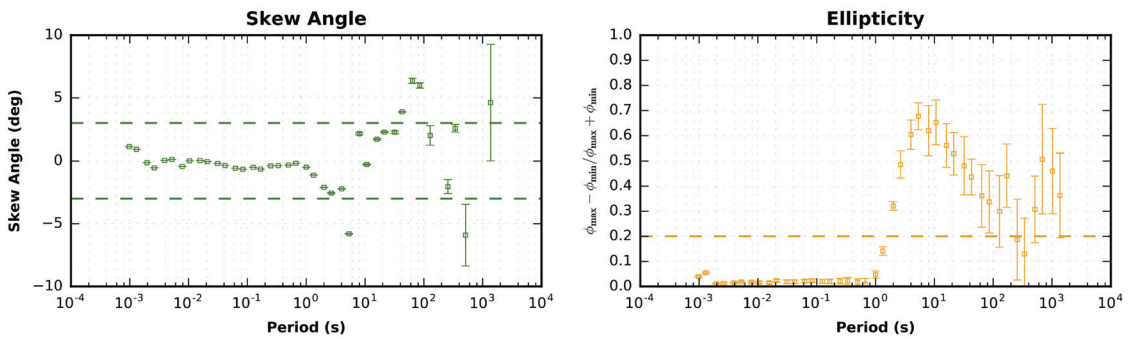
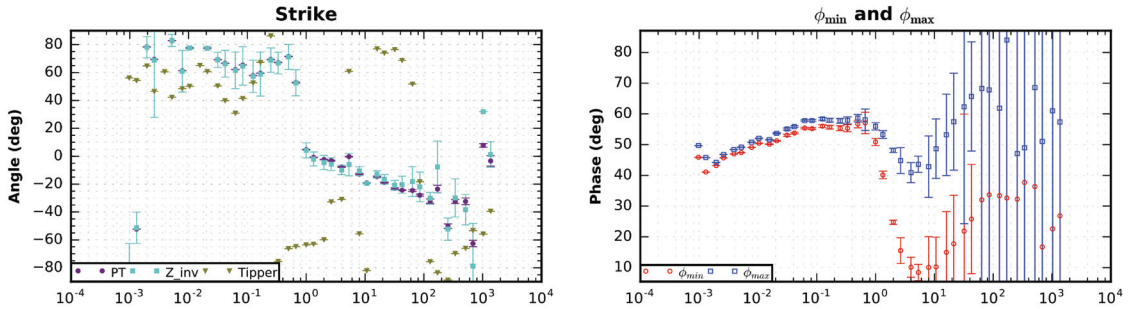


Figure 2.36: MT station #23 phase tensors, dimensionality metrics, and inverse model fits

Phase Tensors



Dimensionality Metrics



Inverse Model Fits

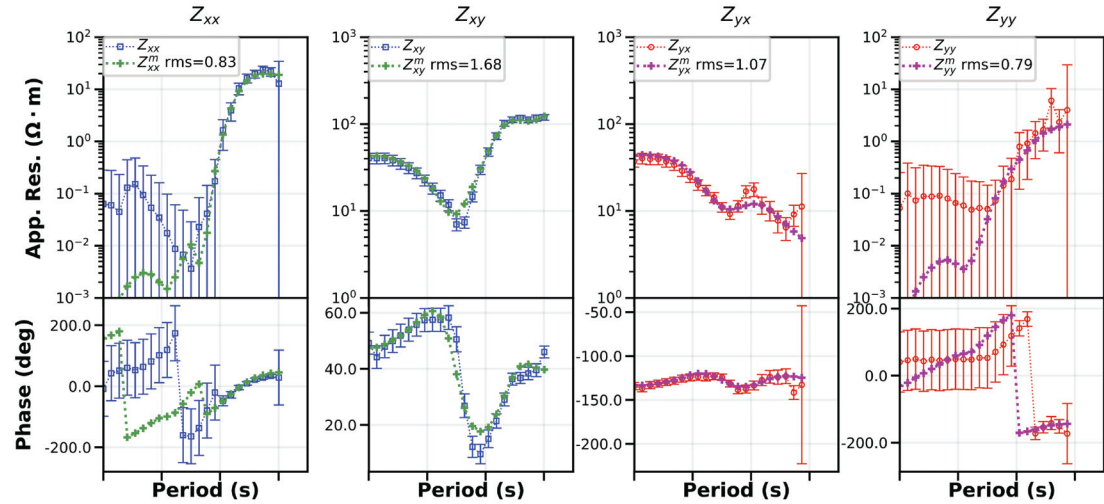
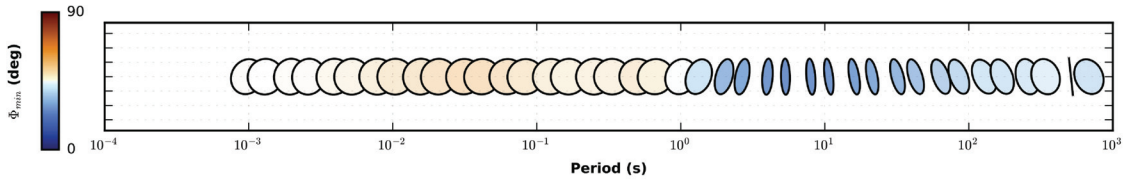
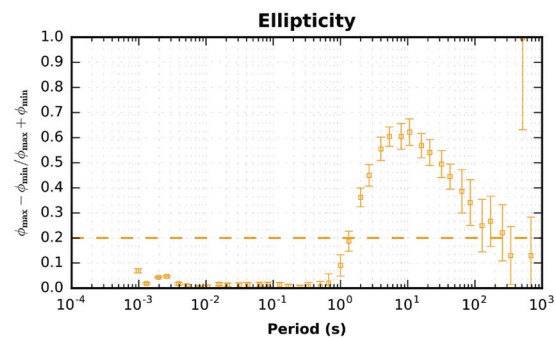
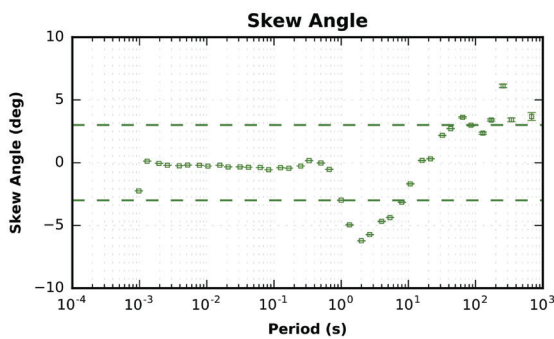
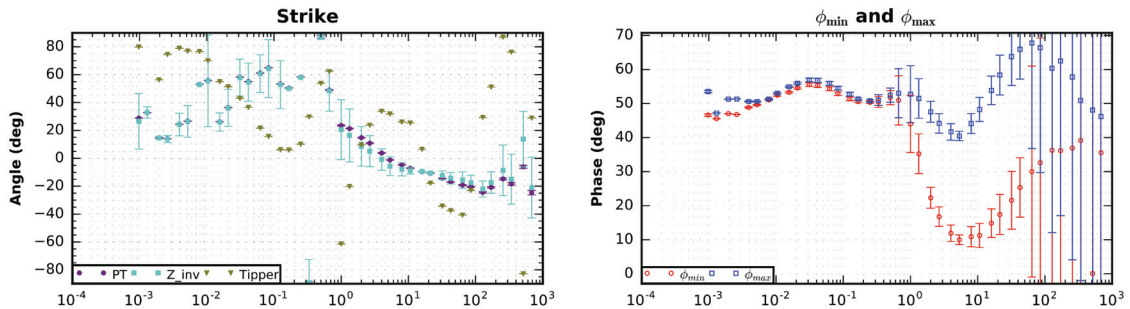


Figure 2.37: MT station #24 phase tensors, dimensionality metrics, and inverse model fits

Phase Tensors



Dimensionality Metrics



Inverse Model Fits

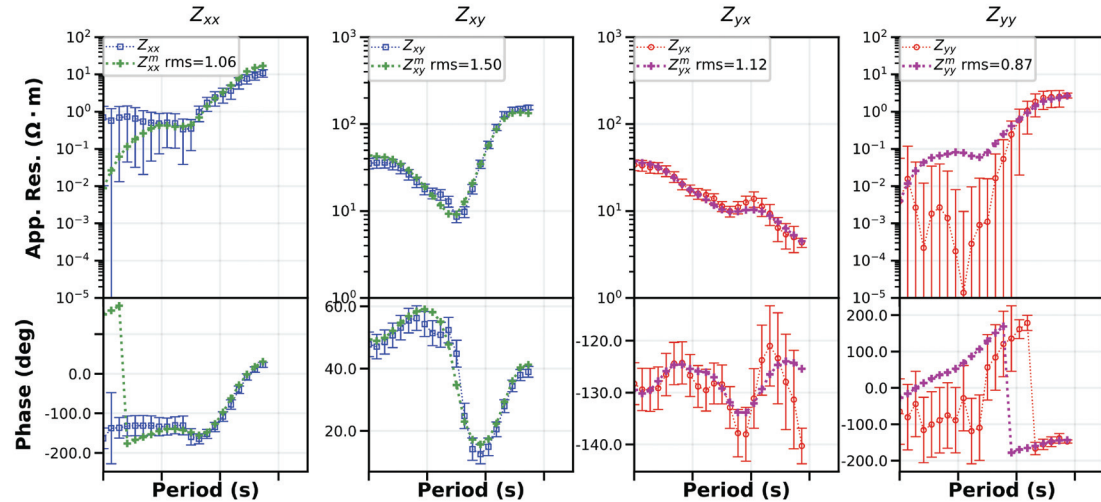
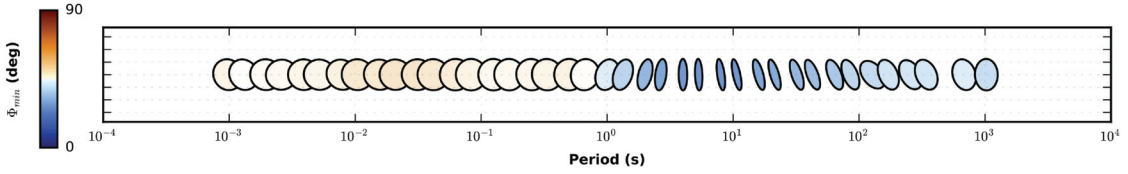
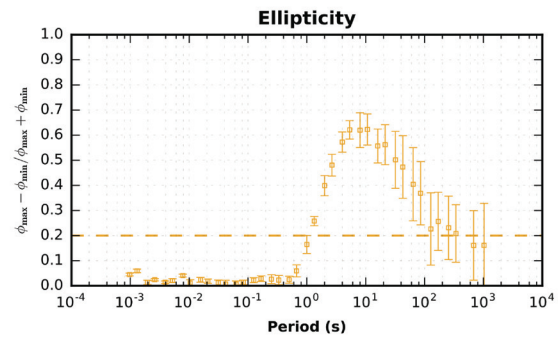
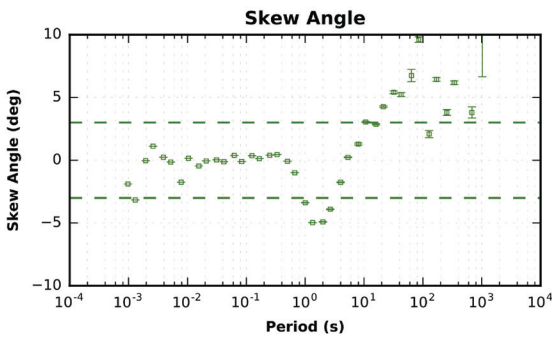
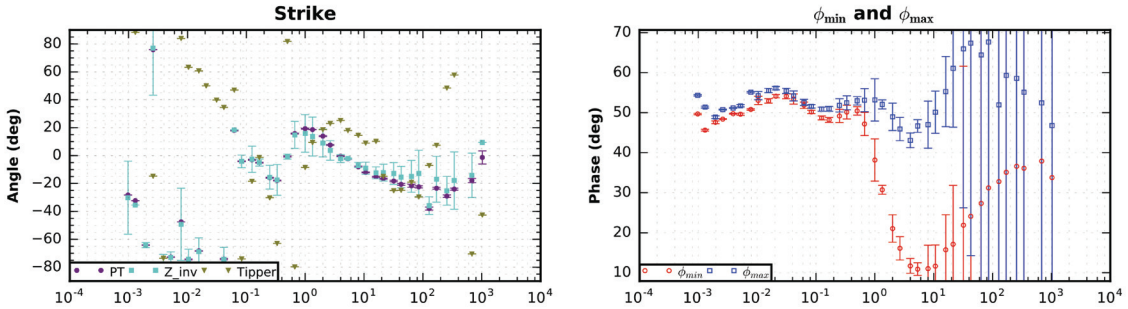


Figure 2.38: MT station #25 phase tensors, dimensionality metrics, and inverse model fits

Phase Tensors



Dimensionality Metrics



Inverse Model Fits

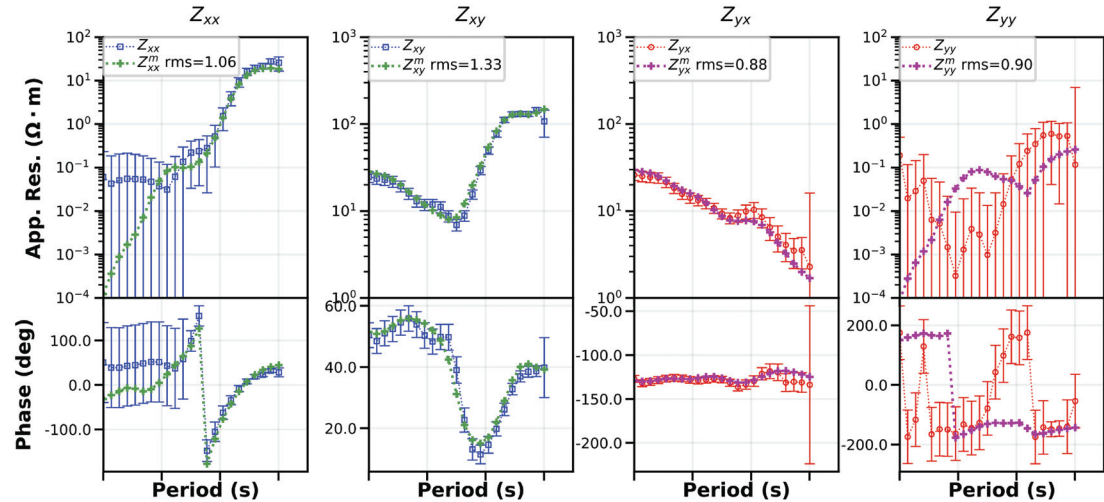
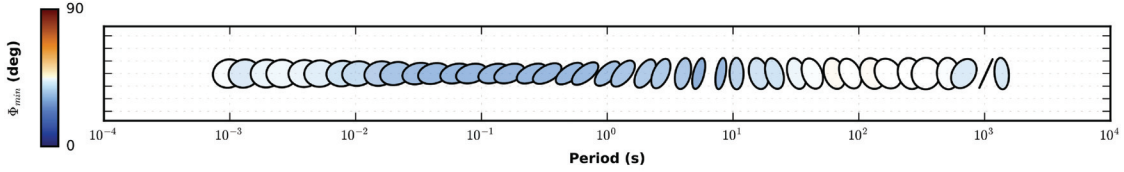
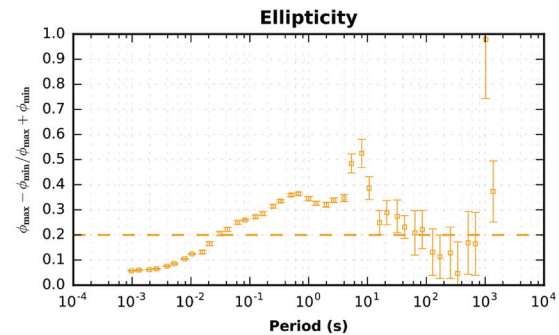
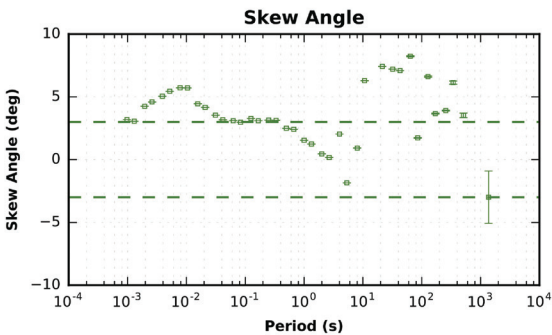
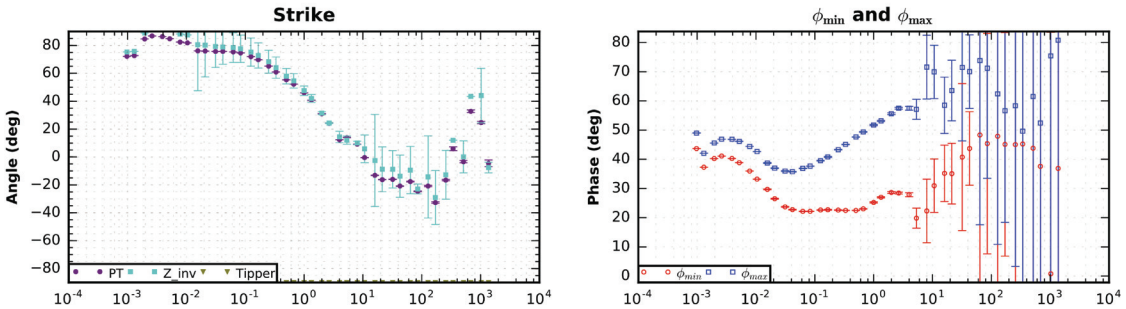


Figure 2.39: MT station #26 phase tensors, dimensionality metrics, and inverse model fits

Phase Tensors



Dimensionality Metrics



Inverse Model Fits

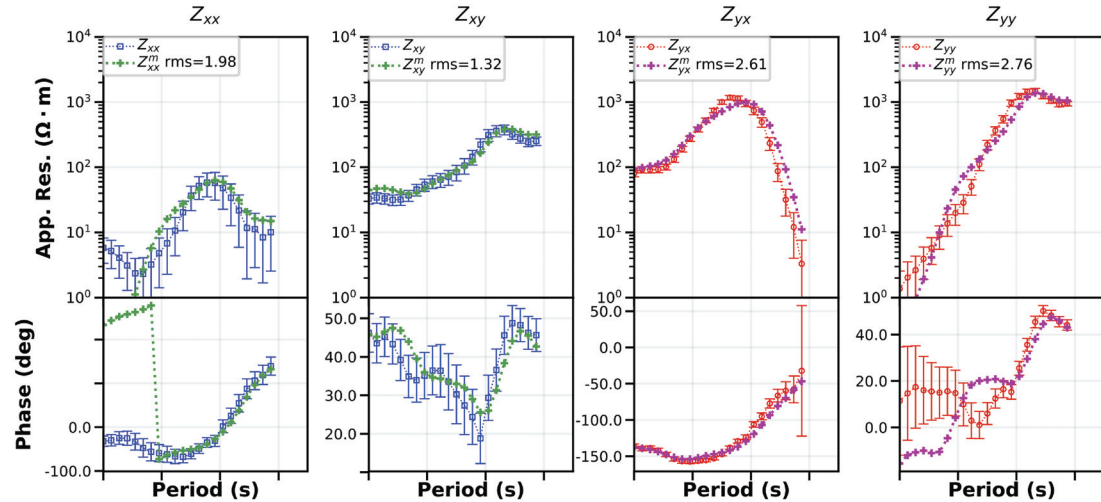
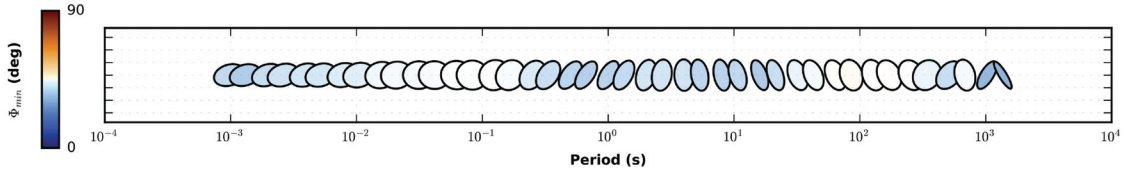
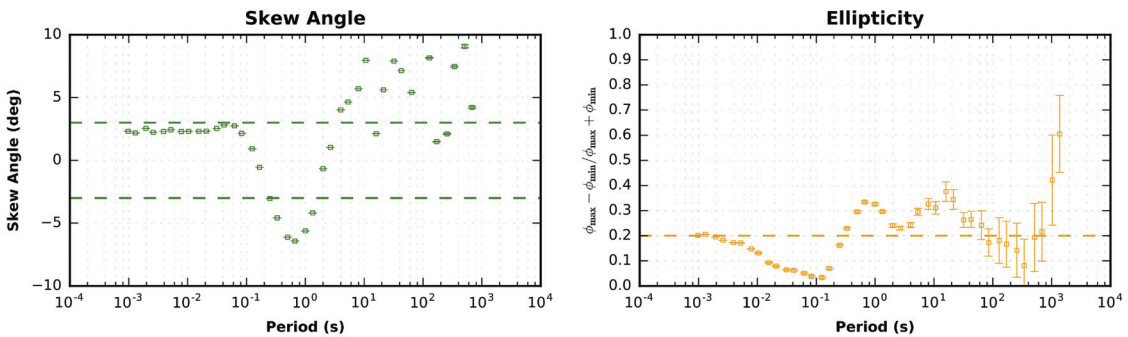
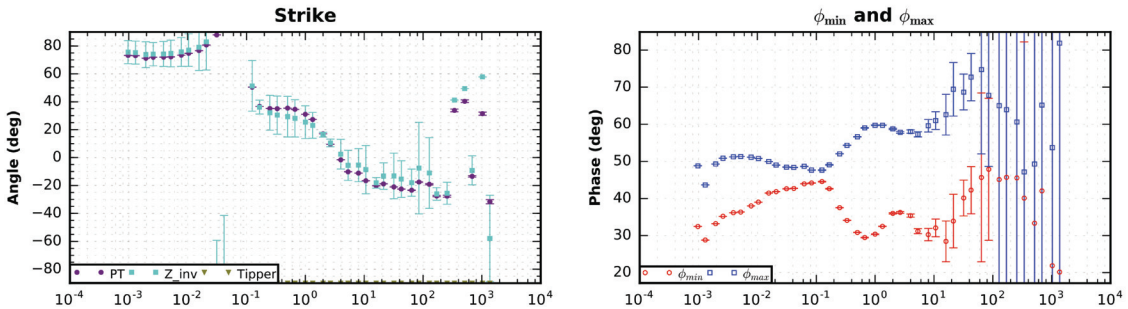


Figure 2.40: MT station #27 phase tensors, dimensionality metrics, and inverse model fits

Phase Tensors



Dimensionality Metrics



Inverse Model Fits

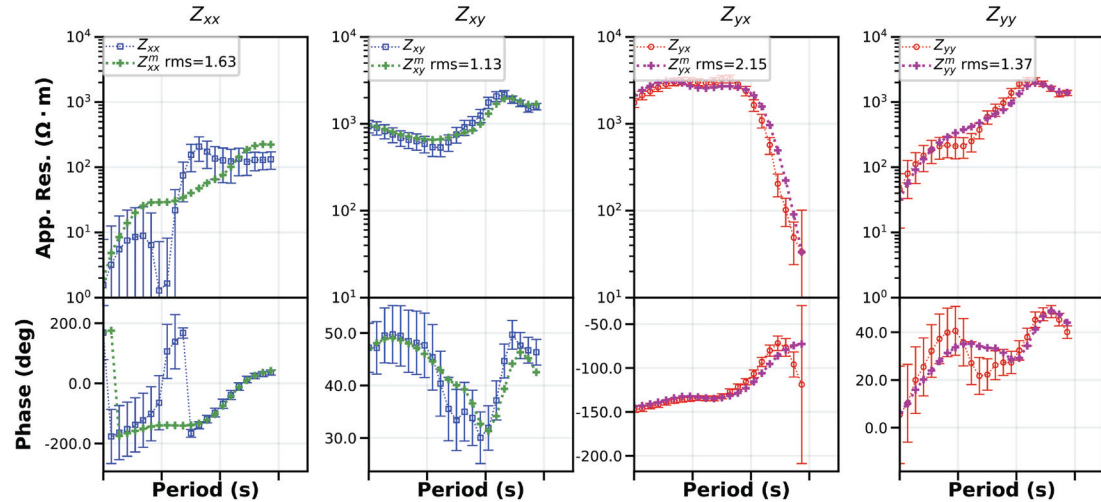
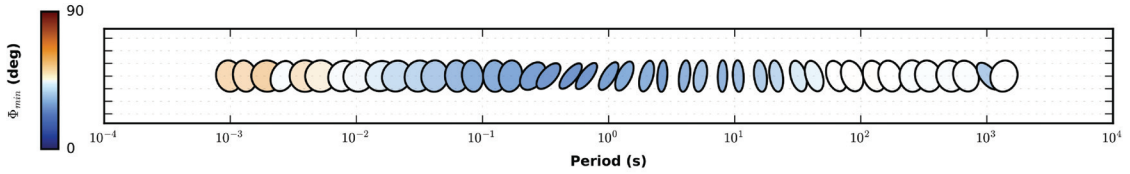
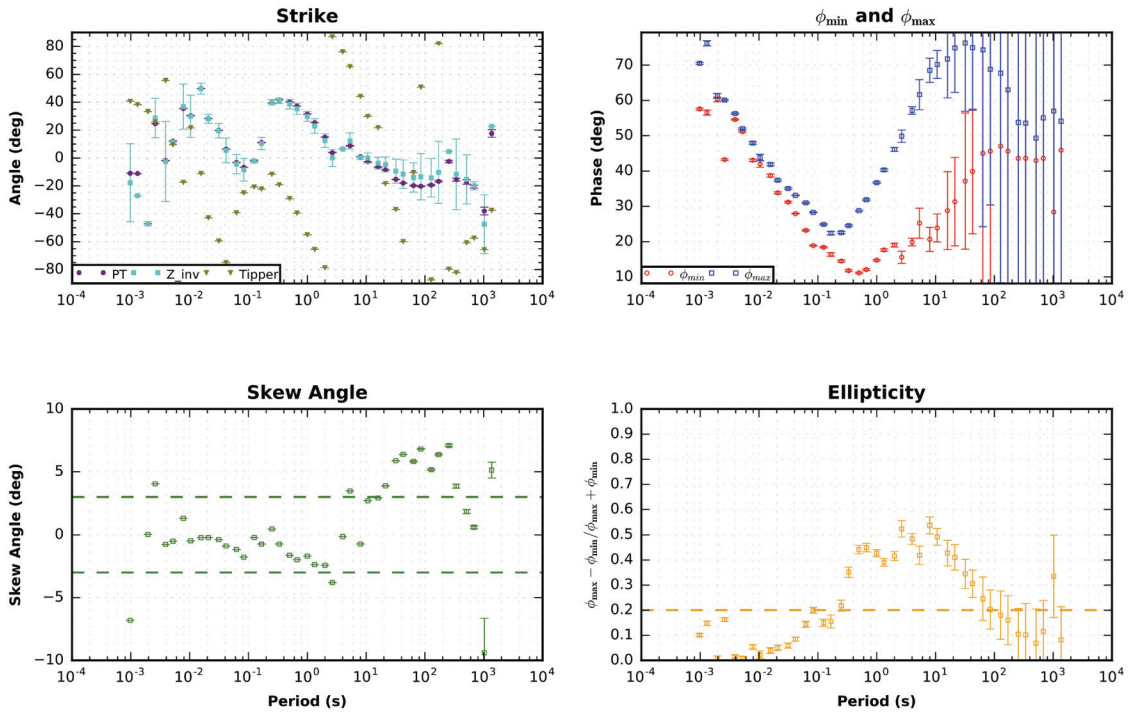


Figure 2.41: MT station #28 phase tensors, dimensionality metrics, and inverse model fits

Phase Tensors



Dimensionality Metrics



Inverse Model Fits

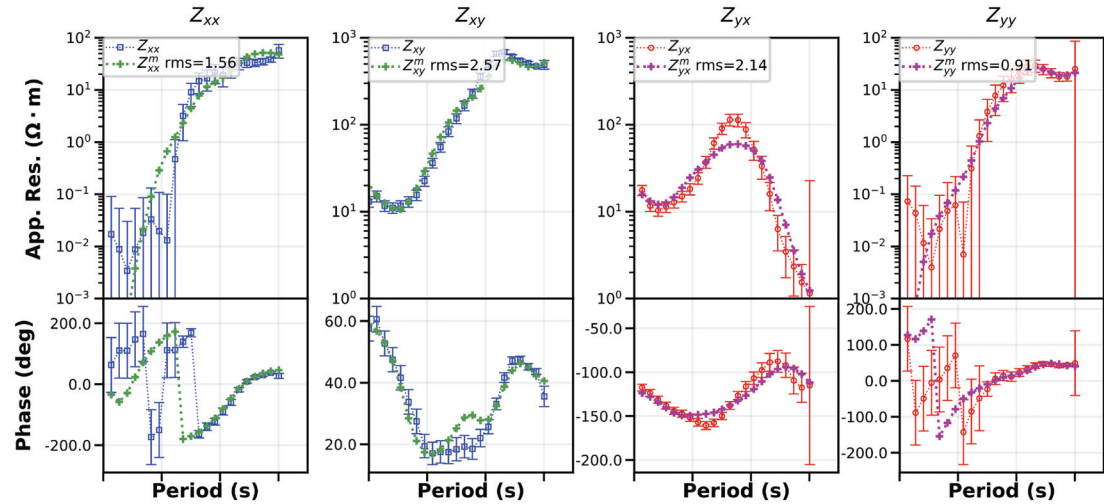
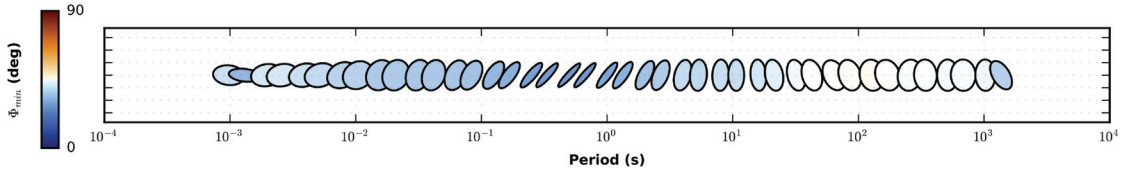
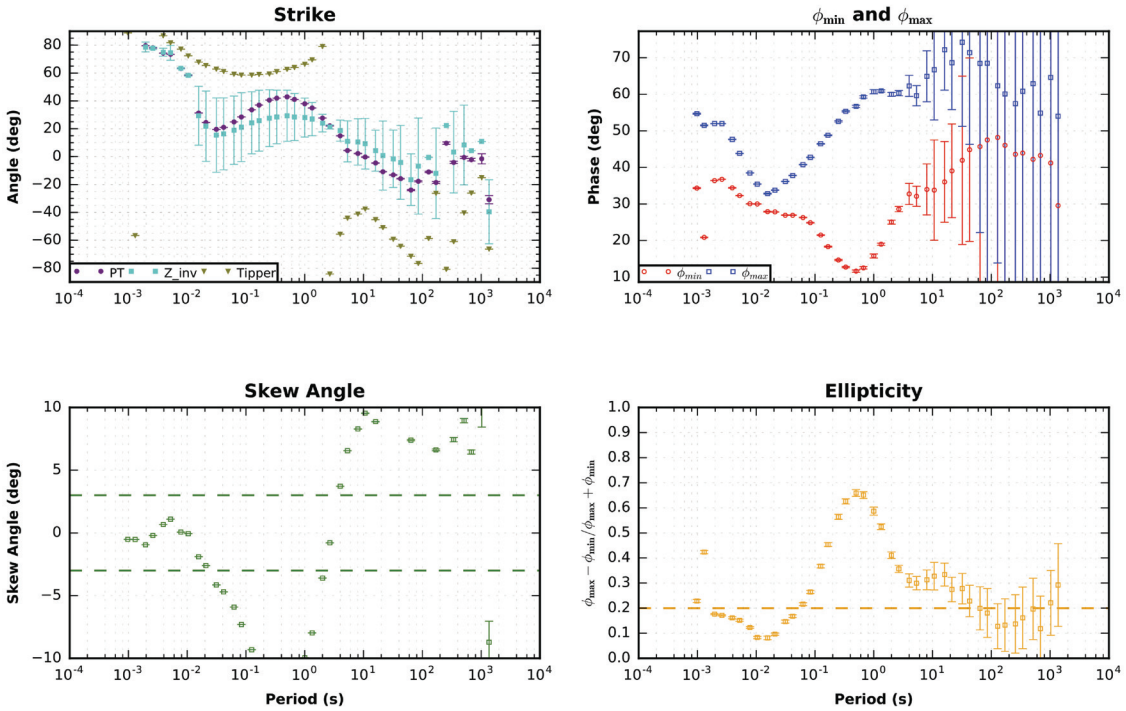


Figure 2.42: MT station #29 phase tensors, dimensionality metrics, and inverse model fits

Phase Tensors



Dimensionality Metrics



Inverse Model Fits

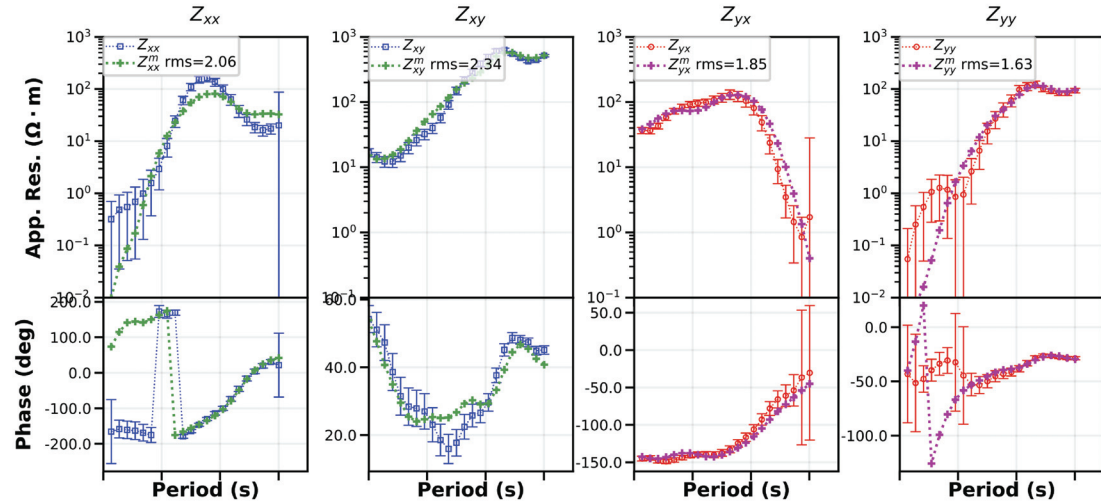
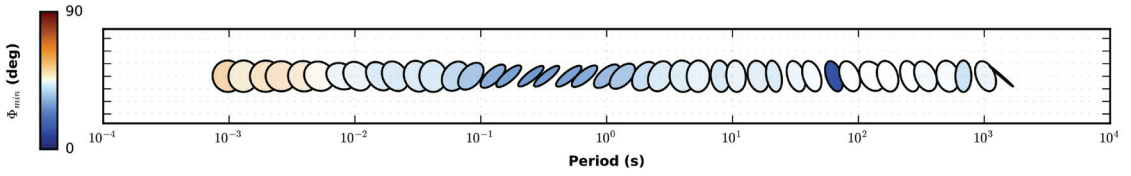
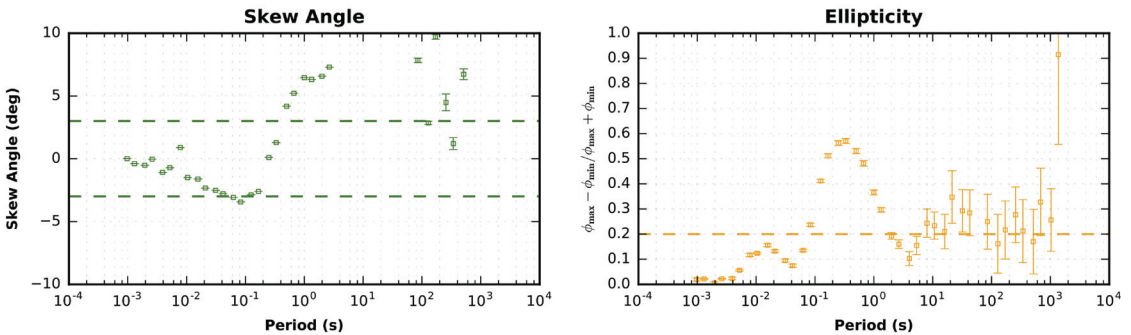
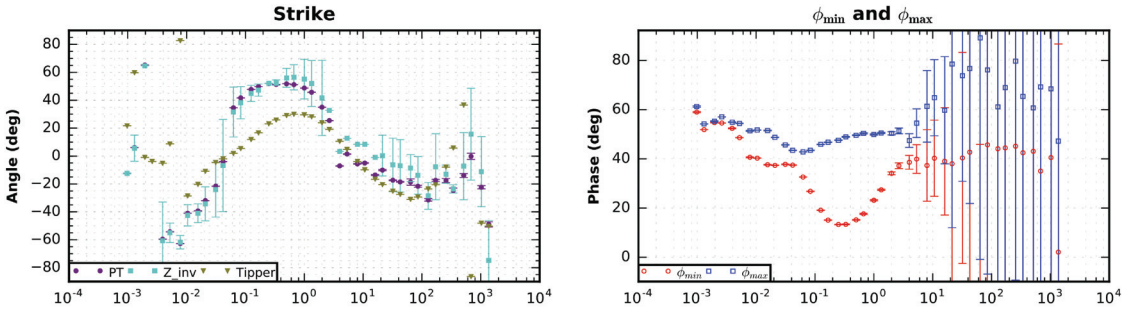


Figure 2.43: MT station #30 phase tensors, dimensionality metrics, and inverse model fits

Phase Tensors



Dimensionality Metrics



Inverse Model Fits

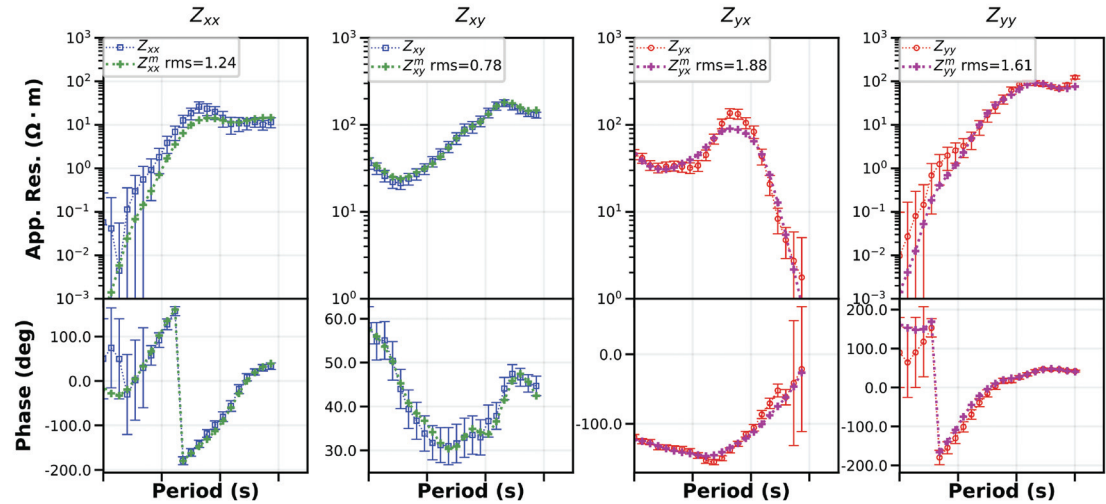
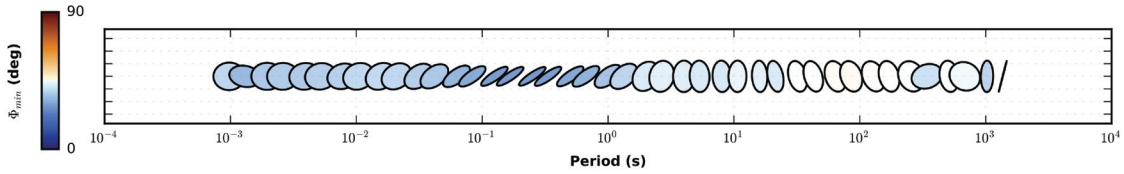
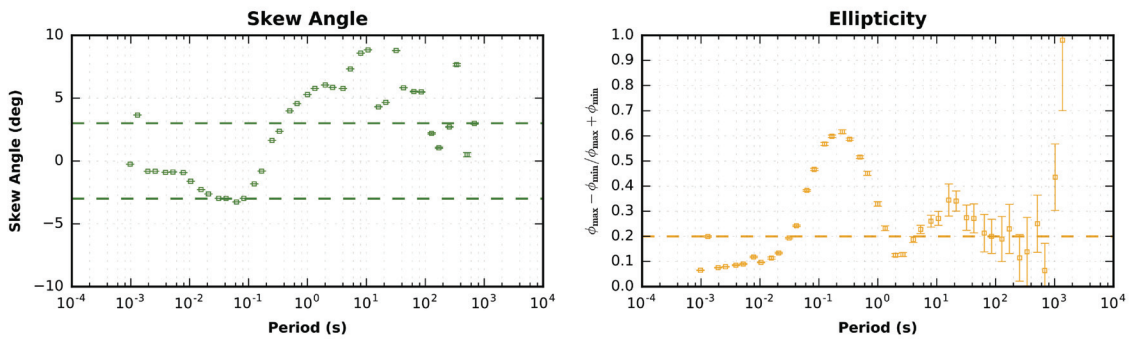
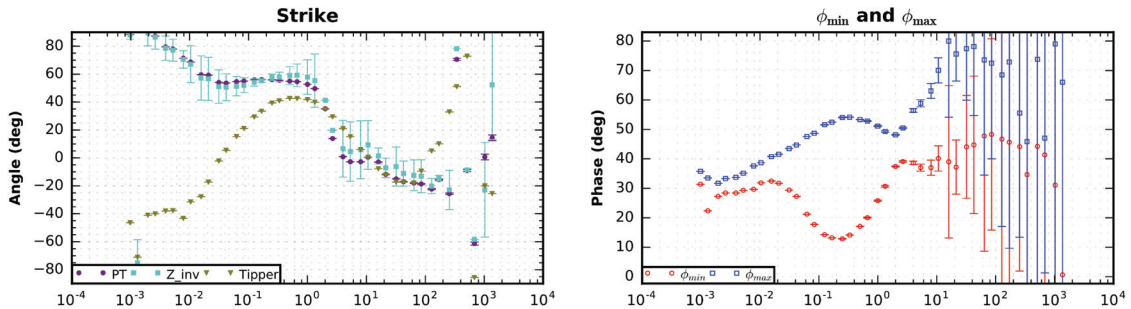


Figure 2.44: MT station #31 phase tensors, dimensionality metrics, and inverse model fits

Phase Tensors



Dimensionality Metrics



Inverse Model Fits

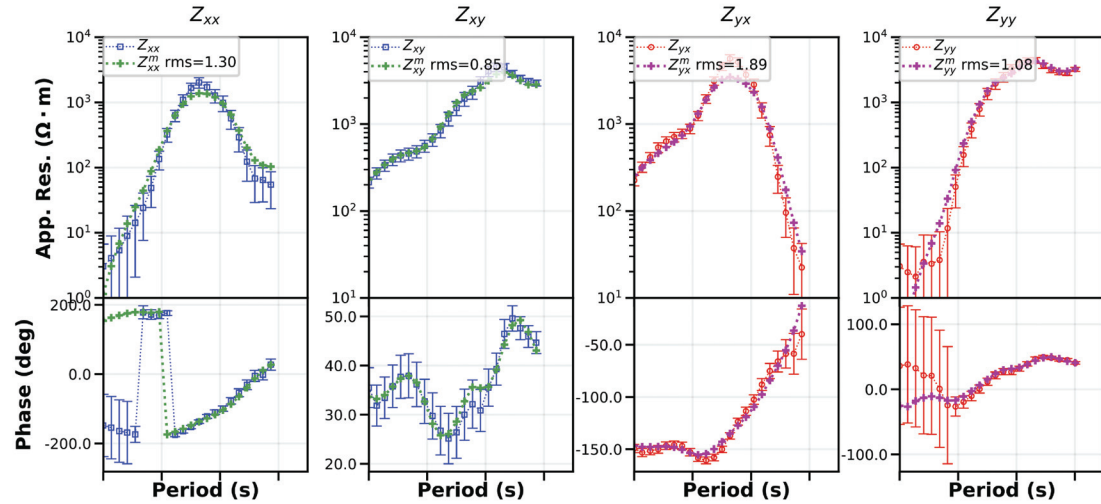


Figure 2.45: MT station #32 phase tensors, dimensionality metrics, and inverse model fits

CHAPTER 3

USING PRINCIPAL COMPONENT ANALYSIS AND CLUSTERING FOR GEOTHERMAL RESOURCE EXPLORATION

This chapter is written as a manuscript in preparation.

Abstract

We combine principal component analysis (PCA) and k-means clustering to discover distinguishing characteristics common among known-geothermal resources (KGRs) in southwest New Mexico. We then use those characteristics to outline a sub-region of higher geothermal potential and then prospect this sub-region by identifying non-KGR locations that are similar to associated KGRs. Twenty geological, thermal, geochemical, and hydrologic datasets are incorporated into this analysis. Our approach indicates that geothermal resources in this area are distinguishable by their physiographic/tectonic province (e.g. Rio Grande rift, Basin and Range) and identifies two primary exploration areas that are related to classic forced-convection geothermal systems and secondary fracture permeability resources, respectively. The secondary permeability region is comprised primarily of low-temperature hot spring systems. The forced-convection region contains some of the hottest liquid-dominated resources in New Mexico, including the Masson Farms geothermal greenhouse facility and the Lightning Dock binary power station. Further analysis of this hotter region indicates that the southeast portion of the study area is most likely to yield new economically-viable geothermal resources. Areas near Lordsburg, Las Cruces, Deming, and south of Socorro are believed to be particularly promising due to their strong relation to developed moderate (90 to 150°C) temperature geothermal resources within the study area. These target areas agree well with a recently published geothermal prospectivity map of the region. The PCA and clustering framework used in this study is most applicable to the preliminary and exploration phases of geothermal resource discovery, as it was able to classify KGRs on a regional scale, while also identifying regions of elevated geothermal potential.

3.1 Introduction

Geothermal resources worldwide have been developed for use in numerous applications such as: space heating, aquaculture, snow melting, recreational hot springs, greenhouse agriculture, and electricity generation (Lund et al. 2011, Quick et al. 2013). Even the non-electricity generation applications that utilize heat from geothermal fluids can have a substantial impact on greenhouse emissions. In the United States, 20% of energy demand was attributed to space and water heating alone in 2006 (Thorsteinsson & Tester 2010). Geothermal development projects are often burdened with steep upfront financial costs and risks. These costs are largely associated with geothermal exploration; reducing them and improving exploration drilling success rates remain primary challenges for the industry to overcome (Harvey & Beardsmore 2014). High risk is associated with the uncertainty of characterizing a resource that typically cannot be observed or measured directly without undertaking costly drilling ventures. A viable geothermal resource requires three main attributes: water, water mobility (i.e. permeability), and heat (Anderson et al. 2011). Exploration efforts tend to analyze large geochemical, geophysical, thermal, and geologic datasets to minimize the uncertainty related to resource location, depth, temperature, productivity, and sustainability (Harvey & Beardsmore 2014). Substantial effort is often invested in developing maps of geothermal potential. These maps are typically constructed by statistically weighting exploration data (e.g. heat flow, proximity to faults, etc.) to estimate the geothermal prospectivity of unexplored areas (Coolbaugh & Shevenell 2004, Bielicki et al. 2016). Some researchers argue that the greatest advancement in the geothermal industry could result from improvements in this exploration phase (Anderson et al. 2011). New innovative approaches to analyze and interpret large geothermal datasets could be a potential catalyst for this advancement.

We experiment with the combined use of principal component analysis (PCA) and clustering methods to better understand geothermal resources in this study. PCA is a dimension-reduction statistical technique that seeks to summarize many variables (i.e. datasets) with fewer representative variables to facilitate easier interpretation, while incurring limited information loss (Hastie et al. 2009, James et al. 2013). Clustering methods further improve interpretability by identifying groupings of similar data points within the PCA results (Everitt et al. 2011). These two methods have been used in conjunction in several research fields including genetics, imagery, chemical analysis, and mining geology (Gazley et al. 2015, Jiang et al. 2015, Gewers et al. 2018). In geothermal applications, PCA and clustering have predominantly been used to analyze geothermal fluid chemistry (Agrawala 2007). Recently, Lindsey et al. (2018) employed PCA and clustering to identify known geothermal resources (KGRs) that should be further evaluated for development; these authors frame their use of PCA and clustering as a low-cost tool for evaluating geothermal resources.

Our work aims to use PCA and clustering to determine distinguishing characteristics of known geothermal resources and identify new promising explo-

ration locations in southwest New Mexico (Figure 1). This study area is selected due to its elevated geothermal potential and high data availability; 20 environmental datasets are considered in this work (Bielicki et al. 2015, 2016). Additionally, a detailed geothermal prospectivity map has already been published for this area by Bielicki et al. (2015, 2016), which provides an independent metric for evaluating the utility of our approach. The existing prospectivity map was constructed using a completely different methodology that includes structural subcrop analysis, recharge and discharge zone identification, hydrologic window mapping, and resource magnitude assessment. Our approach begins by compiling existing data into contoured layers that are continuous throughout the study area. Values of the datasets are interpolated onto a grid of data points at 2 km spacing to assemble a comprehensive data matrix. PCA and clustering are first performed on grid points that are associated with KGR locations to determine distinct classes of KGRs. The results from this analysis are then used to select a group of KGRs that are more commonly associated with economically-viable resources. The PCA results are then used to map out a broad region in which new economically-viable resources are most likely to be located. Finally, PCA is performed a second time, but on this sub-region alone, to focus on non-KGR locations that possess similar characteristics to proven local KGRs. Successful implementation of this approach would provide a new inexpensive mechanism to quickly characterize and explore geothermal regions of various scales and complexity.

3.2 Methods

Our research focuses on prospecting and better understanding the geothermal resources of southwest New Mexico. This portion of New Mexico is a diverse landscape comprised of several physiographic provinces including: Basin and Range, Rio Grande rift, the Mogollon-Datil volcanic field, and the Colorado Plateau (Figure 1; Witcher 1995). The complex geology of this region and its elevated heat flow has resulted in numerous liquid-dominated geothermal resources (Witcher 2002). A small amount (4 MW) of electricity is generated along the westernmost boundary of the study area near Lordsburg, NM, while several other resources have been developed for direct-use applications (Figure 1; Witcher 2002, Witcher et al. 2002, Laney & Brizzee 2003).

We further explore this region for geothermal resources by combining principal component analysis and k-means clustering methods. Principal component analysis (PCA) is a commonly-utilized statistical method that aims to simplify data interpretation by recasting a series of variables as linear combinations of those variables (Hastie et al. 2009, James et al. 2013). These linear combinations are referred to as principal components (PCs) and are derived to capture much of the dataset's variability while using fewer dimensions. PCs are ordered by their proportion of dataset variance explained (i.e. PC1 explains the

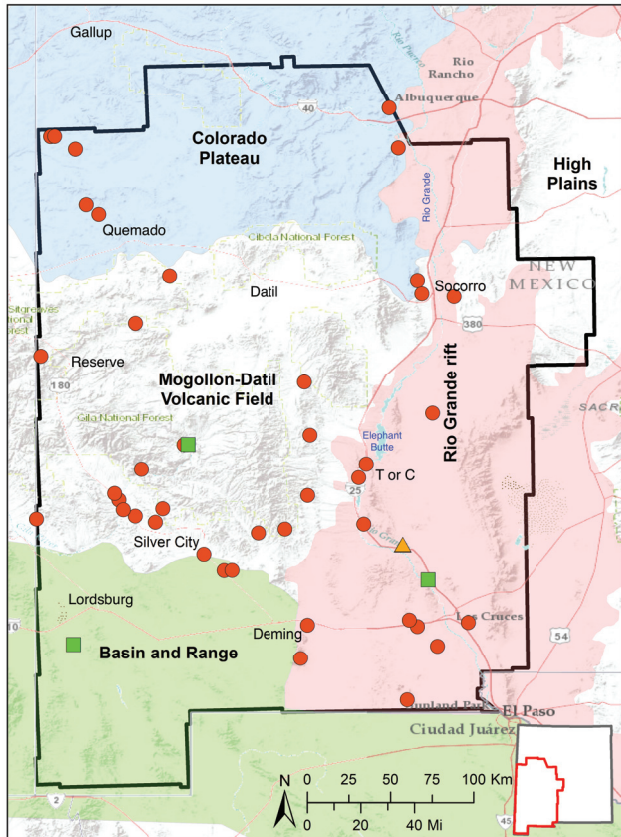


Figure 3.1: Southwest New Mexico study area with known-geothermal resources (KGRs) and regional physiographic provinces indicated. The inset shows the study area's position in New Mexico. Red circles = low-temperature (less than 90°C) KGRs, green squares = moderate temperature (90 to 150°C) KGRs, orange triangle = Rincon KGR.

largest proportion of variance, PC2 the second largest, and so on). There are as many PCs as there are variables considered and they take the following form:

$$PC1 = \beta_1 V_1 + \beta_2 V_2 + \dots + \beta_{nvar} V_{nvar} \quad (3.1)$$

where $PC1$ is the first principal component score value for a given data point (i.e. scores), V_i are the original variables considered, β_i are the PC loadings or weights for the first PC, and $nvar$ is the total number of variables considered in the analysis. The loadings vary between -1 and 1 and therefore scale the influence of the original variables based on their contribution to each PC. Thus, the PCs are linear combinations of the original variables considered in the study. The variables themselves are typically normalized using their variance and centered using their mean, so that variables of differing units and magnitudes do not bias the PCA results (James et al. 2013). Additionally, outliers need to be addressed in a way that they do not skew the analysis; this is often done by removing or winsorizing the outliers (Ghosh & Vogt 2012). Winsorizing entails adjusting the value of an outlier to a less extreme, but still abnormal, value so that it is a diluted version of itself (Ghosh & Vogt 2012). PCA results are often visualized using biplots, which plot the PC scores for two principal components against one another.

It is common practice to invoke clustering methods to identify groupings of PC scores on biplots to ease interpretation; this is done using Euclidean-distance based k-means clustering in this study (Hartigan & Wong 1979). K-means clustering is a well-regarded approach that randomly gives cluster assignments to each data point, calculates the resulting cluster centroids, then iteratively relocates those centroids based on their distance to nearby data points until optimal solutions are found (Everitt et al. 2011, James et al. 2013). The algorithm is repeated for a large number of initial centroid locations to find best-fit final clustering solutions. The Hartigan & Wong (1979) k-means algorithm used in this study identifies and further optimizes best-fit cluster solutions by minimizing the total within-cluster sum of squares of errors (WSS; Morissette & Chartier 2013). This method requires the user to input the number of desired clusters. Several criteria exist to determine the appropriate number of clusters in a given dataset, with one of the most common being the total WSS metric (Everitt and Hothorn 2010). This involves experimenting with a range for the number of clusters and evaluating the compactness of the resulting solution; an elbow in a plot of WSS as a function of the number of clusters is commonly used to denote the appropriate number of clusters present in the data (Everitt and Hothorn 2010, Everitt et al. 2011).

In this study, we first perform PCA and k-means clustering on 20 environmental data variables from locations associated with known geothermal resources (KGRs) to determine groupings of KGRs based on their characteristics. This is followed by using the KGR loadings (i.e. weights) and scaling parameters to project all non-KGR data points onto the KGR biplot to identify similarities between KGR and non-KGR locations. This biplot is then used to select a subset of data that is most likely to host economically-viable geothermal resources.

Lastly, PCA is performed on this subset of data to enable a more selective identification of geothermally-promising non-KGR locations. The remainder of this section describes each of these steps in detail.

3.2.1 Data Compilation and Preparation

Twenty datasets are utilized in this study (Table 3.1). Some of these datasets are used as published by previous researchers, while others were created using existing available data. The datasets can be split into two categories: spatial density layers and contoured layers. Spatial density layers are those that estimate the concentration of spatial features within a given area. Contoured layers are those that were created by contouring the magnitudes of measured parameters, such as elevation and depth to water. Detailed processing steps, data sources, and final surfaces are provided for each data layer in Appendix 3.A. Generally, spatial density layers were created using the kernel density tool in ArcGIS, while contoured layers are previously-published surfaces or were made using standard contouring algorithms in ArcGIS (e.g. inverse-distance weighting, topo-to-raster).

In addition to the aforementioned variables, a known-geothermal resources (KGRs) layer is needed for our study. This layer was created by merging the USGS Identified Hydrothermal, USGS Identified Delineated-Area Geothermal Systems, and USGS Isolated Geothermal Systems layers downloaded from the U.S. Department of Energy National Renewable Energy Laboratory Geothermal Prospector tool (NREL 2018). The final KGR layer represents a combination of these U.S. Geological Survey datasets that identifies low (less than 90°C) and moderate (90 to 150°C) temperature resources in the study area (see Appendix 3.B for KGR table; Reed et al. 1983, Williams et al. 2008). There is a KGR in Rincon, New Mexico that is not included in the USGS KGR layers (Witcher et al. 1992). This resource was not added to our final KGR layer so that it could be used as a test data point to interrogate the accuracy of our exploration approach. Overall, the KGRs in the study area are diverse in that some lie in low elevation, high heat flow regimes, while others are at high elevations in lower heat flow environments. All of these resources are believed to be amagmatic and many have surface expressions, but others are blind systems. The resources are hosted in sediments, crystalline basement, and volcanic intrusions. This diversity is emphasized by the widespread spatial distribution of KGRs throughout the study area (Figure 3.1).

A grid of 2-km spacing was overlain on the study area for data extraction using the "Extract Values to Points" tool in ArcGIS. KGRs were assigned to the nearest grid point using the "join" tool in ArcGIS. These grid data were then combined to form a matrix consisting of 24,076 data points for all 20 variables considered that was then utilized for PCA and clustering in the open-source R programming language (R Core Team 2013).

Table 3.1: Datasets considered in the study. Eight spatial density layers and 12 contoured layers are included for a total of 20 datasets.

Spatial Density Layers	Contoured Layers
Drainage Density	Boron Concentration
Earthquake Density	Crustal Thickness
Quaternary Fault Density	Depth to Basement
Quaternary Fault Intersection Density	Depth to Water
Spring Density	Elevation
State Map Fault Density	Gravity Anomaly
Volcanic Dike Density	Heat flow
Volcanic Vent Density	Hydraulic Gradient
	Lithium Concentration
	Magnetic Intensity
	Precipitation
	Silica Geothermometer Temperature

3.2.2 Analysis of Known Geothermal Resources

The first portion of our PCA approach operates on just the 44 grid points associated with known-geothermal resources (KGRs). Box plots are used to identify outliers in each of the 20 variables at these data points. The "far out" value criteria proposed by Tukey (1977) is used to denote outliers, which is defined as any point greater or less than three times the interquartile range of the data. This method is known as a conservative test to identify outliers and does not require assumptions about the distribution of the data (Iglewicz & Hoaglin 1993). Any point that exceeds these bounds is reduced to the outlier threshold value (i.e. winsorized); thus preserving the outliers as abnormal but less extreme values (Ghosh & Vogt 2012). The data are then scaled and centered using their variances and means, respectively, prior to PCA being performed. An elbow in a plot of each PCs percent of variance explained (i.e. scree plot) is used to determine the number of PCs that should be utilized in the clustering analysis (James et al. 2013).

K-means clustering is then done on the PC scores using 1 to 10 clusters. The results from this are used to create a WSS plot to determine the appropriate number of clusters in the dataset. A Euclidean distance plot is also used to compliment the WSS cluster criteria (Everitt and Hothorn 2010). Once the number of clusters is selected, k-means clustering is performed again using 100,000 initial cluster-centroid locations. Biplots and spatial maps of the clustered results are then constructed to understand the variables contributing to the clusters and cluster spatial patterns.

3.2.3 Comprehensive Dataset Analysis

Next, all non-KGR and KGR data points (i.e. comprehensive dataset) are analyzed with the goal of being able to project all non-KGR data points onto the previously-described KGR biplot to facilitate comparison with KGR sites. Analyzing the 24,076 grid points begins by winsorizing all 20 variables to the same threshold values determined in the KGR analysis. The variables are then centered and normalized using the KGR means and variances, respectively. The loadings from the KGR PCA are then applied to the comprehensive dataset to calculate scores for all non-KGR data points, thereby allowing them to be plotted on the KGR biplot. KGR cluster centroids are then used to assign clusters to all non-KGR data points. The multi-dimensional distance formula used to do this is simply the Euclidean distance formula in n-dimensions and is as follows:

$$d_k = \sqrt{(PC_{1c} - PC_{1s})^2 + (PC_{2c} - PC_{2s})^2 + \dots + (PC_{nc} - PC_{ns})^2} \quad (3.2)$$

where d_k is distance to the k th cluster centroid, PC_{ic} is a k th PC cluster centroid, PC_{is} is the score of a non-KGR data point for a given PC, and n is the total number of PCs considered. This formula is calculated for each data point and for all cluster centroids. Each data point is then assigned to whichever cluster's centroid is nearest. This approach was chosen because it is the same cluster assignment methodology employed in k-means clustering, except in this case the cluster centroids are fixed from the KGR analysis. Simply using Euclidean distance to assign clusters does not include the WSS optimization step that is part of the Hartigan & Wong (1979) k-means algorithm. Therefore, slightly different KGR cluster assignments may result by using just the Euclidean distance criteria in this step (Morissette & Chartier 2013); however, optimizing the WSS of the comprehensive dataset does not fit the objectives of this analysis. At this point, the KGR clustered biplots and spatial maps are re-visited to determine which cluster is most likely to contain undiscovered economically-viable geothermal resources. Once identified, all data points that are assigned to that particular cluster are exported to a data subset so that PCA can be performed on them separately. In addition, this subset is plotted spatially to provide a broad outline of the highest geothermal potential for the study area.

The data subset is first winsorized using the aforementioned "far out" value criteria. The data are then normalized and centered prior to PCA being performed. The subset scores are plotted on a biplot and the KGR points are flagged to make groups of KGRs apparent. Any non-KGR scores that are proximal to KGR scores are then plotted spatially to identify non-KGR locations that are very similar to KGRs. It is these locations that are presumed to be of elevated geothermal potential, since their overall data signature resembles that of previously-discovered geothermal resources.

3.3 Results & Discussion

This section summarizes the results from both the KGR and comprehensive dataset analyses and concludes with a discussion of the applicability of this use of PCA and clustering.

3.3.1 Known-Geothermal Resource Analysis Results

The variables of the 44 KGR data points were first evaluated for outliers. The "far out" value criteria identified no low-value outliers, but designated 11% of the Quaternary fault intersection density dataset and 9% of the spring density dataset to exceed the high-value threshold. Additionally, 2% of the vent density, heat flow, and depth to water datasets were found to be beyond this threshold. In general, the small amount of data that was ultimately identified as outliers is an encouraging sign that the "far out" criteria is unlikely to be identifying false outliers and is appropriate as a relatively conservative metric for this type of analysis. Identified outliers were all winsorized to their respective threshold values to reduce their ability to skew the PCA results. Strong similarity between pre- and post-winsorized Pearson correlation (Benesty et al. 2009) heatmap plots of the KGRs indicates that overall data structure is marginally impacted by the winsorization process (see Appendix 3.C).

PCA was performed on the winsorized KGR dataset. The resulting scree plot (Figure 3.2A) shows an elbow at the fourth PC and another at the seventh PC. Only four are considered for the final analysis, since this elbow is the most pronounced in the scree plot and using fewer PCs fosters a more straightforward interpretation of the PCA results. The four PCs combine to account for 62% of the dataset's overall variation. K-means clustering was then performed using the PC1-PC4 KGR scores. The WSS plot shown Figure 3.2B suggests there are between three and five clusters in the data by using the elbow rule. A Euclidean-distance plot was used to supplement the WSS plot (Figure 3.2C). This plot is interpreted by looking for structure in the pink regions of the plot. Deeper pink colors suggest a given data point is closer, in terms of Euclidean distance, to the corresponding data point. Therefore, large scale structure in these plots alludes to clusters of data. The Euclidean distance plot indicates that three to four main clusters are present in the data, which agrees well with the WSS metric. By combining the results of both metrics, four clusters was settled on for the k-mean analysis.

The clustering results are presented on the PC1 vs. PC2 biplot and spatial plot shown in Figure 3.3. Several distinct clusters are apparent when looking at the first two PCs, even though clustering was done using four PCs. Specifically, clusters one and three are particularly separated from clusters two and four. Clusters two and four actually overlap in this biplot but are distinct when visualized using biplots of the other PCs (see Appendix 3.D). These biplots can be used to understand the underlying characteristics of each KGR cluster. This is done by

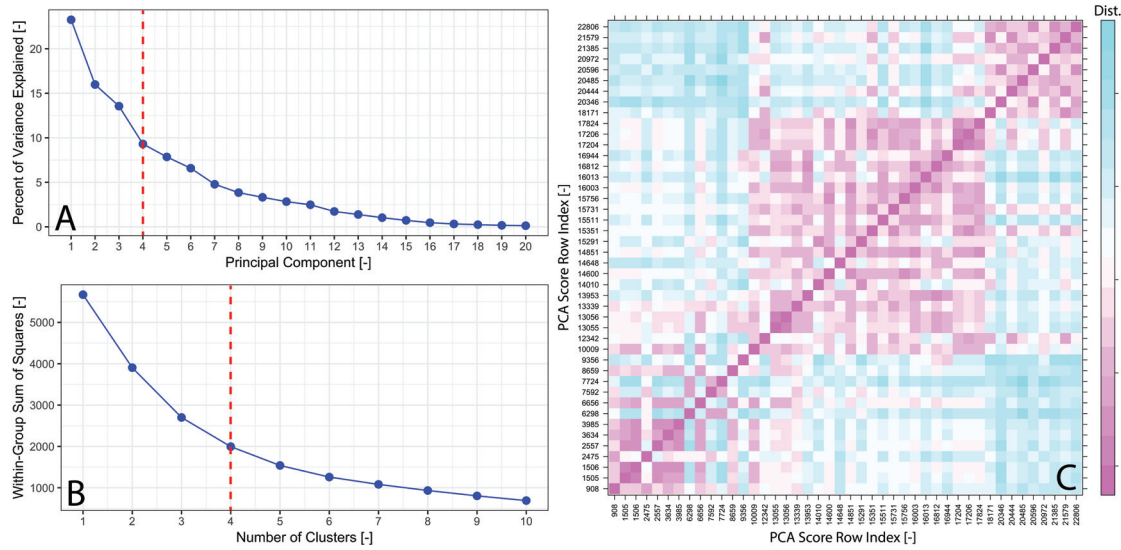


Figure 3.2: PCA scree plot (A), WSS cluster plot (B) and Euclidean-distance plot (C) that are used to determine the appropriate number of PCs and clusters to consider in the KGR analysis. Elbows in the scree and WSS plots along with the structure of the pink regions in the Euclidean distance plot indicate that four clusters and four PCs are appropriate for the analysis.

observing the variable vectors that extend from the origin of each biplot and their relation to each cluster. Larger vectors have a higher influence on data point position relative to shorter vectors. The arrowhead on each vector corresponds to high values of that particular variable. Table 3.2 summarizes the characteristics of each cluster.

Cluster one is associated with high depth to basement, positive gravity anomalies, heat flow, Quaternary fault density, silica geothermometer temperatures, and volcanic vent density. This set of KGRs is also linked to low crustal thickness, drainage density, elevation, hydraulic gradient, and spring density. The spatial distribution of these KGRs is entirely within the southern Rio Grande rift and the Basin and Range provinces (Figure 3.3B). Many of these geographic regions are made up of deep alluvial basins and have the thinnest crust in New Mexico. The spatial distribution and associated parameters of this cluster all suggest that this is a group of "classic" forced-convection geothermal systems. Forced-convection systems typically involve low-aspect ratio, deep circulation of groundwater in permeable sediments in regions of elevated heat flow (Domenico & Palciauskas 1973, Ferguson & Grasby 2011). The high depth to basement, low drainage density, and low spring density suggest high sediment permeability and thickness that permits deep circulation. The positive gravity anomaly signal corresponds well to low crustal thickness, which provides a high heat flow environment that yields high silica geothermometer temperatures for the geothermal waters. Finally, elevated volcanic vent density and Quaternary fault density provide fast paths for ascent of fluids, while low elevation provides a regional hydraulic gradient to drive basin-scale groundwater flow, even though local hy-

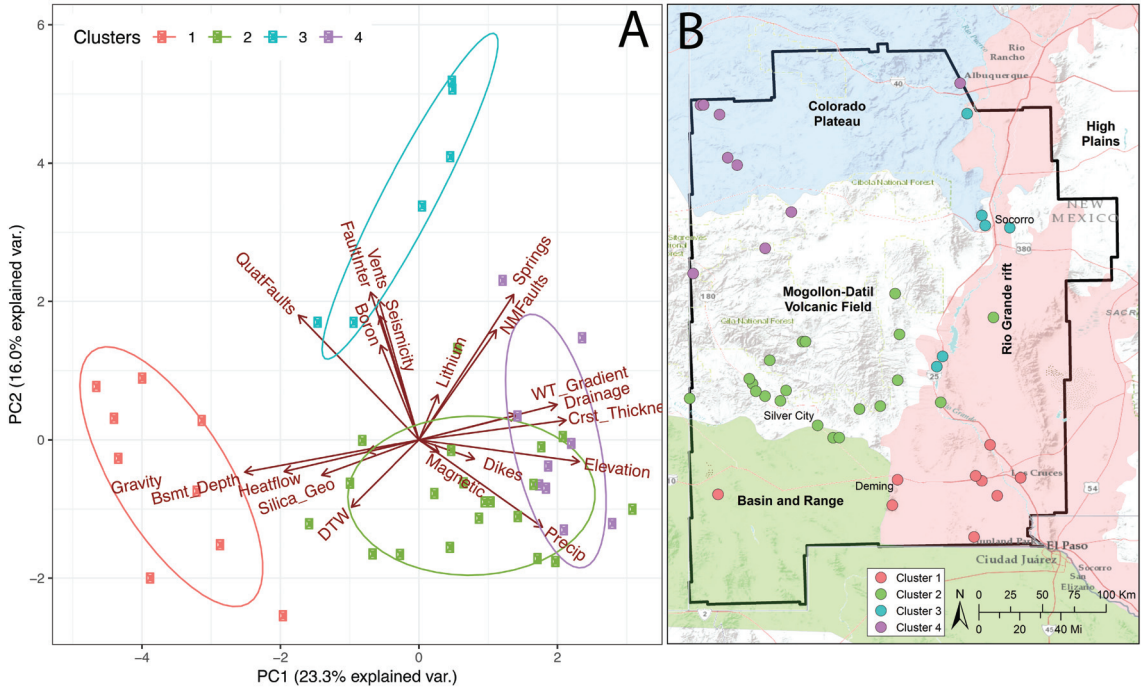


Figure 3.3: PC1 vs. PC2 biplot (A) and spatial map (B) presenting the KGR PCA and clustering results. Distinct clusters are evident in both figures. The biplot yields insight into the underlying characteristics of each cluster by observing the variable vectors and their relation to the clusters (see Appendix 3.D for biplots that consider additional PCs). The spatial plot emphasizes the influence of physiographic province on each cluster. Abbreviations: Bsmt_Depth = Depth to basement, DTW = Depth to water, Precip = Precipitation, Silica Geo = Silica geothermometry temperature, WT_Gradient = Water-table gradient.

Table 3.2: Summary of KGR cluster characteristics. Cluster one portrays "classic" forced-convection geothermal systems, while cluster three represents geothermal resources that rely on high secondary fracture permeability. Clusters two and four are not ideal targets for future geothermal prospectivity.

	Cluster 1	Cluster 2	Cluster 3	Cluster 4
HIGH	Depth to Basement	Dike Density	Boron	Boron
	Gravity	Drainage Density	Earthquake Density	Crustal Thickness
	Heat Flow	Gravity	Q. Fault Density	Drainage Density
	Q. Faults Density	Hyd. Gradient	Q. Fault Intersections	Elevation
	Silica Geotherm.	Precipitation	Spring Density	Precipitation
	Vent Density	Silica Geotherm.	State-Map Fault Density	Spring Density
LOW	Crustal Thickness	Depth to Basement		Gravity
	Drainage Density	Boron		Q. Fault Density
	Elevation	Heat Flow		Q. Fault Intersections
	Hyd. Gradient	Q. Fault Density		Silica Geotherm.
	Spring Density	Q. Fault Intersections		
		Vent Density		

draulic gradients are low. This cluster of KGRs represents the type of geothermal resource that is most commonly sought after and developed in New Mexico. Both the Lightning Dock binary power station and the Masson Farms greenhouse facility are part of this KGR group, which are considered two of the hottest resources in the study area by the U.S. Geological Survey (see Appendix 3.B for KGR table; Reed et al. 1983, Williams et al. 2008).

Cluster two is spatially distributed across the southern portion of the Mogollon-Datil volcanic field (Figure 3.3B). This cluster is associated with high dike density, drainage density, positive gravity anomalies, hydraulic gradient, precipitation, and silica geothermometer temperatures. In addition, this cluster has low depth to basement, boron concentration, heat flow, Quaternary fault density, Quaternary fault intersection density, and volcanic vent density. Many of these variable linkages result from the resources being located in mountainous terrain, such as high precipitation, drainage density, hydraulic gradient, and low depth to basement. From a geothermal exploration perspective, this cluster's low heat flow and low density of young faulting relative to other portions of the study area are not favorable. However, the high water availability, silica geothermometer temperatures, and dike density are encouraging.

Cluster three is mainly composed of the Truth or Consequences (T or C) and Socorro geothermal resources that are located in the central Rio Grande rift (Figure 3.3B). These resources have previously been linked through hydrothermal modeling studies that concluded that they involve deep groundwater circulation through highly-fractured crystalline basement rocks (Mailloux et al. 1999,

Pepin et al. 2015). The characteristics of this cluster corroborates this conceptual model, as indicated by their high Quaternary fault density, Quaternary fault intersection density, and state-map fault density. The Quaternary fault variables within the T or C and Socorro watersheds are exceptionally high relative to the rest of the study area and set them apart from other KGRs. In the Socorro area, seismicity is anomalously high, which lumps this variable with this cluster as well. All of these characteristics suggest this KGR group is distinguished by high secondary permeability in the form of large fracture networks. The elevated spring density of this cluster also indicates that faults may serve as conduits or provide hydrologic windows for groundwater ascent, which is the working model for both the T or C and Socorro geothermal systems. Overall, this cluster is characterized by elevated secondary permeability and represents a good exploration target for low-temperature hot-spring type systems.

Cluster four is mainly located up on the Colorado Plateau (Figure 3.3B). This cluster is associated with high crustal thickness, boron concentration, drainage density, elevation, precipitation, and spring density. It is also linked with low silica geothermometer temperatures, gravity anomalies, Quaternary fault density, and Quaternary fault intersection density. Similar to cluster two, these systems thrive on the large water availability of their physiographic location. However, the low silica geothermometer temperatures, Quaternary fault density, Quaternary fault intersection density and high crustal thickness are not favorable in terms of future geothermal prospecting.

3.3.2 Comprehensive Dataset Analysis Results

Our analysis now turns to projecting the non-KGR data points of the comprehensive dataset onto the KGR biplot to enable identification of target prospecting regions. This first requires the winsorization of the comprehensive dataset to the same threshold values used in the previous KGR analysis. The majority of the dataset required winsorization at levels that affected less than 5% of the data (Appendix 3.E). However, 15% of the gravity anomaly values were deemed to be low value outliers, while appreciable amounts of high value outliers were noted in the earthquake density (14%), volcanic vent density (17%), lithium concentration (11%), elevation (17%), and depth to water (13%) datasets. These levels of adjustment are a result of only considering the KGR locations when setting original threshold limits, which is necessary for the given methodology. The KGRs do not capture the full range of the study area's complexity and the winsorized values represent the extremes of this complexity, so this level of winsorization is anticipated. Fortunately, since the values are adjusted to the "far out" criteria, their general abnormal character is still honored and the impacts of their adjustment are minimized.

The winsorized dataset was then scaled and centered using the KGR variance and mean so that all data points could be projected onto the KGR biplot. The resulting biplot is shown in Figure 3.4A along with KGR cluster centroids

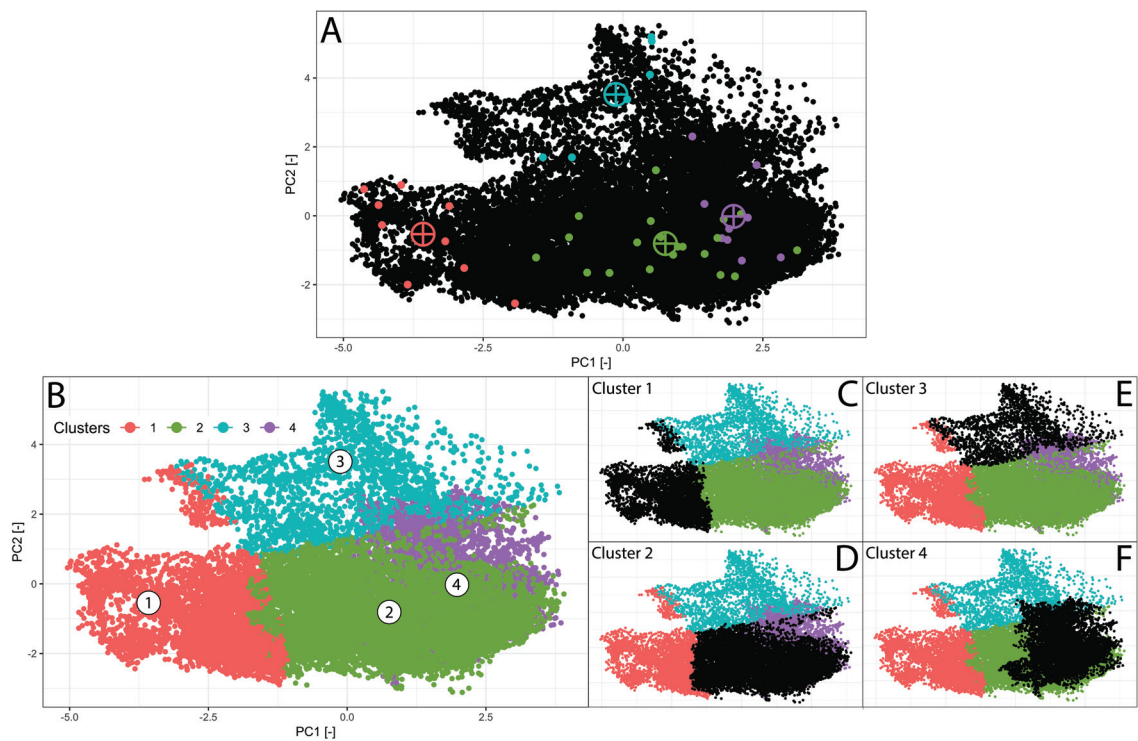


Figure 3.4: All data points projected onto the KGR biplot with original KGR centroids and cluster assignments indicated (A). The data points are assigned to clusters using the original KGR centroids and the Euclidean distance formula in four dimensions (B-F).

and clustered KGR scores. There is substantial overlap of the KGRs with the non-KGR points, but the clusters are not readily apparent due to the large amount of data portrayed on the plot. The Euclidean distance formula (Equation 3.2) using four PCs and the KGR cluster centroids was employed to assign clusters to the comprehensive dataset (Figure 3.4B-F). The resulting clusters are plotted spatially to facilitate easier interpretation in Figure 3.5.

Like the KGR clusters, the comprehensive dataset clusters are strongly related to physiographic province. Cluster one is entirely encompassed within the southern Rio Grande rift and the Basin and Range provinces (Figure 3.5A). This region includes both the Lightning Dock binary power station and the Masson Farms geothermal greenhouse facility, which the USGS classify as moderate (90 to 150°C) temperature geothermal resources. An undeveloped KGR in Rincon, New Mexico that is not included in the USGS KGR layer is also included in this cluster. Cluster two is predominantly in the Mogollon-Datil volcanic field, but also extends into the Rio Grande rift and Basin and Range provinces (Figure 3.5B). This is the most spatially extensive cluster and has the appearance of a transitional group that bridges the northern and southern portions of the study area. Cluster three includes areas within the Rio Grande rift as well as areas along its western margin (Figure 3.5C). The Truth or Consequences geothermal system watershed is well-defined and distinct from the rest of the cluster. The Socorro geothermal system watershed is also part of the cluster, along with a zone that extends northward towards Albuquerque. This cluster covers the least amount of the study area. Cluster four is mainly in the Colorado Plateau but also extends down into the Mogollon-Datil volcanic field (Figure 3.5D).

The KGR analysis identified clusters one and three as being the most promising for future geothermal exploration. Both of these clusters are less spatially extensive clusters and their confinement to regions of elevated heat flow further supports this notion. However, cluster three is essentially the low-temperature Truth or Consequences and Socorro geothermal watersheds along with a region north of Socorro. Cluster one includes two of the three higher temperature geothermal KGRs in the study area, as classified by the USGS (see Appendix 3.B). This area is also associated with classically favorable geothermal prediction variables (Table 3.2) and includes the Rincon geothermal resource. It is the area that is defined by this cluster that is therefore thought to represent a region of highest geothermal potential and an area of most immediate importance for further geothermal exploration.

We further prospect within the cluster one dataset by performing a separate PCA on this subset alone, with the goal being to identify more specific zones that seem geothermally favorable. These data are first winsorized using the "far out" value criteria. In 16 of the 20 datasets, 2% or less of the data were affected by the winsorization (Appendix 3.E). Quaternary fault intersection density (4%), Quaternary fault density (5%), and earthquake density (7%) were affected at slightly higher levels, while 17% of the volcanic vent density dataset was deemed to be high-value outliers. The adjusted volcanic vent values are west of Las Cruces near Kilbourne Hole and the Potrillo Mountain ranges. This region is

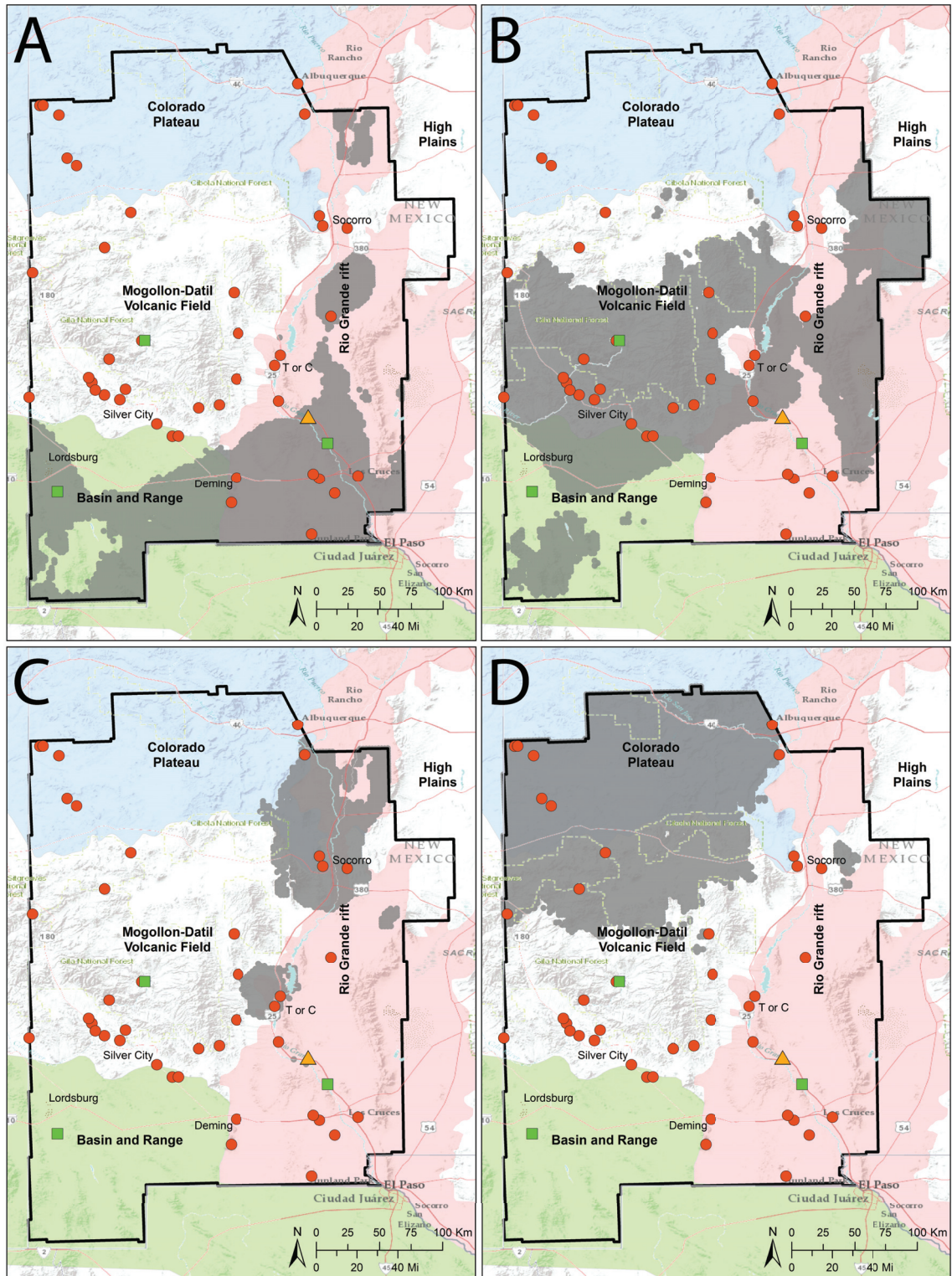


Figure 3.5: All comprehensive dataset clusters plotted spatially. Like the KGR clusters, the comprehensive dataset clusters are strongly linked with physiographic province. A = cluster 1, B = cluster 2, C = cluster 3, D = cluster 4, red circle = low temperature KGR, green square = moderate (90 to 150°C) temperature KGR, orange triangle = Rincon KGR.

associated with extremely elevated vent density relative to the rest of the subset cluster one area, so its values being reduced to less extreme values during the winsorization process is appropriate.

Much can be gleaned from examination of the PCA PC1 vs. PC2 biplot (Figure 3.6A). These two PCs combine to account for 33% of the variation in the data, and the KGRs group together quite well in the plot. This grouping of KGRs can be used as a prospecting tool, since underlying non-KGR data points are inherently very similar to the overlying KGR points. A box has been illustrated on Figure 3.6A that includes 80% of the KGRs located within the cluster one subset. The underlying non-KGR data points are plotted spatially in Figure 3.6B and are considered regions of higher geothermal potential based on their pervasive similarity to KGRs. It is worth noting that our test Rincon KGR location plots far away from this KGR group on the biplot, suggesting a large proportion or all of the cluster one subset is geothermally relevant. The two highest temperature geothermal resources are included in this box and are adjacent to one another in the biplot (Figure 3.6A). Grouping these two locations along with a proximal KGR delineates regions that are specifically similar to these two developed and economically productive resources (Figure 3.6C-D). Finally, selecting the data directly underlying the two hottest KGRs identifies locations that are most similar, and therefore thought to be most promising, to these developed resources.

The results of this geothermal prospectivity exercise are compiled in Figure 3.7A. This map suggests that the southern portion of the study area is its most spatially extensive region of elevated geothermal potential. Land near Las Cruces and Lordsburg is unsurprisingly found to be very promising, given its relation to the two hottest geothermal systems in the data subset. More notable are the high potential targets (deep red color) identified by Deming and south of Socorro. These two locations are 10 to 20 miles away from KGRs and their prevalent similarity to the two hot KGRs strongly suggests further exploration in these areas is warranted.

It is noteworthy that this methodology successfully grouped geothermal systems and non-KGR locations by their underlying characteristics, which are strongly linked to physiographic province. Additionally, this approach delineated a broad zone of elevated geothermal potential that includes the test Rincon KGR location. By making the assumption that the data locations that are most similar to the two developed moderate (90 to 150°C) temperature resources are of highest potential, we are able to identify to additional regions near Deming and south of Socorro that may yield economically viable resources.

Further insight into the utility of this methodology can be gained by considering the study area's previously-published geothermal prospectivity map of Bielicki et al. (2015, 2016; Figure 3.7B). The methodology used to construct their prospectivity map was dramatically different and entailed a more elaborate effort that included structural mapping/analysis, identification of recharge and discharge zones, and crystalline basement temperature extrapolation. Their final prospecting map incorporates ten variables including: heat flow, basement temperature, known faults, inferred faults, lithium concentration, boron concen-

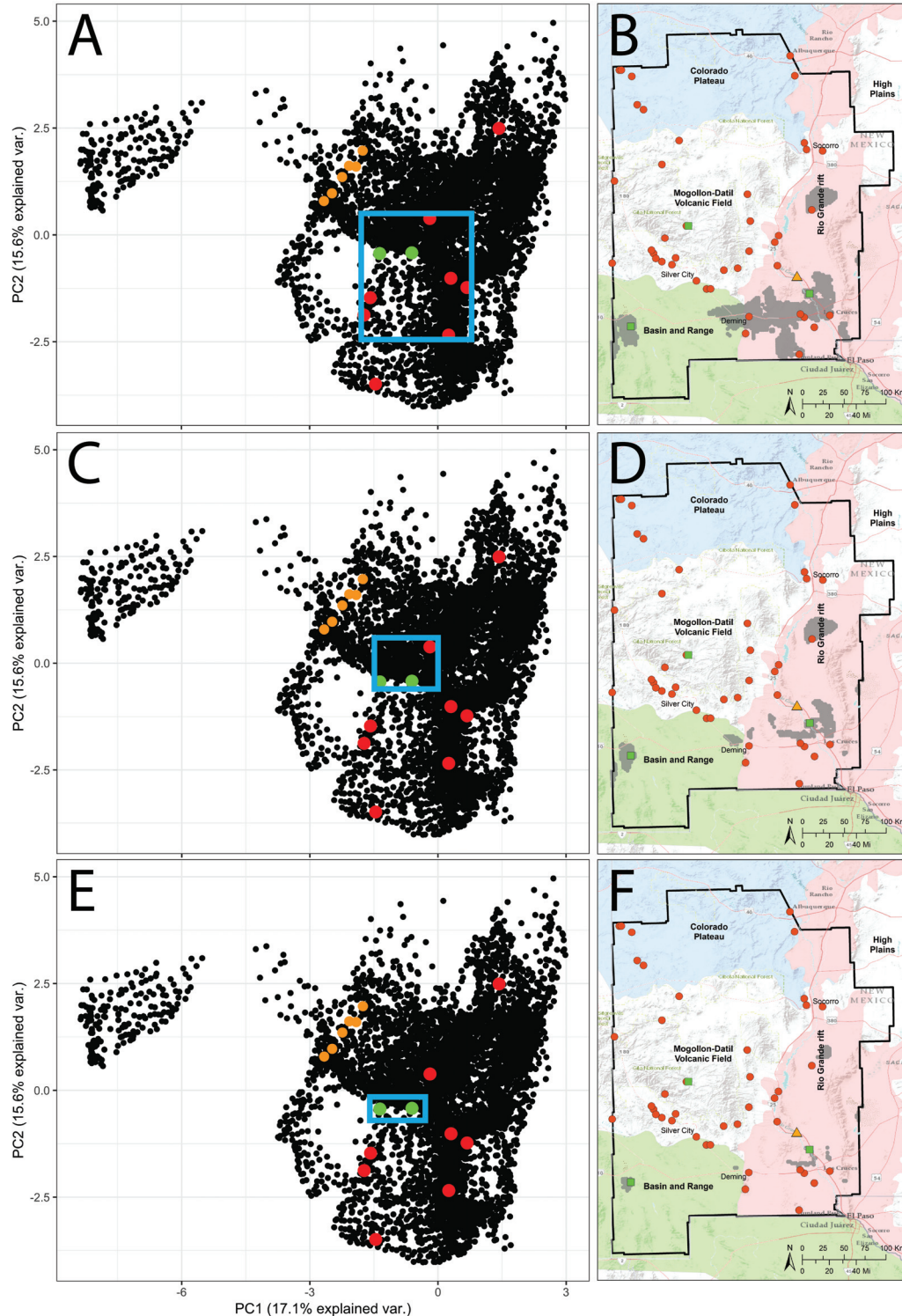


Figure 3.6: PCA results for the cluster one sub-dataset. Locations that underlie 80% of this subset's KGRs (A), underlie the moderate (90 to 150°C) temperature geothermal KGRs and a proximal KGR (C), and directly underlie the two hottest KGRs (E) are selected and plotted spatially in B, D, and F. These select groups are thought to be of higher geothermal potential due to their similarity to KGRs in the study area.

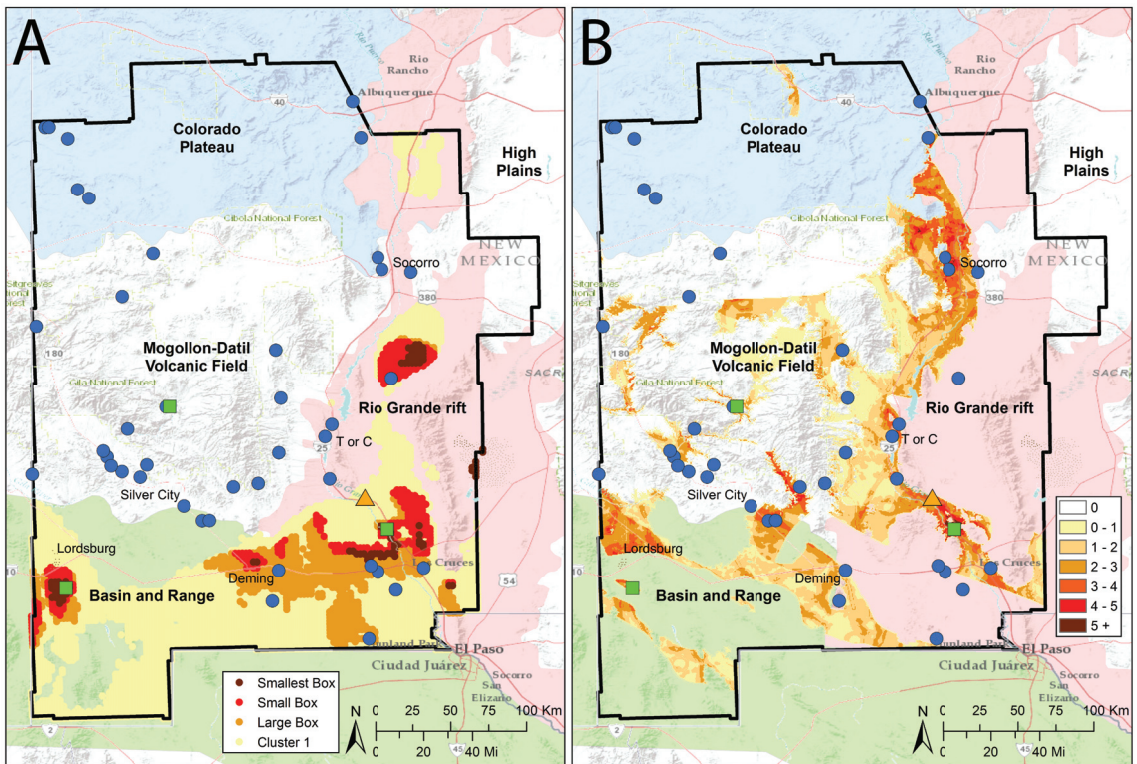


Figure 3.7: Geothermal potential results from this study (A) and prospectivity contours of Bielicki et al. (2015, 2016) for comparison (B). Deeper red colors in (A) denote locations that are most similar to the moderate (90 to 150°C) temperature geothermal KGRs in the cluster one subset and therefore deemed to be of higher geothermal potential. High potential regions are identified by Lordsburg, Deming, Las Cruces, and south of Socorro. These locations are in good agreement with areas outlined by previous researchers (B), despite dramatic differences in methodology. Blue circles = low-temperature (less than 90 °C) KGRs, green squares = moderate (90 to 150°C) temperature KGRs, orange triangle = Rincon KGR, color scale in (B) is for geothermal potential where zero denotes lowest prospectivity and 5+ is greatest.

tration, earthquakes, hydraulic gradient, subcrop geology, and discharge zones. Additionally, a "stripped aquitards", or hydrologic window, layer is used as an exclusionary layer in their analysis to narrow in on regions where hydrologically confining units have been breached or tectonically/erocially stripped away; the overall shape of their prospectivity map is strongly dependent on this layer. We did not include binary variables, such as their hydrologic window layer, in our analysis due to complications and biases that arise when performing PCA on mixed data types; inclusion of this type of data in future maps should be explored however, as these datasets will likely improve the prospectivity results. Despite the differences in methodology, the two maps have similar overall structure and readily apparent localized similarities (Figure 3.7). For instance, both maps argue that the zone surrounding Las Cruces is a very high potential region and that the majority of high potential geothermal targets are in the southern portion of the study area within the Rio Grande rift and Basin and Range provinces. The elevated potential region near Lordsburg and the high potential zone near Deming are also identified in both maps. Our map fails to delineate their zone of high potential near Socorro and Truth or Consequences. This discrepancy is the result of methodology differences, since these areas are well-represented by the secondary permeability KGR cluster (i.e. cluster three) that was set aside to focus on the "classic" forced convection geothermal systems (Figure 3.5C). However, our approach did identify this group of KGRs and therefore these locations as strong geothermal targets for hot-spring type systems. Their map does not include our high potential zone located south of Socorro, although this area is still considered a primary geothermal exploration target due to its similarity to two moderate (90 to 150°C) temperature economically-productive geothermal resources in the study area. Overall, the maps capture similar large-scale trends and compliment each other well, despite stark differences in methodology. The agreement between the maps encourages the idea that this application of PCA and clustering can be a high-quality geothermal exploration tool in complex study areas.

3.3.3 Applicability & Limitations

This use of PCA should be most effective in the preliminary and exploration phases of geothermal resource discovery. The preliminary phase includes a review and analysis of geological, hydrological, thermal, anecdotal, and remote sensing data, with the aim of identifying geologic settings that favor geothermal resources (Harvey & Beardsmore 2014). The KGR analysis techniques applied in this study provide a means to consider many variables concurrently to better understand the physiographic provinces and controls on these systems in a given study area. The exploration phase is more focused on identifying locations that should be targeted for additional data collection. This stage commonly starts out with a broad regional scope that narrows in as data is collected and encouraging sites are identified (Harvey & Beardsmore 2014). The comprehensive dataset analysis techniques employed in this study are ideal for this type of exploration,

in that they are able to locate promising targets of various scales by looking at overlap of unexplored regions with previously discovered geothermal resources. This use of PCA should also aid in the siting of expansion wells at operational geothermal facilities. This could be done by flagging already-drilled wells by their productivity and then doing a localized PCA in which locations that have similar characteristics to highly productive wells could be identified.

As with any prospecting tool, uncertainty remains regarding the accuracy of the identified high potential target areas. While the identification of Rincon and the similarities to the previously-published prospectivity map are encouraging, this methodology should still be validated using an extensive test dataset in a study area that has been well-characterized by subsurface drilling. Our KGR-only analysis ultimately distinguished KGRs predominately by their physiographic/tectonic setting. These settings are well defined and have been extensively studied. Therefore, this result is intuitive and implies that the classification aspect of the methodology is more certain and may readily be applied in other regions to better understand the regional fundamental controlling factors on KGR locations.

This approach suffers from non-uniqueness associated with the selection of variables to include in the analysis, the method of handling outliers, and the employed clustering algorithm. For instance, the earthquake density variable utilized in our study uses a minimum magnitude threshold of two and is dominated by seismicity associated with the Socorro magma body (Figure 3.10). This variable may provide new insight or affect the distribution of clusters if an alternative threshold is used. Removing the seismicity variable all together does not appreciably change the KGR PC1 vs. PC2 biplot, but this is likely a product of the large number of variables considered in this study; analyses that consider fewer variables will be more susceptible to larger sensitivities associated with variable selection and handling. In practice, determining which datasets to include and how to represent them in the analysis will likely going to depend on the types of geothermal systems that are prevalent in the study area. For example, the geothermal systems typically developed in New Mexico are amagmatic forced-convection geothermal systems; prospecting for these types of systems should not be as reliant on datasets that are relevant to magmatic geothermal systems. However, including resources more relevant to magmatic geothermal systems may have a pronounced impact on the results. Therefore, a general understanding of the prominent geothermal controls for a given study area is advised and an adaptive investigatory approach should be taken. The handling of outliers may also have a noticeable impact on results. However, a secondary analysis (not presented) of this dataset that used the more restrictive "outside values" criteria of Tukey (1977) to identify outliers still yielded the same KGR cluster assignments, even though significantly higher proportions of the data were winsorized. Additionally, the implemented k-means clustering algorithm or using a different clustering method entirely (e.g. hierarchical clustering) may alter the results. A significant advancement to our approach would be to employ ensemble techniques, such as Monte Carlo methods, that consider different combinations and representations of variables, outlier criteria, and clustering methods to gain a bet-

ter understanding of these non-uniqueness issues for a given study area and find best-fit solutions. Generally, the approach applied in this study still yields a substantial amount of information regarding the geothermal prospects of the region that agrees well with previous work, while utilizing a relatively straightforward methodology.

3.4 Conclusions & Future Work

In this study, combined use of PCA and k-means clustering has proven to be a valuable tool for classifying known-geothermal resources and identifying locations of elevated geothermal potential within southwest New Mexico. Our work indicates that known-geothermal resource locations are largely controlled by their physiographic/tectonic province. Two primary broad future exploration regions are identified. The first is characterized by secondary permeability parameters such as elevated fault density, seismicity, and fault intersection density. This group includes the Socorro and Truth or Consequences low-temperature hot spring geothermal systems. The second identified future exploration region is associated with variables describing classic forced-convection geothermal systems including high heat flow, depth to basement, silica geothermometer and low crustal thickness and elevation. This region includes the Lightning Dock geothermal binary power station and the Masson Farms geothermal greenhouse facility, which are two of the hottest resources in the study area. Further analyzing this second region suggests that the southeast portion of the study area is most likely to yield new economically-viable geothermal resources. Areas near Lordsburg, Las Cruces, Deming, and south of Socorro are believed to be particularly promising due to their strong relation to higher temperature geothermal resources within the study area. These target areas agree well with the Bielicki et al. (2015, 2016) geothermal prospectivity map of the region.

This use of PCA and clustering is best suited for use during the preliminary and exploration phases of geothermal resource discovery to interpret large amounts of geothermal data. Even though the prospectivity and characterization results discovered here agree well with previous work, this methodology should still be validated in a more controlled manner using an extensive test dataset in a study area that is already very well understood. Our results are non-unique and depend on the variables considered and how those variables are represented. A significant improvement to the methodology would include the incorporation of ensemble approaches, such as Monte Carlo methods, to find best-fit solutions that are more robust to the choice of clustering algorithm, data variables, and handling of outliers. Overall, the valuable geothermal insight provided by using our approach emphasizes the potential that conjunctive use of PCA and clustering has to greatly advance the geothermal industry. The ability of this approach to collectively analyze a large number of variables at the same time over an appreciable area might argue for the collection of additional geophysical and geochemical datasets in an exploration campaign.

Acknowledgments

We thank Matthew Folsom for his contributions to an early version of this work. Funding was provided by National Science Foundation grant EAR 1830172 and EPSCoR Energize New Mexico grant IIA-1301346. Several of the datasets utilized in this study are from Bielicki et al. (2015) and are available at <https://gdr.openei.org/submissions/597>.

3.A Dataset Preparation Processing Steps and Metadata

This appendix presents the final data layers and their associated metadata for all data used in this study. The datasets are divided into spatial density and contoured layers. The spatial density layers estimate the concentration of spatial features within a given region, while contoured layers are interpolated models of measured values.

3.A.1 Extraction Grid

A grid of 2 km spacing was created in ArcGIS that covers the study area. The "Extract Values to Points" ArcGIS tool was used to append underlying data values for all 20 data layers to the grid points. This comprehensive dataset consisting of 24,076 data rows was then exported into a comma-separated values file for use in R (R Core Team 2013).

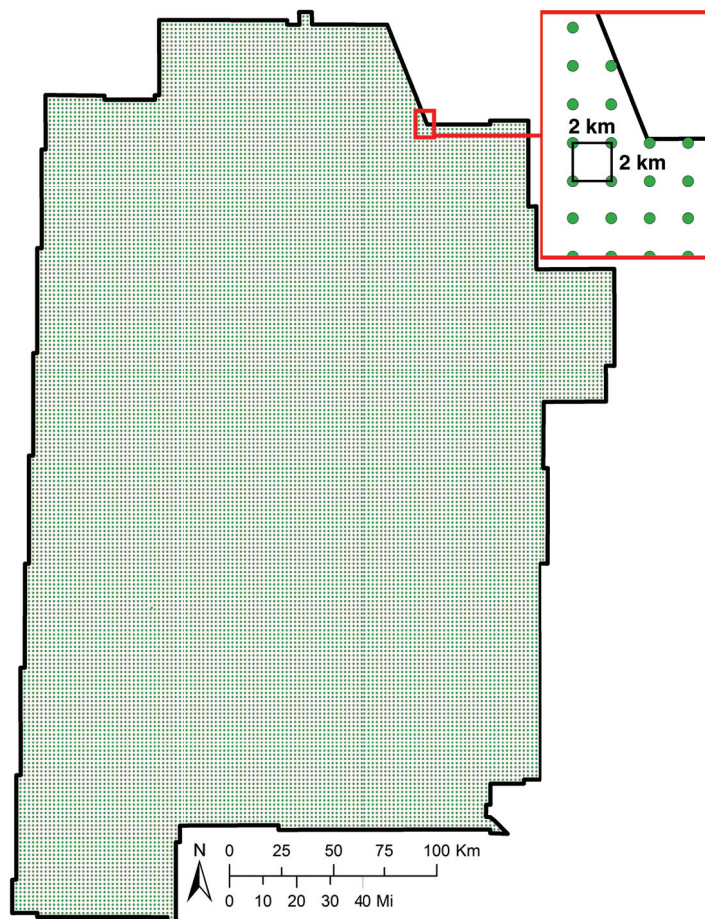


Figure 3.8: Grid used to extract data values for all data layers.

3.A.2 Spatial Density Layers

Drainage Density Construction of this data layer began by downloading the drainage dataset of Bielicki et al. (2015). This layer was qualitatively checked against a digital elevation model of the area to ensure its accuracy. The "Kernel Density" ArcGIS tool was then employed to make the spatial density map by using the geodesic method and a 0.001 cell size; all other settings were left at their default values.

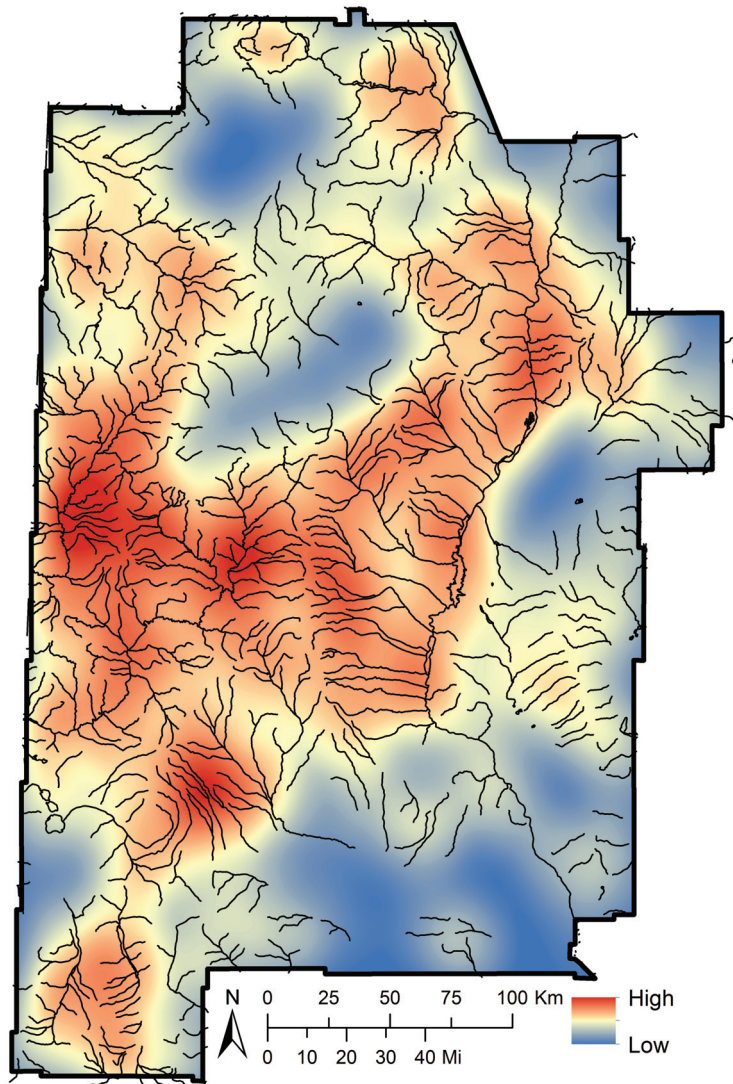


Figure 3.9: Drainage density layer. Black lines = surface water drainages, shaded colors = spatial density.

Earthquake Density An comprehensive New Mexico earthquake catalog spanning 1962 to 2009 was created by combining the data presented in Sanford et al. (2002), Sanford et al. (2006), and Pursely et al. (2013). Earthquake locations recorded in the U.S. Geological Survey's Earthquake Catalog (USGS 2018a) were then added to this dataset for 2010 through 2017, thereby forming the final dataset that spans 1962 to 2017. All earthquakes are those with a magnitude of two or greater. Spatial density of these earthquake locations was then calculated using the "Kernel Density" tool in ArcGIS with the geodesic method and a 0.001 cell size; all other settings were left at their default values.

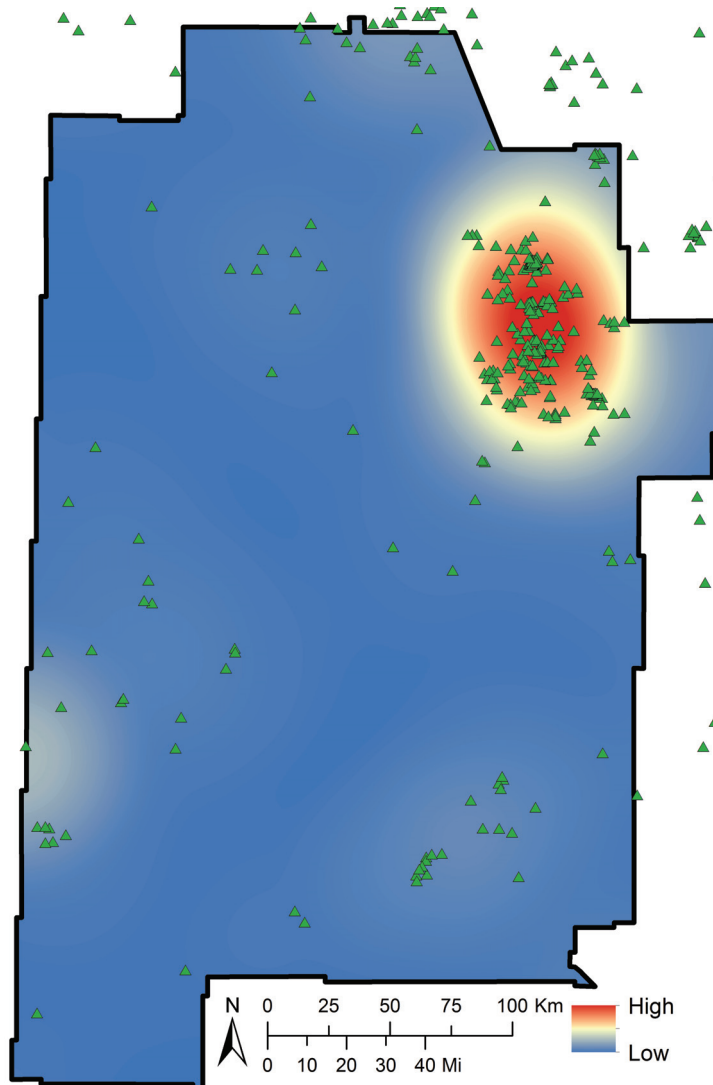


Figure 3.10: Earthquake density data layer. Green triangles are seismic event locations and shaded contours are their spatial density.

Quaternary Fault Density The Quaternary fault layer used in this analysis was provided by Shari Kelley and Andy Jochems of the New Mexico Bureau of Geology and Mineral Resources. The faults digitized are generally those that are mapped at the 1:24,000 scale and show Quaternary displacement. Spatial density was computed using the planar method (geodesic not compatible) of the "Kernel Density" tool in ArcGIS with a cell size of 0.001; defaults were used for all remaining settings.

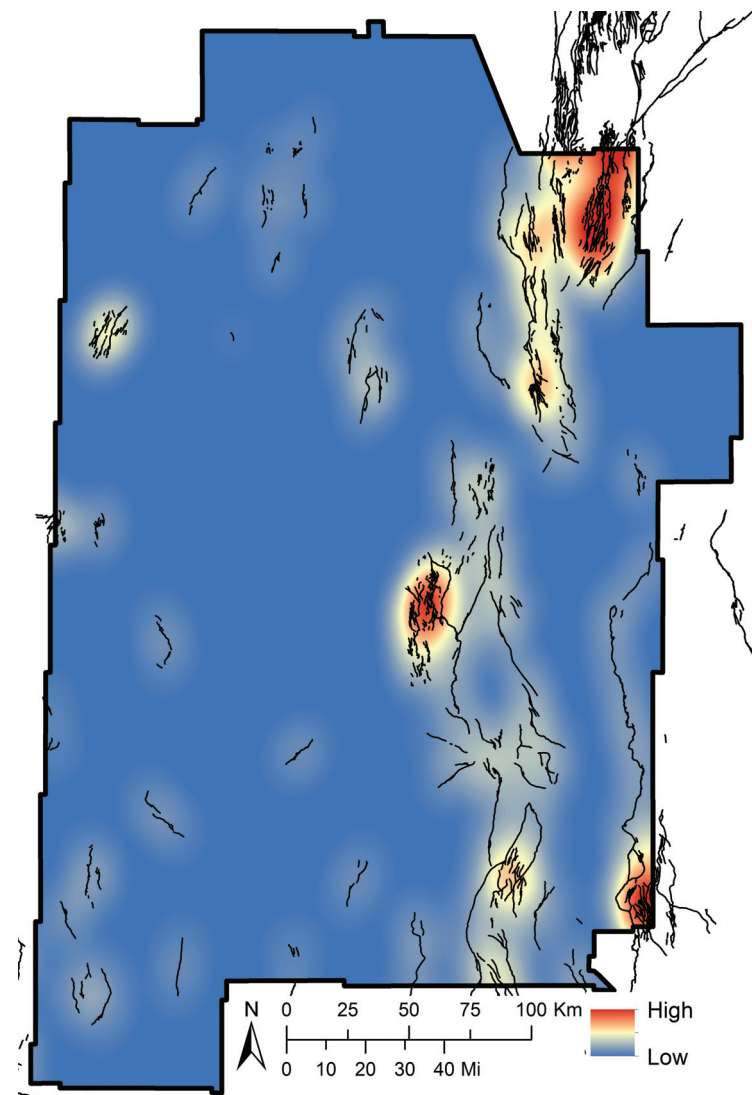


Figure 3.11: Quaternary fault density data layer. Black lines are fault locations and shaded contours are their spatial density.

Quaternary Fault Intersection Density Intersections of Quaternary faults were manually digitized in ArcGIS by using the previously-described 1:24,000 Quaternary fault dataset. The spatial density map was then made using the geodesic method of the "Kernel Density" tool in ArcGIS with a cell size of 0.001 and otherwise default parameters.

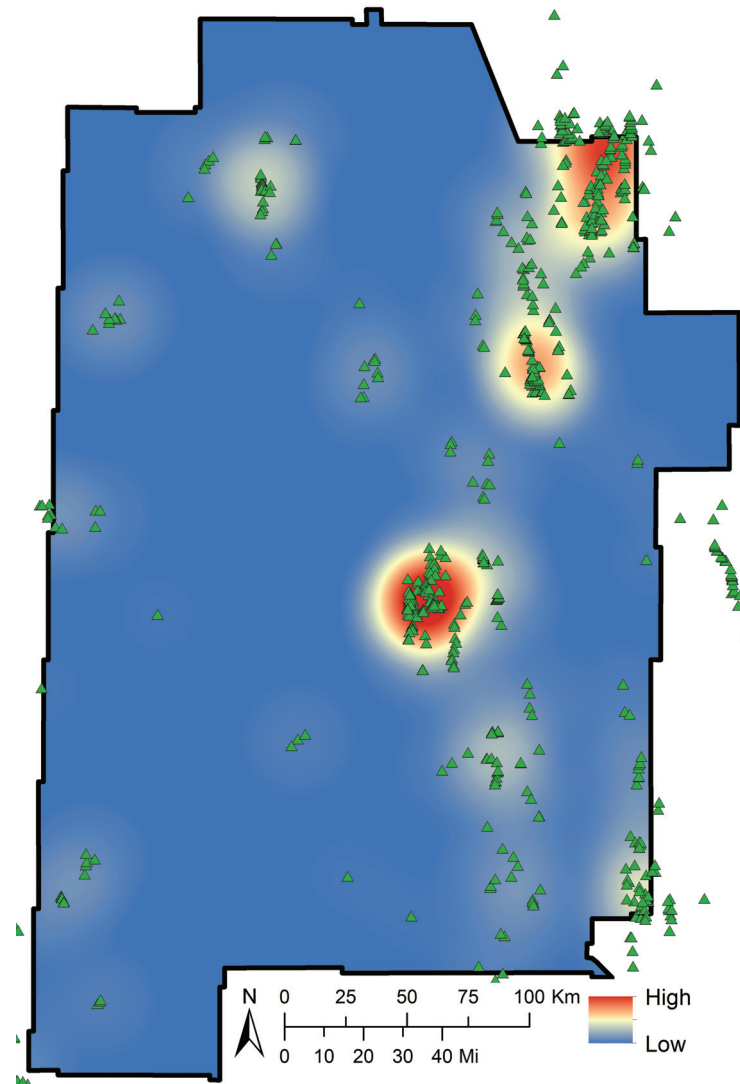


Figure 3.12: Quaternary fault intersection data layer. Green triangles are fault intersections and shaded contours are their spatial density.

Spring Density Groundwater spring locations were provided by Andrew Robertson of the USGS New Mexico Water Science Center that were extracted from the USGS National Water Information System (USGS 2018b). Spatial density of the springs was computed using the "Kernel Density" tool in ArcGIS with the geodesic method, a 0.001 cell size, and defaults for all additional parameters.

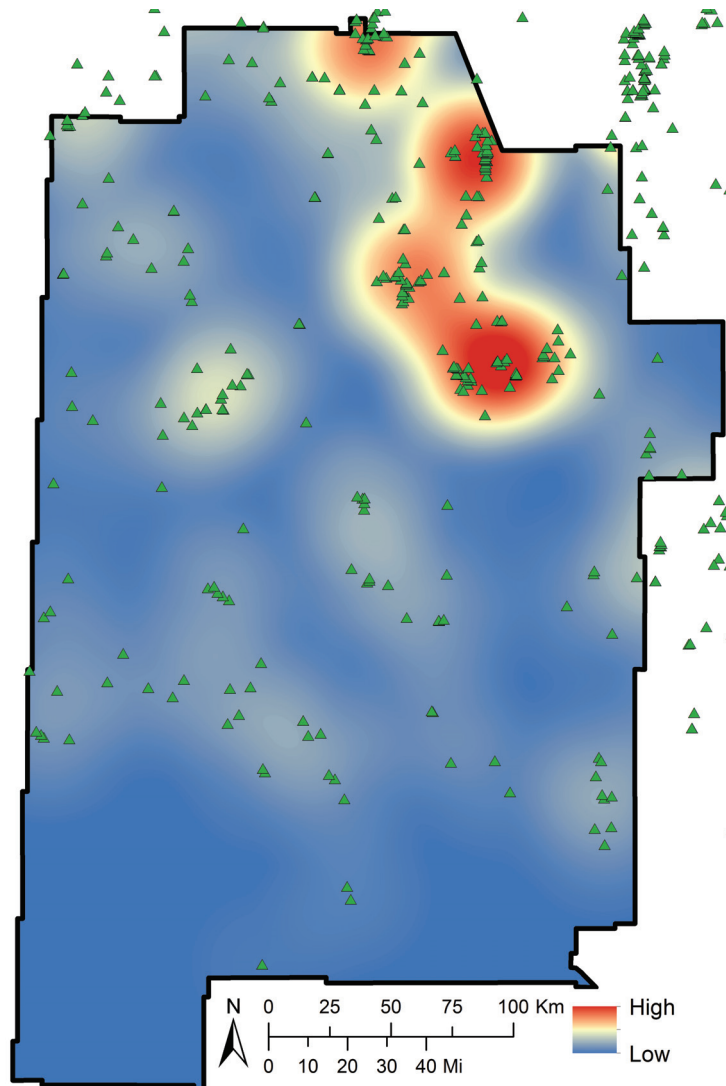


Figure 3.13: Spring density data layer. Green triangles are groundwater springs, while shaded contours are spring density.

State Map Fault Density The “New Mexico Faults” layer was first downloaded from the USGS Energy and Environment in the Rocky Mountain Area Database (USGS 2018c). These faults are those that are presented on the statewide geologic map of New Mexico. The “Kernel Density” tool in ArcGIS was then applied to this layer using the planar method (geodesic not compatible), a 0.001 cell size, and default parameters for all other settings.

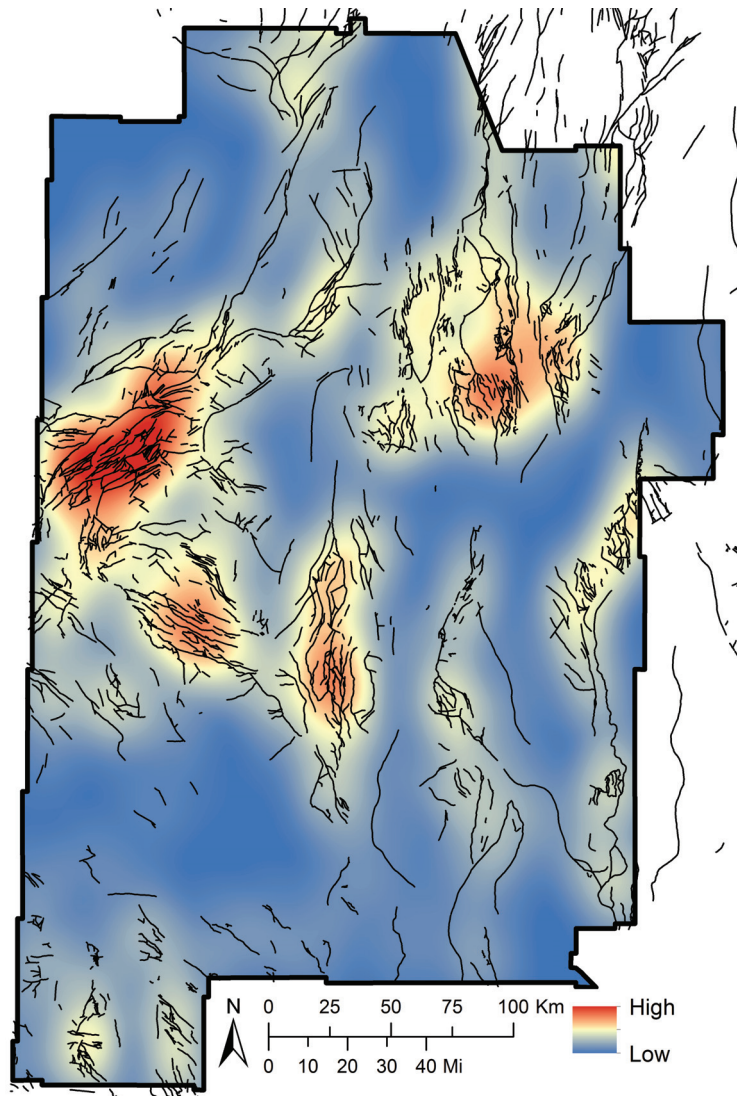


Figure 3.14: State map fault density data layer. Black lines are faults that are presented on the statewide geologic map of New Mexico. Shaded contours are spatial density.

Volcanic Dike Density The “New Mexico Dikes” layer was first downloaded from the USGS Energy and Environment in the Rocky Mountain Area Database (USGS 2018c). These volcanic dikes are those that are included on the statewide geologic map of New Mexico. The “Kernel Density” tool in ArcGIS was then applied to this layer using the planar method (geodesic not compatible), a 0.001 cell size, and default parameters for all other settings.

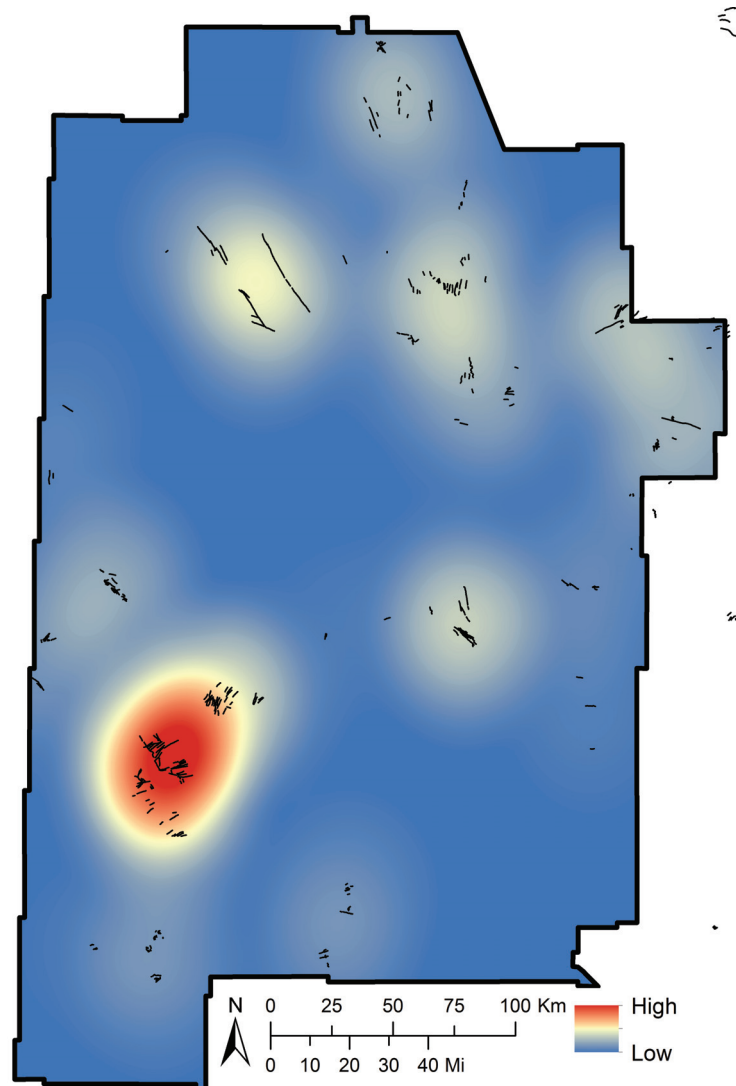


Figure 3.15: Volcanic dike density data layer. Black lines are dikes that are presented on the statewide geologic map of New Mexico. Shaded contours are spatial density.

Volcanic Vent Density The volcanic vent dataset was downloaded from the Earth Data Analysis Center of the University of New Mexico (UNM 2018). This dataset includes volcanic vents that are mapped on the statewide geologic map of New Mexico. The “Kernel Density” tool was then employed in ArcGIS by using the geodesic method, a cell size of 0.001, and default parameters for all other settings.

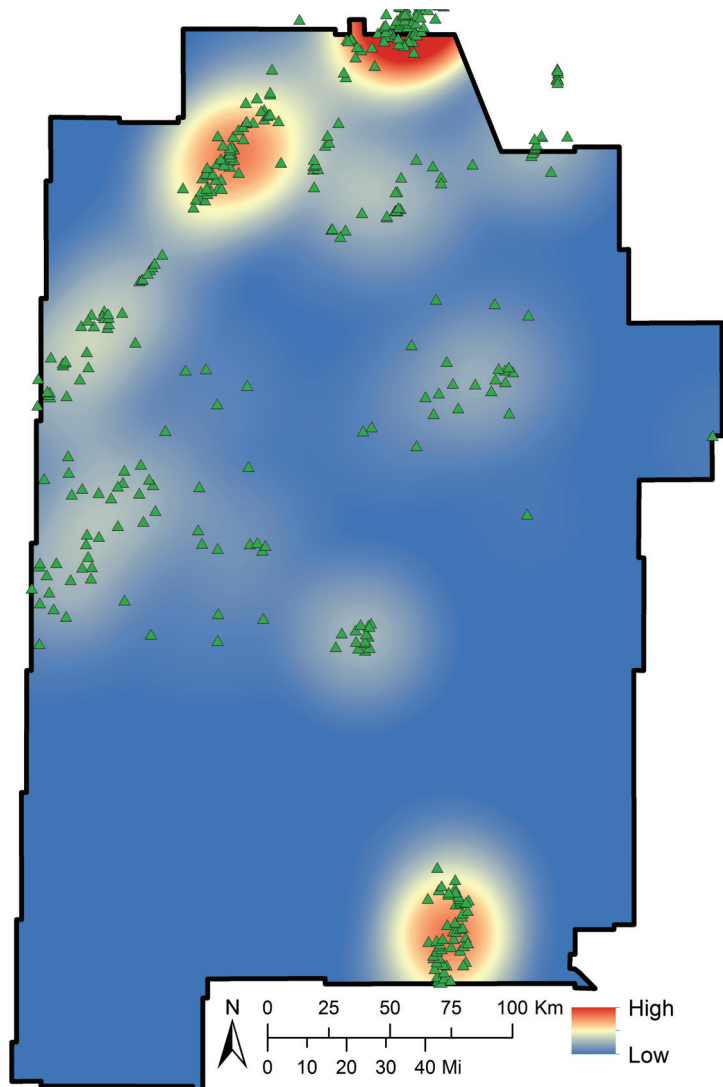


Figure 3.16: Volcanic vent density data layer (UNM 2018). Green triangles = volcanic vents, shaded contours = spatial density.

3.A.3 Contoured Layers

Boron Concentration Boron concentration point data was used from Bielicki et al. (2015). There are multiple data sources included in their study; these were merged into a comprehensive shapefile. Concentrations of zero (<5% of data) were removed so that the dataset could be natural log transformed to make it normally distributed. The data's semivariogram was examined but showed no structure. Inverse-distance weighting interpolation was performed on the transformed dataset using $p = 1$, max neighbors = 16, min neighbors = 1, semi-axis size = 10, and shape = circle; these values were selected after performing a sensitivity analysis in which each parameter was varied until RMS prediction error was minimized. These parameters were further examined by randomly splitting the dataset into 50% test and 50% training data. The training data was then used to interpolate the surface while using the best-fit parameters. Mean prediction errors of the test data were confirmed to equal approximately zero. Taking the exponential of the values in this dataset returns concentrations in mg/L.

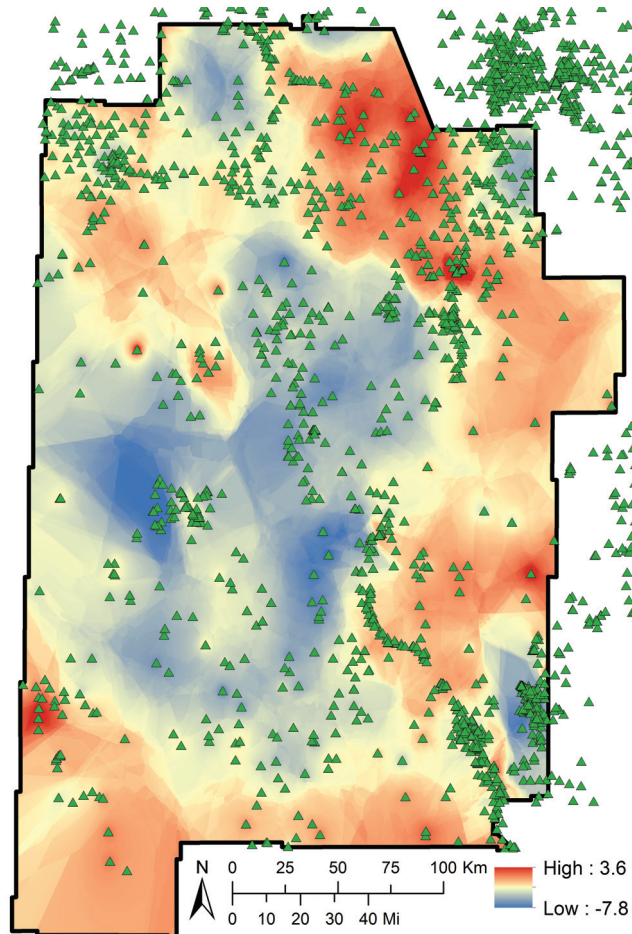


Figure 3.17: Boron concentration data layer in $\ln(\text{ppm})$. Green triangles = data locations.

Crustal Thickness The statewide crustal thickness contours in Figure 4 of Keller et al. (1991) were manually digitized and then rasterized using the "Topo2raster" tool in ArcGIS. The 28, 30, and 32 km contours were extended slightly beyond the New Mexican border prior to rasterization so that the interpolation algorithm would predict a surface that covers the entire study area. This layer is in units of kilometers.

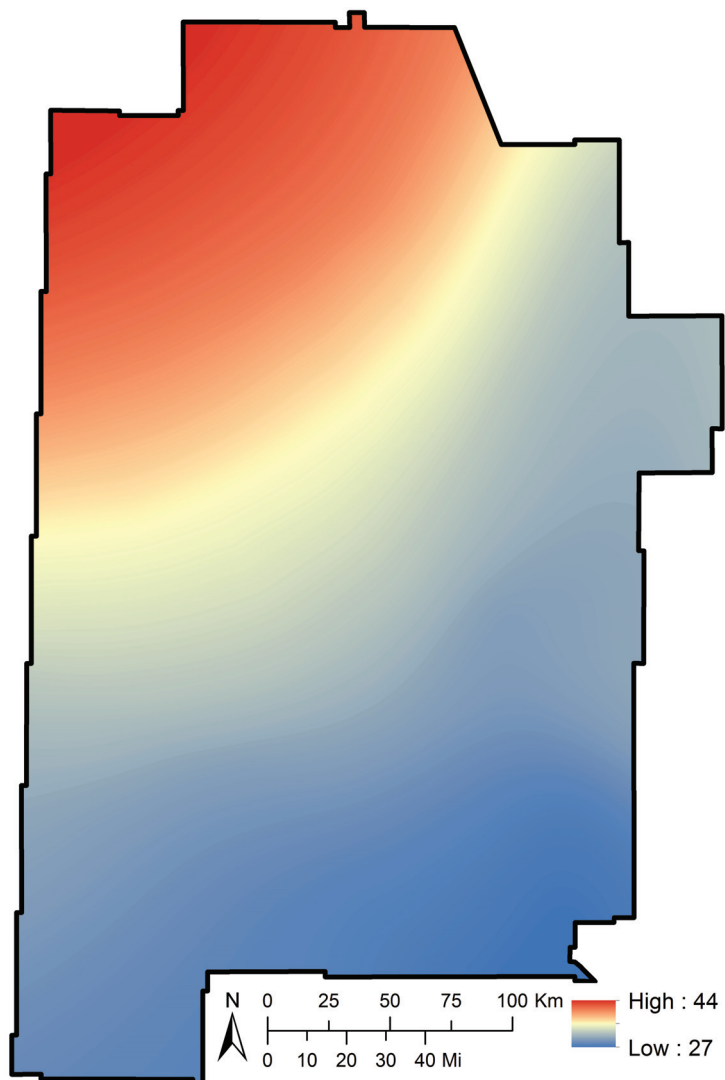


Figure 3.18: Crustal thickness data layer in units of kilometers (after Keller et al. 1991).

Depth to Basement Creation of this data layer began by downloading the basement elevation dataset of Bielicki et al. (2015). The reported values of basement elevation were verified with several basement outcrops in Google Earth for quality assurance purposes. The basement elevation raster was then converted from units of feet to meters using ArcGIS. This raster layer was then subtracted from a 30m digital elevation model to calculate depth to basement in meters below land surface. The smoothing and accuracy for each of these layers differs, thereby resulting in some negative depths. Relative differences are what is most important for the methodology used in this study, so the resulting data layer accuracy was deemed to be adequate despite these artifacts.

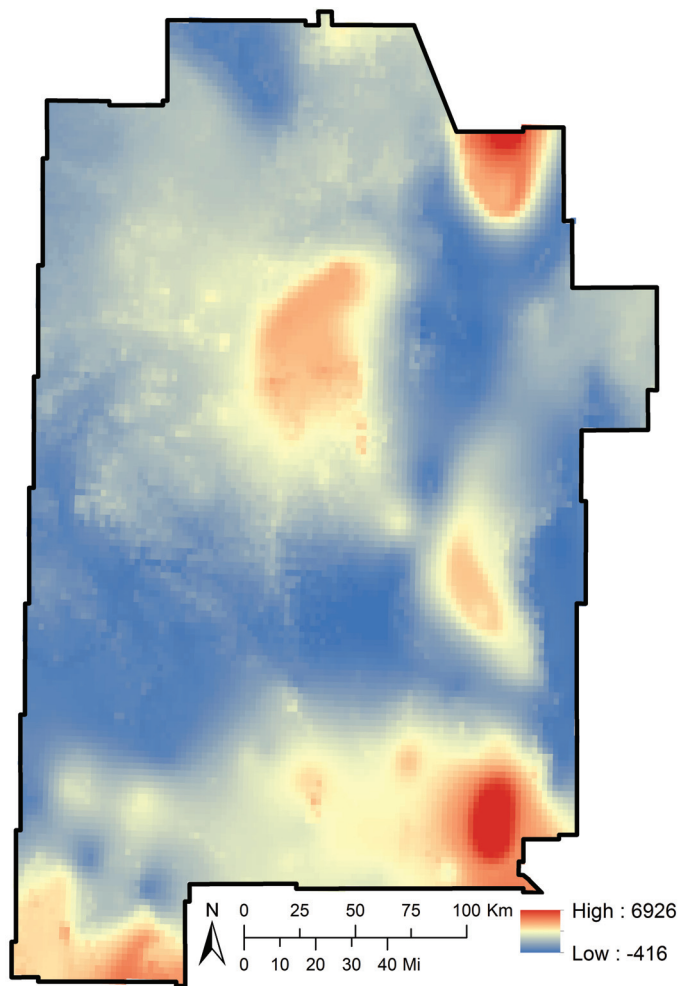


Figure 3.19: Depth to basement data layer in meters below land surface. Negative values are artifacts due to smoothing differences between the digital elevation model and basement elevation layers used to create this layer.

Depth to Water This layer is used as published by Bielicki et al. (2015) and is in units of meters. Negative values occur in some areas, presumably due to differences in the roughness of the digital elevation model and interpolated water table elevation surface used to calculate depth to water.

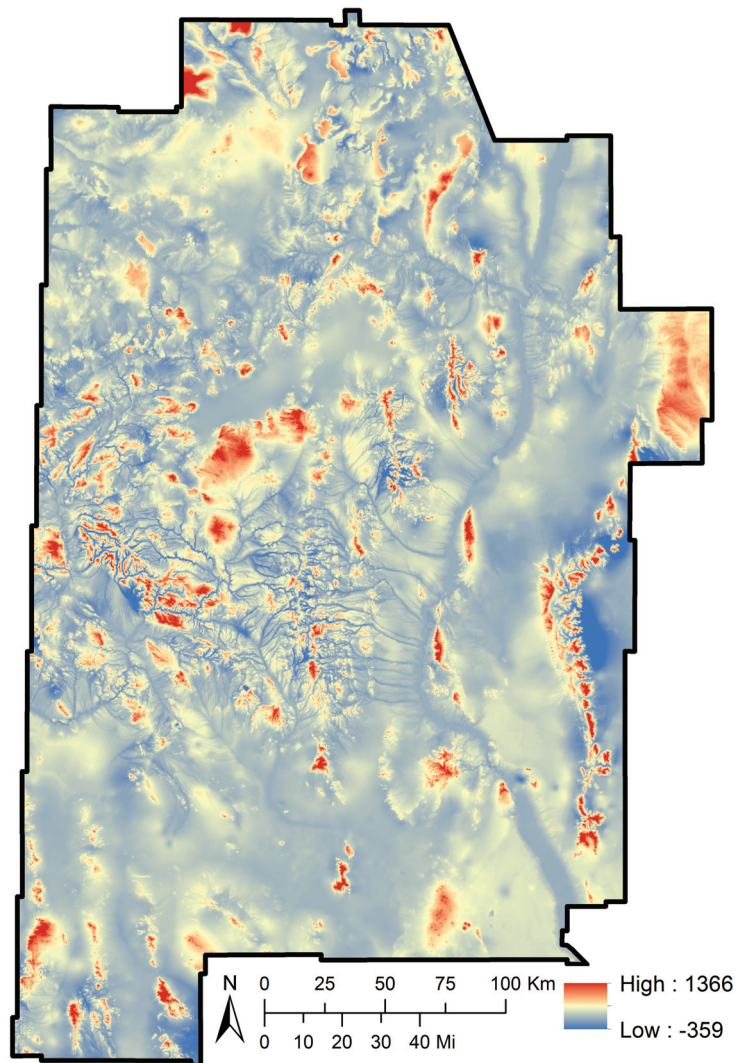


Figure 3.20: Depth to water data layer in units of meters (after Bielicki et al. 2015).

Elevation This 30-meter digital elevation model is used as published by Bielicki et al. (2015) and is in units of meters.

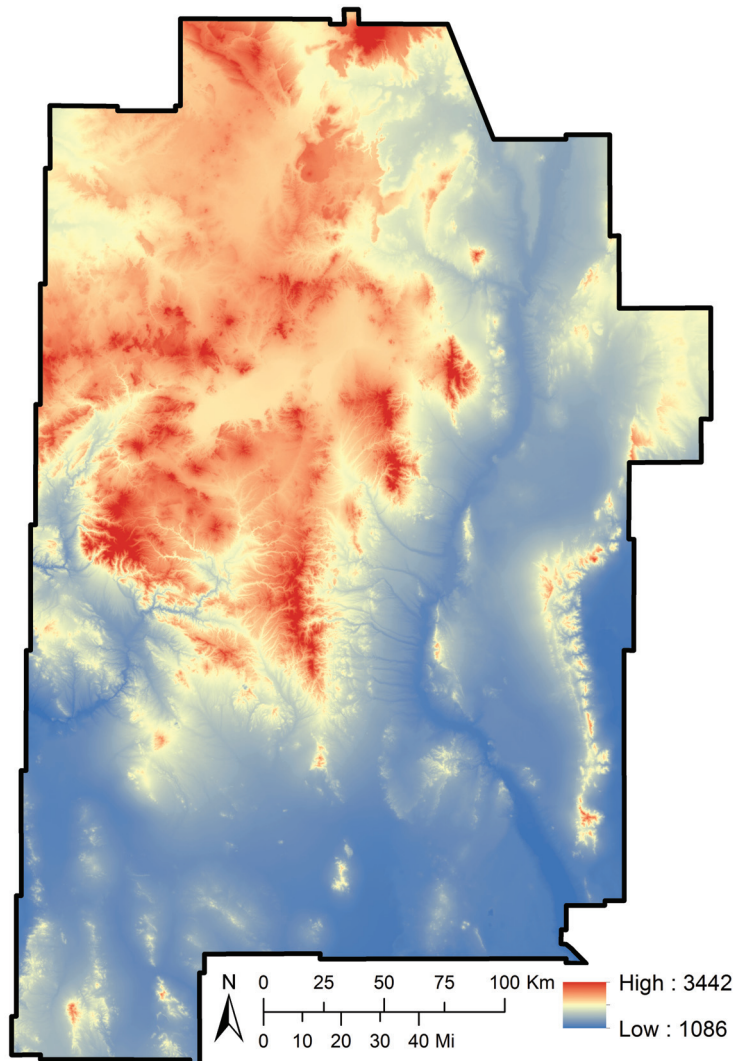


Figure 3.21: Elevation data layer in units of meters (after Bielicki et al. 2015).

Gravity Anomaly This Bouger gravity anomaly map is used as published by Bielicki et al. (2015) and is in units of milligal.

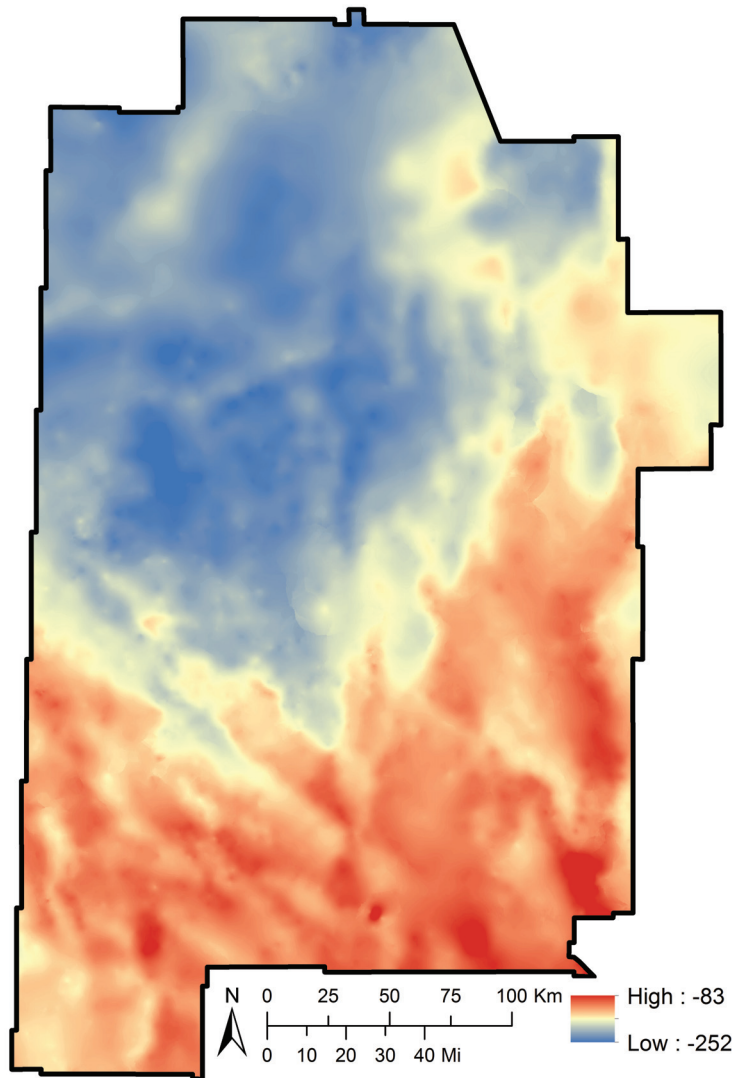


Figure 3.22: Gravity anomaly data layer in units of milligal (after Bielicki et al. 2015).

Heat flow Heat flow point data was used from Bielicki et al. (2015). The dataset was natural log transformed to make it normally distributed. The data's semi-variogram was examined but showed no structure. Inverse-distance weighting interpolation was then performed on the transformed dataset using $p = 1.4$, max neighbors = 13, min neighbors = 1, semi-axis size = 10, and shape = circle; these values were selected after performing a sensitivity analysis in which each parameter was varied until RMS prediction error was minimized. These best-fit parameters were further examined by randomly splitting the dataset into 30% test and 70% training data. The training data was then used to interpolate the surface while using the best-fit parameters. Mean prediction errors of the test data were confirmed to equal approximately zero. Taking the exponential of the values in this dataset returns concentrations in mW/m^2 .

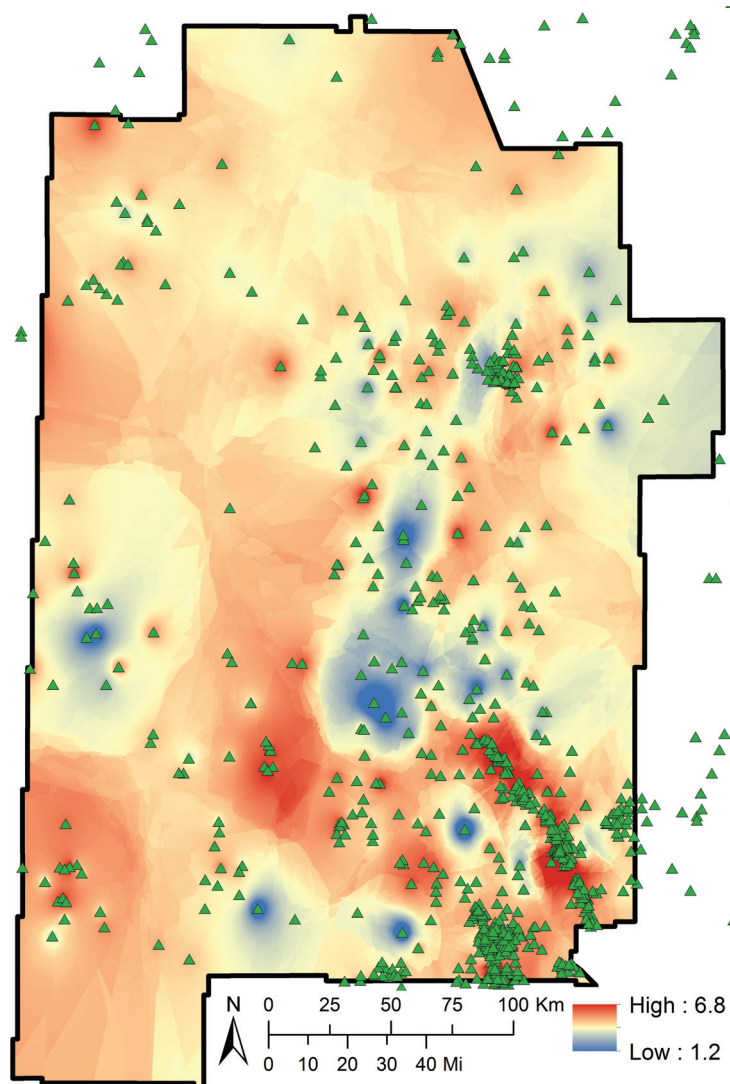


Figure 3.23: Heat flow data layer in units of $\ln(\text{mW/m}^2)$.

Hydraulic Gradient The water table elevation data layer was first acquired from Bielicki et al. (2015). This surface was then used to calculate our gradient map in units of degrees by using the "Slope" tool in ArcGIS.

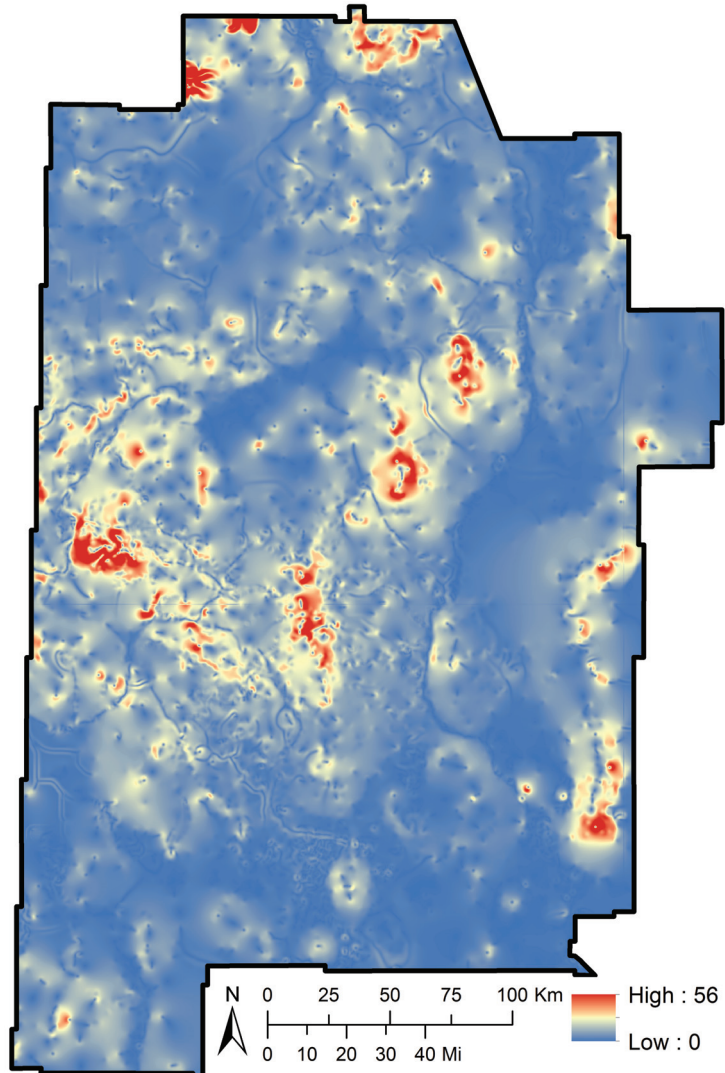


Figure 3.24: Hydraulic gradient layer in units of degrees.

Lithium Concentration Lithium concentration point data was used from Bielicki et al. (2015). There are multiple lithium data sources included in their study; these were all merged into one comprehensive shapefile. Concentrations of zero were changed to 10^{-6} mg/L, the minimum reported concentration, so that the dataset could be natural log transformed to make it normally distributed. The data's semivariogram was examined but showed no structure. Inverse-distance weighting interpolation was then performed on the transformed dataset using $p = 1$, max neighbors = 12, min neighbors = 1, semi-axis size = 10, and shape = circle; these values were selected after performing a sensitivity analysis in which each parameter was varied until RMS prediction error was minimized. These best-fit parameters were further examined by randomly splitting the dataset into 30% test and 70% training data. The training data was then used to interpolate the surface while using the best-fit parameters. Mean prediction errors of the test data were confirmed to equal approximately zero. Taking the exponential of the values in this dataset returns concentrations in mg/L.

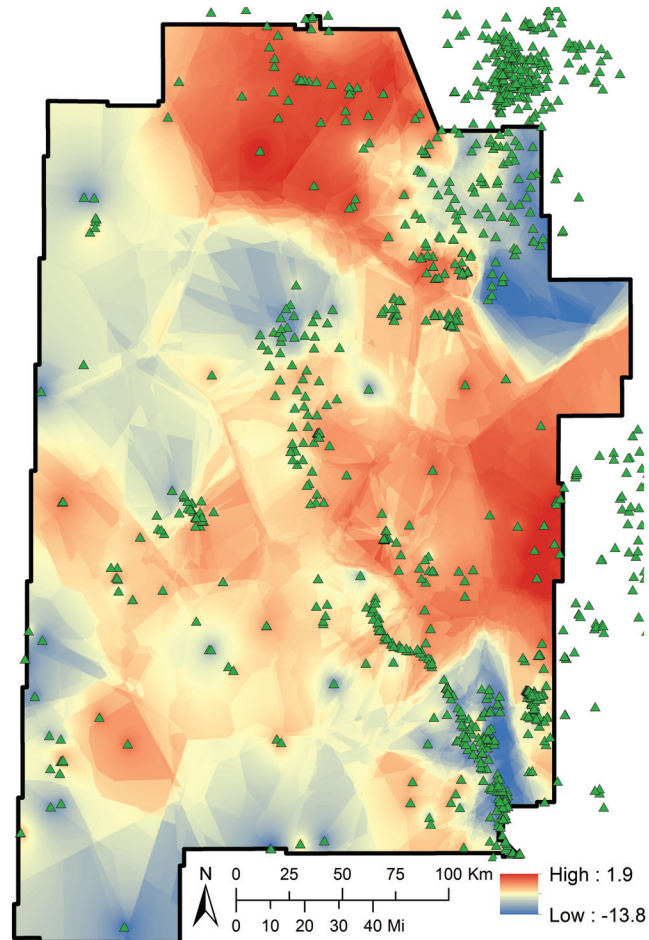


Figure 3.25: Lithium concentration data layer in units of $\ln(\text{ppm})$.

Magnetic Intensity This magnetic intensity map is used as published by Bielicki et al. (2015) and is in units of nanotesla.

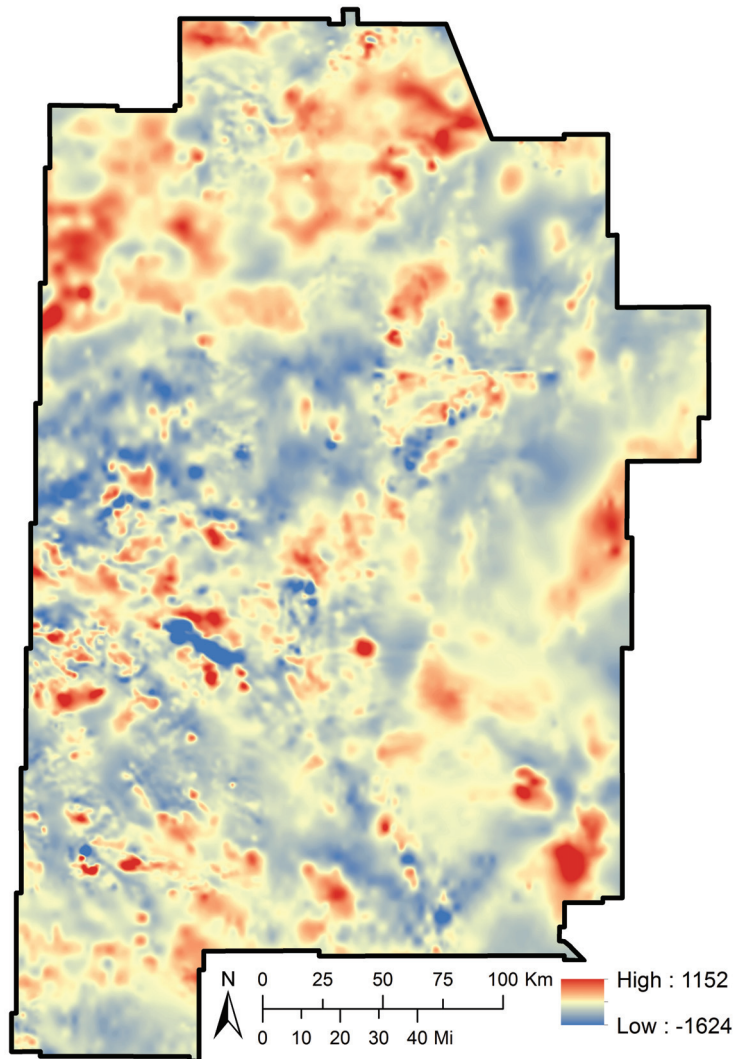


Figure 3.26: Magnetic intensity data layer in units of nanotesla (after Bielicki et al. 2015).

Precipitation This dataset is an 800-meter resolution, 30-year normal annual precipitation map spanning 1981 through 2010; this layer was used as published by PRISM (2012) and is in units of millimeters.

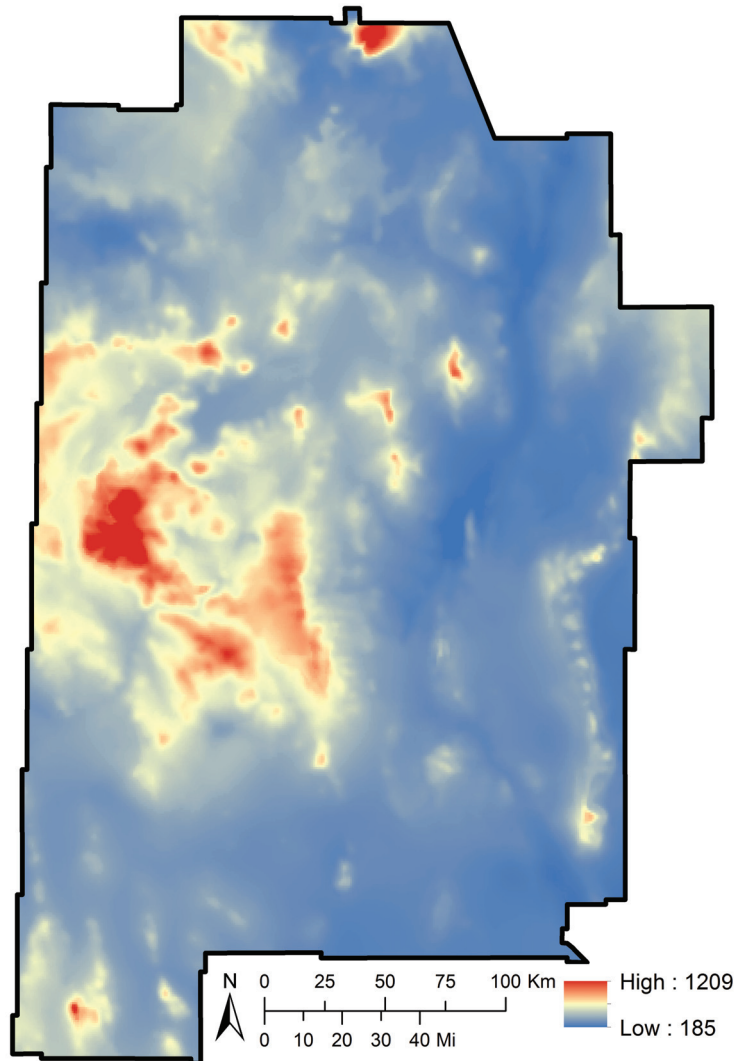


Figure 3.27: Precipitation data layer in units of millimeters (after PRISM 2012).

Silica Geothermometer Temperature Chalcedony geothermometer temperature point data was used from Bielicki et al. (2015). The data's semivariogram was examined and showed structure, but kriging interpolation followed by cross-validation yielded models that contained significant algorithmic artifacts. Inverse-distance weighting interpolation in ArcGIS was then performed using default parameters, as this provided a smooth and representative surface. Predicted residuals were confirmed to have a mean of approximately zero and the map was qualitatively verified to honor the data well. Negative temperature values are the result of low groundwater silica concentrations. While these negative temperatures are physically unrealistic, they still capture the relative differences between areas of high silica concentration and those of low concentrations. The methodology used in this study focuses on these relative differences rather than the magnitudes of input variables; the negative temperatures are therefore not a concern for our purposes. This map is in units of degrees Celsius.

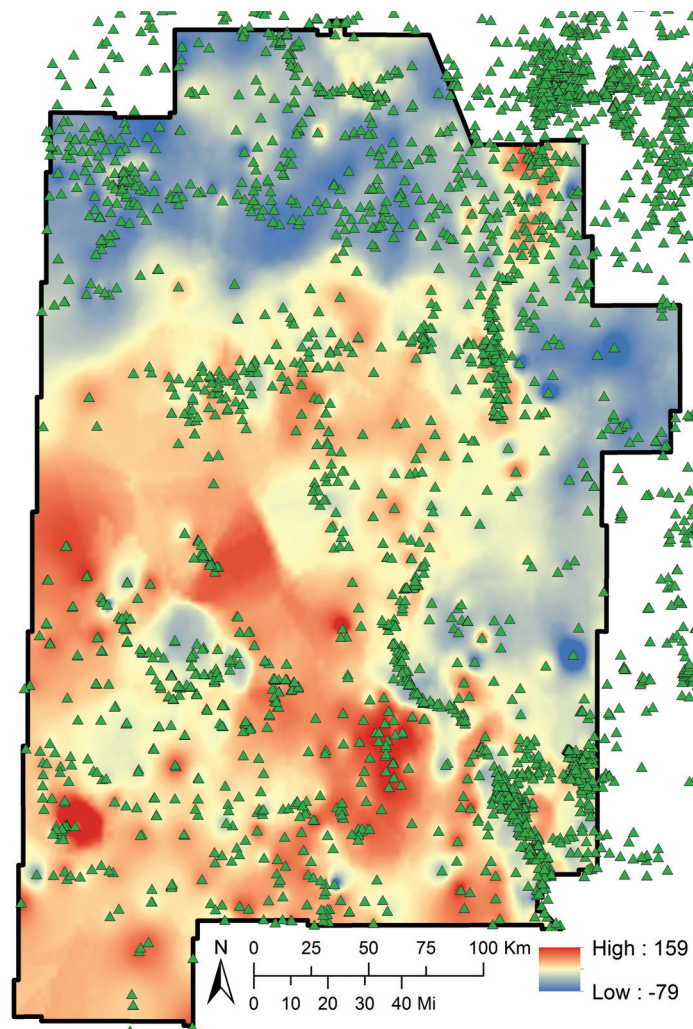


Figure 3.28: Silica geothermometer temperature data layer in degrees Celsius.

3.B Compiled USGS Known-Geothermal Resource Layer

Table 3.3: Compiled USGS known-geothermal resource layer. ID = Generic identification number, Name = USGS provided name, X = easting in NAD83 decimal degrees, Y = northing in NAD83 decimal degrees, Temp. [°C] = Estimated reservoir temperature in degrees Celsius from Reed et al. (1983) and Williams et al. (2008) as reported by the NREL geothermal prospector (NREL 2018), Type = USGS temperature classification, Source Layer = the corresponding layer from the NREL geothermal prospector (NREL 2018). See Section 3.2.1 for details regarding the creation of this layer. Reservoir temperatures are estimated from chemical geothermometers, flow rates, temperature gradients, and geologic setting characteristics by Reed et al. 1983 and Williams et al. 2008)

ID	Name	X	Y	Temp. [°C]	Type	Source Layer
1	Alamos Spring	-107.1320013	35.05997808	22	Low	USGS Isolated Geothermal Systems 90C
2	Allen Springs	-108.361498	32.88537943	26	Low	USGS Isolated Geothermal Systems 90C
3	Apache Tejo Warm Springs well	-108.1288346	32.64342861	53	Low	USGS Isolated Geothermal Systems 90C
4	Aragon Springs	-108.5015179	33.8980584	21	Low	USGS Isolated Geothermal Systems 90C
5	Ash Spring	-108.4086804	32.82013436	22	Low	USGS Isolated Geothermal Systems 90C
6	B. Iorio 1 well	-107.3004828	33.06008651	56	Low	USGS Isolated Geothermal Systems 90C
7	Cliff Warm Spring	-108.6296824	32.97425032	25	Low	USGS Isolated Geothermal Systems 90C
8	Dent windmill well	-108.8341989	34.83836562	23	Low	USGS Isolated Geothermal Systems 90C
9	Derry Warm Springs	-107.2774808	32.79542752	52	Low	USGS Isolated Geothermal Systems 90C
10	Faywood Hot Springs	-107.9954975	32.55479841	75	Low	USGS Isolated Geothermal Systems 90C
11	Federal H 1 well	-107.0304698	31.86012291	80	Low	USGS Isolated Geothermal Systems 90C
12	Freiborn Canyon Spring	-109.0255299	33.70839468	49	Low	USGS Isolated Geothermal Systems 90C
13	Garton well	-107.6954912	32.7700933	67	Low	USGS Isolated Geothermal Systems 90C
14	Gila Hot Springs	-108.2379968	33.23532887	65	Low	USGS Identified Delineate Area Low Temp 90C
15	Gila Hot Springs	-108.2333776	33.23335195	100	Moderate	USGS Identified Hydrothermal
16	Goat Camp Spring	-109.0468227	32.82881514	21	Low	USGS Isolated Geothermal Systems 90C
17	Jerry well	-108.70786	34.47287558	24	Low	USGS Isolated Geothermal Systems 90C
18	Kennecott Warm Springs well	-108.027165	32.56176475	72	Low	USGS Isolated Geothermal Systems 90C
19	Laguna Pueblo	-107.0884494	34.83616034	30	Low	USGS Identified Delineate Area Low Temp 90C
20	Lightning Dock	-108.8318216	32.14839123	130	Moderate	USGS Identified Hydrothermal
21	Los Alturas Estates	-106.7054638	32.28011145	88	Low	USGS Isolated Geothermal Systems 90C
22	Mangas Springs	-108.5116787	32.84308792	27	Low	USGS Isolated Geothermal Systems 90C
23	Mimbres Hot Springs	-107.8371613	32.74842671	78	Low	USGS Isolated Geothermal Systems 90C
24	Ojitos Springs	-106.98269	34.11672	21	Low	USGS Isolated Geothermal Systems 90C
25	Ojo Caliente	-107.5936768	33.5738481	28	Low	USGS Isolated Geothermal Systems 90C
26	Ojo De las Canas	-106.778669	34.0310306	26	Low	USGS Isolated Geothermal Systems 90C
27	Pueblo windmill well	-108.7776956	34.5400402	34	Low	USGS Isolated Geothermal Systems 90C
28	Radium Hot Springs	-106.9251093	32.50011372	90	Moderate	USGS Identified Hydrothermal
29	Rainbow Spring	-108.9510357	34.91052995	36	Low	USGS Isolated Geothermal Systems 90C
30	Riverside Store well	-108.6005147	32.93008504	70	Low	USGS Isolated Geothermal Systems 90C
31	Sacred Spring	-108.9593692	34.90836329	21	Low	USGS Isolated Geothermal Systems 90C
32	Socorro Canyon	-106.9467942	34.05771634	50	Low	USGS Identified Delineate Area Low Temp 90C
33	Spring	-107.5804893	32.95308848	90	Low	USGS Isolated Geothermal Systems 90C
34	Spring Canyon Warm Spring	-108.583814	32.876787	50	Low	USGS Isolated Geothermal Systems 90C
35	Truth or Consequences spring	-107.2538154	33.13508457	117	Low	USGS Isolated Geothermal Systems 90C
36	Turkey Creek Spring	-108.4835128	33.10808042	74	Low	USGS Isolated Geothermal Systems 90C
37	Victoria Land and Cattle Co. well	-106.9004746	33.40007849	34	Low	USGS Isolated Geothermal Systems 90C
38	Warm Springs	-107.5634907	33.2790793	31	Low	USGS Isolated Geothermal Systems 90C
39	Well 1	-108.3195149	34.15805219	22	Low	USGS Isolated Geothermal Systems 90C
40	Well 2	-107.0204717	32.28011029	32	Low	USGS Isolated Geothermal Systems 90C
41	Well 3	-107.6104853	32.08011405	36	Low	USGS Isolated Geothermal Systems 90C
42	Well 4	-106.9768037	32.25511119	73	Low	USGS Isolated Geothermal Systems 90C
43	Well 5	-106.8704672	32.14011503	75	Low	USGS Isolated Geothermal Systems 90C
44	Well south of Carne	-107.5809855	32.25344229	92	Low	USGS Isolated Geothermal Systems 90C

3.C Correlation Heatmaps for Known Geothermal Resources

This section includes pre- and post-winsorized KGR Pearson correlation (Benesty et al. 2009) heatmaps. Any differences emphasize the importance of addressing outliers prior to performing PCA, since these abnormal values can bias correlations.

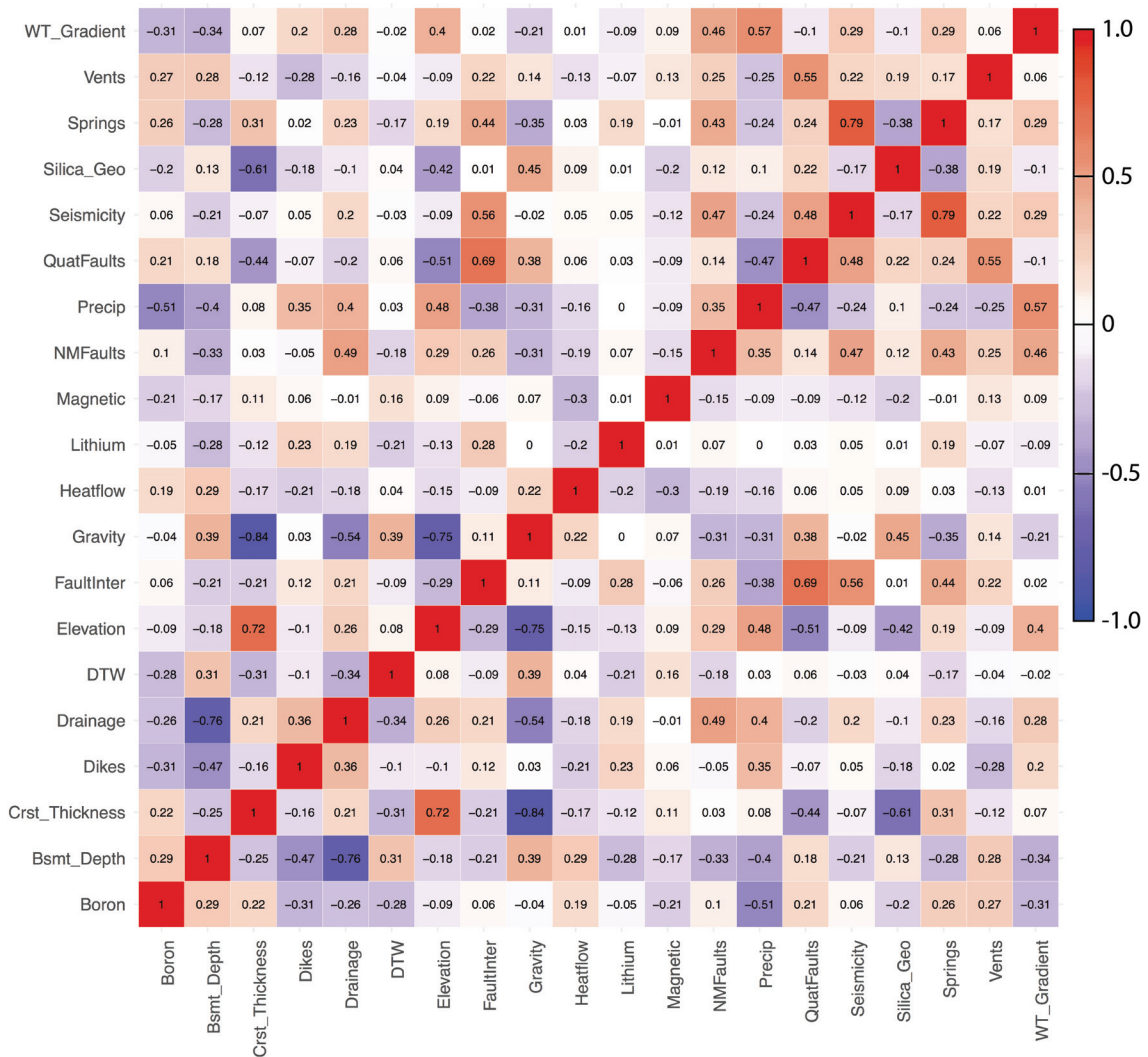


Figure 3.29: Known-geothermal resource Pearson correlation heatmap before winsorization.

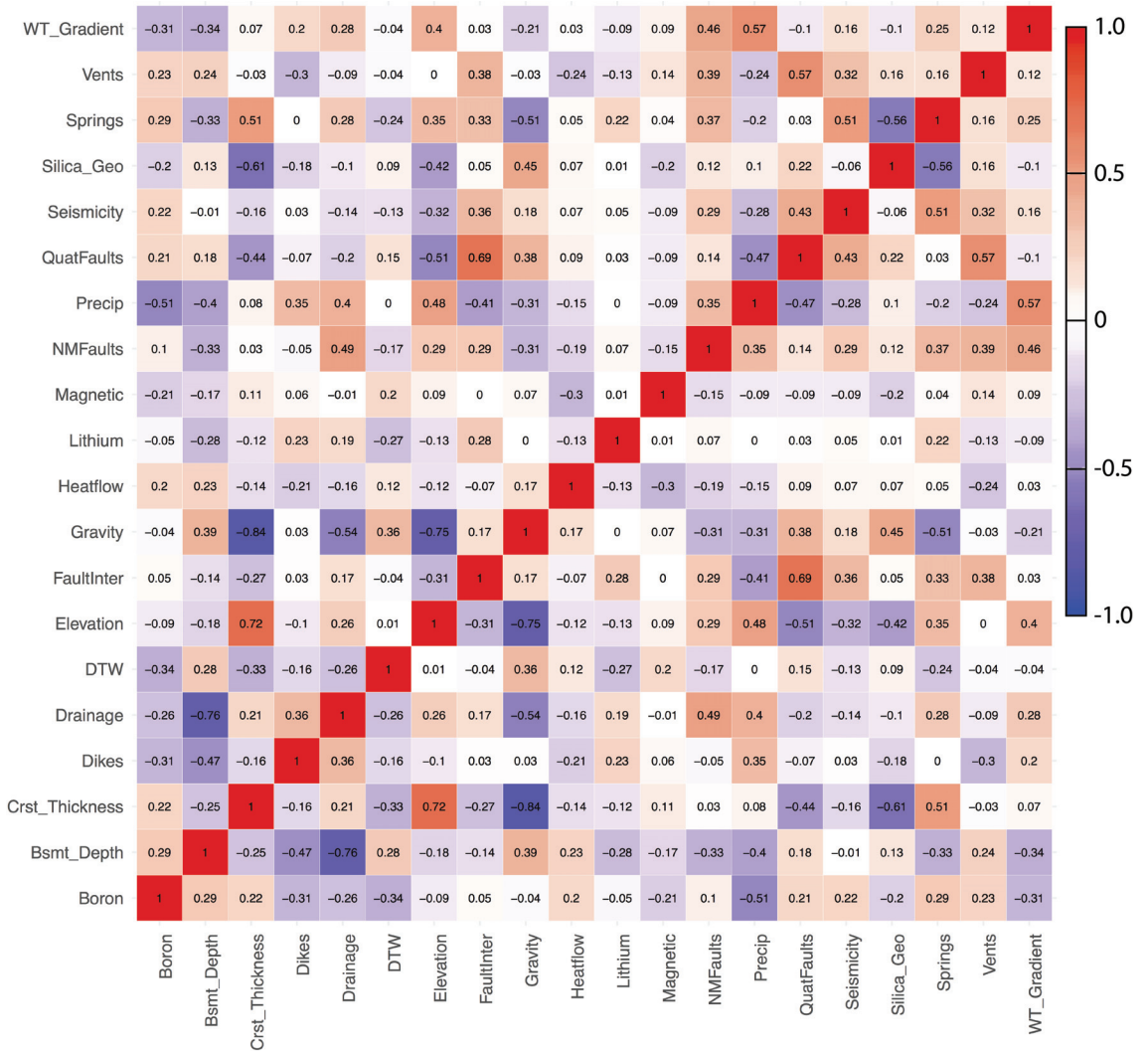


Figure 3.30: Known-geothermal resource Pearson correlation heatmap after winsorization.

3.D Additional Known Geothermal Resource Analysis Biplots

This section includes additional clustered biplots resulting from the known-geothermal resource PCA. These plots were utilized, in addition to Figure 3.3A, when formulating the interpretations presented in Table 3.2. These biplots can aid in understanding the underlying characteristics of each KGR cluster. This is done by observing the variable vectors that extend from the origin of each biplot and their relation to each cluster. Larger vectors have a higher influence on data point position relative to shorter vectors. The arrowhead on each vector corresponds to high values of that particular variable. Table 3.2 summarizes the KGR cluster characteristics.

Variable abbreviations: Bsmt_Depth = Depth to basement, DTW = Depth to water, Precip = Precipitation, Silica Geo = Silica geothermometry temperature, WT_Gradient = Water-table gradient.

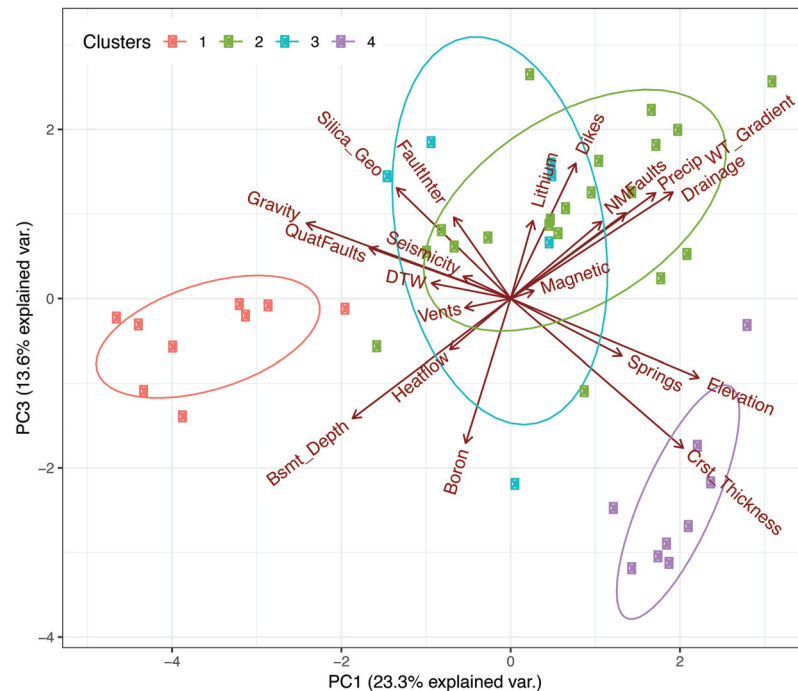


Figure 3.31: PC1 vs. PC3 KGR biplot.

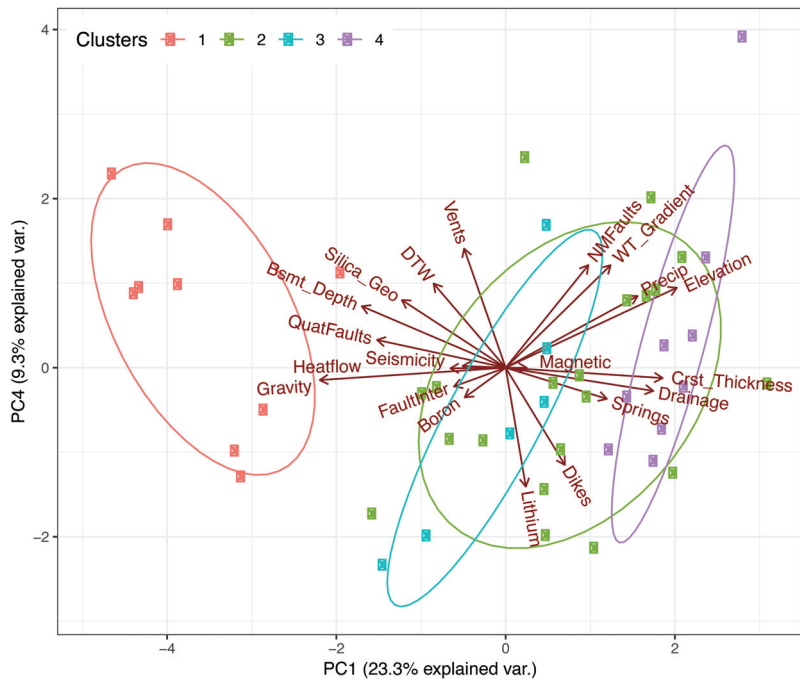


Figure 3.32: PC1 vs. PC4 KGR biplot.

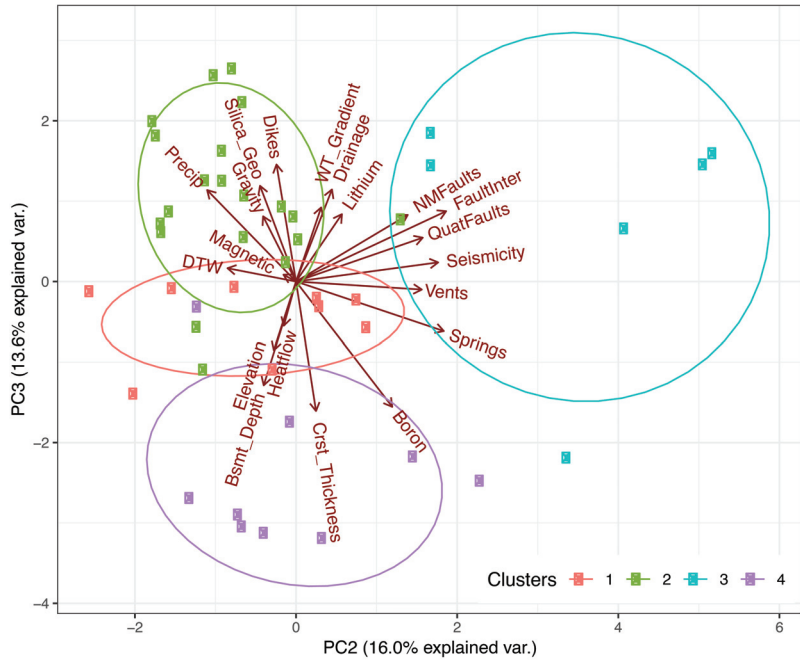


Figure 3.33: PC2 vs. PC3 KGR biplot.

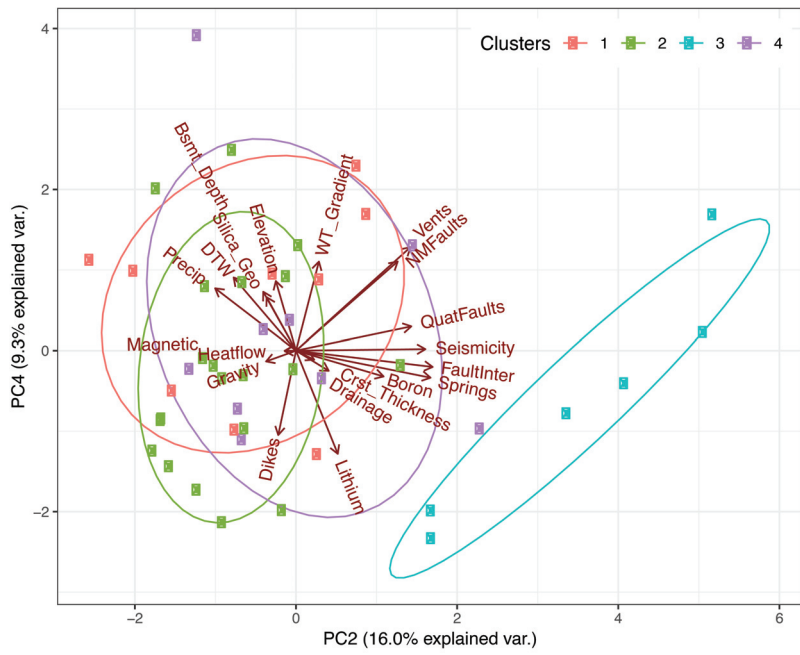


Figure 3.34: PC2 vs. PC4 KGR biplot.

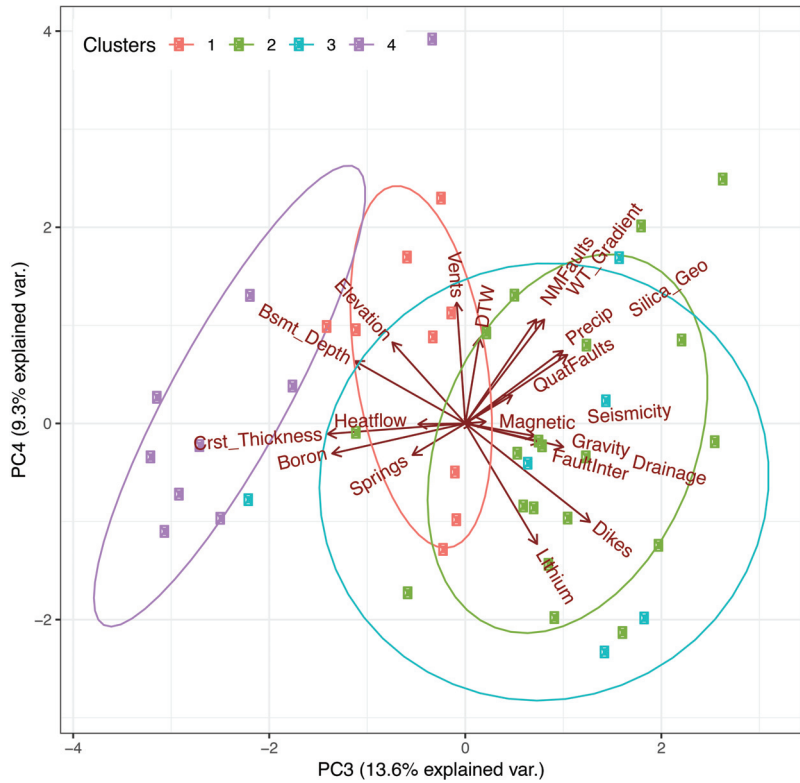


Figure 3.35: PC3 vs. PC4 KGR biplot.

3.E Winsorization Summary

When doing PCA, outliers need to be addressed in a way that they do not skew the analysis; this is typically done by removing or winsorizing the outliers (Ghosh & Vogt 2012). Winsorizing entails adjusting the value of an outlier to a less extreme, but still abnormal, value so that it is a diluted version of itself. Table 3.3 summarizes the percentage of data values that required winsorization during the various phases of our approach.

Table 3.4: Percentage of each dataset that is affected by winsorizing in all three phases of the study. KGR analysis = Analysis of KGR locations only, Comprehensive = Projection of all data points onto KGR biplot, Localized PCA = PCA on the cluster 1 subset only. The low column denotes the percentage of data during a given phase that was identified as a low-value outlier using the "far out" point criteria described in the methods. These values were winsorized to the low threshold. The high column indicates the same information except it refers to values exceeding the high threshold, while the total column is the sum of the low and high columns.

Variable	KGR Analysis			Comprehensive			Localized PCA		
	Low	High	Total	Low	High	Total	Low	High	Total
Boron Concentration	0	0	0	0	0	0	0	0	0
Crustal Thickness	0	0	0	1	0	1	0	2	2
Depth to Basement	0	0	0	1	1	2	0	0	0
Depth to Water	0	2	2	4	13	18	0	1	1
Drainage Density	0	0	0	2	2	4	0	0	0
Earthquake Density	0	9	9	3	14	17	0	7	7
Elevation	0	0	0	3	17	20	0	0	0
Gravity Anomaly	0	0	0	15	1	15	2	0	2
Heat Flow	0	2	2	2	0	2	1	0	1
Hydraulic Gradient	0	0	0	4	2	7	0	1	1
Lithium Concentration	0	0	0	1	11	12	0	0	0
Magnetic Intensity	0	0	0	1	1	2	0	1	1
Precipitation	0	0	0	5	6	11	0	1	1
Q. Fault Density	0	0	0	0	3	3	0	5	5
Q. Fault Intersections	0	11	11	0	5	5	0	4	4
Silica Geothermometry	0	0	0	4	0	4	0	0	0
Spring Density	0	9	9	0	7	7	0	1	1
State Map Fault Density	0	0	0	0	1	1	0	0	0
Volcanic Dike Density	0	0	0	0	2	2	0	1	1
Volcanic Vent Density	0	2	2	0	17	17	0	17	17

3.F KGR Scatter Plots and Correlations of Data Layers with Estimated Reservoir Temperature

Additional insight on the controls of known geothermal resources (KGRs) within the study area may be gained by evaluating correlations and constructing scatter plots of data layer variables against estimated reservoir temperatures. Reed et al. (1983) and Williams et al. (2008) interpreted chemical geothermometers, groundwater flow rates, temperature gradients, and geologic provinces (e.g. Basin and Range, Rio Grande rift) to estimate reservoir temperatures for each KGR used in this study. These reservoir temperatures are used as reported in the KGR source layers from the U.S. Department of Energy National Renewable Energy Laboratory Geothermal Prospector tool (NREL 2018; Appendix 3.B). Estimating reservoir temperatures is challenging in absence of comprehensive drilling. Chemical geothermometers are typically relied upon, but are subject to large uncertainties and their associated assumptions can often be violated (Fournier 1989, Karingithi 2009). Therefore, the reservoir temperature estimates that are analyzed herein are considered highly-uncertain, first-order approximations of subsurface conditions. Despite their uncertainty, using these estimates is preferred over temperature measurements in wells or hot springs, since the latter are strongly influenced by measurement conditions (e.g. well depth, spring discharge rate) and do not make any attempt to take conductive cooling of the measured waters into account. Potential outliers in the data variables have not been removed or altered in any way during this analysis (i.e. pre-winsorization).

Table 3.5 presents the Pearson correlation (Benesty et al. 2009) between estimated reservoir temperatures and all data layers considered in this study. Variables with the most pronounced correlations are plotted against reservoir temperature in Figure 3.36. Silica geothermometer temperature (0.69), gravity anomaly (0.45), heat flow (0.23), Quaternary fault density (0.23), and depth to basement (0.15) have the highest positive correlations to reservoir temperature. The rather strong positive correlation with silica geothermometer temperature is anticipated, since chemical geothermometers are used in the derivation of the reservoir temperature estimates. The highest gravity anomalies in the study area are located within the Rio Grande rift and Basin and Range physiographic provinces (Figure 3.22). The overall spatial distribution of gravitational highs corresponds very well with our KGR cluster 1 distribution, which we found to represent the most promising exploration target (Figure 3.5A, 3.7). Therefore, the positive correlation between temperature and gravity anomaly is encouraging and suggests that deep groundwater circulation within thick alluvial basins is an important control on the hottest KGRs. This notion is further emphasized by the positive correlation of temperature with depth to basement, although this correlation is not as pronounced since some of the hottest reservoir temperatures are also found in regions of shallow basement (e.g. Truth or Consequences). Previous work has linked these shallow depth-to-basement resources with deep circulation within highly-fractured basement rocks (Mailloux et al. 1999, Pepin et al. 2015). The positive correlation of Quaternary fault density with reservoir temperature is further evidence that young faulting plays an important role in providing

avenues for geothermal fluids to ascend to the shallow subsurface.

Crustal thickness (-0.53), elevation (-0.47), groundwater spring density (-0.38), earthquake density (-0.21), and hydraulic gradient (-0.19) have the highest negative correlations with reservoir temperature. The correlation between high temperatures with low crustal thickness and low elevation both support the argument that the hottest resources in the study area are classic forced convection systems that result from deep groundwater circulation. The linkage with low hydraulic gradient, in addition to low elevation, indicates these resources are located in regional lowlands where gradients are small relative to mountainous terrains. Correlation with low groundwater spring density implies that permeability and/or aquifer thickness is high where reservoir temperatures are hottest. The correlation of low seismicity with high temperatures is somewhat surprising, however, inspection of a seismicity scatter plot verses reservoir temperature shows several high leverage points associated with the Socorro area that bias the trend (and correlation) between the two variables. Overall, the scatter plots and correlations of these KGRs suggests that the hottest and most promising exploration targets will be in settings that permit deep groundwater flow, where discharge locations are in lowlands or controlled by Quaternary faulting (i.e. regional forced-convection systems).

Table 3.5: KGR data layer correlations with reservoir temperature. Correlation is the Pearson correlation and ranges between -1 and 1. Divergence from zero is due to either positive or negative correlations between the specified variable with estimated geothermal reservoir temperature. Reservoir temperature estimates are from Reed et al. (1983) and Williams et al. (2008) and are based on analysis of chemical geothermometers, flow rate, temperature gradient, and geologic setting. Scatter plots of values flagged with an asterisk (*) are presented in Figure 3.36.

Data Layer	Correlation
Silica Geothermometer Temperature	0.69*
Gravity Anomaly	0.45*
Heat flow	0.23*
Quaternary Fault Density	0.23*
Depth to Basement	0.15*
Quaternary Fault Intersection Density	0.15
Volcanic Vent Density	0.05
Lithium Concentration	0.05
Depth to Water	0.04
Precipitation	-0.04
Boron Concentration	-0.09
State Map Fault Density	-0.09
Drainage Density	-0.12
Magnetic Intensity	-0.13
Volcanic Dike Density	-0.17
Hydraulic Gradient	-0.19
Earthquake Density	-0.21
Spring Density	-0.38*
Elevation	-0.47*
Crustal Thickness	-0.53*

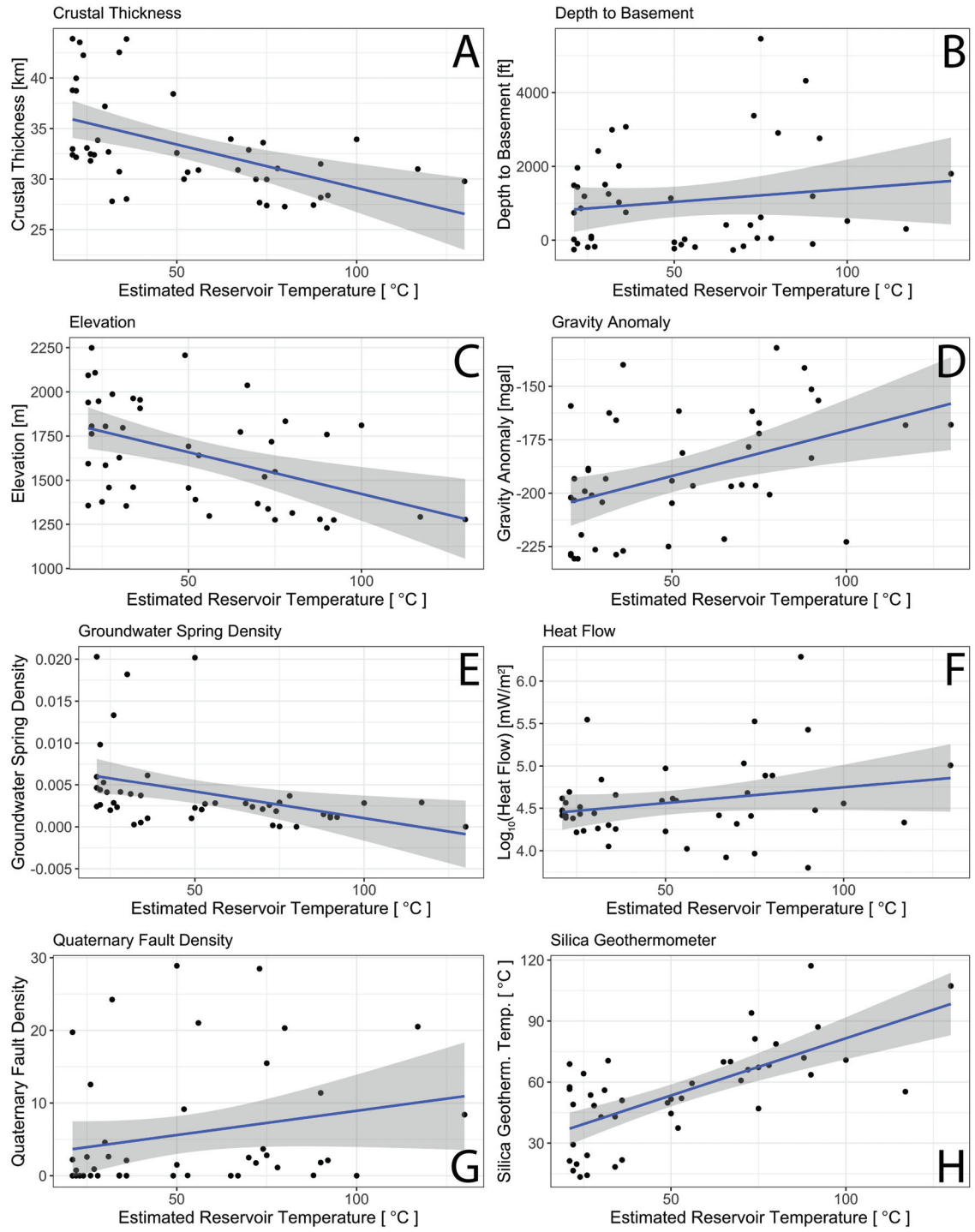


Figure 3.36: Scatter plots for select KGR variables vs. estimated reservoir temperature. A linear regression line (blue) with 0.95 confidence intervals (shaded gray) are shown for each data set. Correlations for all KGR variables with reservoir temperature are given in Table 3.5. Reservoir temperature estimates are from Reed et al. (1983) and Williams et al. (2008) and are based on analysis of chemical geothermometers, flow rate, temperature gradient, and geologic setting.

CONCLUSION

This work has developed two new approaches to characterizing and exploring continental crust. The first of these approaches considers the potential for electrical resistivity from magnetotelluric (MT) data to aid in estimating hydraulic permeability. By using hydrologic, forward magnetotelluric (MT), and inverse MT modeling, we determine that MT can likely estimate permeability by being integrated into hydrologic model calibration. Successful implementation of this approach hinges on having adequate control of subsurface porosity, mineralogy, and solute reaction rates. For this reason, this technique is likely most suitable for less complex geologic environments that can be more easily characterized. This methodology should be validated at several regional flow systems in which permeability is well constrained. In general, the incorporation of electrical resistivity into hydrologic models has the potential to significantly advance our knowledge of regional permeability patterns.

The second new approach resulting from this study involves combining principal component analysis (PCA) with k-means clustering to discover distinguishing characteristics between known-geothermal resources and identify future exploration targets. Applying this methodology to southwest New Mexico indicates known-geothermal resources in this region are mainly distinguishable by their tectonic/physiographic setting. Additionally, our approach identified several regions of elevated geothermal potential, which agree well with previous research in this area. This use of PCA and clustering is best suited for use during the preliminary and exploration phases of geothermal resource discovery to interpret large amounts of geothermal data. Even though our PCA results agree well with previous work in our study area, this methodology should still be validated in a more controlled manner using an extensive test dataset in a study area that is already very well understood. Our PCA results are non-unique and depend on the variables considered and how those variables are represented. A significant improvement to the methodology would include the incorporation of ensemble approaches, such as Monte Carlo methods, to find best-fit solutions that are more robust to the choice of clustering algorithm, data variables, and handling of outliers. Overall, the valuable geothermal insight provided by using our approach emphasizes the potential that conjunctive use of PCA and clustering has to foster geothermal industry advancement.

We have also further evaluated the conceptual model for basement-hosted geothermal systems within the Rio Grande rift of New Mexico by focusing on the Truth or Consequences, New Mexico geothermal resource. Previous hydrothermal modeling studies identify this system as likely involving deep (6 to 10 km) groundwater circulation within extremely permeable (10^{-12} m^2) crystalline base-

ment rocks (Person et al. 2013, Pepin et al. 2015). Aquifer testing, regional electrical resistivity observations, and hydrothermal modeling implies that the crystalline basement within the T or C geothermal watershed is some of the most permeable basement discovered to date; although comprehensive drilling and deep aquifer testing is required to undoubtedly confirm this notion. Regional groundwater flow does not appear to be compartmentalized by faults, although they may serve as conduits for ascending groundwater. High-permeability basement conditions seem to extend to depths exceeding 10 km, which is thought to be the result of prevalent interconnected fractures. This work is further evidence that active rift settings with extensive tectonic histories may contain large regions of naturally-elevated secondary fracture permeability to great depth. Generally, geothermal exploration and development efforts undertaken in rift settings should strongly consider the possibility of highly-fractured crystalline rocks hosting deep groundwater circulation and governing regional geothermal groundwater flow patterns. Hydrogeologists typically view the crystalline basement as being nearly impermeable at depth. The deep groundwater flow patterns and associated high permeability conditions implied by this study suggest that the crystalline basement is not always impermeable and that it may greatly influence regional flow patterns. This finding is further support that nuclear waste isolation projects should avoid tectonically active environments and that groundwater flow within the basement should be considered for regional studies. Lastly, this work provides additional evidence that electromagnetic geophysical methods (e.g. MT and TEM) when used in conjunction with hydrothermal models can aid in regional permeability quantification and conceptual model refinement.

REFERENCES

- Adams JJ, Bachu S (2002) Equations of state for basin geofluids: algorithm review and intercomparison for brines. *Geofluids*, **2**, 257271
- Agrawala GK (2007) Regional ground water interpretation using multivariate statistical methods. Center for Environmental Resource Management, The University of Texas at El Paso, PhD Dissertation, 148 p.
- Aizawa K, Koyama T, Hase H, Uyeshima M, Kanda W, Utsugi M, Yoshimura R, Yamaya Y, Hashimoto T, Yamazaki K, Komatsu S, Wantanabe A, Miyakawa K, Ogawa Y (2013) Three-dimensional resistivity structure and magma plumbing system of the Kirishima Volcanoes as inferred from broadband magnetotelluric data. *Journal of Geophysical Research: Solid Earth*, **119**, 198–215.
- Anderson A, Prencipe L, Todaro RM, Cuyler D, Eide E, Nathwani J, Thorsteinsson H, Stillman G (2011) Federal interagency geothermal activities. *Office of Energy Efficient & Renewable Energy DOE Geothermal Technologies Program Working Draft Report*, 38 p.
- Archie GE (1942) The Electrical Resistivity Log as an Aid in Determining Some Reservoir Characteristics. *Transactions of the AIME*, **146**, 9 p.
- Arehart GB, Coolbaugh MF, Poulson SR (2003) Evidence for a magmatic source of heat for the Steamboat Springs geothermal system using trace elements and gas geochemistry. *Geothermal Resources Council Transactions*, **27**, 269–274.
- Baars RM, Owens L, Tobin H, Norman D, Cumming W, Hill G (2006) Exploration and targeting of the Socorro, New Mexico direct use geothermal exploration well, a Gred III project. *Proceedings 31st Workshop on Geothermal Reservoir Engineering*, **SGP-TR-179**, 8 p.
- Baldridge WS, Keller GR, Haak V, Wendlandt E, Jiracek GR, Olsen KH (1995) The Rio Grande Rift. In: *Continental Rifts: Evolution, Structure, Tectonics* (ed. Olsen KH), Elsevier, Amsterdam. *Developments in Geotectonics*, **25**, 233–265.
- Barroll MW, Reiter M (1990) Analysis of the Socorro hydrogeothermal system: Central New Mexico. *Journal of Geophysical Research*, **95**, 21949–21963.
- Batzle M, Wang Z (1992) Seismic properties of pore fluids. *Geophysics*, **57**, 1396–1408.

- Bear J (1972) *Dynamics of Fluids in Porous Media*, American Elsevier Publishing Company, 764 p.
- Beven K (2006) A manifesto for the equifinality thesis. *Journal of Hydrology*, **320**, 18–36.
- Beven K, Freer J (2001) Equifinality, data assimilation, and uncertainty estimation in mechanistic modelling of complex environmental systems using the GLUE methodology. *Journal of Hydrology*, **249**, 11–29.
- Bibby HM, Caldwell TG, Brown C (2005) Determinable and non-determinable parameters of galvanic distortion in magnetotellurics. *Geophysical Journal International*, **163**, 915–930.
- Bielicki J, Blackwell D, Harp D, Karra S, Kelley R, Kelley S, Middleton R, Pepin J, Person M, Sutula G, Witcher J (2015) Hydrogeologic windows: regional signature detection for blind and traditional geothermal play fairways. *Los Alamos National Laboratory Final Report, LA-UR-15-28360*, 94 p.
- Bielicki J, Blackwell D, Harp D, Karra S, Kelley R, Kelley S, Middleton R, Person M, Sutula G, Witcher J (2016) Hydrogeologic windows and estimating the prospectivity of geothermal resources. *41st Workshop on Geothermal Reservoir Engineering Proceedings, SGP-TR-209*, 8 p.
- Benesty J, Chen J, Huang Y, Cohen I (2009) Pearson Correlation Coefficient. In: *Noise Reduction in Speech Processing*. Springer Topics in Signal Processing, vol 2. Springer, Berlin, Heidelberg.
- Booker JR (2014) The magnetotelluric phase tensor: A critical review. *Surv. Geophys.*, **35**, 7–40.
- Bourdet D, Ayoub JA, Pirard YM (1989) Use of pressure derivative in well-test interpretation. *SPE Formation Evaluation*, 293–302.
- Bourdet D, Whittle TM, Douglas AA, Pirard YM (1983) A new set of type curves simplifies well test analysis. *World Oil*, 95–106.
- Brace WF (1980) Permeability of crystalline and argillaceous rocks. *International Journal of Rock Mechanics and Mining Sciences & Geomechanics Abstracts*, **17**, 241–251. Abstract only.
- Brady PV, Arnold BW, Freeze GA, Swift PN, Bauer SJ, Kanney JL, Rechard RP, Stein JS (2009) Deep Borehole Disposal of High– Radioactive Waste. *Sandia Report, SAND2009–4401*, 75 p.
- Butler Jr. JJ (1988) Pumping tests in nonuniform aquifers - the radially symmetric case. *Journal of Hydrology*, **101**, 15–30.
- Butler Jr. JJ, Zhan X (2004) Hydraulic tests in highly permeable aquifers. *Water Resources Research*, **40**, 12 p.

- Caldwell TG, Bibby HM, Brown C (2004) The magnetotelluric phase tensor. *Geophys. J. Int.*, **158**, 457–469.
- Cather SM, Timmons JM, Karlstrom KE (2005) Regional tectonic inferences for the 1.4 Ga-Holocene lateral slip history of the Picuris-Pecos and related faults, northern New Mexico. *New Mexico Geological Society 56th Annual Fall Conference Guidebook*, 93–105.
- Chave A, Jones A (2012) *The Magnetotelluric Method: Theory and Practice*. Cambridge University Press, Cambridge, United Kingdom, 570 p.
- Christiansen AV, Auken E, Sorensen K (2009) The transient electromagnetic method. *Groundwater Geophysics*, 2nd Edition, 179–226.
- Cooper HH, Jacob CE (1946) A generalized graphical method for evaluating formation constants and summarizing well field history. *American Geophysical Union Transactions*, **27**, 526–534.
- Domenico PA, Palciauskas VV (1973) Theoretical analysis of forced convective heat transfer in regional ground-water flow. *Geological Society of America Bulletin*, **84**, 3803–3814.
- Egbert GD, Kelbert A (2012) Computational recipes for electromagnetic inverse problems. *Geophysical Journal International*, **189**, 251–267.
- Ellis AJ, Mahon WAJ (1964) Natural hydrothermal systems and experimental hot water/rock interactions. *Geochimica et Cosmochimica Acta*, **28**, 1323–1357.
- Ellis AJ, Mahon WAJ (1967) Natural hydrothermal systems and experimental hot water/rock interactions (Part II). *Geochimica et Cosmochimica Acta*, **31**, 519–538.
- Everitt BS, Hothorn T (2010) *A handbook of statistical analyses using R*. Taylor and Francis Group, LLC, Boca Raton, Florida, USA, 361 p.
- Everitt BS, Landau S, Leese M, Stahl D (2011) *Cluster Analysis*. John Wiley & Sons, Ltd., West Sussex, United Kingdom, 348 p.
- Ferguson G, Grasby SE (2011) Thermal springs and heat flow in North America. *Geofluids*, **11**, 294–301.
- Fetter CW (2001) *Applied Hydrogeology*. Prentice-Hall, Inc., Upper Saddle River, New Jersey, 598 p.
- Fournier R (1989) Lectures on geochemical interpretation of hydrothermal waters. *UNU Geothermal Training Programme, Reykjavik Iceland*, **10**, 54 p.
- Franssen HJH, Alcolea A, Riva M, Bakr M, van der Wiel N, Stauffer F, Guadagnini A (2009) A comparison of seven methods for the inverse modelling of groundwater flow. Application to the characterisation of well catchments. *Advances in Water Resources*, **32**, 851–872.

- Frape SK, Blyth A (2003) Deep Fluids in the Continent: II. Crystalline Rocks. In: *Surface and Groundwater, Weathering, and Soils* (eds. Drever JI, Holland HD, Turekian KK), 5, Elsevier-Pergamon, Oxford, 541–580.
- Freeze RA, Cherry JA (1979) *Groundwater*. Prentice Hall, Englewood Cliffs, NJ, USA 604 p.
- Furbish DJ (1997) Fluid physics in geology: An introduction to fluid motions on Earths surface and within its crust. Oxford University Press, New York, New York, 476 p.
- Gamble T, Goubau W, Clarke J (1979) Magnetotellurics with a remote magnetic reference. *Geophysics*, **44**, 53–68.
- Garg SK, Pritchett JW, Wannamaker PE, Combs J (2007) Characterization of geothermal reservoirs with electrical surveys: Beowawe geothermal field. *Geothermics*, **36**, 487–517.
- Gazley MF, Collins KS, Robertson J, Hines BR, Fisher LA, McFarlane A (2015) Application of principal component analysis and cluster analysis to mineral exploration and mine geology. *AusIMM New Zealand Branch Annual Conference*, 131–139.
- Geosystem SRL (1998) A guide to using WinGLink. Geosystem SRL. Milan, Italy, 473 p.
- Gewers FL, Ferreira GR, de Arruda HF, Silva FN, Comin CH, Amancio DR, da F. Costa L (2018) Principal Component Analysis: A Natural Approach to Data Exploration. *CoRR*, **abs/1804.02502**, 31 p.
- Ghosh D, Vogt A (2012) Outliers: An evaluation of methodologies. *Section on Survey Research Methods JSM*, 6 p.
- Gleeson T, Ingebritsen S (2017) *Crustal Permeability*. 1st edition, Wiley-Blackwell, 396 p.
- Glover PWJ, Hole MJ, Pous J (2000) A modified Archie's law for two conducting phases. *Earth and Planetary Science Letters*, **180**, 369–383.
- Harrison R, Cather S (2004) The Hot Springs fault systems of south-central New Mexico evidence for northward translation of the Colorado Plateau during the Laramide orogeny. *New Mexico Bureau of Geology and Mineral Resources Bulletin* **160**, 161–180.
- Harrison R, Lozinsky R, Eggleston T, McIntosh W (1993) Geologic map of the Truth or Consequences 30x60 minute quadrangle. *New Mexico Bureau of Mines and Mineral Resources Open-file Report 390*, Socorro, 1:100,000 scale, 1 sheet, 16 p.
- Hartigan JA, Wong MA (1979) A K-means clustering algorithm. *Applied Statistics*, **28**, 100108.

- Harvey C, Beardsmore G (2014) *Best practices guide for geothermal exploration*. Bochum University of Applied Sciences, Bochum, Germany, 196 p.
- Hastie T, Tibshirani R, Friedman J (2009) *The elements of statistical learning: Data mining, inference, and prediction*. Springer Science + Business Media, New York, New York, 745 p.
- Heise W, Caldwell TG, Bibby HM, Brown C (2006) Anisotropy and phase splits in magnetotellurics. *Physics of the Earth and Planetary Interiors*, **158**, 107–121.
- Hersir GP, Flovenz OG (2013) Resistivity surveying and electromagnetic methods. *IGA Academy Report*, **0110**, 10 p.
- Ho PC, Bianchi H, Palmer DA, Wood RH (2000) Conductivity of dilute aqueous electrolyte solutions at high temperatures and pressures using a flow cell. *Journal of Solution Chemistry*, **29**, 217–235.
- Hyndman RD, Shearer PM (1989) Water in the lower continental crust: modelling magnetotelluric and seismic reflection results. *Geophysical Journal International*, **98**, 343–365.
- Iglewicz B, Hoaglin DC (1993) Volume 16: How to detect and handle outliers. *American Society for Quality Control: Statistical Techniques*, 77 p.
- Ingebritsen S, Sanford W, Neuzil C (1998) *Groundwater in geologic processes*. Second edition, Cambridge University Press, New York, 536 p.
- Ingebritsen SE, Manning CE (2010) Permeability of the continental crust: dynamic variations inferred from seismicity and metamorphism. *Geofluids*, **10**, 193–205.
- James G, Witten D, Hastie T, Tibshirani R (2013) *An introduction to statistical learning with applications in R*. Springer Science + Business Media, New York, New York, 426 p.
- Jeanloz R, Stone H (2013) Enhanced geothermal systems. *U.S. Department of Energy Report, JSR-13-320*, 147 p.
- Jiang X, Wan L, Wang J, Yin B, Fu W, Lin C (2014) Field identification of groundwater flow systems and hydraulic traps in drainage basins using a geophysical method. *Geophysical Research Letters*, **41**, 2812–2819.
- Jiang Y, Guo H, Jia Y, Cao Y, Hu C (2015) Principal component analysis and hierarchical cluster analyses of arsenic groundwater geochemistry in the Hetao basin, Inner Mongolia. *Chemie der Erde*, **75**, 195–205.
- Jiracek GR, Kinn CL, Scott CL, Kuykendall MG, Baldridge WS, Biehler S, Braile LW, Ferguson JF, Gilpin B (1996) Tracing crustal isotherms under the western margin of the Jemez Mountains using SAGE and industry magnetotelluric data. *New Mexico Geological Society Guidebook*, **47**, 129–133.

- Jochems AP, Koning DJ (2014) Geologic Map of the Williamsburg 7.5–Minute Quadrangle, Sierra County, New Mexico. *New Mexico Bureau of Geology and Mineral Resources Open-File Digital Geologic Map, OF-GM 250*.
- Jones AG (1992) Electrical conductivity of the continental lower crust. *Continental Lower Crust*, 81–143.
- Juhlin C, Sandstedt H (1989) Storage of nuclear waste in very deep boreholes: Feasibility study and assessment of economic potential. Part I: Geological considerations. Part II: Overall facility plan and cost analysis. Swedish Nuclear Fuel and Waste Management CO, Technical Report 89–39, 245 p.
- Karingithi C (2009) Chemical geothermometers for geothermal exploration. *Short Course IV on Exploration for Geothermal Resources, organized by UNU-GTP, KenGen and GDC*, 12 p.
- Keller GR, Khan MA, Morgan P, Wendlandt RF, Baldridge WS, Olsen KH, Prodehl C, Braile LW (1991) A comparative study of the Rio Grande and Kenya rifts. *Tectonophysics*, **197**, 355–371.
- Kelley SA, Chapin CE (1997) Cooling histories of mountain ranges in the southern Rio Grande Rift based on apatite fission-track analysis a reconnaissance survey. *New Mexico Geology*, **19**, 1–14.
- Koning DJ, Jochems AP, Foster R, Cox B, Lucas S, Mack GH, Zeigler KE (2018) Geologic map of the Cuchillo 7.5–Minute Quadrangle, Sierra County, New Mexico. *New Mexico Bureau of Geology and Mineral Resources Open-File Digital Geologic Map, OF-GM 271*, 169 p.
- Krieger L, Peacock JR (2014) MTpy: A Python toolbox for magnetotellurics. *Computers & Geosciences*, **72**, 167–175.
- Laney P, Brizzee J (2003) New Mexico Geothermal Resources. *Idaho National Engineering and Environmental Laboratory, INEEL/MISC-2002-395 Rev. 1*, 1 p.
- Langmuir D (1997) *Aqueous Environmental Geochemistry*. 1st edition, Upper Saddle River, NJ, Prentice Hall, 600 p.
- Lemieux JM, Sudicky EA, Peltier WR, Tarasov L (2008a) Simulating the impact of glaciations on continental groundwater flow systems: 1. Relevant processes and model formulation. *Journal of Geophysical Research: Earth Surface*, **113**, 12 p.
- Lemieux JM, Sudicky EA, Peltier WR, Tarasov L (2008b) Simulating the impact of glaciations on continental groundwater flow systems: 2. Model application to the Wisconsinian glaciation over the Canadian landscape. *Journal of Geophysical Research: Earth Surface*, **113**, 18 p.
- Lide DR, Haynes WM (2009) *Handbook of chemistry and physics*. 90th edition, CRC Press, Boca Raton, Florida.

- Lindsey CR, Neupane G, Spycher N, Fairley JP, Dobson P, Wood T, McLing T, Conrad M (2018) Cluster analysis as a tool for evaluating the exploration potential of known geothermal resource areas. *Geothermics*, **72**, 358–370.
- Lindsey NJ, Kaven JO, Davatzes N, Newman GA (2017) Compartmentalization of the Coso East Flank geothermal field imaged by 3-D full-tensor MT inversion. *Geophysical Journal International*, **208**, 652–662.
- Lund JW, Freeston DH, Boyd TL (2011) Direct utilization of geothermal energy 2010 worldwide review. *Geothermics*, **40**, 159–180.
- Lundquist JD, Cayan DR (2007) Surface temperature patterns in complex terrain: Daily variations and long-term change in the central Sierra Nevada, California. *Journal of Geophysical Research: Atmospheres*, **112**, 15 p.
- MacInnes S (2010a) *TEMAVGW Documentation*. Zonge Engineering and Research Organization, Tucson, AZ, USA 29 p.
- MacInnes S (2010b) *MTEdit Documentation*. Zonge Engineering and Research Organization, Tucson, AZ, USA 14 p.
- MacInnes S (2014a) *MTMerge Documentation*. Zonge Engineering and Research Organization, Tucson, AZ, USA 15 p.
- MacInnes S (2014b) *MTFT24 Documentation*. Zonge Engineering and Research Organization, Tucson, AZ, USA 23 p.
- MacInnes S, Raymond M (2009) *STEMINV Documentation: ZONGE Data Processing, Smooth-Model TEM Inversion*. Zonge Engineering and Research Organization, Tucson, AZ, USA 29 p.
- Mailloux B, Person M, Kelley S, Dunbar N, Cather S, Strayer L, Hudleston P (1999) Tectonic controls on the hydrogeology of the Rio Grande Rift, New Mexico. *Water Resources Research*, **35**, 2641–2659.
- Manning CE, Ingebritsen SE (1999) Permeability of the continental crust: the implications of geothermal data and metamorphic systems. *Reviews of Geophysics*, **37**, 127–150.
- Martinec J, Rango A (1986) Parameter values for snowmelt runoff modelling. *Journal of Hydrology*, **84**, 197219.
- Mazurek, M (2000) Geological and hydraulic properties of water-conducting features in crystalline rocks. In: *Hydrogeology of Crystalline Rocks* (eds Stober I, Bucher K), pp. 3–26. Kluwer Academic Publishers, Dordrecht
- McKenna JR, Blackwell DD (2004) Numerical modeling of transient Basin and Range extensional geothermal systems. *Geothermics*, **33**, 457–476.

- Mikucki JA, Auken E, Tulaczyk S, Virginia RA, Schamper C, Sorensen KI, Doran PT, Dugan H, Foley N (2015) Deep groundwater and potential subsurface habitats beneath an Antarctic dry valley. *Nature Communications*, **6**, 9 p.
- Moeck IS (2014) Catalog of geothermal play types based on geologic controls. *Renewable and Sustainable Energy Reviews*, **37**, 867–882.
- Morgan P, Seager WR, Golombek MP (1986) Cenozoic thermal mechanical and tectonic evolution of the Rio Grande Rift. *Journal of Geophysical Research*, **91**, 6263–6276.
- Morgan P, Witcher JC (2011) Geothermal resources along the southern Rocky Mountains and the Rio Grande rift. *The Mountain Geologist*, **48**, 81–93.
- Morissette L, Chartier S (2013) The k-means clustering technique: general considerations and implementation in Mathematica. *Tutorials in Quantitative Methods for Psychology*, **9**, 15–24.
- Munoz G (2014) Exploring for geothermal resources with electromagnetic methods. *Survey Geophysics*, **35**, 101–122.
- Nabighian MN, Macnae JC (1991) Time domain electromagnetic prospecting methods. *Electromagnetic Methods in Applied Geophysics*, **3**, 427–520.
- National Research Council (1930) *International Critical Tables of Numerical Data, Physics, Chemistry and Technology*. Washington, DC, The National Academies Press.
- Nesbitt BE (1993) Electrical resistivities of crustal fluids. *Journal of Geophysical Research*, **98**, 4301–4310.
- Newman GA, Gasperikova E, Hoversten GM, Wannamaker PE (2008) Three-dimensional magnetotelluric characterization of the Coso geothermal field. *Geothermics*, **37**, 369–399.
- Noyes AA (1907) *The electrical conductivity of aqueous solutions*. Cornell University Library. 374 p
- NREL (2018) Geothermal Prospector. *National Renewable Energy Laboratory*. <https://maps.nrel.gov/geothermal-prospector/>
- Olhoeft GR (1985) Low-frequency electrical properties. *Geophysics*, **50**, 2492–2503.
- Palacky GJ (1988) Resistivity characteristics of geologic targets. *Electromagnetic Methods in Applied Geophysics—Theory*, **1**, 53–129.
- Park YJ, Sudicky EA, Sykes JF (2009) Effects of shield brine on the safe disposal of waste in deep geologic environments. *Advances in Water Resources*, **32**, 1352–1358.

Parkinson WD (1983) *Introduction to Geomagnetism*, Scottish Academic Press, New York, USA 433 p.

Peacock JR, Mangan MT, McPhee D, Ponce DA (2015) Imaging the magmatic system of Mono Basin, California with magnetotellurics in three dimensions. *Journal of Geophysical Research: Solid Earth*, **120**, 7273–7289.

Peacock JR, Thiel S, Heinson GS, Reid P (2013) Time-lapse magnetotelluric monitoring of an enhanced geothermal system. *Geophysics*, **78**, B121–B130.

Pellerin L, Hohmann GW (1990) Transient electromagnetic inversion: A remedy for magnetotelluric static shifts. *Geophysics*, **55**, 1242–1250.

Pellerin L, Johnston JM, Hohmann GW (1996) A numerical evaluation of electromagnetic methods in geothermal exploration. *Geophysics*, **61**, 121–130.

Pepin J, Person M, Phillips F, Kelley S, Timmons S, Owens L, Witcher J, Gable C (2015) Deep fluid circulation within crystalline basement rocks and the role of hydrologic windows in the formation of the Truth or Consequences, New Mexico low-temperature geothermal system. *Geofluids*, **15**, 139–160.

Person M, Banerjee A, Hofstra D, Sweetkind D, Gao Y (2008) Hydrologic models of modern and fossil geothermal systems within the Great Basin: implications for Carlin-Type gold mineralization. *Geosphere*, **4**, 888–917.

Person M, Phillips F, Kelley S, Timmons S, Pepin J, Blom L, Haar K, Murphy M (2013) Assessment of the sustainability of geothermal development within the Truth or Consequences Hot-Springs District, New Mexico. *New Mexico Bureau of Geology and Mineral Resources Open-file Report*, **551**, 65 p.

Philipp SL, Gudmundsson A, Oelrich A (2007) How structural geology can contribute to make geothermal projects successful. *Proceedings European Geothermal Congress, June 2007*, 10 p.

Polsky Y, Capuano Jr. L, Finger J, Huh M, Knudsen S, Mansure AJ, Raymond D, Swanson R (2008) Enhanced Geothermal Systems (EGS) Well Construction Technology Evaluation Report. *Sandia Report*, SAND2008–7866, 108 p.

Powell WC (1929) Report of an investigation of the Hot Springs Artesian Basin, Hot Springs, New Mexico. *Ninth Biennial Report of the State Engineer of New Mexico*, 1929–1930, 120–129.

PRISM (2012) United States Average Annual Precipitation, 1981-2010 (800m; BIL). *PRISM Climate Group at Oregon State University*. <http://prism.oregonstate.edu/ normals/>

Pritchett JW (2004) Finding Hidden Geothermal Resources in the Basin and Range Using Electrical Survey Techniques: A computational Feasibility Study. *Department of Energy Report*, INEEL/EXT–04–02539, 211 p.

- Provost AM, Voss CI, Neuzil CE (1998) Glaciation and regional ground-water flow in the Fennoscandian shield. *Geofluids*, **12**, 79–96.
- Pursley J, Bilek SL, Ruhl CJ (2013) Earthquake catalogs for New Mexico and bordering areas: 2005-2009. *New Mexico Geology*, **35**, 1, 3–12.
- Quick H, Michael J, Arslan U, Huber H (2013) Geothermal application in low-enthalpy regions. *Renewable Energy*, **49**, 133–136.
- Quist AS, Marshall WL (1968) Electrical conductances of aqueous sodium chloride solutions from 0 to 800°C and at pressures to 4000 bars. *The Journal of Physical Chemistry*, **72**, 684–703.
- R Core Team (2013) R: A Language and Environment for Statistical Computing. *R Foundation for Statistical Computing*, Vienna. <http://www.R-project.org/>
- Ranjram M, Gleeson T, Luijendijk (2015) Is the permeability of crystalline rock in the shallow crust related to depth, lithology or tectonic setting?. *Geofluids*, **15**, 106–119.
- Reed MJ, Mariner RH, Brook CA, Sorey ML (1983) Selected data for low-temperature (Less than 90°C) geothermal systems in the United States; reference data for U.S. Geological Survey circular 892. *U.S. Geological Survey Open-File Report*, **83-250**, 82 p.
- Refsgaard JC, Christensen S, Sonnenborg TO, Seifert D, Hojberg AL, Troldborg L (2012) Review of strategies for handling geological uncertainty in ground-water flow and transport modeling. *Advances in Water Resources*, **36**, 36–50.
- Reiter M, Eggleston R, Broadwell B, Minier J (1986) Estimates of terrestrial heat flow from deep petroleum tests along the Rio Grande Rift in Central and Southern New Mexico. *Journal of Geophysical Research*, **91**, 6225–6245.
- Rinehart EJ, Sanford AR (1981) Upper crustal structure of the Rio Grande rift near Socorro, New Mexico, from inversion of microearthquake S-wave reflections. *Bulletin of the Seismological Society of America*, **71**, 437–451.
- Rojstaczer SA, Ingebritsen SE, Hayba DO (2008) Permeability of continental crust influenced by internal and external forcing. *Geofluids*, **8**, 128–139.
- Sanford AR, Lin K, Tsai I, Jaksha LH (2002) Earthquake catalogs for New Mexico and bordering areas: 1869-1998. *New Mexico Bureau Geology Mineral Resources Circular*, **210**, 1–110.
- Sanford AR, Mayeau TM, Schlue JW, Aster RC, Jaksha LH (2006) Earthquake catalogs for New Mexico and bordering areas II: 1999-2004. *New Mexico Geology*, **28**, 4, 99–109.
- Schwartz FW, Zhang H (2003) *Fundamentals of Ground Water*. 1st edition, John Wiley & Sons, 583 p.

- Seager WR, Mack GH (2003) Geology of the Caballo Mountains, New Mexico. *New Mexico Bureau of Geology and Mineral Resources Memoir* 49, 136 p.
- Seager WR, Morgan P (1979) Rio Grande Rift in southern New Mexico, west Texas, and northern Chihuahua. In: *Rio Grande Rift-Tectonics and Magmatism* (ed. Riecker RE), 87–106. American Geophysical Union, Washington, DC, USA.
- Simpson F, Bahr K (2005) *Practical Magnetotellurics*. Cambridge University Press, Cambridge, United Kingdom, 272 p.
- Smith L, Chapman DS (1983) On the thermal effects of groundwater flow: 1. Regional scale systems. *Journal of Geophysical Research*, **88**, 593–608.
- Spane Jr. FA, Wurstner SK (1993) DERIV: A computer program for calculating pressure derivatives for use in hydraulic test analysis. *Groundwater*, **31**, 814–822.
- Spichak V, Manzella A (2009) Electromagnetic sounds of geothermal zones. *Journal of Applied Geophysics*, **68**, 459–478.
- Stober I, Bucher K (2007) Hydraulic properties of the crystalline basement. *Hydrogeology Journal*, **15**, 213–224.
- Stober I, Bucher K (2015a) Hydraulic conductivity of fractured upper crust: insights from hydraulic tests in boreholes and fluid–rock interaction in crystalline basement rocks. *Geology*, **15**, 161–178.
- Stober I, Bucher K (2015b) Significance of Hydraulic Conductivity as Precondition to Fluid Flow in Fractured and Faulted Crystalline Basement and its Impact on Fluid–Rock Interaction Processes. *Proceedings World Geothermal Congress April 2015*, p 6.
- Telford WM, Geldart LP, Sheriff RE (1990) *Applied geophysics*. Cambridge University Press, Cambridge, United Kingdom, 770 p.
- Theis CV, Taylor GC, Murray CR (1941) Thermal waters of the Hot Springs Artesian Basin, Sierra County, NM. *Fourteenth and Fifteenth Biennial Reports of the State Engineer of New Mexico*, 1938–1942, 421–492.
- Thorsteinsson HH, Tester JW (2010) Barriers and enablers to geothermal district heating system development in the United States. *Energy Policy*, **38**, 2, 803–813.
- Townend J, Zoback MD (2000) How faulting keeps the crust strong. *Geology*, **28**, 399–402.
- Tukey JW (1977) *Exploratory Data Analysis*. Pearson, 712 p.
- Ucok H, Ershaghi I, Olhoeft G (1980) Electrical resistivity of geothermal brines. *Journal of Petroleum Technology*, 717–727.

- UNM (2018) Digital Geologic Map of New Mexico - Volcanic Vents. *Earth Data Analysis Center, University of New Mexico*. <https://catalog.data.gov/dataset/digital-geologic-map-of-new-mexico-volcanic-vents>
- Ussher G, Harvey C, Johnstone R, Anderson E (2000) Understanding the resistivities observed in geothermal systems. *Proceedings World Geothermal Congress*, 1915–1920.
- USGS (2018a) Earthquake Hazards Program Earthquake Catalog. *U.S. Geological Survey*. <https://earthquake.usgs.gov/earthquakes/search/>
- USGS (2018b) National Water Information System. *U.S. Geological Survey*. <https://waterdata.usgs.gov/nwis>
- USGS (2018c) Energy and Environment in the Rocky Mountain Area. *U.S. Geological Survey*. <https://my.usgs.gov/eerma/>
- Vozoff K (1991) The magnetotelluric method. *Electromagnetic Methods in Applied Geophysics*, 2, 641–711.
- Wahba G (1990) *Spline models for observations data*. Society for Industrial and Applied Mathematics, Philadelphia, Pennsylvania, 169 p.
- Wallace JM, Hobbs PV (2006) *Atmospheric Science: An Introductory Survey*. 2nd edition, Academic Press, 504 p.
- Wannamaker PE, Doerner WM, Hasterok DP (2006) Cryptic faulting and multi-scale geothermal fluid connections in the Dixie Valley-Central Nevada seismic belt area; implications from MT resistivity surveying. *Proceedings, 31st Workshop on Geothermal Reservoir Engineering*, SGP-TR-179, 8 p.
- Wannamaker PE, Maris V, Hasterok DP, Doerner WM (2010) Extensional Tectonism, Magmatic–Hydrothermal Connections and Geothermal Systems of the Southwestern United States as Revealed Through Magnetotelluric Surveying. *SEG Denver 2010 Annual Meeting*, 3908–3912.
- Wannamaker P, Maris V, Sainsbury J, Iovenitti J (2013) Intersecting fault trends and crustal-scale fluid pathways below the Dixie Valley Geothermal Area, Nevada, inferred from 3D magnetotelluric surveying. *Proceedings 38th Workshop on Geothermal Reservoir Engineering*, SGP-TR-198, 9 p.
- Wannamaker PE, Rose PE, Doerner WM, Berard BC, McCulloch J, Nurse K (2004) Magnetotelluric surveying and monitoring at the Coso geothermal area, California, in support of the enhanced geothermal systems concept: survey parameters and initial results. *Proceedings 29th Workshop on Geothermal Reservoir Engineering*, SGP-TR-175, 8 p.
- Wannamaker PE, Ward SH, Hohmann GW, Sill WR (1983) Deep Resistivity Structure in Southwestern Utah and Its Geothermal Significance. *Department of Energy Report*, 12079—89, 106 p.

- Wells SG, Granzow H (1981) Hydrogeology of the thermal aquifer near Truth or Consequences, New Mexico. In: *State-Coupled Low-Temperature Geothermal Resource Assessment Program*, Fiscal Year 1980, 3–5 to 3–51.
- Williams CF, Reed MJ, Mariner RH, DeAngelo J, Galanis Jr. SP (2008) Assessment of moderate- and high-temperature geothermal resources of the United States. *U.S. Geological Survey Fact Sheet 2008–3082*, 4 p.
- Winther PK (2009) Magneotelluric investigation of the Santo Domingo Basin, Rio Grande Rift, New Mexico. *San Diego State University M.S. Thesis*, 148 p.
- Witcher JC (1988) Geothermal resources of southwestern New Mexico and southeastern Arizona. *New Mexico Geological Society Guidebook*, **39**, 191–198.
- Witcher JC, Reiter M, Bland D, Barroll MW (1992) Geothermal resources in New Mexico. *New Mexico Geology*, 3 p.
- Witcher JC (1995) Geothermal resource data base New Mexico. *Southwest Technology Development Institute, New Mexico State University*, 38 p.
- Witcher JC (2002) Geothermal energy in New Mexico. *GHC Bulletin*, 5 p.
- Witcher JC, Lund JW, Seawright DE (2002) Lightning Dock KGRA New Mexico's largest geothermal greenhouse, largest aquaculture facility, and first binary electrical power plant. *GHC Bulletin*, 5 p.
- Zhang Y, Edel S, Pepin J, Person M, Broadhead R, Ortiz JP, Bilek S, Mozley P, Evans J (2016) Exploring the Potential Linkages Between Oil-Field Brine Reinjection, Crystalline Basement Permeability, and Triggered Seismicity for the Dagger Draw Oil Field, Southeastern New Mexico, USA Using Hydrologic Modeling. *Geofluids*, **16**, 971–987.
- Zimmerman GH, Gruszkiewicz MS, Wood RH (1995) New apparatus for conductance measurements at high temperatures: conductance of aqueous solutions of LiCl, NaCl, NaBr, and CsBr at 28 MPa and water densities from 700 to 260 kg m⁻³. *Journal of Physical Chemistry*, **99**, 11612–11625.

NEW APPROACHES TO
GEOTHERMAL RESOURCE EXPLORATION
AND CHARACTERIZATION

by

Jeffrey Donald Pepin

Permission to make digital or hard copies of all or part of this work for personal or classroom use is granted without fee provided that copies are not made or distributed for profit or commercial advantage and that copies bear this notice and the full citation on the last page. To copy otherwise, to republish, to post on servers or to redistribute to lists, requires prior specific permission and may require a fee.

